

# Important Notice

This copy may be used only for the purposes of research and private study, and any use of the copy for a purpose other than research or private study may require the authorization of the copyright owner of the work in question. Responsibility regarding questions of copyright that may arise in the use of this copy is assumed by the recipient.

UNIVERSITY OF CALGARY

Exploring a Maya Pyramid Ruin using Seismic and Radar Tomography

by

Matthew David Allen

A THESIS

SUBMITTED TO THE FACULTY OF GRADUATE STUDIES  
IN PARTIAL FULFILMENT OF THE REQUIREMENTS FOR THE  
DEGREE OF MASTER OF SCIENCE

DEPARTMENT OF GEOSCIENCE

CALGARY, ALBERTA

APRIL, 2009

© Matthew Allen 2009

UNIVERSITY OF CALGARY  
FACULTY OF GRADUATE STUDIES

The undersigned certify that they have read, and recommend to the Faculty of Graduate Studies for acceptance, a thesis entitled "Exploring a Maya Pyramid Ruin using Seismic and Radar Tomography" submitted by Matthew Allen in partial fulfilment of the requirements of the degree of Master of Science.

---

*Supervisor, Dr. Robert R. Stewart, Department of Geoscience*

---

*Dr. Don Lawton, Department of Geoscience*

---

*Dr. Brian Moorman, Department of Geography*

---

*Date*

## Abstract

A number of seismic surveys, in addition to a ground penetrating radar (GPR) test, have been conducted on a Maya pyramid ruin at the Maax Na archaeological site in Belize, Central America. The purpose of these surveys was to determine whether seismic and GPR tomography techniques could be used to create images of the pyramid's carbonate rubble interior and locate regions of archaeological interest. The hammer seismic signal transmitted through the entire 15 m high pyramid. Transmitted wave first breaks (time and amplitude) were picked for all the surveys and used in various inversions to create velocity and attenuation maps of the interior

The majority of interior seismic velocities fall within the range of 200 to 1000 m/s for all the different surveys. This velocity range falls into the expected values found using ultrasonic measurements of rock samples from the pyramid. The derived attenuation values for the interior of the pyramid also fell within a common range for all the different surveys. The majority of attenuation values fell between 0.1 and 5 Np/m. The derived models produced similar results in expected velocity and attenuation ranges thereby, providing confidence in the model. The derived models displayed interesting anomaly areas inside the pyramid. These areas may be associated with regions of archaeological significance.

A GPR test was performed on the pyramid to determine the viability of GPR in performing tomography on large structures. The GPR signal failed to penetrate through the entire pyramid. However, with the first breaks that were available a model was derived with reasonable velocities (0.08 to 0.12 m/ns).

## Acknowledgements

I would like to thank the following people for their contribution to this thesis.

- I would like to thank my supervisor Dr. Rob Stewart for suggesting a thesis topic that enabled me to have many exciting experiences while continuing my education.
- I thank Dr. Bing Zhou, for answering my many emails for help about his 2Dray\_tomo program, and going to the extent of modifying his code just for me despite never having met in person.
- I am thankful to Paul Hebert and the rest of Quantum Seismic Services for their discussions about processing and producing the shot stacks used in this thesis.
- I would like to thank those associated with the Maax Na Archaeological Project for allowing us to use our geophysical techniques on such a unique site.
- I am grateful to all the students, staff and faculty who have made doing my study more enjoyable.
- Finally, I would like to thank my wife and the rest of my family for providing the encouragement and support I needed throughout my many years of university. I could not have done this without all of you.

## **Dedication**

To my wife Amber and my parents; this thesis only exists because of all of you.

## Table of Contents

Approval Page.....	ii
Abstract.....	iii
Acknowledgements.....	iv
Dedication.....	v
Table of Contents.....	vi
List of Tables.....	ix
List of Figures and Illustrations.....	xii
List of Symbols, Abbreviations and Nomenclature.....	xxiii
CHAPTER ONE: INTRODUCTION.....	1
1.1 Introduction.....	1
1.2 Thesis Objectives.....	2
1.3 Physical Setting.....	3
1.3.1 Geography.....	3
1.3.2 Geology.....	5
1.4 The Maya.....	8
1.4.1 Maya Culture.....	8
1.4.2 Mayan Pyramid Architecture.....	9
1.4.3 Maax Na.....	11
1.5 Previous Research.....	14
CHAPTER TWO: ROCK PROPERTIES.....	18
2.1 Rock Type.....	18
2.2 Ultrasonic Method.....	20
2.2.1 Transducers.....	20
2.2.2 Velocity Measurement.....	21
2.3 Dry Measurements.....	22
2.3.1 P and S velocities.....	22
2.3.2 Velocity and Frequency.....	25
2.3.3 Vp/Vs.....	27
2.3.4 Density.....	30
2.4 Saturated Measurements.....	33
2.4.1 Vp and Vs Measurements.....	33
2.4.2 Vp/Vs Value.....	37
2.4.3 Density.....	39
2.5 Porosity.....	41
2.6 Summary.....	44
CHAPTER THREE: SEISMIC TOMOGRAPHY.....	46
3.1 Hammer Seismic Viability.....	46
3.2 Current Surveys.....	50
3.2.1 Lower 2D Seismic Survey.....	50
3.2.2 Upper 2D Seismic Survey.....	52
3.2.3 Lower 3D Seismic Survey.....	54
3.2.4 Upper 3D Seismic Survey.....	55

3.2.5 Combined 3D Survey .....	56
3.3 Grid Size and Fold .....	56
3.3.1 2D Surveys .....	56
3.3.2 3D Surveys .....	58
3.4 Straight Ray Traveltime Tomography Results .....	59
3.4.1 Lower 2D Survey .....	60
3.4.2 Upper 2D Survey .....	64
3.4.3 Lower 3D Survey .....	68
3.4.4 Upper 3D Survey .....	71
3.4.5 Combined 3D survey .....	74
3.5 Straight Ray Amplitude Tomography Results .....	77
3.5.1 Lower 2D Survey .....	78
3.5.2 Upper 2D Survey .....	79
3.5.3 Lower 3D Survey .....	82
3.5.4 Upper 3D Survey .....	83
3.5.5 Combined 3D Survey .....	87
3.6 Curved Ray Traveltime Tomography .....	89
3.6.1 Lower 2D Survey .....	91
3.6.2 Upper 2D Survey .....	96
3.7 Curved Ray Amplitude Tomography .....	100
3.7.1 Lower 2D Survey .....	100
3.7.2 Upper 2D Survey .....	103
3.8 Summary .....	105
CHAPTER FOUR: GPR TOMOGRAPHY .....	108
4.1 Data Analysis .....	109
4.2 2D Straight Ray Tomography .....	113
4.3 3D Straight Ray Tomography .....	116
4.4 2D Curved Ray Tomography .....	118
4.5 Summary .....	124
CHAPTER FIVE: CONCLUSIONS AND FUTURE WORK .....	126
5.1 Conclusions .....	126
5.1.1 Seismic and GPR Viability .....	126
5.1.2 Straight Ray Tomography .....	126
5.1.3 Curved Ray Tomography .....	127
5.1.4 Regions of Archaeological Significance .....	127
5.2 Future Work .....	129
REFERENCES .....	133
APPENDIX A: ROCK PROPERTY VALUES .....	140
A.1. Photographs of Rock Samples .....	140
A.2. Tables of Measurements for Dry and Saturated Maax Na Samples .....	141
APPENDIX B: INVERSION TECHNIQUES .....	146
B.1. Traveltime Picking .....	146

B.2. Amplitude Picking .....	146
B.3. Straight Ray Techniques .....	147
B.3.1. Direct Division (DD) .....	147
B.3.2. Damped Least Squares (DLS) .....	149
B.3.3. Singular Value Decomposition (SVD) .....	153
B.3.4. Conjugate Gradient (CG).....	158
B.4. Curved Ray Technique.....	160
B.4.1. Shortest Path Calculation.....	160
B.4.2. Finding the distance (Jacobian) matrix.....	164
B.4.3. Iterative Inversion Algorithm .....	166
B.5. Amplitude Inversion.....	167
APPENDIX C: ADDITIONAL CURVED RAY MODELS.....	169
C.1. Upper 2D Survey.....	169
C.1.1. Traveltime Tomography .....	169
C.1.2. Amplitude Inversion .....	171
C.2. 3D Models Plotted by Vertical slice .....	172
APPENDIX D: RESOLUTION AND ERROR ANALYSIS.....	179
D.1. Error in Traveltime Picks.....	179
D.2. Resolution Matrices .....	180
D.2.1. 2D Seismic Surveys.....	181
D.2.2. 3D Seismic Surveys.....	183
D.2.3. GPR Survey .....	185
APPENDIX E: COMPARISON OF STRAIGHT RAY INVERSION METHODS.....	188
E.1. Seismic Surveys .....	188
E.1.1. Lower 2D Survey .....	188
E.1.2. Upper 2D Survey .....	194
E.1.3. Lower 3D survey.....	197
E.1.4. Upper 3D Survey .....	198
E.2. GPR Survey.....	199
E.3. Summary .....	203

## List of Tables

Table 2.1: The P-wave velocities (m/s) of the rock samples found using the 1 MHz transducers. ....	23
Table 2.2: The P-wave velocities (m/s) of the rock samples found using the 100 kHz transducers. ....	23
Table 2.3: The S-wave velocities (m/s) of the rock samples found using the 1 MHz transducers. ....	24
Table 2.4: Vp/Vs ranges for common reservoir lithologies (Blaylock, 1999).....	28
Table 2.5: The weight (g) of the Maax Na samples while dry and water saturated. ....	39
Table A.1: The distances (mm) measured for all sides and samples. ....	141
Table A.2: Traveltimes ( $\mu\text{s}$ ) of ultrasonic pulse through the dry rock samples using 1 MHz P-wave transducers. ....	141
Table A.3: Traveltimes ( $\mu\text{s}$ ) of ultrasonic pulse through the dry rock samples using 1 MHz S-wave transducers. ....	142
Table A.4: Traveltimes ( $\mu\text{s}$ ) of ultrasonic pulse through the rock samples using 100 kHz P-wave transducers.....	142
Table A.5: The differences (m/s) between the velocities found with the 1 MHz transducers and the 100 kHz transducers.....	143
Table A.6: The Vp/Vs measurements for all samples using the measurements from the 1 MHz transducers. ....	143
Table A.7: The Gardner derived densities ( $\text{g}/\text{cm}^3$ ) of the dry rock samples using Vp and Vs from the 1 MHz and 100 kHz transducers. A coefficient of 1.47 was used for the Vs calculation. ....	143
Table A.8: Traveltimes ( $\mu\text{s}$ ) of ultrasonic pulse through the water saturated rock samples using 1 MHz P-wave transducers.....	144
Table A.9: Traveltimes ( $\mu\text{s}$ ) of ultrasonic pulse through the water saturated rock samples using 1 MHz S-wave transducers.....	144
Table A.10: The P and S-wave velocities (m/s) of the water saturated rock samples found using the 1 MHz transducers. ....	144
Table A.11: The Vp/Vs measurements for water saturated sample one using the 1 MHz transducers. ....	145

Table A.12: The Gardner derived densities ( $\text{g/cm}^3$ ) of the water saturated rock samples using $V_p$ and $V_s$ from the 1 MHz transducers. A coefficient of 1.93 was used for the $V_s$ calculation.....	145
Table A.13: The estimated porosity using the dry limestone and dolomite relations of Batzle (2006), the wet limestone relations of Assefa (2003) and the density relations.....	145
Table E.1: The standard deviation and average of the differences between the observed and calculated traveltimes for the lower 2D survey. ....	191
Table E.2: The number of unphysical values in the velocity models of the lower 2D surveys. ....	194
Table E.3: The run times in seconds of the inversion techniques for the lower 2D survey.....	194
Table E.4: The standard deviation and average of the differences between the observed and calculated traveltimes for the lower 2D survey. ....	195
Table E.5: The number of unphysical values in the velocity models of the lower 2D surveys. ....	196
Table E.6: The run times in seconds of the inversion techniques for the upper 2D survey.....	196
Table E.7: The standard deviation and average of the differences between the observed and calculated traveltimes for the lower 3D survey. ....	197
Table E.8: The number of unphysical values in the velocity models of the lower 2D surveys. ....	198
Table E.9: The run times in seconds of the inversion techniques for the lower 3D survey.....	198
Table E.10: The standard deviation and average of the differences between the observed and calculated traveltimes for the upper 3D survey. ....	199
Table E.11: The number of unphysical values in the velocity models of the upper 3D survey.....	199
Table E.12: The run times in seconds of the inversion techniques for the lower 3D survey.....	200
Table E.13: The standard deviation and average of the differences between the observed and calculated traveltimes for the GPR 2D and 3D survey.....	202

Table E.14: The number of unphysical values in the velocity models of the 2D and 3D GPR surveys.....	203
Table E.15: The run times in seconds of the inversion techniques for the 2D GPR survey.....	203

## List of Figures and Illustrations

Figure 1.1: Map of Belize with Maax Na marked by a red circle (Modified from the Perry-Castañeda Library Map Collection).....	3
Figure 1.2: Map of the Programme for Belize Archaeological Project with nearby sites (PfBAP, 2005). .....	4
Figure 1.3: Tectonic Map of Belize (Belize Environmental Consultancies Ltd., 2006). ...	6
Figure 1.4: The approximate erosion pattern when the sea was a) 180 ft, b) 100 ft, and c) 50 ft above present day levels and the current level as seen in d (Wright et al., 1959). .....	7
Figure 1.6: Temple of the Inscriptions at Palenque (photo from the Canadian Museum of Civilization, 2004). .....	10
Figure 1.7: A Maya pyramid built over an existing structure (Fasquelle and Fash, 1991). .....	11
Figure 1.8: Map of the Maax Na archaeological site in Belize, Central America (courtesy of Maax Na Archaeology Project). .....	12
Figure 1.9: A 3D contour map (left) and actual view (right) of the pyramid at the Maax Na archaeological site in Belize.....	13
Figure 1.10: The topographic map of structure A-15 at Chan Chich. Annotations are in meters. Shots are marked in blue while geophone receivers are marked in red for summer 2000 on the left (Xu and Stewart, 2000) and spring 2001 on the right (Xu and Stewart, 2001). .....	15
Figure 1.11: The final velocity contour maps from Chan Chich from the survey in 2000 (right) and 2001 (left) (Xu and Stewart, 2001). .....	16
Figure 1.12 The final velocity contour map from the 2001 survey on the Maax Na pyramid (Xu and Stewart, 2002).....	16
Figure 2.1: The three core samples from the Maax Na pyramid after being shaped.....	19
Figure 2.2: The 1 MHz ultrasonic transducer (left) along with the larger 100 kHz transducer (right). Quarter placed in picture for scale. ....	20
Figure 2.3: Method and apparatus used to determining the ultrasonic velocity of the core samples.....	22
Figure 2.4: The velocity versus porosity of dry and saturated limestone samples (Baechle, 2005). .....	25

Figure 2.5: Comparison of P-wave velocities from the 1 MHz and 100 kHz transducers. ....	27
Figure 2.6: $V_p$ versus $V_s$ of the dry samples with several constant $V_p/V_s$ values annotated. ....	28
Figure 2.7: Measured $V_p/V_s$ of the dry samples with several empirical lines plotted. ....	30
Figure 2.8: Display of manually calculated density and the Gardner predicted densities for all three sides of the rock samples using $V_p$ from the 1 MHz transducers. ....	32
Figure 2.9: Display of manually calculated density and the Gardner predicted densities for all three sides of the rock samples using $V_p$ from the 100 kHz transducers. ....	32
Figure 2.10: Display of manually calculated density and the Gardner predicted densities for all three sides of the rock samples using $V_s$ from the 1 MHz transducers and a coefficient of 1.47. ....	33
Figure 2.11: The P wave velocities of the dry and wet cores plotted along with the differences between the two.....	34
Figure 2.12: The S wave velocities of sample 1 when dry and wet plotted along with the differences between the two.....	35
Figure 2.13: Normalized compressional and shear velocities for cracked rocks ( $V_{rock}/V_{mineral}$ ) both dry and saturated using the Kuster Toksöz (1974) method (From Batzle 2006). ....	37
Figure 2.14: $V_p$ versus $V_s$ of sample one with several constant $V_p/V_s$ values annotated. The dry sample values are shown in blue with the water saturated in red. ....	38
Figure 2.15: Measured $V_p/V_s$ of sample one with several empirical lines plotted. The dry sample values shown in blue and water saturated values shown in red. ....	38
Figure 2.16: Display of manually calculated density and the Gardner predicted densities for all three sides of the water-saturated rock samples using $V_p$ from the 1 MHz transducers. ....	40
Figure 2.17: Display of manually calculated density and the Gardner predicted densities for all three sides of the water-saturated rock samples using $V_s$ from the 1 MHz transducers and a coefficient of 1.93. ....	40
Figure 2.18: Comparison of porosity measurements found using empirical relations between the P and S-wave velocities of dry dolomite and limestone (Batzle,	

2006), the water saturated P and S-wave velocities of limestone (Assefa et al., 2003) and the porosity derived from the measured densities.....	43
Figure 3.1: The seismic sections from a sledgehammer strike against a 12-inch circular plate where a) is Shot 1 and b) is shot 2. First break travel-times are in black. Receiver 1 and 35 are dead traces. ....	47
Figure 3.2: Graph of the first break travel-times between shot 1 (green X's) and shot 2 (blue dots). ....	48
Figure 3.3: Graph of the first break travel-times including both shots on the round plate and the shot on the square plate. ....	49
Figure 3.4: The average amplitude spectrum of a) round plate shot 1, b) round plate shot 2, and c) square plate. The shapes are similar but not exactly the same. ....	49
Figure 3.5: The initial source and receiver layout for the lower perimeter of the Maax Na pyramid. Sources are indicated in blue and receivers are indicated in red. ....	50
Figure 3.6: The amplitude spectrum for the average data trace of shot 1023.....	51
Figure 3.7: A sample shot from the lower perimeter with a 500ms AGC. First break picks are shown in blue. Receivers 1 and 35 are dead.....	52
Figure 3.8: The final source and receiver layout for the lower perimeter of the Maax Na pyramid. Sources are indicated in blue and receivers are indicated in red. ....	52
Figure 3.9: The source and receiver layout for the upper perimeter of the Maax Na pyramid. Sources are indicated in blue and receivers are indicated in red. Approximate location of looter's trench in green. ....	53
Figure 3.10: A view of the looters' trench located in the upper 2D survey .....	54
Figure 3.11: A sample shot from the upper perimeter. First break picks are shown in black.....	54
Figure 3.12: Source receiver layout for lower 3D seismic survey in 3D view (left) and 2D top or plane view (right). Sources are shown in blue and receivers in green. ....	55
Figure 3.13: Source receiver layout for upper 3D seismic survey in 3D view (left) and 2D top or plane view (right). Sources are shown in blue and receivers in green. ....	55
Figure 3.14: Source receiver layout for combined 3D seismic survey in 3D view (left) and 2D top or plane view (right). Sources and receivers shown in purple and black respectively from the upper 3D survey and green and blue for the lower 3D survey. ....	56

Figure 3.15: Total fold (rays crossing per pixel) for straight ray tracing of the lower 2D survey. The x and y axes are the horizontal dimension of the survey and are given in meters.....	57
Figure 3.16: Total coverage of rays per pixel for straight ray tracing of the upper 2D survey. The x and y axis are the horizontal dimension of the survey and are given in meters.....	58
Figure 3.17: Total coverage of rays per pixel for straight ray tracing of the upper 2D survey with all rays passing through the looters trench being ignored.....	58
Figure 3.18: The total fold (m) of a 2m vertical level from straight ray tracing for the a) lower 3D survey, b) the upper 3D survey and c) the combined 3D survey.....	59
Figure 3.19: The final velocity (m/s) map of the Maax Na pyramid found using damped least squares. All negatives values have been set equal to zero and all velocities greater than 3000m/s are set equal to 3000m/s.....	62
Figure 3.20: The slowness values of the lower 2D survey found using damped least squares. Slowness values greater than 20 s/km were set equal to 20 s/km for display purposes.....	62
Figure 3.21: The observed first-break times and calculated times from the lower 2D survey using the damped least squares inversion estimated slowness model.....	63
Figure 3.22: Differences between observed and calculated traveltimes found for the lower 2D survey using damped least squares slowness model.....	64
Figure 3.23: The slowness model of the upper 2D survey found using damped least squares. All slowness values greater than 20 s/km have been set equal to 20 s/km. All negative values are set equal to 0.....	65
Figure 3.24: The velocity model of the upper 2D survey found using damped least squares. All velocity values greater than 3000m/s have been set equal to 3000m/s. All negative values are set equal to 0.....	65
Figure 3.25: The slowness model of the upper 2D survey found using damped least squares where all rays passing through the trench have been removed. All slowness values greater than 20 s/km have been set equal to 20 s/km. All negative values are set equal to 0.....	66
Figure 3.26: The velocity model of the upper 2D survey found using damped least squares when all rays passing through the trench have been removed. All velocity values greater than 3000m/s have been set equal to 3000m/s. All negative values are set equal to 0.....	67

Figure 3.27: Differences between observed and calculated traveltimes found for the upper 2D survey with all rays included (left) and upper 2D survey with trench removed (right) using damped least squares slowness model. ....	68
Figure 3.28: The derived velocity in km/s (top) and slowness in s/km (bottom) models for the lower 3D survey. ....	70
Figure 3.29: Differences between observed and calculated traveltimes found for the lower 3D survey using damped least squares slowness model. ....	71
Figure 3.30: The derived velocity in km/s (top) and slowness in s/km (bottom) models for the upper 3D survey. ....	73
Figure 3.31: The difference between the observed and calculated traveltimes found for the upper 3D survey using DLS. ....	74
Figure 3.32: The derived velocity in km/s (top) and slowness in s/km (bottom) models for the combined 3D survey. ....	76
Figure 3.33: The difference between the observed and calculated traveltimes found for the combined 3D survey using CG with 250 iterations. ....	77
Figure 3.34: The attenuation model of the lower 2D survey found using the DLS method. ....	79
Figure 3.35: The differences between the measure and calculated values of $\ln(A_o/A)$ for the lower 2D survey using DLS. ....	79
Figure 3.36: The attenuation model of the upper 2D model found using all rays with the DLS method. ....	80
Figure 3.37: The attenuation model of the upper 2D model with all rays passing through the trench disregarded. ....	81
Figure 3.38: The difference between the observed and calculated values of $\ln(A_o/A)$ for the upper 2D survey with trench included (left) and removed (right). ....	82
Figure 3.39: The derived inverse attenuation (top) and attenuation (bottom) models for the lower 3D survey. ....	84
Figure 3.40: The differences between the observed and calculated amplitude ratios of the lower 3D survey. ....	85
Figure 3.41: The derived inverse attenuation (top) and attenuation (bottom) models for the upper 3D survey. ....	86
Figure 3.42: The differences between observed and calculated amplitude ratios found for the upper 3D survey. ....	87

Figure 3.43: The derived inverse attenuation (top) and attenuation (bottom) models for the combined 3D survey.....	88
Figure 3.44: The differences between observed and calculated amplitude ratios found for the upper 3D survey. ....	89
Figure 3.45: The RMS( $\delta t$ ) values versus iterations for different velocity ranges on the lower 2D survey.....	91
Figure 3.46: The standard deviation and average of the differences between observed first break traveltimes and calculated traveltimes.....	93
Figure 3.47: The derived velocity model (km/s) of the lower 2D survey found using a velocity range of 0.001 to 2.0 km/s. Skipped pixels designated in black. ....	93
Figure 3.48: The final raypaths from the first 35 sources in the lower 2D survey with velocity range of 0.001 to 2km/s. Sources and receivers displayed in red and green respectively. ....	94
Figure 3.49. The derived velocity model (km/s) of the lower 2D survey found using a velocity range of 0.001 to 5.0 km/s.....	95
Figure 3.50: The 2 km/s max velocity model (left) and the 5 km/s max velocity model with all velocities greater than 2 km/s set equal to 2 km/s (right) found using curved ray tracing. ....	95
Figure 3.51: Differences between observed and calculated traveltimes found for the lower 2D survey with a velocity model with a range of 0.001km/s to 2km/s. ....	96
Figure 3.52: The starting velocity model (km/s) with the trench included.....	97
Figure 3.53: The RMS( $\delta t$ ), average and standard deviation of the differences between the observed and calculated traveltimes for multiple velocity constraints. ....	98
Figure 3.54: The final velocity model of the upper 2D survey the trench starting velocity model and velocity constraints of 0.15 to 0.5 km/s. ....	99
Figure 3.55: Differences between observed and calculated traveltimes found for the upper 2D survey with a velocity model with a range of 0.15 km/s to 0.5 km/s. ....	99
Figure 3.56: The RMS of the amplitude ratio values versus iterations for different inverse attenuation ranges on the lower 2D survey. ....	101
Figure 3.57: The inverse attenuation (left) and attenuation (right) model of the 97 <sup>th</sup> iteration with the range of 0.2 to 10 m/Np of the lower 2D survey.....	102
Figure 3.58: The differences between the observed and calculated amplitude ratios of the lower 2D survey found using an inverse attenuation range of 0.2 to 10 m/Np.	102

Figure 3.59: The RMS( $\ln(A_o/A)$ ), average and standard deviation of the differences between the observed and calculated amplitude ratios for multiple inverse attenuation constraints. ....	104
Figure 3.60: The inverse attenuation (left) and attenuation (right) model of upper 2D survey with the range of 0.2 to 20 m/Np. ....	104
Figure 3.61: The differences between the observed and calculated amplitude ratios of the upper 2D survey found using an inverse attenuation range of 0.2 to 20 m/Np. ....	105
Figure 4.1: Sensors and Software's pulseEKKO PRO system. (Sensors and Software, 2006) .....	109
Figure 4.2: Layout of the GPR survey in 2D (left) and 3D (right) perspective. Receiver locations are shown in blue and transmitter locations in red. ....	110
Figure 4.3: A raw shot gather from the GPR survey with the airwave marked in yellow and the direct wave marked in red .....	110
Figure 4.4: The a) amplitude frequency graph and b) amplitude time graph for shot 2. ....	111
Figure 4.5: The initial FK spectrum (left) and final FK spectrum (right) after applying the FK filter. ....	112
Figure 4.6: The raw shot gather (left) and the shot gather after applying the FK filter.. ....	112
Figure 4.7: The final 2D velocity (m/ns) structure derived from straight ray traveltimes inversion. All negative values set to 0 m/ns. All velocities greater than 0.2 m/ns are set equal to 0.2 m/ns. ....	114
Figure 4.8: The straight ray paths (left) and fold (right) for the GPR survey using straight ray tomography. ....	115
Figure 4.9: The difference between the measured and calculated traveltimes of the 2D GPR survey. ....	115
Figure 4.10: The measured and calculated traveltimes from the GPR velocity model. . ....	116
Figure 4.11: The straight ray fold for the 3D GPR survey (left) and the difference between the 3D and 2D GPR survey folds (m) (right). ....	117
Figure 4.12: The final 3D velocity (m/ns) structure derived from straight ray traveltimes inversion. All negative values set to 0 m/ns. All velocities greater than 0.2 m/ns are set equal to 0.2 m/ns. ....	117
Figure 4.13: The difference between the measured and calculated traveltimes of the 3D GPR survey. ....	118

Figure 4.14: The RMS( $\delta t$ ) values for the GPR survey with several different velocity ranges. ....	120
Figure 4.15: Comparison between the average and standard deviation of the differences between the observed and calculated traveltimes for the 100 <sup>th</sup> iteration for multiple velocity ranges. ....	121
Figure 4.16: Average of the differences between measured and calculated traveltimes for each iteration of curved ray traveltimes inversion. ....	121
Figure 4.17: The final velocity model (m/ns) derived from the curved ray traveltimes inversion. Parts of the initial model of 0.1 m/ns remain in areas of no ray coverage. ....	122
Figure 4.18: The raypaths from the 47 <sup>th</sup> iteration of the GPR survey found using curved ray tracing and a velocity range of 0.08 to 0.12 m/ns. ....	122
Figure 4.19: Differences between measured and calculated traveltimes for the 47 <sup>th</sup> iteration velocity model. ....	123
Figure 4.20: The observed and calculated traveltimes of the 47 <sup>th</sup> iteration of the GPR survey with a velocity constraint of 0.08 to 0.12m/ns. ....	124
Figure 5.1: The stack of the lower 2D seismic survey (courtesy of Paul Hebert). ....	130
Figure 5.2: The stack of the GPR surveys after an FK filter removed the airwave. Survey was scaled to use ms instead of the original ns. (courtesy of Paul Hebert). ....	130
Figure 5.3: The distance from source to receiver vs. the traveltimes for the a) lower 2D, b) upper 2D, c) lower 3D and d) upper 3D surveys. ....	131
Figure 5.4: The distance from source to receiver vs. the amplitude for the a) lower 2D, b) upper 2D, c) lower 3D and d) upper 3D surveys. ....	132
Figure A.1: The three cores taken from the Maax Na pyramid before any modifications (left) and after being cut (right). ....	140
Figure B.1: A shot gather with 500ms AGC (left) and a zoomed in portion of the shot gather with traveltimes picks in blue. ....	146
Figure B.2: A shot gather (left) and a zoomed in portion of the shot gather with amplitude picks in blue. ....	147
Figure B.3: A ray propagating through a) a single pixel where $d_j^i$ is the distance that ray $i$ travels in pixel $j$ and $p_j$ is the slowness of pixel $j$ and the traveltimes is given by $t = dp$ , (Stewart, 1991) and b) a series of pixels where the travel time is given by $t_i = \sum_{j=i}^M d_j^i p_j$ (reproduced from Lines and Newrick, 2004). ....	148

Figure B.4: Cell organization of a network (a) Dashed lines: cell boundaries. Black circles: nodes. Solid lines: connections. (b) Shortest paths from one node to other nodes in a homogeneous model (Moser, 1991). .....	161
Figure B.5: The tree structure of a heap (Moser, 1991).....	164
Figure C.1: The derived velocity model (km/s) of the upper 2D survey found using a velocity range of 0.001 to 2.0 km/s. Skipped pixels designated in black. ....	169
Figure C.2: The raypaths for the first 20 sources of the upper 2D survey solved with a curved ray tracer and a velocity range of 0.001 and 2 km/s. ....	169
Figure C.3: The final velocity model (km/s) of the third iteration found using the trench starting velocity model and velocity constraints of 0.01 to 2 km/s.....	170
Figure C.4: The final velocity model (km/s) of the upper 2D survey using the third iteration found, the trench starting velocity model and velocity constraints of 0.01 to 1 km/s.....	170
Figure C.5: The final velocity model (km/s) of the upper 2D survey using the 10th iteration found, the trench starting velocity model and velocity constraints of 0.1 to 0.8 km/s.....	171
Figure C.6: The inverse attenuation (left) and attenuation (right) model found using the 74 <sup>th</sup> iteration of the 0.4 to 10 m/Np constrained curved ray tomography of the upper 2D survey.....	171
Figure C.7: The inverse attenuation (left) and attenuation (right) model found using the 69 <sup>th</sup> iteration of the 0.4 to 10 m/Np constrained curved ray tomography of the upper 2D survey with the trench starting model. ....	172
Figure C.8: The velocity structure (m/s) found using damped least squares for the lower 3D survey. All negative values are set equal to 0 and all values greater than 3000 m/s set equal to 3000 m/s. ....	173
Figure C.9: The velocity structure (m/s) found using damped least squares for the upper 3D survey. All negative values are set equal to 0 and all values greater than 3000 m/s set equal to 3000 m/s. ....	174
Figure C.10: The velocity structure (m/s) of the combined 3D survey found using the conjugate gradient method with 250 iterations. All negative values are set equal to 0 and all values greater than 3000 m/s set equal to 3000 m/s.....	175
Figure C.11: The attenuation model (Np/m) of the lower 3D survey found using DLS. All negative values have been set equal to zero and all values greater than 5 have been set equal to 5.....	176

Figure C.12: The attenuation model (Np/m) of the upper 3D survey found using DLS. All negative values have been set equal to zero and all values greater than 5 have been set equal to 5.....	177
Figure C.13: The attenuation structure (Np/m) for the combined 3D survey found using CG with 250 iterations. All negative values and values greater than 2.5 have been set to 0 and 2.5 respectively for display purposes. ....	178
Figure D.1: Display of the diagonal elements of the eigenvalue matrix L for the 2D lower survey (left) and 2D upper survey (right). ....	181
Figure D.2: Display of the diagonal elements of the model space resolution matrix $V_p V_p^T$ for the 2D lower survey (left) and 2D upper survey (right).....	182
Figure D.3: Display of the diagonal elements of the data space resolution matrix $U_p U_p^T$ for the 2D lower survey (left) and 2D upper survey (right).....	183
Figure D.4: Display of the diagonal elements of the eigenvalue matrix L for the 3D lower survey (left) and 3D upper survey (right). ....	184
Figure D.5: Display of the diagonal elements of the model space resolution matrix $V_p V_p^T$ for the 3D lower survey (left) and 3D upper survey (right).....	184
Figure D.6: Display of the diagonal elements of the data space resolution matrix $U_p U_p^T$ for the 3D lower survey (left) 3D upper survey (right). ....	185
Figure D.7: Display of the diagonal elements of the eigenvalue matrix $\Lambda$ for the 2D (left) and 3D (right) GPR survey. ....	186
Figure D.8: Display of the diagonal elements of the model space resolution matrix $V_p V_p^T$ for the 2D (left) and 3D (right) GPR matrix. ....	187
Figure D.9: Display of the diagonal elements of the data space resolution matrix $U_p U_p^T$ for the 2D (left) and 3D (right) GPR survey.....	187
Figure E.1: The derived velocity structures of the lower 2D survey found using a) DD, b) DLS, c) SVD and d) CG with 30 iterations. All values greater than 3000 m/s and less than 0 m/s are set equal to 3000 m/s and 0 m/s respectively.....	189
Figure E.2: The derived velocity structure in m/s of the lower 2D survey found using CG with 250 iterations .....	190
Figure E.3: The differences between the observed and calculated traveltimes found using the velocity models derived from a) DD b) DLS c) SVS d) CG with 30 iterations and e) CG with 250 iterations. ....	191

Figure E.4: The unphysical velocity locations found using a) DD b) DLS c) SVD d) CG with 30 iterations and e) CG with 250 iterations. Negative velocities shown in blue with velocities greater than 3000 m/s shown in red..... 193

Figure E.5: The differences between the observed and calculated traveltimes found using the velocity model derived from SVD. .... 195

Figure E.6: The unphysical velocity locations found using a) DD, DLS, SVD b) CG with 30 iterations and c) CG with 250 iterations for the upper 2D survey. Negative velocities shown in blue with velocities greater than 3000 m/s shown in red. .... 196

Figure E.7: The derived velocity structures of the 2D GPR survey found using a) DD, b) DLS, c) SVD d) CG with 30 iterations and e) CG with 250 iterations. All values greater than 0.2m/ns and less than 0 m/ns are set equal to 0.2 m/ns and 0 m/ns respectively. .... 201

## List of Symbols, Abbreviations and Nomenclature

<u>Symbol</u>	<u>Definition</u>
2D	two dimensional
3D	three dimensional
$\alpha$	aspect ratio
$\lambda$	damping factor
CG	conjugate gradient
DD	direct division
DLS	damped least squares
GPR	ground penetrating radar
m	meters
MHz	megahertz ( $10^6$ Hz)
ns	nanosecond ( $10^{-9}$ s)
Np	Neper; a unit for the natural log of the ratio between two measurements of power
P-wave	pressure or compressional wave
	quality factor = $\frac{\pi}{\alpha\lambda}$ , where $\alpha$ is attenuation and $\lambda$ is the wave length.
Q	
S-wave	shear wave
RMS	root mean squared
SVD	singular value decomposition
$V_p$	P-wave velocity
$V_s$	S-wave velocity
VSP	vertical seismic profile

## Chapter One: Introduction

### 1.1 Introduction

Currently, in geophysics there is significant interest in the process of tomography. This method has been used in many situations in the oil industry as well as outside to provide an accurate picture of the interior of many different objects. While the objects in question may be of many different shapes and sizes, the methods used are often similar. The most common method used in geophysics is *seismic* tomography. However, ground penetrating radar tomography is being increasingly used in near-surface applications. One of the newest applications for tomography is in the field of archaeology.

Archaeologists generally concentrate on detailed excavations often on the order of a few meters at a time. These excavations are both costly and time consuming. When looking at a large area such as an ancient city it would be impractical to excavate the whole area. To solve this problem, geophysical practices are being investigated as inexpensive non-invasive techniques. This might allow archaeologists to better direct their excavation and potentially avoid excavating areas with few items of significance.

In the past, geophysical methods have been used to help determine the near surface to help distinguish areas of interest for excavation. These methods included reflection GPR and seismic surveys as well as resistivity analysis (Carrara et al., 2001; Cararelli et al., 2001, *ibid*, 2007; *ibid*. 2008; Aitken and Stewart, 2003; *ibid*, 2004; Goodman et al., 2004). These methods are effective when the objects are buried but can be limited when determining the interior of existing buildings and structures.

Tomography is beginning to be used as a tool to assist archaeologists in mapping ancient structures and their foundations (Merlanti and Musante, 1994; Polymenakos and

Papamarinopoulos, 2005; *ibid*, 2007). To better manage the efforts of archaeologists, tomography can be used as a relatively fast and inexpensive way of determining promising excavation locations.

Both seismic and GPR tomography techniques will be examined as each has advantages and disadvantages. Seismic tomography has been shown to provide good wave penetration through larger areas providing clear first breaks for analysis (Schicht et al., 2007). However, seismic equipment is typically bulky and difficult to move which makes it very difficult to work with in remote areas. GPR provides an advantage over seismic methods by requiring less equipment allowing for greater mobility in harsh regions. The disadvantages of GPR tomography are its limited depth penetration and greater noise affecting the transmitted wave. If the transmitted wave cannot significantly penetrate the structure the number of distinguishable traveltimes available are limited resulting in a less accurate result. Also, as the first arriving wave in a GPR shot gather is typically the air-wave not the wave transmitted through the pyramid, it is more difficult to pick traveltimes as they are subject to a larger amount of noise. Both techniques were applied to the pyramid at Maax Na to determine whether they could accurately create images of the pyramids carbonate rubble interior.

## **1.2 Thesis Objectives**

This thesis has three objectives. The main objective of this thesis is to determine the interior structure of the Maax Na pyramid and identify any regions of archaeological significance. The second objective is to test different tomography techniques and find the most effective methods for determining the interior structure. The final objective is to

determine if GPR is capable of penetrating through the structure and producing a viable image of the interior of the pyramid.

### 1.3 Physical Setting

#### 1.3.1 Geography

Belize is located in Central America. It is a part of the Yucatan Peninsula bordered by Mexico on the north, Guatemala on the west and south and finally the Caribbean Sea on the east (Figure 1.1). Belize's north and south borders are defined by the courses of two rivers, the Hondo and the Sarstoon. The country stretches over 22,960 square kilometres and is the only nation in Central America without a coastline on the Pacific Ocean (Library of Congress, 2005).



**Figure 1.1: Map of Belize with Maax Na marked by a red circle (Modified from the Perry-Castañeda Library Map Collection).**

The study location, Maax Na, is located in the Orange walk district of north-western Belize (Figure 1.1). Maax Na is one of many Maya sites located in the Rio Bravo Conservation area (Figure 1.2). The Rio Bravo conservation area is an area of 260,000 acres owned by the Programme for Belize. This land is the largest private and the second largest single protected area in Belize. The Programme for Belize is dedicated to promoting “the conservation of the natural heritage of Belize and to promote wise use of its natural resources” (PFB, 2003).

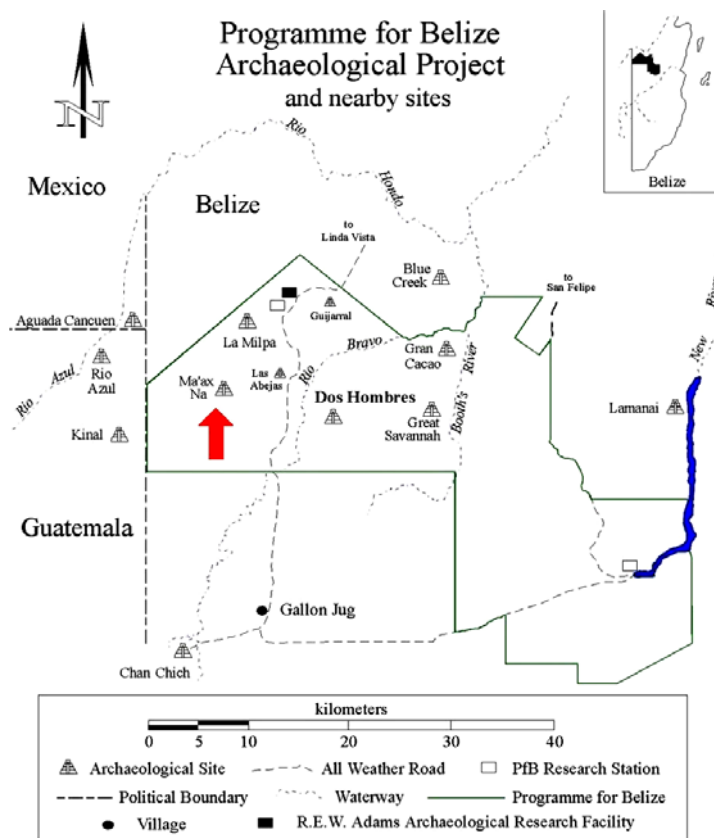


**Figure 1.2: Map of the Programme for Belize Archaeological Project with nearby sites (PFBAP, 2005).**

University of Texas archaeological surveyors discovered Maax Na in 1995, when they climbed a hill to find a corbelled vault at the top (a corbelled vault is a distinctive form of Mayan stone roof). Apparently, when they discovered the site they made so much

noise cheering that they disturbed a local spider monkey troupe (Allum, 2004). The monkeys attacked the archaeologists by screaming, shaking branches and throwing twigs and dung at them. This resulted in the archaeologists naming the site Maax Na that stands for “Monkey House” in local Mayan (Allum, 2004).

### ***1.3.2 Geology***

Geologically speaking, Belize can be divided into three distinct sections with the Corozal Basin in the north and the Belize basin in the south separated by the Maya mountains (Figure 1.3). The Corozal Basin forms part of the North Peten Basin, which covers northern Belize, northern Guatemala as well as south-eastern Mexico. The Corozal basin can be further divided into two subunits the Blue Creek sub-basin to the west and the orange walk sub-basin to the east (Belize Environmental Consultancies, 2006).

Belize consists largely of varieties of limestone with the exception of the Maya Mountains. The Maya mountains are a large intrusive block of granites and other Paleozoic sediments. These sediments run in a northeast to southeast direction through the central portion of Belize (Library of Congress, 2005). The Maya mountains are of geological interest as they are the only outcrops of Palaeozoic rocks to the north of the outcrops found in central Guatemala (Bateson and Hall, 1977). The hills alongside the Maya mountains are formed from Cretaceous limestone. This region is subject to sinkholes, ravines and underground streams typical of karst topography (Library of Congress, 2005).

The Corozal Basin lies on the Yucatan Platform, which is a tectonically stable region. This allows the region to be mostly level, with a few pockets of hills that exhibit

karst topography (Library of Congress, 2005). Around sixty million years ago, a sea covered the entire upland area of Belize. This resulted in several hundred feet of limestone created by the deposition of primeval crustacean shells. As the sea level fell, the limestone eroded resulting in streams cutting deep into the granite and shale of the Maya Mountains. This resulted in soil being deposited to the north as seen in Figure 1.4 (Wright et al., 1959). As a result of this erosion, northern Belize is dominated to the west by escarpments cut by ancient rivers with flat limestone gently sloping to the sea in the

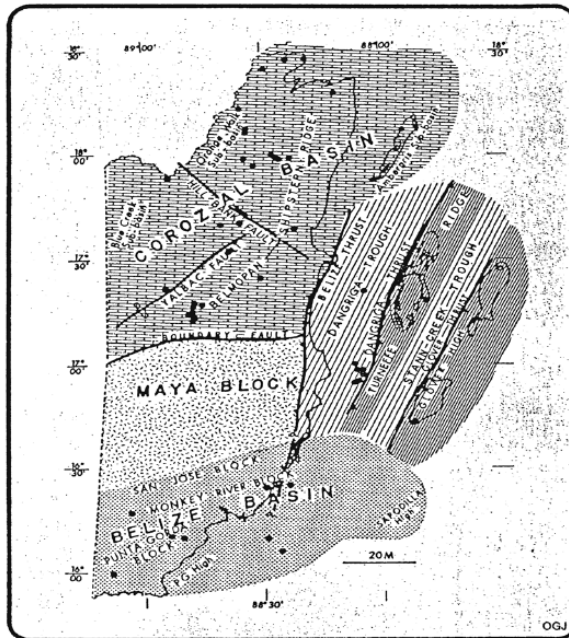


**Figure 1.3: Tectonic Map of Belize (Belize Environmental Consultancies Ltd., 2006).**

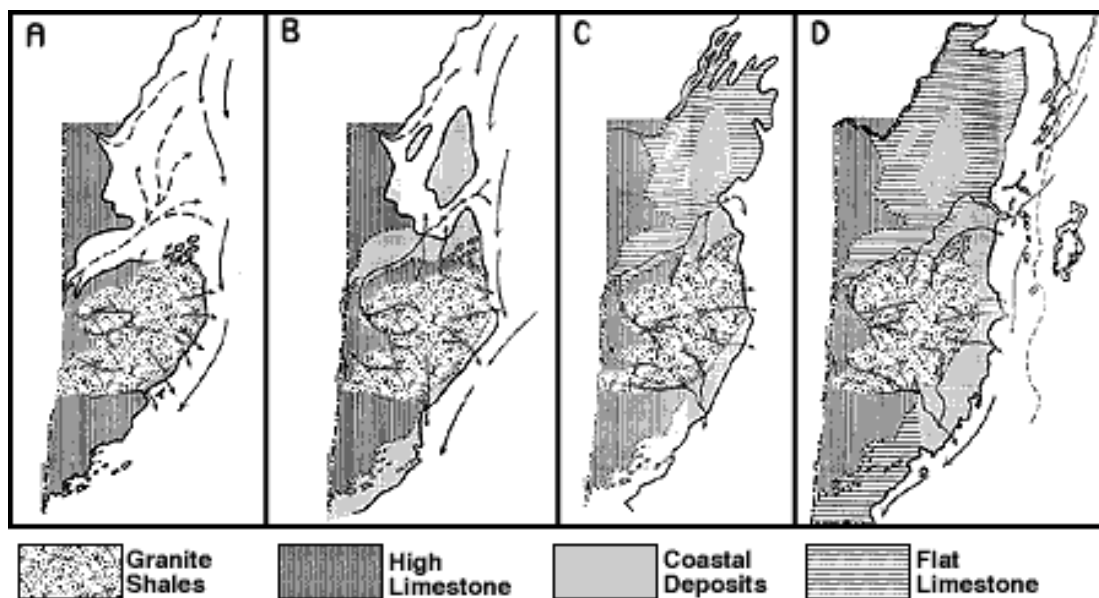


**Figure 1.4:** The approximate erosion pattern when the sea was a) 180 ft, b) 100 ft, and c) 50 ft above present day levels and the current level as seen in d (Wright et al., 1959).

east (Figure 1.5). The near surface consists of a layer of soil with cobbles of limestone, which covers the limestone bedrock.

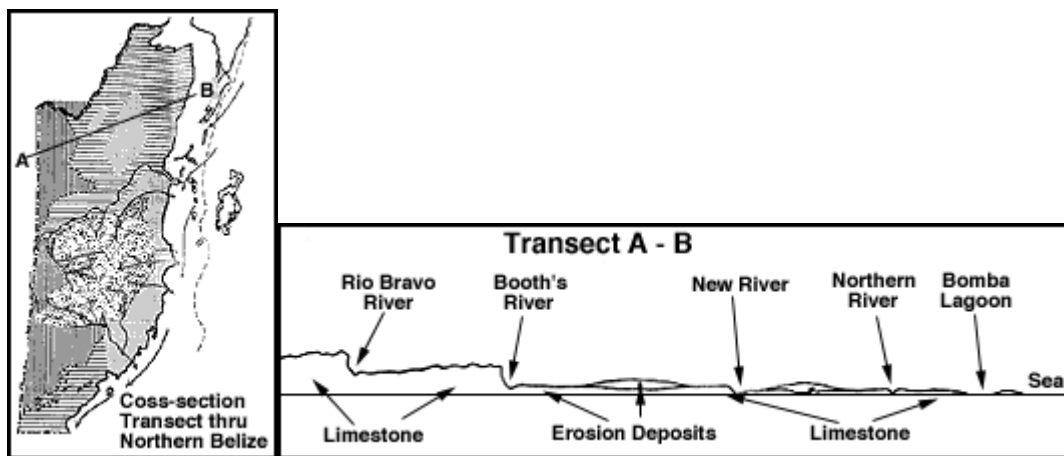


**Figure 1.5:** A cross section through northern Belize (Wright et al., 1959).

## **1.4 The Maya**

### ***1.4.1 Maya Culture***

Maya civilization rose to prominence during the Classic period from 300-900 AD. Prior to this time the Maya's lived in small villages and were believed to have been farmers. The Classic period saw the development of many of the structures that we now associate with the Maya. The Classic period was a time of a flourishing economy, large populations and widespread trade among the Mesoamerican people (Coe, 2001).

Maya culture is thought to have developed in three different areas during the Classic period. The first and most urban region was the lowlands in the central region of south Guatemala. The principle city in this region was Tikal; however, the urban centers stretched as far south as Honduras (Hooker, 1996). The second region of development was the Guatemalan highlands to the north. This region was less developed than the central regions and was thought to provide many of the natural resources to the urban centers. The final region of development was on the Yucatan peninsula. This area was a dry region and while it contained some urban centers it is believed that this was a culturally marginal area (Hooker, 1996).

Almost all urban centers built by the Maya were in tropical rainforest. These cities were ceremonial centers. The architecture erected in these cities, such as pyramids, temples and plazas, were erected to pay homage to the gods and bring balance to the cosmos (Aitken and Stewart, 2003). The Maya used similar layouts in the development of their urban centers. The city would often have great plaza areas that were linked to pyramids and other structures with stelae spread out in-between. Many of the Maya used pre-existing topography to create their structures. The Maya believed that mountains

were a place of connection with their deities and ancestors. As a result, many of their structures were built on hills and outcrops to bring them closer with the cosmos (Aitken and Stewart, 2003).

#### ***1.4.2 Mayan Pyramid Architecture***

To help understand what anomalies could be in the structure of the pyramid, it is useful to understand Mayan architecture. Since the structure upon which we have data is a pyramid the emphasis will be on pyramid architecture.

Mayan pyramids are not pyramids in a purely geometric sense. They have been known to have square, rectangular or even oval bases. The function of these pyramids can differ. Two main uses of the pyramids are thought to be as an artificial hill supporting a temple or as a tomb (Stierlin, 1964). While most pyramids fall under one of these categories there are examples that are different or fall under both. The artificial hill pyramids are believed to have been used as a monumental pedestal. This pedestal would be used to establish a “vertical movement between the world below and that of the gods” (Stierlin, 1964). There have been many pyramids found that contain tombs. One example of such is the Temple of the Inscriptions at Palenque seen in Figure 1.6. This temple contained a tomb at ground level that was accessible only from a staircase in the floor of the temple (Canadian Museum of Civilization, 2004). Maya pyramids also frequently employed number symbolism that reminded viewers of their cosmic significance. One example of this is the temples at Tikal and Palenque are constructed of nine levels that are representative of the nine layers of the underworld (Woolf, 2005).



**Figure 1.6: Temple of the Inscriptions at Palenque (photo from the Canadian Museum of Civilization, 2004).**

On the outside of the pyramids there are often steps leading up one or more of the faces. These steps often ascend a slope of between 45 and 60 degrees. There are many different forms of stairs that can be used on the Maya pyramids. In some of the pyramids the stairs are embedded into the side of the pyramid, whereas in others they protrude from the face. Further deviation is possible as some of the staircases are bounded by plain or ornate strips of rock (Stielin, 1964).

Another possible feature of Mayan pyramid architecture is an upper temple. On the top platform of most of the pyramids there is a temple structure. Most of these temples had similar design features. They were often reached by a small flight of stairs leading towards a square doorway. These temples typically had a steeply inclined roof topped by a lofty crest of stone (Stielin, 1964). The interior of these temples consisted of small rooms.

Finally, the Maya rarely demolished any of their structures. Instead, if another building was needed the new larger structure was built overtop or abutted to the older

structure as depicted in Figure 1.7. Using this technique the structures were rebuilt again and again throughout the centuries (Aitken, 2008).



**Figure 1.7: A Maya pyramid built over an existing structure (Fasquelle and Fash, 1991).**

### *1.4.3 Maax Na*

Maax Na sits on the top of a long hill which when examined on a topographic map resembles that of bird with outstretched wings (Allum, 2004). Since 1996 archaeologists have been performing excavations at the Maax Na site. These excavations have revealed more than 25 intact structures as displayed in Figure 1.8 (Aitken and Stewart, 2003). Through archaeological excavations most structures were determined to have been built during the Classic period, which dates from 300-900 AD. However, the Maya were determined to have inhabited the site as early as the late Pre-classic period of 250-300 A.D. (Allum, 2004).

Maax Na consists of a large central area with large open plazas surrounded by building build on platforms overlooking the plaza. These buildings are believed to have

been used as housing, public market areas and ceremonial venues (Allum, 2004). In addition to these structures, a large ball court was discovered.

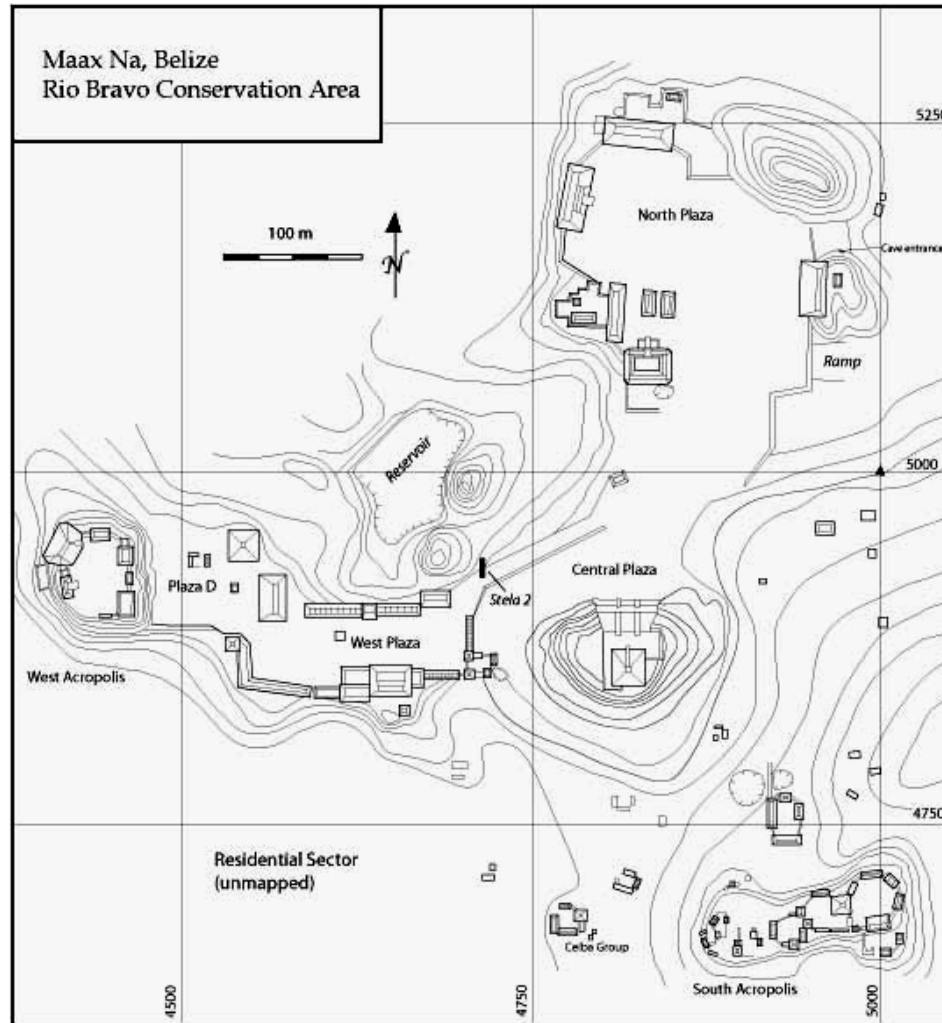


**Figure 1.8: Map of the Maax Na archaeological site in Belize, Central America (courtesy of Maax Na Archaeology Project).**

The largest structure in Max Na is a pyramid to the south. This pyramid was approximately 28m by 28m at its base and rose to a height of 15m. The pyramid sits atop a ridge overlooking agricultural land. The pyramid was build upon two platform steps that were created from two natural terraces, rising approximately 40m from the base of the first step to the top of the pyramid. In the past it would likely have supported a steep

staircase leading to the top of the pyramid (Allum, 2004). Similar to the rest of the Maax Na site, the pyramid has been reclaimed by the jungle with a layer of jungle detritus coating its entirety and multiple trees have grown along the sides (Figure 1.9). As a result, it is impossible to visually determine whether this pyramid has interior cavities or was built on a previous structure.



**Figure 1.9: A 3D contour map (left) and actual view (right) of the pyramid at the Maax Na archaeological site in Belize.**

Since limestone is the most common rock in the area, most of the Maya pyramids were built using limestone in the form of cobbles, blocks and even stucco (Aitken and Stewart, 2003). Limestone was used in construction of all major structures at Maax Na, including the ball court and stelae. By knowing what materials comprise the pyramid, we can get a better idea of what velocities to expect. The pyramid is under a layer of vegetation therefore, it is important for us to have a background in Mayan architecture. Using our knowledge we can infer what the temple would look like and have an idea of what might be located in the interior.

## 1.5 Previous Research

In 2000 and 2001, seismic surveys were performed on two different Maya pyramids in Belize. The purpose of these tests was to determine whether the hammer seismic technique would produce adequate energy to propagate through the pyramid and produce an accurate picture of its interior structure (Xu and Stewart, 2002). The first pyramid that was tested was located at Chan Chich, Belize, which is located just south of the Bravo conservation area along the Guatemalan border.

In the summer of 2000 and the spring of 2001 seismic imaging was used on the large A-15 pyramid at Chan Chich. The A-15 pyramid is approximately 30m by 30m and stands about 18 m high. In the summer of 2000 the seismic data was acquired using six hammer-seismic sources on one side of the pyramid along with ten 3-component geophones on the adjacent perpendicular side (Xu and Stewart, 2000). These receivers had 2 m horizontal spacing and were spread along a 2 m contour level up from the base of the pyramid. The shots were located along the same vertical contour as the receivers with a 4 m horizontal spacing (Figure 1.10). After viewing the seismic section it was noticed that channel 5 was dead and channel 1 was very noisy therefore their traveltimes were ignored (Xu and Stewart, 2000). This left 6 shots and 8 receivers resulting in 48 traveltime picks.

In 2001, another survey of the pyramid at Chan Chich was conducted. This time the number of receivers and shots was increased to twenty and twenty-seven respectively. The receivers used were once again 3-component geophones, which were spread around a contour on the north side of the pyramid as seen in Figure 1.10. The geophones had a spacing of 2.5 m with shots half spaced in between (Xu and Stewart, 2001). When

looking at the seismic traces it was again decided to use the vertical component as it showed the cleanest first break picks. Due to ambiguities in their geometry the first four shots were ignored leaving 460 first arrival times. By increasing the number of shots and receivers the number of traces through each pixel are increased resulting in a more accurate picture of the interior velocity structure.

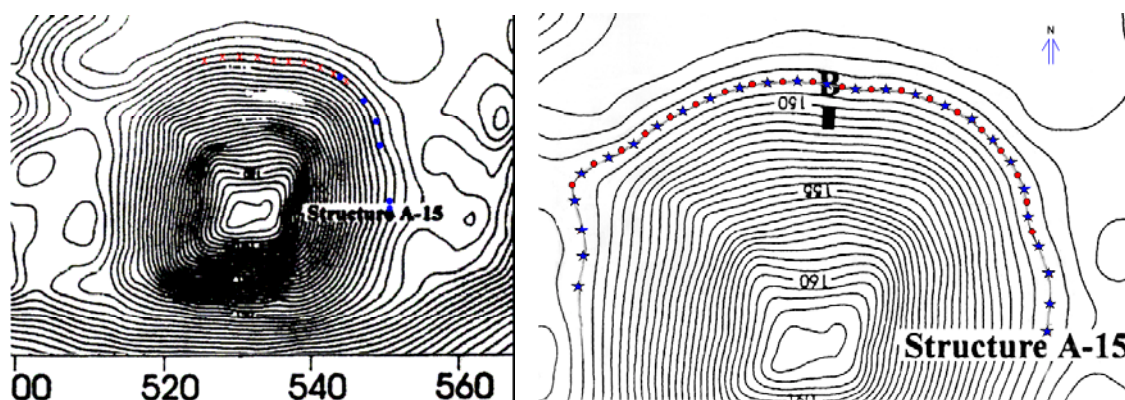


**Figure 1.10: The topographic map of structure A-15 at Chan Chich. Annotations are in meters. Shots are marked in blue while geophone receivers are marked in red for summer 2000 on the left (Xu and Stewart, 2000) and spring 2001 on the right (Xu and Stewart, 2001).**

Both surveys were solved using straight ray traveltimes inversion techniques. A pixel size of 4 m by 4 m was used. The resulting velocity structures, Figure 1.11, show similar high velocity peaks bordered by a low velocity region. Both of the structures also show a similar range of velocities ranging from approximately 200 m/s to 700 m/s. Also in 2001, an initial test on the Maax Na pyramid was performed. This test was performed using a string of twenty 3-component geophones with 2.5 m spacing with hammer shots in the middle of the receivers. The first 16 shots and receivers were used to perform the traveltimes inversion. Similar to the Chan Chich data, the first breaks were picked off the vertical component. A pixel size of 3 m by 3 m was used to analyze the results (Xu and Stewart, 2002). The resultant velocity map in Figure 1.12 shows similar results to that of

Chan Chich. Both maps show similar velocities with superficial area velocities around 200-300 m/s and core velocities around 700 m/s.

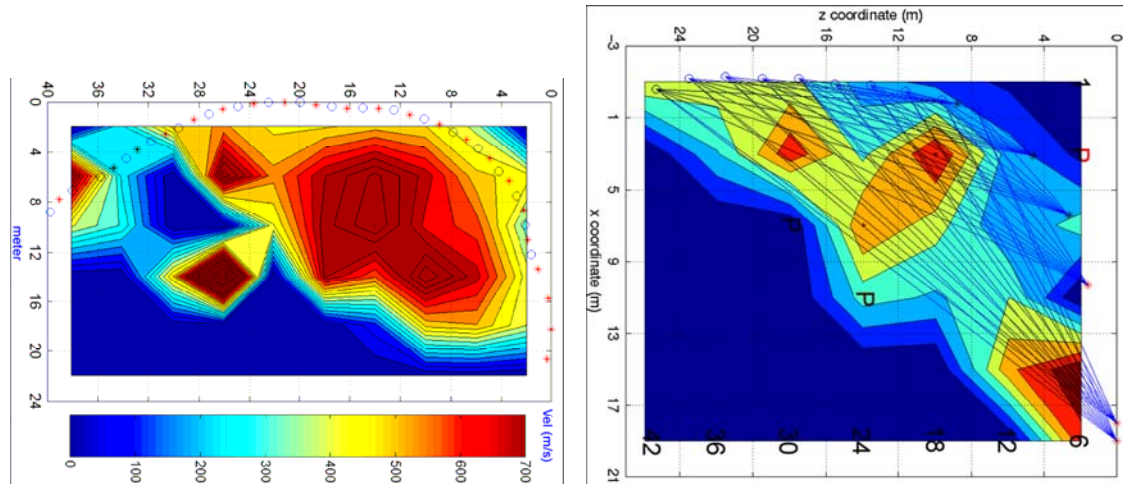


**Figure 1.11: The final velocity (m/s) contour maps from Chan Chich from the survey in 2000 (right) and 2001 (left) (Xu and Stewart, 2001).**

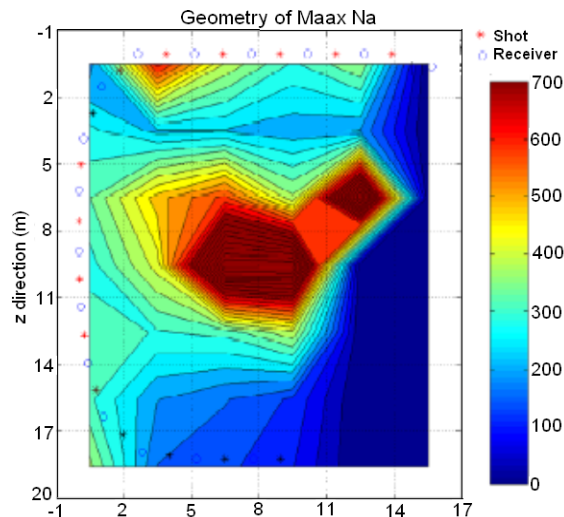


**Figure 1.12 The final velocity (m/s) contour map from the 2001 survey on the Maax Na pyramid (Xu and Stewart, 2002).**

The similar result between both Chan Chich surveys gives confidence that the travelt ime inversion is resulting in a precise velocity structure. Since the vast majority of Maya structures in the area are made from limestone found in the region we would expect that Chan Chich and Maax Na would contain similar materials and therefore would have

velocity structures within the same range. Since traveltimes inversion on both Maax Na and Chan Chich produced similar velocities the velocity structures are believed to be reasonable.

## **Chapter Two: Rock Properties**

To better understand the actual rock comprising the pyramid, three different rock samples were acquired. These samples were collected (with permission) from a rubble pile located at the base of the looters' trench. This pile of rocks is believed to have been created from rock inside the pyramid and was excavated by the looters when digging the trench. These three hand samples were brought back to the lab in Calgary where they were cut into rectangular shape (Figure 2.1) so that ultrasonic measurements could be undertaken. The cores were all cut to try and maintain as much of the sample as possible while providing adequate flat surfaces for testing. Since the rocks were initially rounded on the edges (see Appendix A) there are some corners that are not squared. Also due to existing fractures and weak points in the rock, some corners were chipped during the cutting. After shaping, the cores were left for a period of two weeks to ensure any excess moisture obtained by the wet saw had evaporated.

### **2.1 Rock Type**

The rock samples taken from the Maax Na pyramid are similar to samples tested from nearby monuments and quarry sites that produced the building material for the Maax Na site. Two different varieties of limestone were used at Maax Na, one of which is white and soft and the other is tan and hard (M. L. Brennan, personal communication, 2008). In the three samples from the pyramid, sample one and two are the hard tan limestone while sample three is the softer white variety. Both varieties of rock were chemically determined to be slightly dolomitic limestone with magnesium (Mg) contents of approximately 0.5% for the tan rock and 5% for the white stone. This was determined using a scanning electron microscope with an energy dispersive spectrometer (SEM-

EDS). To help differentiate between the two varieties a search for heavy metals or trace elements was undertaken using inductively coupled plasma mass spectrometry (ICP-MS) (M. L. Brennan, personal communication, 2008). ICP-MS analyses rock material in solution for minor and trace elements. There appears to be no distinct chemical difference between the white and tan rock. The current theories as to the differences are that they result from differences in porosity and weathering (M. L. Brennan, personal communication, 2008).



**Figure 2.1: The three core samples from the Maax Na pyramid after being shaped.**

While the colour and strength are the two most obvious attributes of the rock samples there are other distinctive characteristics that are clearly visible. Sample one and three appear to be fairly homogenous with sample one having small empty pockets dotting the surface of the rock. Sample two has small crystalline pockets and appears to

be fractured in multiple places. These differences will likely play a part in the differences among the velocities as well as the densities of the rock.

## 2.2 Ultrasonic Method

### 2.2.1 Transducers

Ultrasonic pulse measurements were used to determine the P- and S-wave velocities of the rock samples. These measurements were undertaken using contact or single element transducers. The active element of the transducers is a piezoelectric ceramic. A piezoelectric ceramic will change shape in response to an applied voltage resulting in ultrasonic vibrations. These ceramics will also work in reverse by translating mechanical energy in the form of ultrasonic vibration back into electrical energy. Therefore the transducer can be used as both a transmitter and receiver of ultrasonic vibrations. Measurements were taken using a P-wave transducer with a resonant frequency of 1 MHz as well as a larger transducer with a resonant frequency of 0.1 MHz as seen in Figure 2.2. The S-waves were measured using only a 1 MHz S-wave transducer.

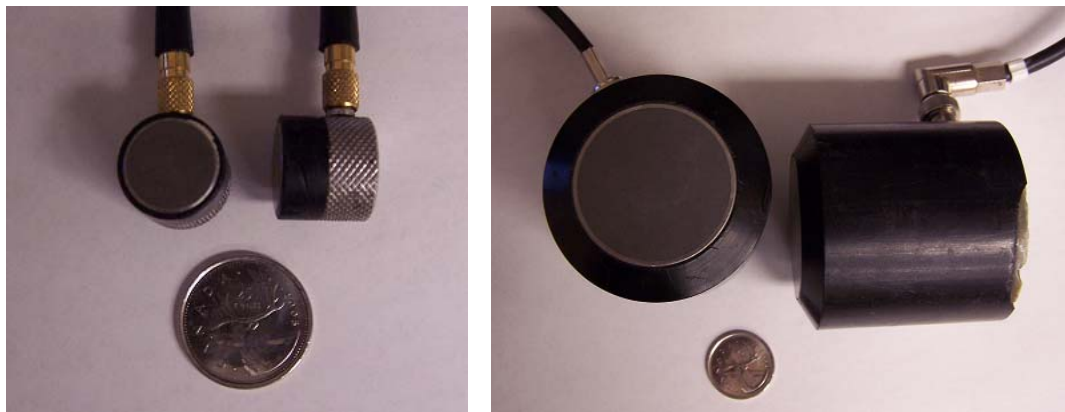


**Figure 2.2: The 1 MHz ultrasonic transducer (left) along with the larger 100 kHz transducer (right). Quarter placed in picture for scale.**

### ***2.2.2 Velocity Measurement***

To obtain the velocities of the samples using the ultrasonic transducers the transmission time of the ultrasonic pulse through the sample is measured. Using this traveltime and the length of the sample measured using calipers, it is possible to find the velocity by dividing the distance by the time. To get an accurate traveltime the waveform is recorded on an oscilloscope. Using the oscilloscope the first break of the wave is picked. This first break pick is the time the pulse was first received by the receiving transducer (see Figure 2.3). This same method was used to find both the P- and S-waves using the different transducers.

Multiple locations on each core were measured using this procedure to determine any heterogeneity of the cores. In addition to multiple sites on one side of the core, all three dimensions of the core were also measured. To reduce the error of each pick, five traveltimes were taken for each location and averaged (see Appendix A for all traveltimes). Due to waveform shape the exact location of the first break is difficult to distinguish. Due to this fact a 5% error is found when solving the traveltimes with the 1 MHz P-wave transducer. Since the 100 kHz transducer is much larger good coupling is harder to achieve this results in a higher potential error of approximately 10%. This is the same error expected for the 1 MHz S-wave traveltimes as the S-wave is not as strong as the P-wave resulting in a less clear first break. In addition to the error expected from the traveltime picking, there is also an error associated with the distance measured with the calipers. Since the rock surfaces are not perfectly flat the distance measurement may not be the exact distance through the rock. Based on multiple distance measurements in nearby locations on the rock samples an error of 2% is expected for the distances with the

smaller 1 MHz transducers. Since the 100 kHz transducer is much bigger it is reliant on a larger area of the rock resulting in a larger potential error. Using distance measurements from side 1 of the first rock sample a potential error of 5% is expected.

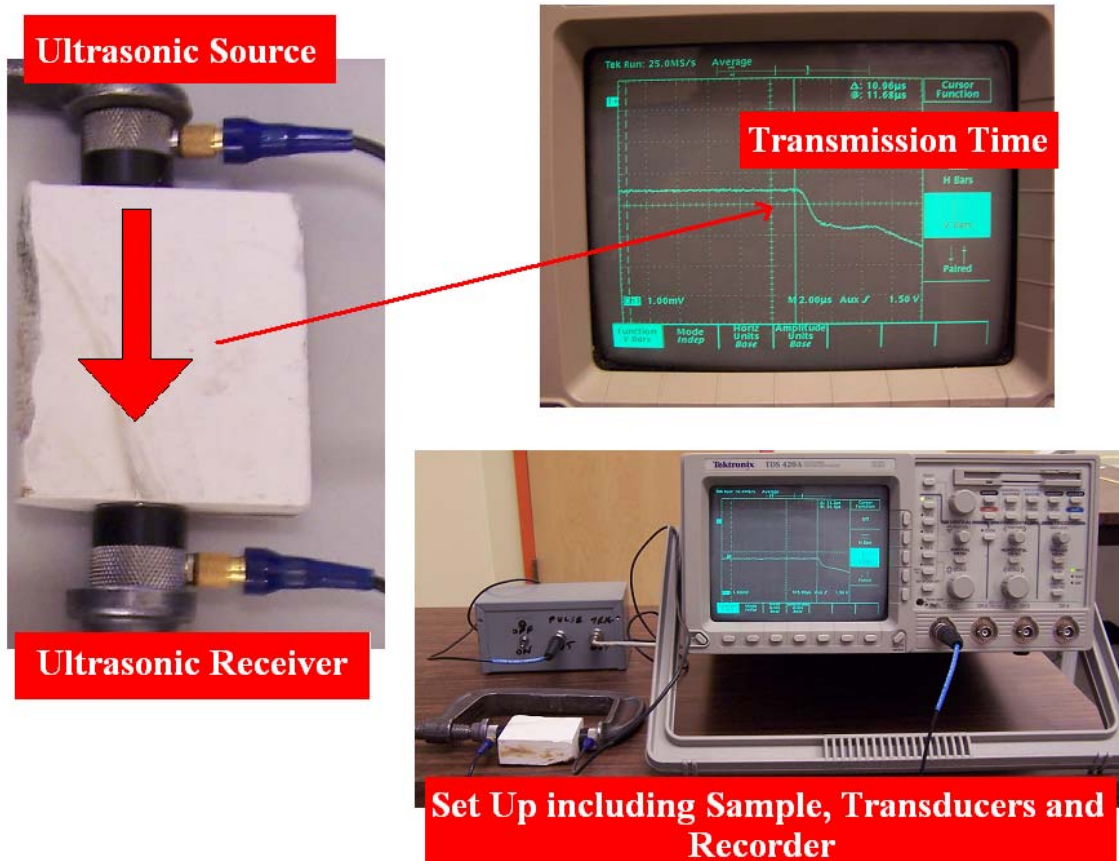


**Figure 2.3: Method and apparatus used to determining the ultrasonic velocity of the core samples.**

## 2.3 Dry Measurements

### 2.3.1 *P and S velocities*

The measured P-wave velocities using the 1 MHz transducers are shown in Table 2.1 and the 100 kHz transducers in Table 2.2. Due to the size of the 100 kHz transducers, multiple measurement positions per side were not possible therefore only a single measurement position in the middle of each side was undertaken. The P-wave velocities

appear to be relatively homogeneous with small velocity changes depending on the orientation of the transducers. The one exception to this is side one on sample three. This velocity was found to be approximately 400 m/s slower than its other sides in both the 1 MHz and 100 kHz velocities.

The S-wave velocities found using the 1 MHz S-wave transducers (Table 2.3) show a similar trend as the P-wave velocities. All the velocities from each location for samples one and two are close to each other signifying a fairly homogeneous sample. Sample three, however, shows a significant difference between side one and the other two sides with side one being once again significantly slower. This difference in velocities can be possibly attributed to fractures orientated across this side and its associated anisotropy resulting in slower velocities through side one. Since the ultrasonic pulse has to travel through a longer area of rock for side two and three there is a greater amount of confidence placed on these values than that of side one.

<b>Sample 1</b>	Side1	Side 2	Side 3
Middle	3921	3913	3709
Left	3980	3892	
Right	4129	4037	
<b>Sample 2</b>			
Middle	3071	3261	3150
<b>Sample 3</b>			
Middle	1390	1744	1766

**Table 2.1: The P-wave velocities (m/s) of the rock samples found using the 1 MHz transducers.**

<b>Sample 1</b>	Side1	Side 2	Side 3
Middle	3544	3583	3023
<b>Sample 2</b>			
Middle	2394	2521	2626
<b>Sample 3</b>			
Middle	1122	1567	1623

**Table 2.2: The P-wave velocities (m/s) of the rock samples found using the 100 kHz transducers.**

<b>Sample 1</b>	Side1	Side 2	Side 3
Middle	2230	2241	2183
Left	2312	2291	
Right	2401	2396	
<b>Sample 2</b>			
Middle	1659	1813	1791
<b>Sample 3</b>			
Middle	653	944	956

**Table 2.3: The S-wave velocities (m/s) of the rock samples found using the 1 MHz transducers.**

These velocities appear to be much slower than the expected values in limestones and dolomites given in the literature. For example, Asquith and Kryowski (2004) give a predicted P-wave velocity of approximately 5500 to 6000 m/s for limestone and 7000 to 8000 m/s for dolomites. Geis et al. (1990) report P-wave velocities ranging from 5200 m/s – 5800 m/s and S-wave velocities ranging from 2850 m/s – 3000 m/s for Paleozoic carbonates in Canada and Abdalrasoul Khoshood et al. (2007) report P-wave velocities of 5200m/s and S-wave velocities of 3000m/s for the Asmari carbonate formation in Iran. The most likely reasons for the lower velocity in the Maax Na samples is an increase in porosity and weathering and the rocks are at bench top pressures. The core samples are a much softer rock therefore more loosely consolidated than the typical limestone studied in the literature. Assefa et al. (2003) and Baechle et al (2005; *ibid*, 2008) both report that the velocity is dependent on the porosity in carbonates. As the porosity increases in the sample both the S-wave and P-wave velocities tend to decrease. Baechle et al. (2005) reported P-wave velocities as low as 3100 m/s and S-wave velocities as low as 1600 m/s on dry limestone cores with a porosity of approximately 30% as seen in Figure 2.4. Using the data of Baechle, the assumption can be made that the Maax Na samples should be of high porosity to obtain the lower velocities measured.

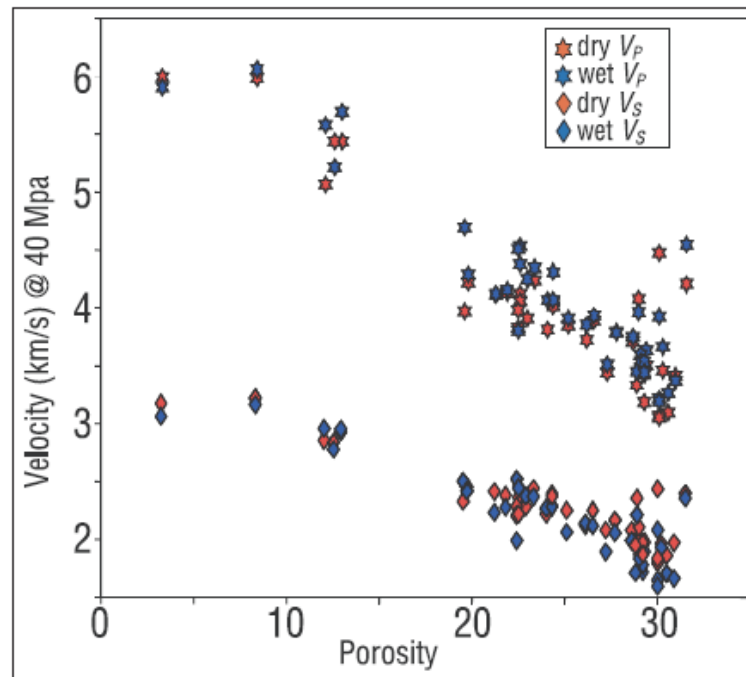


**Figure 2.4: The velocity versus porosity of dry and saturated limestone samples (Baechle, 2005).**

### 2.3.2 Velocity and Frequency

Since the P-wave measurements differed with the frequency of the transducer it can be asked whether ultrasonic measurements can correlate to the frequencies used in the seismic experiments (See Appendix A for differences). From the surveys on the Maax Na pyramid it was seen that the seismic hammer shots have an average frequency range of 10-250 Hz that is much lower than both the 1 MHz and 100 kHz frequencies of the transducers. Colpaert et al. (2006) found that the velocities found from logging, seismic and ultrasonic frequency bands correlated well in carbonate rocks from the Norwegian Finnmark Platform. This suggests that frequency is independent of the velocity. This frequency independence was also discovered by Hagin and Zoback (2004) in dry unconsolidated sand using the frequency range from 0.1 Hz to 10 MHz.

However, since velocity differences are clearly seen in our data, there could well be some relation between the frequency and the velocity. Assuming that there is an element of attenuation in the rock, lower velocities with lower frequencies would be expected. This result was reported by Sams et al. (1997) where they tested sedimentary rocks in multiple different frequency bands ranging from 30 Hz to 900 kHz. They discovered that both shear and compressional wave velocity relied significantly on the frequency with differences up to 20%. They also found that the compressional wave intrinsic attenuation is also dependent on frequency with the peak in attenuation being in the sonic frequency range (8-24 kHz). This velocity dispersion can also be predicted using Q values. Barton (2007) gives a Q value for oolitic limestones at 50 MPa effective pressure in the range of 10-100. Similarly, Watanabe and Sassa (1996) give a similar Q value of 22 for a carbonate. Using the dispersion relationship of Stewart et al. (1984) a lower velocity of 30% from ultrasonic (MHz) to seismic (100 Hz) frequency bands was found for a Q value of 10. However, when they used a Q value of 100, the velocity change predicted was reduced to 3%. There have been other reports that indicate a frequency dependence on velocity when comparing sonic logs to VSP surveys. De et al. (1994) found that the velocities found through sonic logs were 1% to 7% higher than their VSP counterparts. This was once again confirmed by Schmitt (1999) who tested heavy oil sands and found a velocity dispersion of approximately 20%. Finally, Batzle (2006) reported that the velocity dispersion between ultrasonic and seismic frequencies for a carbonate saturated with heavy oil is small when the temperature is low (25°C). However, when the temperature increases the velocity dispersion also increases up to a maximum of about 50%.

The velocity dispersion seen in Figure 2.5 is at a maximum 22.7% with the average being approximately 15%. This seems to correlate well to some of the estimates, where the velocity dispersion could be around 20%. Since this velocity dispersion took place from the frequencies of 1 MHz down to 100 kHz, further velocity dispersion might be expected when dealing with the seismic frequencies in the range of 10-250 Hz.

While there does appear to be velocity dispersion in the rock samples it is also possible that the change in velocities is due to error in the measurements. As the first break time has an error of 10% and the distance measurement has an error of 5% for the 1 kHz transducers it is possible that these velocity differences are a result of errors and not legitimate velocity dispersion.

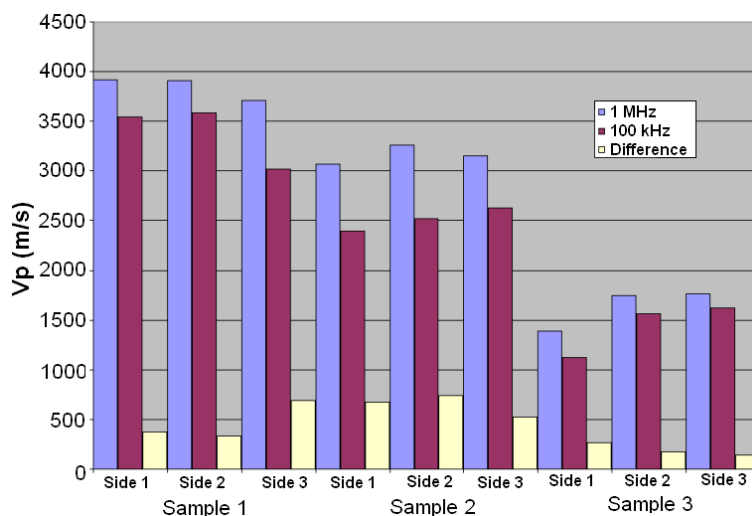


**Figure 2.5: Comparison of P-wave velocities from the 1 MHz and 100 kHz transducers.**

### 2.3.3 $V_p/V_s$

Since both the  $V_p$  and  $V_s$  of the rock samples were found using the 1 MHz transducers it is possible to examine the  $V_p/V_s$  values of the samples. The  $V_p/V_s$  value provides a method of determining the lithology of the samples.  $V_p/V_s$  was found for all

samples and locations on the samples. The plot of the ratios with respect to constant values is shown in Figure 2.6.  $V_p/V_s$  values are almost all between the values of 1.7 and 1.9. There is a range of  $V_p/V_s$  values for dolomite and limestone found in the literature, Blaylock (1999) found a  $V_p/V_s$  for dolomite of 1.78 – 1.84 and limestone of 1.84 – 1.99 as seen in Table 2.4 while Baechle (2005) reported that  $V_p/V_s$  can have a wide range of 1.65 - 1.9 for dry limestone. The  $V_p/V_s$  values found for the Maax Na samples fall reasonably well into these ranges reassuring the chemical analysis that the samples are indeed a dolomitic limestone.

Lithology	$V_p/V_s$ Range
Sandstone	1.59 - 1.76
Dolomite	1.78 – 1.84
Limestone	1.84 – 1.99
Shale	1.70 - 3.00

**Table 2.4:  $V_p/V_s$  ranges for common reservoir lithologies (Blaylock, 1999).**

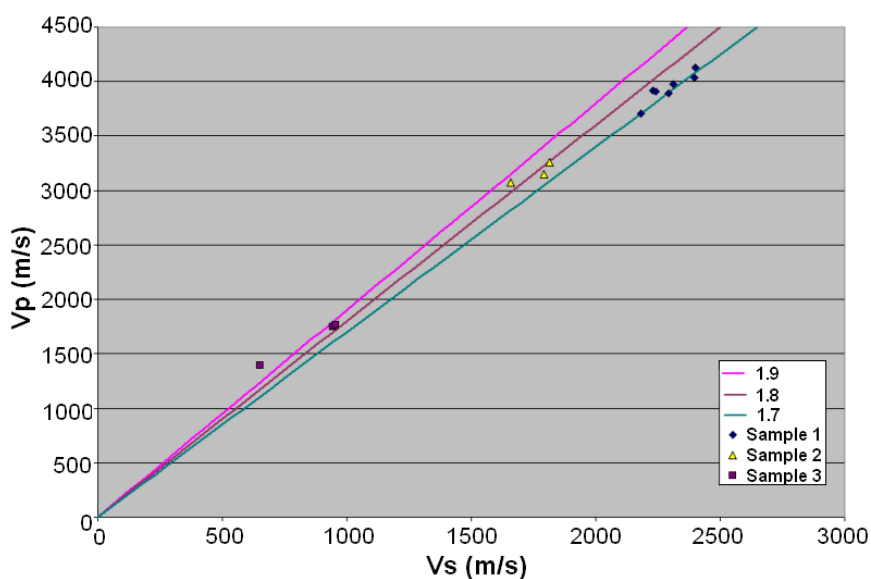


**Figure 2.6:  $V_p$  versus  $V_s$  of the dry samples with several constant  $V_p/V_s$  values annotated.**

$V_p/V_s$  values were also plotted in Figure 2.7 with relationships derived by Castagna (1993) and discussed in Mavko (1998) for water-saturated rock. The relationship derived for limestone was given as

$$V_s = -0.055V_p^2 + 1.017V_p - 1.031, \quad (2.1)$$

where  $V_s$  and  $V_p$  are the velocities of the shear and compressional wave in km/s respectively. The other two relationships described in Mavko (1998) are

$$V_s = 0.583V_p - 0.078 \quad (2.2)$$

for dolomites and

$$V_s = 0.862V_p - 1.172 \quad (2.3)$$

for the mudrock line. Despite these relationships being derived for water-saturated rock it can be advantageous to compare it to the bench-dried samples. Since the Maax Na rock samples were just air-dried it is possible that some liquid remains in the samples and are therefore viable for comparison. It is also known that  $V_p/V_s$  tends to increase with saturation. Therefore, it can be interpreted that the dry results will appear slight lower on the graph than the final saturated values. The Castagna dolomite line provides a good fit for  $V_p/V_s$  as shown in Figure 2.7. This is the expected range for the dry  $V_p/V_s$ . If the samples were to be saturated the points will move closer to the limestone line. This again confirms the chemical diagnosis that the rock samples are dolomitic limestone and gives greater confidence in the accuracy of the velocity measurements.

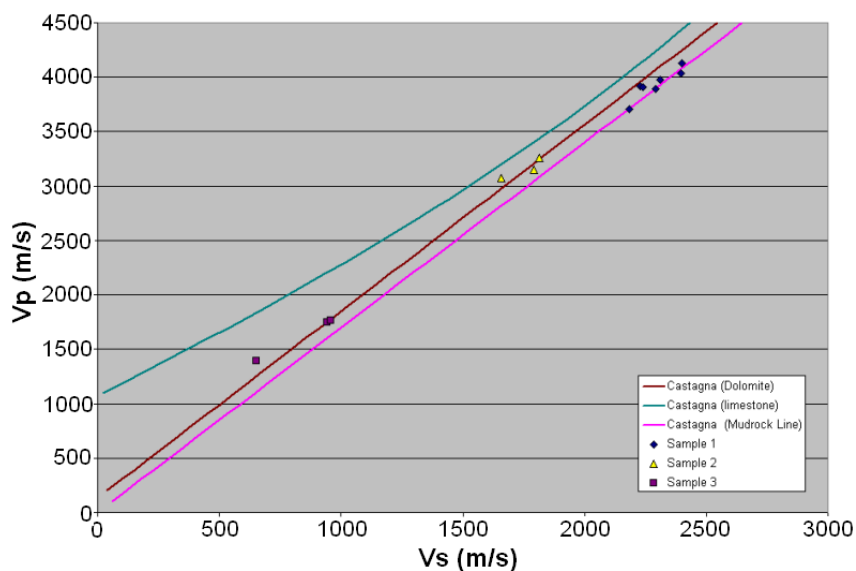


**Figure 2.7: Measured  $V_p/V_s$  of the dry samples with several empirical lines plotted.**

### 2.3.4 Density

The first measurement taken on the rock samples was an approximation of their dry density. To find the density, the volume was estimated using calipers, which was then divided by the weight of the rock, found on a scale. Corrections for the imperfections in the shape of the rock were applied to the volume before solving for the density. This method has been tested in the past using lab tested densities found by Core Labs Calgary. Cores measured with calipers to find the density resulted in a less than 5% error in density calculations. The densities measured for the three samples are  $2.00 \text{ g/cm}^3$ ,  $1.66 \text{ g/cm}^3$  and  $1.24 \text{ g/cm}^3$ . The densities are ordered as would be expected by looking at the rock samples. Sample one was the most uniform and appeared to be the strongest where as sample three is composed of the weaker white limestone. The densities of all three samples are well below the average densities of dolomite ( $2.877 \text{ g/cm}^3$ ) and limestone

(2.710 g/cm<sup>3</sup>). This drop in density can be possibly explained by the existence of fractures and a high porosity or by a more loosely consolidated rock.

These densities were compared with Gardner predicted values (Gardner et al., 1974) using the P-wave velocity and  $\rho=0.31(V_p)^{1/4}$ , where  $\rho$  is density in g/cm<sup>3</sup> and  $V_p$  is the P-wave velocity in m/s. This comparison was performed for velocities found using both the 1 MHz (Figure 2.8) and 100 kHz transducers (Figure 2.9). Since velocities differed on each side of the samples the Gardner predicted density was found for each side using the velocity taken in the centre of the side. All the measured densities appear to be below those estimated using Gardner's equations (Gardner et al., 1974). This is the case using both the 1 MHz and 100 kHz velocities. The measured densities were also compared to Gardner predicted densities found using  $V_s$  and  $\rho=1.47(V_s)^{1/4}$ , where  $\rho$  is the density in g/cm<sup>3</sup> and  $V_s$  is the S-wave velocity in km/s (Figure 2.10). Since there is no set coefficient for Gardner's equation for S-wave velocities a best-fit value of 1.47 was chosen. The S-wave Gardner densities show less of a discrepancy than both the P-wave values. However, since a best fit coefficient was used this is to be expected.

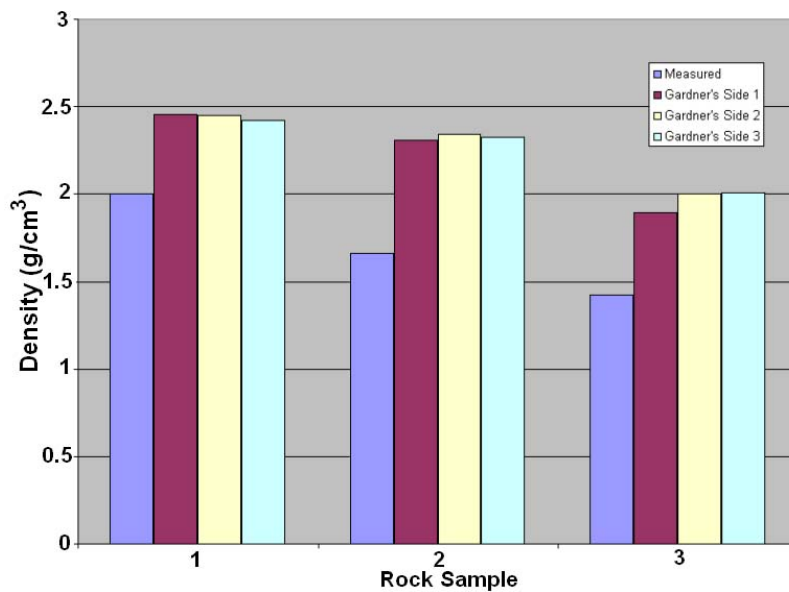


**Figure 2.8:** Display of manually calculated density and the Gardner predicted densities for all three sides of the rock samples using  $V_p$  from the 1 MHz transducers.

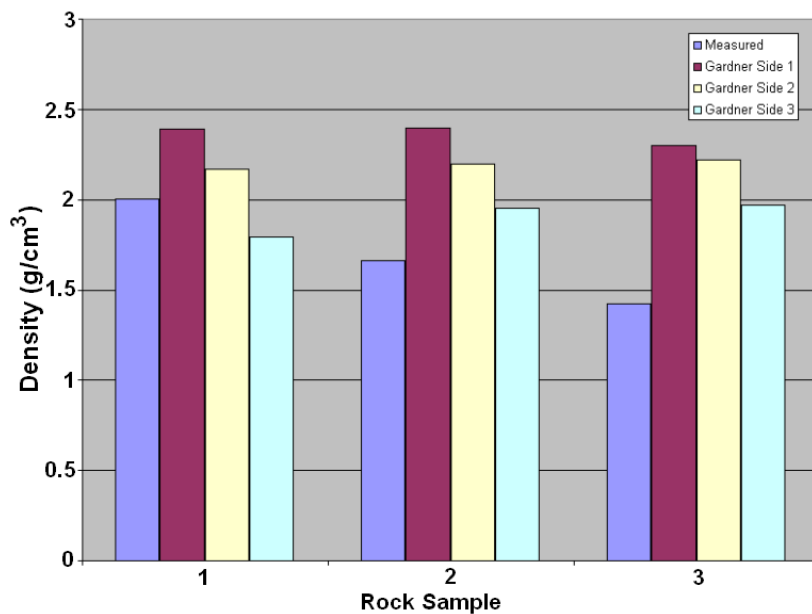


**Figure 2.9:** Display of manually calculated density and the Gardner predicted densities for all three sides of the rock samples using  $V_p$  from the 100 kHz transducers.

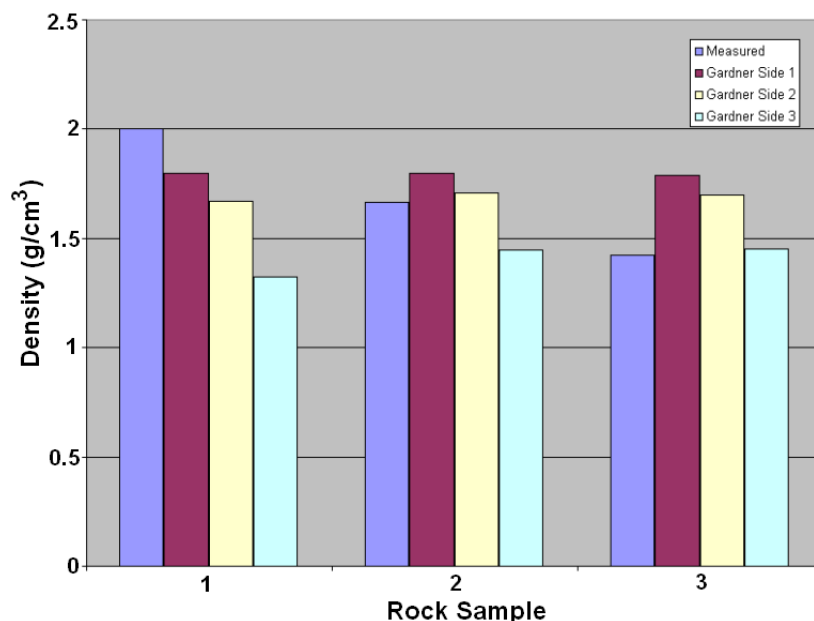


**Figure 2.10: Display of manually calculated density and the Gardner predicted densities for all three sides of the rock samples using  $V_s$  from the 1 MHz transducers and a coefficient of 1.47.**

## 2.4 Saturated Measurements

Since Maax Na is located in a region of very high rainfall it is important to look at measurements of the rock samples taken when saturated. To saturate the samples they were submersed in tap water at atmospheric pressure for two months. The measurements were redone using the saturated core. To maintain saturation as soon as a measurement was completed the sample was placed back into the tap water.

### 2.4.1 $V_p$ and $V_s$ Measurements

The P-wave and S-wave velocities were again calculated using the traveltimes from the 1 MHz receivers (See Appendix A for full traveltimes and velocities). Multiple traveltimes were used to ensure quality of the traveltimes. Due to saturation of the rock samples limited measurements were undertaken on sample two and three. When these samples were saturated, their strength greatly diminished resulting in the samples being

too weak to withstand the pressure placed on the rock to ensure good coupling between the transducer and the rock. This pressure caused minor fractures to occur in sample 3 and caused a section to break off on sample 2. To save the integrity of the sample, measurements were ceased with only side three being sampled on sample three with the P-wave transducers and only sample one being sampled with the S-wave transducers.

When comparing the dry velocities with the wet velocities, the wet velocity appears to be lower in both the P-wave and S-wave cases (Figure 2.11 and Figure 2.12). The differences between the velocities vary from one sample to another. The highest variability is seen in sample one, sample two and finally sample three with very little difference in velocity.

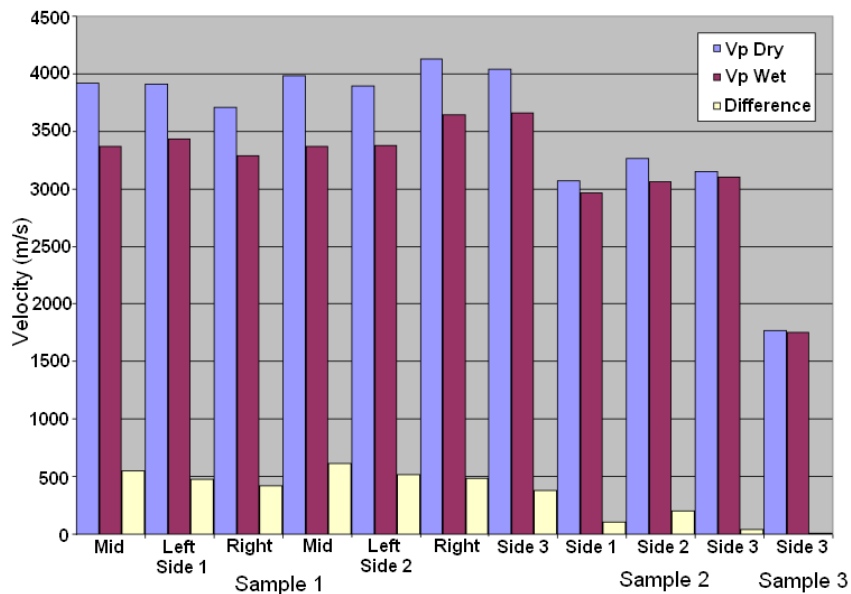


**Figure 2.11: The P wave velocities of the dry and wet cores plotted along with the differences between the two.**

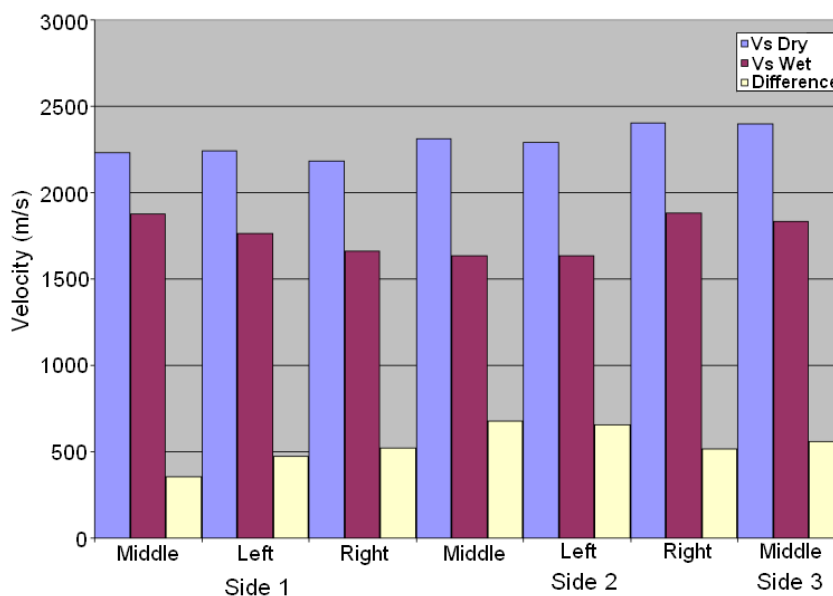


**Figure 2.12: The S wave velocities of sample 1 when dry and wet plotted along with the differences between the two.**

Colpaert et al. (2006) found, using carbonate rocks from the Norwegian Finnmark Platform, that in general saturation lowers the S-wave velocity while raising the P-wave velocity. They also found that in mudstone-wackestone samples some of the clay in the samples softened the rock so that the bulk and shear modulus dropped significantly. Assefa et al. (2003) reported that the shear modulus in water-saturated rock could be lower than dry rock by as much as 2 GPa in carbonates from the Great Oolite Limestone Formation of the Weald sub-basin in Hampshire, England. Colpaert (2007) shows a similar result using ultrasonic measurements on 26 upper Paleozoic carbonate samples from the Barents Sea. He finds that generally the S-wave velocity decreases while the P-wave wave velocity increases from a dry sample to ethanol and finally to a brine saturated state. This result is confirmed by many other papers including Jones et al. (1976) using Berea sandstones, King (1996) using Boise sandstone and Johnston (1978) using Navajo sandstone.

The results obtained for the S-waves using the three Maax Na cores follow the findings of these papers. The results can also be explained by examining the equations for the P-wave and S-wave velocities given as

$$V_p = \sqrt{\frac{K + \frac{4}{3}\mu}{\rho}}, \quad (2.4)$$

and

$$V_s = \sqrt{\frac{\mu}{\rho}}, \quad (2.5)$$

where K is the bulk modulus and  $\mu$  is the shear modulus.

Using the findings of Colpaert et al. (2006) and Assefa (2003), the shear modulus or rigidity is expected to greatly decrease due to the softening of the rock. This drop in shear modulus is expanded on by an increase in the density due to the water saturation resulting in a large drop in the S-wave velocities expected by Equation 2.5. This is the result seen in the experimental data.

In contrast to the majority of results in the literature, the P-wave velocities of the Maax Na samples tend to decrease when saturated. Colpaert et al. (2006) can once again explain this using the findings that occasionally if the saturated rock softens both the bulk and shear modulus decrease. Taking into account Equation 2.4, if both the bulk and shear modulus decrease, then the total P-wave velocity will decrease. Even if the bulk modulus and shear modulus only slightly decrease, the increase in density due to the additional water present will continue to reduce the P-wave velocity. Another possible reason for the decrease in P-wave velocity is the pore shape and size. Assefa (2003) reported that despite the majority of saturated P-wave velocities being larger than that of the dry

velocities there were a few samples that displayed the opposite trend (Figure 2.4). The Kuster and Toksoz method described in Batzle (2006) for fluid substitution reports that if the pores are close to spherical (aspect ratio<sup>1</sup> >0.5) in shape the pores are stiff causing the density change to dominate resulting in a decrease in velocity. The same effect is seen with the S-wave velocities (Figure 2.13). The Kuster-Toksöz method has been shown by Wang et al. (1991) to be very efficient for estimating the velocities of water-saturated limestone.

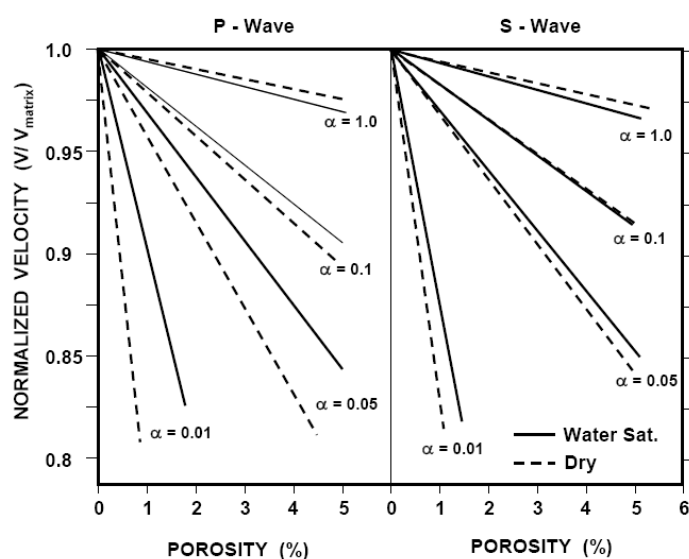


**Figure 2.13: Normalized compressional and shear velocities for cracked rocks ( $V_{\text{rock}}/V_{\text{mineral}}$ ) both dry and saturated using the Kuster Toksöz (1974) method (From Batzle 2006).**

#### 2.4.2 $V_p/V_s$ Value

Since only sample one had both compressional and shear wave velocities taken when saturated with water it was only possible to look at  $V_p/V_s$  of the one sample. The saturated  $V_p/V_s$  values were compared with their dry counterparts and plotted along with several constant values (Figure 2.14). The values again match up well to the values found

<sup>1</sup> The aspect ratio ( $\alpha$ ) is the ratio of the ellipse semiminor (a) to semimajor (b) axis,  $\alpha=a/b$ .

in literature. Baechle (2005) reported a range of  $V_p/V_s$  for water-saturated limestone from Cretaceous and Miocene reservoirs to be 1.75 – 2.05. Colpaert (2006) found a similar range of  $V_p/V_s$  of approximately 1.75 to 2 for wet carbonates from the Upper Palaeozoic of the Norwegian Finnmark Platform.

The saturated  $V_p/V_s$  ratio was also compared to the empirical relations of Castagna for saturated rock (Equation 2.1-2.3). The saturated values are near the limestone line giving the result expected from the chemical analysis of the rock type.

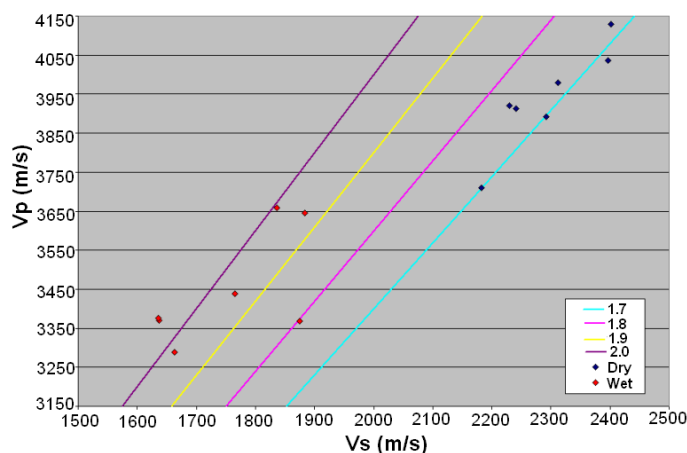


**Figure 2.14:  $V_p$  versus  $V_s$  of sample one with several constant  $V_p/V_s$  values annotated. The dry sample values are shown in blue with the water saturated in red.**

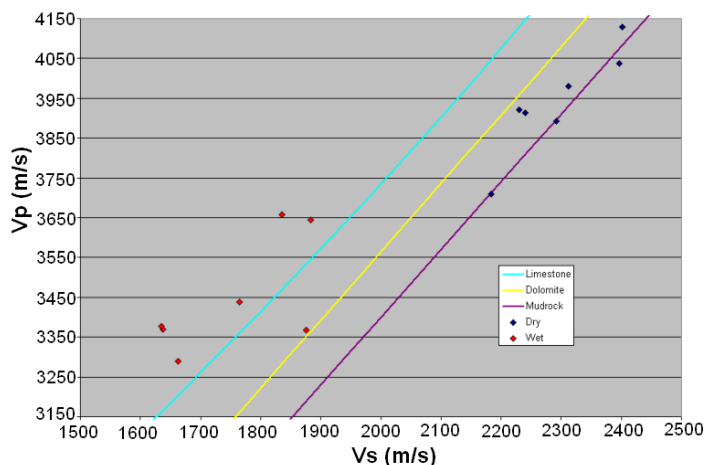


**Figure 2.15: Measured  $V_p/V_s$  of sample one with several empirical lines plotted. The dry sample values shown in blue and water saturated values shown in red.**

### 2.4.3 Density

The density of the saturated samples was measured using the same technique as the dry samples. The samples were taken out of the water and immediately measured on a scale. As soon as the weight was determined the sample was placed back into the water. The weight of all three cores increased as is expected by the input of the water with sample three having the greatest increase in weight followed by sample two then sample one (Table 2.5). This is to be expected as sample three is the softest rock and least consolidated and therefore has a greater porosity. Sample two had several small fractures, which would allow it to intake a greater percentage of water than the nearly homogenous sample one. The densities of samples one, two and three all increased from their dry densities to  $2.23 \text{ g/cm}^3$ ,  $2.07 \text{ g/cm}^3$  and  $1.96 \text{ g/cm}^3$  respectively. Since the size of the core did not change significantly and only the weight changed the percent difference between the dry and wet weight is equal to the percent difference of the densities.

	Sample 1	Sample 2	Sample 3
<b>Dry</b>	247.1	111.9	86.2
<b>Wet</b>	274.6	139	118.7
<b>Difference</b>	27.5	27.1	32.5
<b>% Difference</b>	11.1	24.2	37.7

**Table 2.5: The weight (g) of the Maax Na samples while dry and water saturated.**

Once again the measured densities were compared to the Gardner predicted densities from P and S-wave velocities and plotted in Figure 2.16 and Figure 2.17 respectively. Due to the weakness of the rock no P-wave velocity measurements were taken for side one and two in sample three and no S-wave velocities were taken for samples two and three. Therefore, only those sides with velocity measurements can be included in the Gardner predictions. The densities predicted by the saturated P-wave

velocities are much closer to the measured value than the dry values. The water has allowed the rock to seem more homogenous allowing Gardner's predictions to become more accurate than highly porous dry samples. When considering the S-wave predictions a best-fit coefficient of 1.93 was used to minimize the difference between the predicted and measured values.

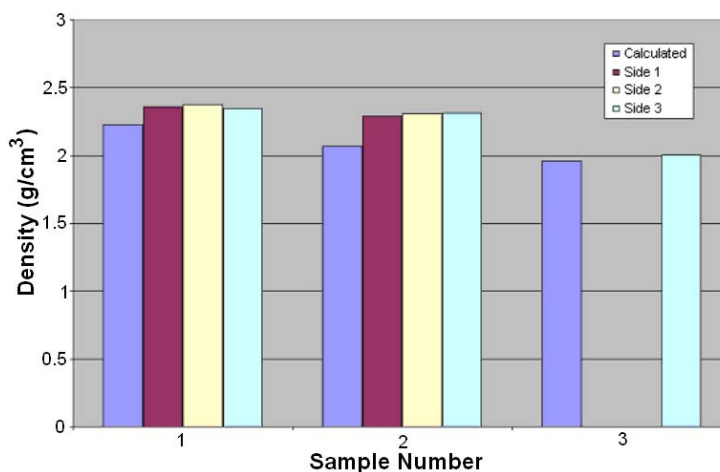


**Figure 2.16: Display of manually calculated density and the Gardner predicted densities for all three sides of the water-saturated rock samples using  $V_p$  from the 1 MHz transducers.**

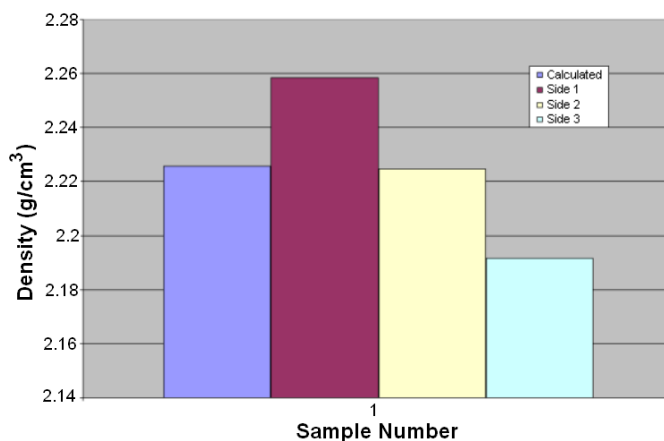


**Figure 2.17: Display of manually calculated density and the Gardner predicted densities for all three sides of the water-saturated rock samples using  $V_s$  from the 1 MHz transducers and a coefficient of 1.93.**

## 2.5 Porosity

Throughout this section, various reasons for lower than average velocities have been made based on the thought that the rocks contain a high porosity. Now that measurements for the velocities and densities have been found a prediction of the porosity can be obtained. Batzle (2006) gives empirical relationships to find porosity of dry dolomites and limestones based on compressional and shear wave velocity. The relationships for porosity of dry limestone using  $V_p$  and  $V_s$  are given by

$$V_p = 6.19 - 9.80\phi, \quad (2.6)$$

and

$$V_s = 3.20 - 4.90\phi, \quad (2.7)$$

where,  $\phi$  is the porosity and  $V_p$  and  $V_s$  are given in km/s. Similarly, the relationships for dolomites are

$$V_p = 6.78 - 9.80\phi, \quad (2.8)$$

and

$$V_s = 3.72 - 5.20\phi.$$

Another set of porosity – velocity relations are described in Assefa et al. (2003). Instead of using the dry velocities like Batzle, Assefa's relations are derived from the water-saturated velocities of limestones. The equations are given as

$$V_p = 5317 - 89\phi, \quad (2.9)$$

for P-wave velocities and

$$V_s = 2844 - 49\phi, \quad (2.10)$$

for S-wave velocities, where  $V_p$  and  $V_s$  are given in m/s.

The approximate porosity can also be found using the densities of the samples.

The relationships is expressed as

$$\phi = \frac{\rho_w - \rho_d}{\rho^*}, \quad (2.11)$$

where  $\rho_w$ ,  $\rho_d$  and  $\rho^*$  are the densities of the wet sample, dry sample and water respectively. Since an exact measure of density for the tap water used was unavailable the density of pure water ( $1 \text{ g/cm}^3$ ) was used as an approximation.

The results of all the empirical relationships are plotted in Figure 2.18. The  $V_p$  and  $V_s$  values used in the relations were taken from the middle of each side (porosities found using all sides can be seen in Appendix A). Since the density of the rock was measured for the whole rock the same porosity found from the measured densities will be used for each side of the samples.

P-wave velocity appears to give lower porosity than the other methods for sample two and three. In contrast, Batzle's P-wave dry limestone relation appears to over-predict the porosity of sample three. Assefa (2003) derived his relations for a porosity range of 0-20%, beyond that range the relations are untested and may become inaccurate. This may be why the wet limestone relations become increasingly different from the other methods as the porosity increases.

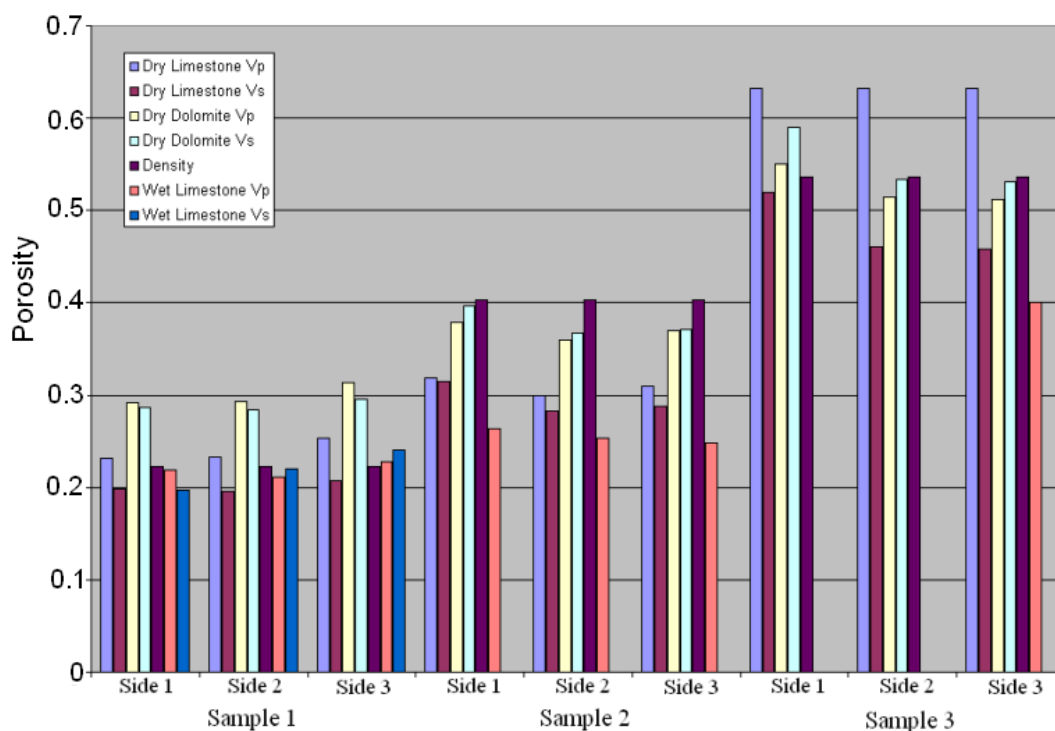


**Figure 2.18: Comparison of porosity measurements found using empirical relations between the P and S-wave velocities of dry dolomite and limestone (Bazle, 2006), the water saturated P and S-wave velocities of limestone (Assefa et al., 2003) and the porosity derived from the measured densities.**

The results from this chart compare with what was expected. Sample one has the smallest porosity (~21%), sample two is in the middle (~33%) and sample three has the highest with an approximate porosity of 50%. All of these samples have porosities on the high end of the range for limestones. Domenico (1984) reported that the majority of limestone samples fall in the range of 0.006 to 0.229. He went on to report that a third of his samples studied fell into the range of 0.025 to 0.050. Norikatsu et al. found a similar range of effective porosities in samples from the Ryukyu limestone of 0.03 to 0.35 with the mean value of 0.123. With the exception of sample one the porosities found appear to be outside the range of Domenico. This can possibly be explained by the increased weathering the samples have been exposed to. The samples

found at Maax Na were found exposed to the elements as well were likely exposed at the surface over geologic time intervals then perhaps broken into rubble for construction. This exposure may have affected the strength and porosity of the rock. The porosities estimated also back up the hypothesis that the soft white limestone may be of higher porosity than the tan limestone as sample three was found to have 20% greater porosity than the other samples.

## **2.6 Summary**

Three rock samples were taken from a pile of rocks believed to have been exhumed from the pyramid when the looters dug their trench. These samples agree physically with other samples from Maax Na that were chemically determined to be dolomitic limestone. The three samples were measured for the compressional and shear wave velocities using ultrasonic transducers. These velocities were found to be lower than the typical range for limestones for both dry and saturated suggesting that the samples contain high porosity. By examining the  $V_p/V_s$  values, the chemical diagnosis of dolomitic limestone was confirmed. Finally, using density calculations and velocities for the dry and saturated samples, the porosities were measured. The porosities were found to be high compared to many of the values found in literature (21% for sample one, 33% for sample two and 50% for sample three).

The ultrasonic P-wave velocities for the rock samples ranged from approximately 1200 m/s to 4000 m/s. The seismic velocity expected in the interior of the pyramid is expected to be lower than the velocity of the hand samples. As described previously, there may be velocity dispersion with frequency. The seismic data has a frequency in the range of 100 Hz and the ultrasonic measurements were taken in the 100 kHz to 1 MHz

range, an approximately 20% lower velocities could be expected. As well, the pyramid is composed both of limestone blocks as well as limestone rubble and plaster. As the rubble and plaster are more loosely consolidated a lower velocity is again expected. These core velocities serve as a guideline for the upper limit of velocities expected whereas the interior of the pyramid is expected to give velocities significantly lower.

### **Chapter Three: Seismic Tomography**

In 2002, four seismic surveys were conducted on the pyramid at Maax Na by a team from University of Calgary led by Dr R. Stewart and Robert Birch with assistance from the archaeologists of the Maax Na Archaeology Project. These surveys involved two different 2D surveys conducted in rings around the perimeter of the pyramid. These 2D surveys were expanded to include additional shots along the slopes of the pyramids. All four surveys will be solved using traveltimes and amplitude inversions.

#### **3.1 Hammer Seismic Viability**

Before concentrating on the different surveys, it is important to establish if hammer seismic is a viable technique for traveltimes tomography. Since tomography is dependent on having accurate travel-time and amplitude picks the quality of the shot is important. In this case the shot used was a sledgehammer strike against a metal plate. Since the shot used could not vary, the shape of the metal plate and shot repeatability were instead investigated. The first step in investigating the hammer sources viability was to see if a shot was repeatable using the same plate. If the shots have a high repeatability the data is accurate and able to be compared. A single strike against a 12-inch circular plate was used. This strike was repeated in the same location giving two distinct seismic sections (Figure 3.1). As can be seen on the seismic sections receivers 1 and 35 are dead and therefore excluded from any further analysis. The first break traveltimes were then computed and compared to each other. The results showed that the shot was repeatable. All the travel-times from both shots were within 0.5 ms except for three, which were within 1.5 ms (Figure 3.2). Since the sampling rate of the data was 0.5 ms the results were very close.

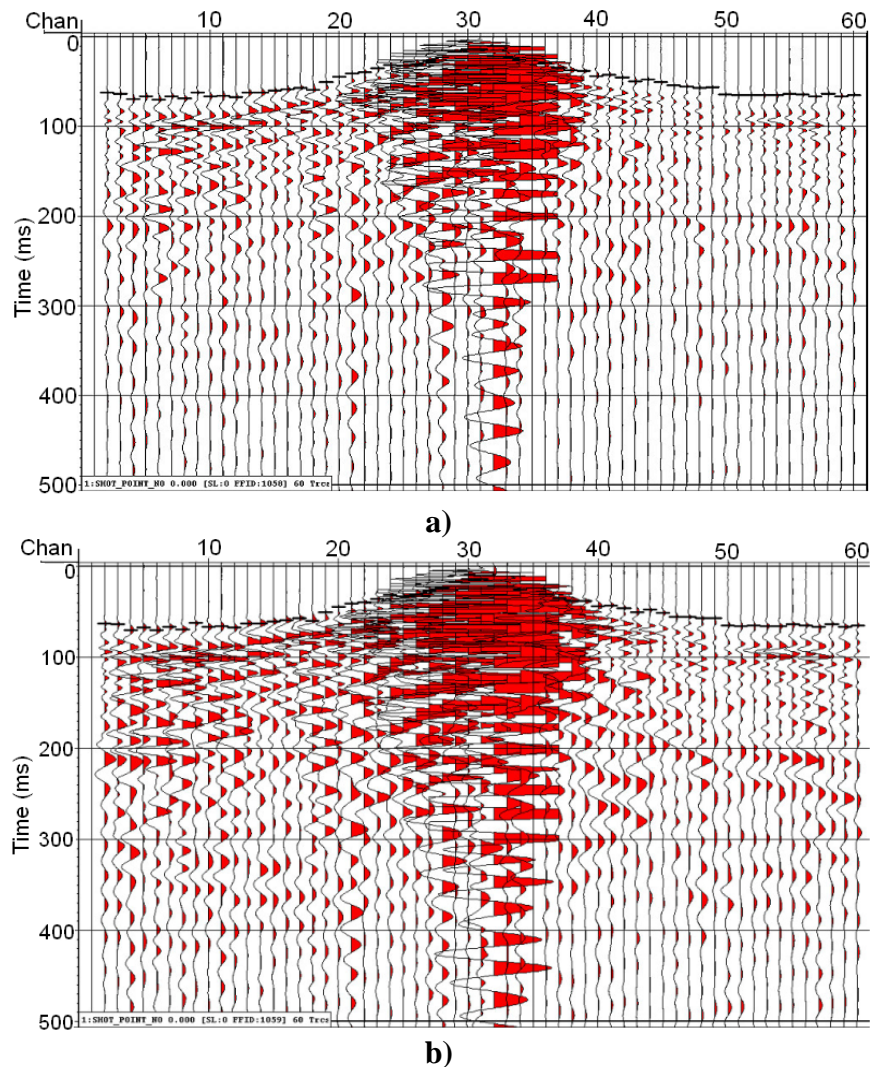


**Figure 3.1: The seismic sections from a sledgehammer strike against a 12-inch circular plate where a) is Shot 1 and b) is shot 2. First break travel-times are in black. Receiver 1 and 35 are dead traces.**

Since the shots have been proven to be repeatable we can now look at a different configuration for the metal plate. Instead of the circular plate a square plate was used. The shot was once again taken from the same location and first break picks were analyzed. Once again the results correlated very closely. The comparison between the first circular shot and the square plate yielded a difference of no more than 1.5 ms. This is in the same range of differences as the two round plates. The comparison between the square plate and the second shot on the round plate yields even better results than

between the two round plates resulting in all differences being between 0.5 ms (Figure 3.3).

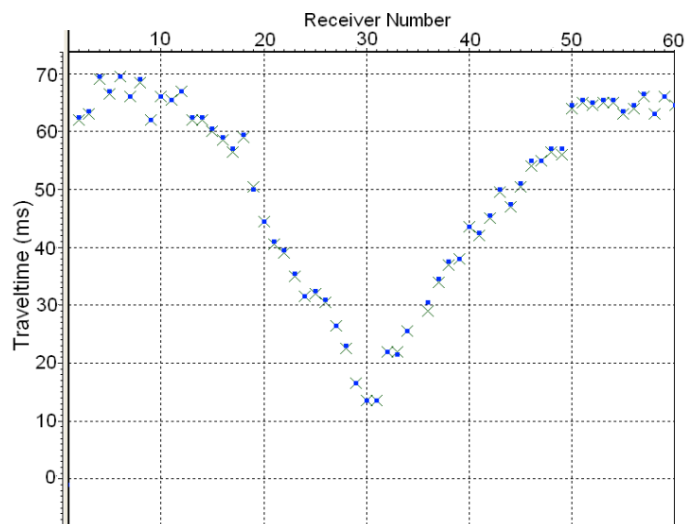


**Figure 3.2: Graph of the first break travel-times between shot 1 (green X's) and shot 2 (blue dots).**

When using a hammer source it is very difficult to strike the plate exactly the same way twice. Since the strikes on the plate produce slightly different frequency outputs (Figure 3.4) there is an expectation of differing first break travel-times between shots. When comparing the two round plate shots and the square shot all the travel-times were within a difference of 1.5 ms. This is a small difference and is therefore probably a result of the differing outputs from the hammer strike. Therefore, the shape of the strike plate does not greatly affect the quality of the shot.

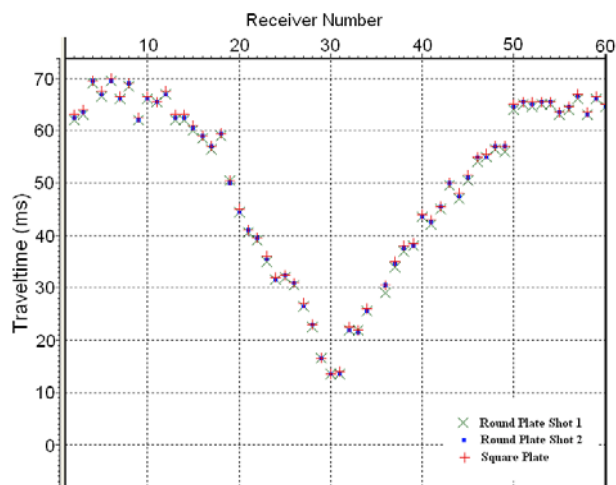


**Figure 3.3: Graph of the first break travel-times including both shots on the round plate and the shot on the square plate.**

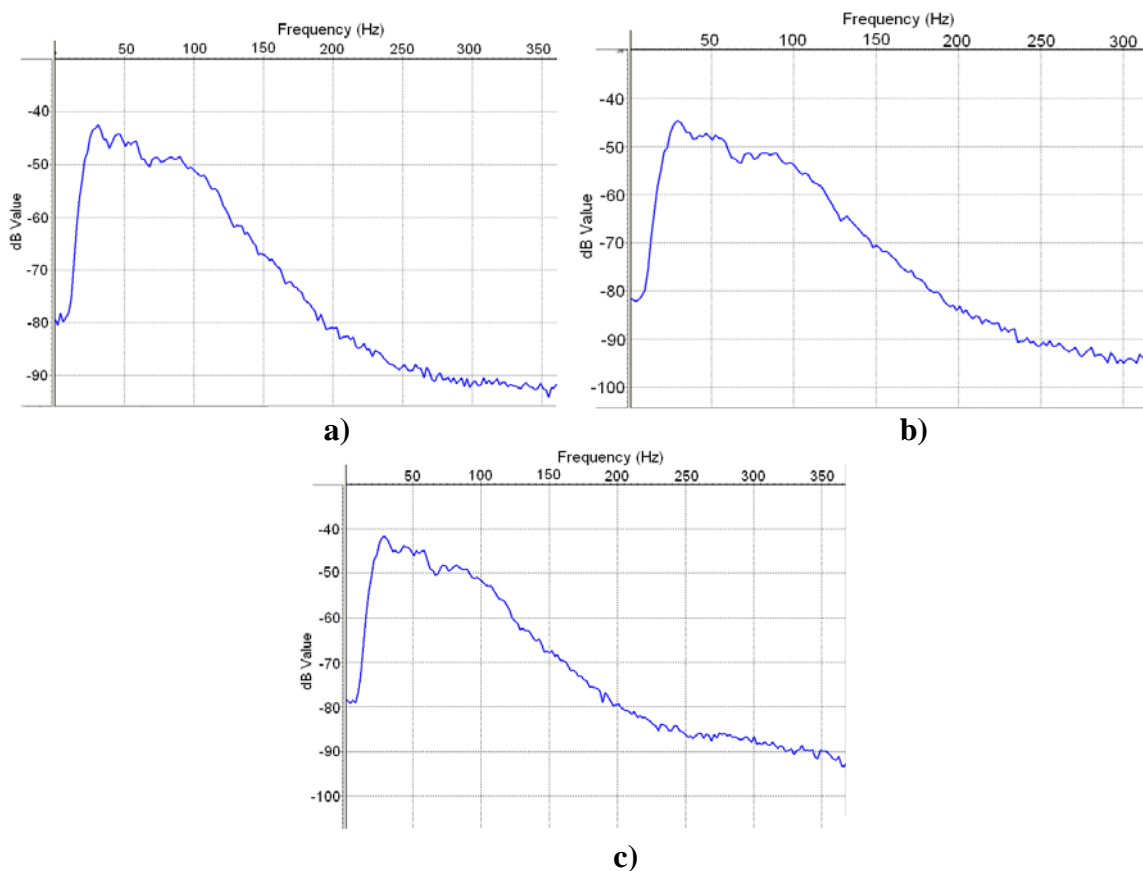


**Figure 3.4: The average amplitude spectrum of a) round plate shot 1, b) round plate shot 2, and c) square plate. The shapes are similar but not exactly the same.**

## 3.2 Current Surveys

### 3.2.1 Lower 2D Seismic Survey

The first survey was performed on the lower section of the pyramid. This survey involved the use of sixty 1-component geophones planted vertically. These geophones had a horizontal receiver spacing of 2 m and were spread along a contour level near the base of the pyramid. The shots were placed along the same vertical contour space in-between the receivers. A total of sixty-one source points with two meter spacing were placed between the receivers. As the circumference of the pyramid was not large enough to accommodate all of the receivers, the final four receivers were placed perpendicular to the circumference and placed going down the pyramid (Figure 3.5).

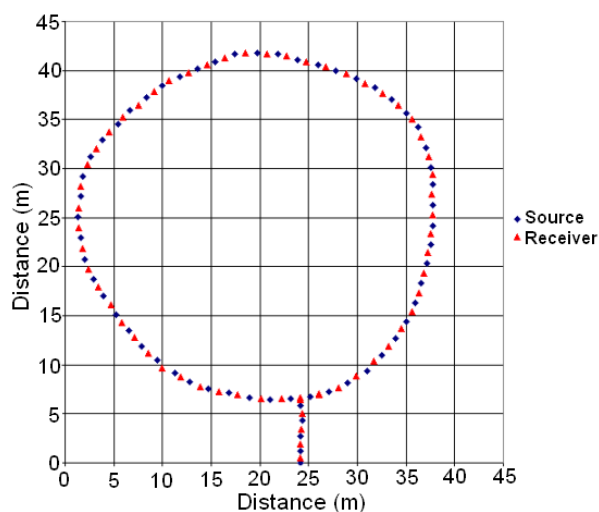


**Figure 3.5: The initial source and receiver layout for the lower perimeter of the Maax Na pyramid. Sources are indicated in blue and receivers are indicated in red.**

The hammer-seismic source produced on average a relatively broadband signal up to 250 Hz with a minimum frequency of 10 Hz with some shots producing signal up to 300 Hz. These variations can be associated with differences in hammer speed and power. Figure 3.6 shows the amplitude spectrum of a sample shot. The remaining shots display

similar results. This same frequency spectrum was found for all 2D and 3D surveys. This is to be expected as the hammer source is being used on the same pyramid structure for all surveys.

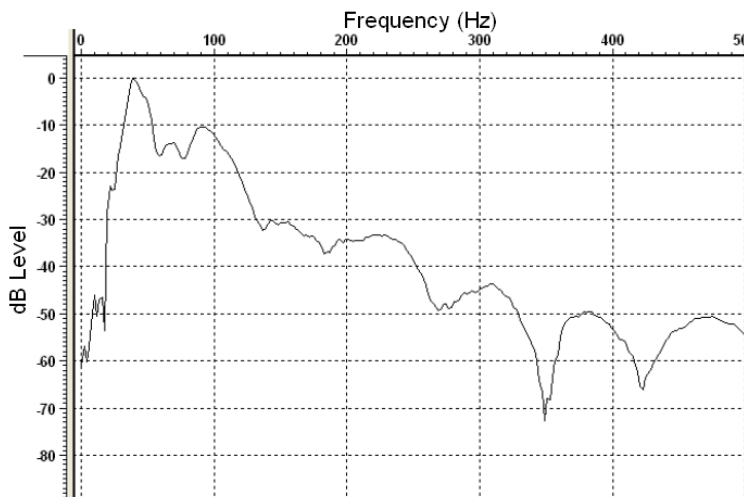


**Figure 3.6: The amplitude spectrum for the average data trace of shot 1023.**

Before processing the traveltimes an examination of the seismic gathers is undertaken. Since the lower perimeter started with sixty receivers and sixty-one shots, a total of 3660 traveltimes are expected. However, in assessing the survey (See Figure 3.7) channel 1 and channel 35 appear to be dead traces and were removed from the processing. During acquisition, four source positions had to be abandoned due to an angry wasps' nest. Finally, since we are using 2D traveltimes inversion further exclusion of sources and receivers must be made. To perform an accurate inversion all locations must be on the same vertical contour. However, extra sources and receivers were placed further down the pyramid than the others and therefore must be removed. These shots can be re-included if 3D inversion techniques are applied. After the exclusion of these sources and receivers there will be a total of nine shots and six receivers being excluded resulting in the final layout seen in Figure 3.8. Taking this information into account the

lower perimeter is left with 54 receivers and 52 shots resulting in 2808 traveltimes instead of the original 3660.

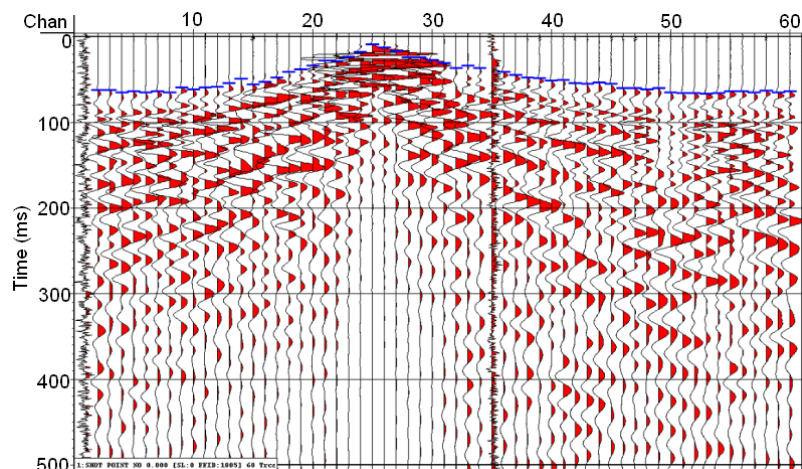


**Figure 3.7: A sample shot from the lower perimeter with a 500ms AGC. First break picks are shown in blue. Receivers 1 and 35 are dead.**

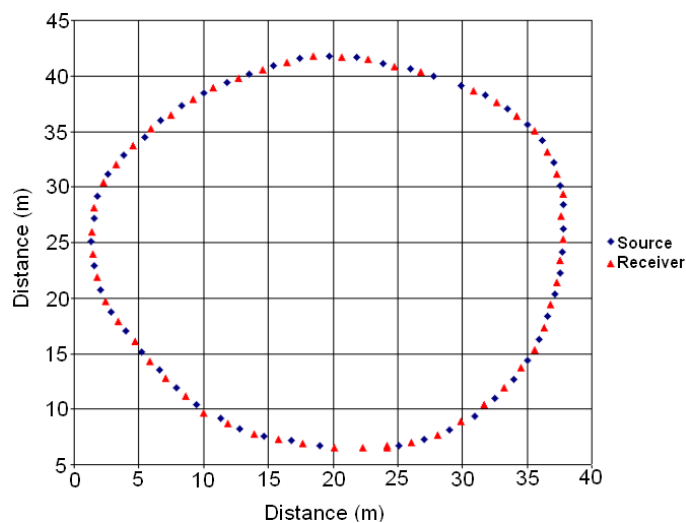


**Figure 3.8: The final source and receiver layout for the lower perimeter of the Maax Na pyramid. Sources are indicated in blue and receivers are indicated in red.**

### 3.2.2 Upper 2D Seismic Survey

The second survey once again used sixty 1-component geophones with sixty-one hammer source locations. This survey was performed further up the pyramid on a vertical contour 5.25 m above that of the lower 2D survey. The horizontal receiver spacing used

was reduced to 1 m with the hammer-sources once again being placed between the receivers. In this survey, there were not adequate receivers to cover the entire circumference therefore a gap in the coverage was left along the eastern side of the pyramid as seen in Figure 3.9. Inside this gap in coverage on the east side of the pyramid is a large looter's trench (Figure 3.10).

The upper perimeter did not experience the difficulties of the lower perimeter. Looking at a sample section, Figure 3.11, it can be determined that all channels are now active and therefore viable. The upper survey also took place on the same vertical contour allowing all locations to be used in 2D inversion. The results of this mean that we are left with the initial number of 3660 traveltimes.

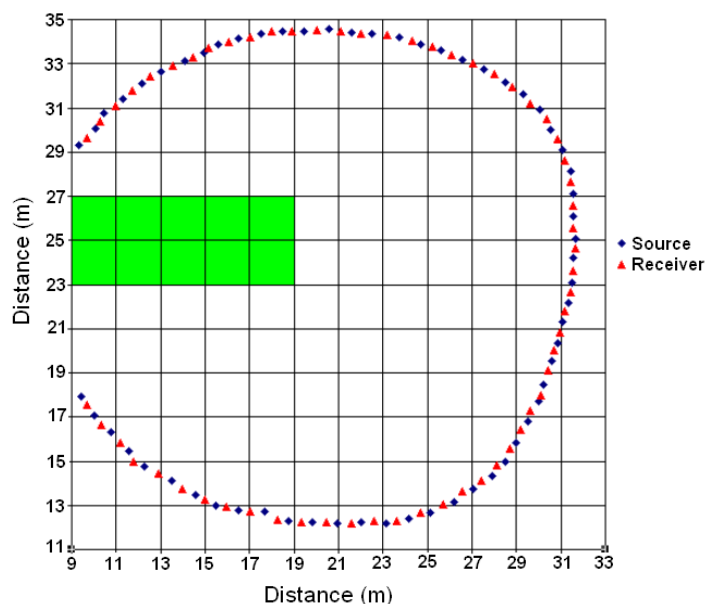


**Figure 3.9: The source and receiver layout for the upper perimeter of the Maax Na pyramid. Sources are indicated in blue and receivers are indicated in red. Approximate location of looter's trench in green.**



**Figure 3.10: A view of the looters' trench located in the upper 2D survey**

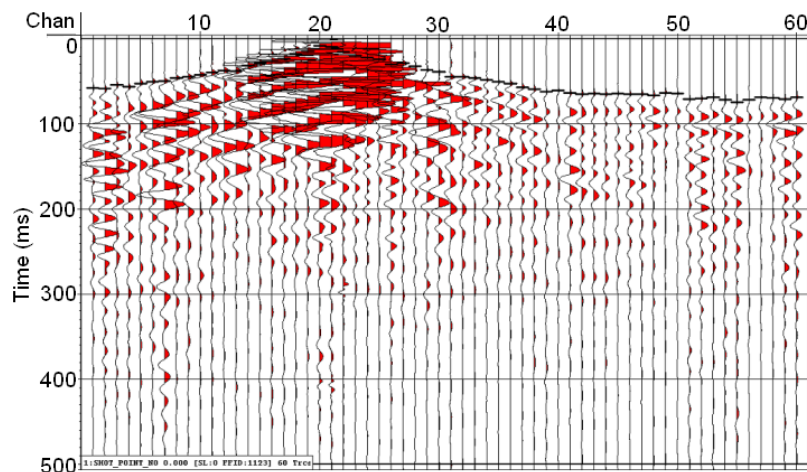


**Figure 3.11: A sample shot from the upper perimeter. First break picks are shown in black.**

### ***3.2.3 Lower 3D Seismic Survey***

The lower 3D survey starts with the final layout of the lower 2D survey. Since we are now dealing in three dimensions the shot and receivers that were previously excluded from the 2D survey for being on different vertical contours can now be included.

However, the shots near the hornets' nest remain absent and geophone 1 and 35 remain dead. In addition three lines of sources with 2 m diagonal spacing were placed up the sides of the pyramid as see in Figure 3.12. A fourth line on the back of the pyramid was

not performed due to the steepness of the slope. Adding all these lines onto the 2D survey a total of fifty-eight receivers and ninety-six source points were used resulting in 5568 traveltimes.

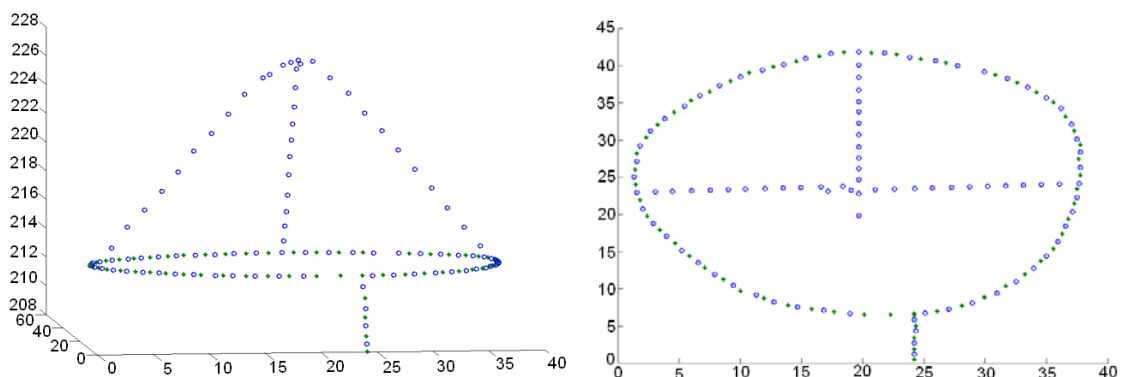


**Figure 3.12: Source receiver layout for lower 3D seismic survey in 3D view (left) and 2D top or plane view (right). Sources are shown in blue and receivers in green.**

### 3.2.4 Upper 3D Seismic Survey

Like the lower 3D survey, the upper 3D survey is based on its 2D counterpart. All sixty receivers and sixty-one shot positions are reused. We once again have three shot lines going from the bottom of the pyramid to the top (Figure 3.13). The source lines are spaced with a two-meter diagonal spacing. In total the upper 3D seismic survey has sixty receivers and ninety-seven shot points resulting in 5820 traveltimes.

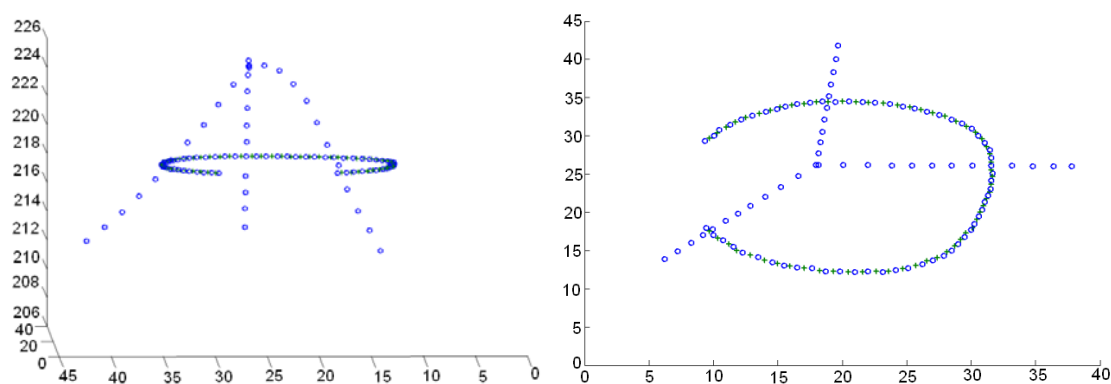


**Figure 3.13: Source receiver layout for upper 3D seismic survey in 3D view (left) and 2D top or plane view (right). Sources are shown in blue and receivers in green.**

### 3.2.5 Combined 3D Survey

A final survey that was undertaken was combining the upper and lower 3D surveys into a large more encompassing survey. When combined there are a total of 118 geophone locations with 193 source locations. However, the upper 3D survey shot locations are recorded only by the upper 3D receiver locations and the lower 3D shot locations only by the lower 3D receiver locations resulting in 11388 rays.

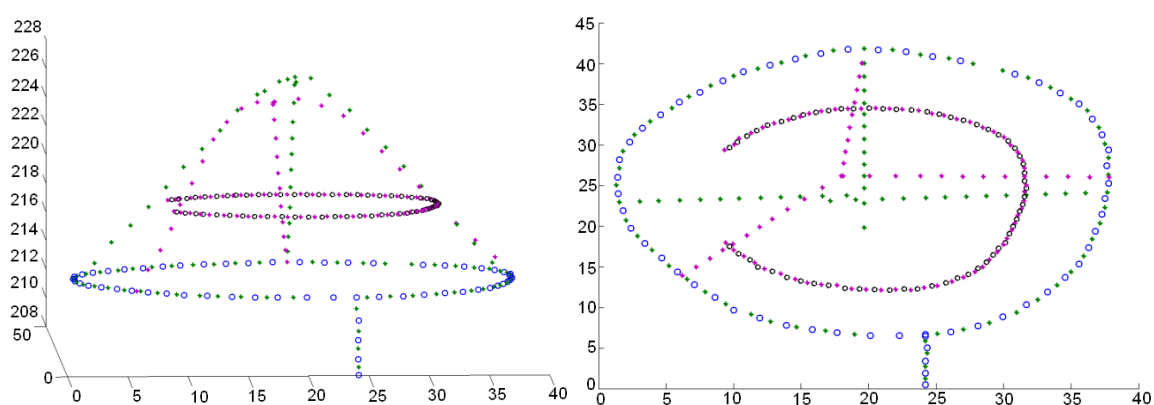


**Figure 3.14: Source receiver layout for combined 3D seismic survey in 3D view (left) and 2D top or plane view (right). Sources and receivers shown in purple and black respectively from the upper 3D survey and green and blue for the lower 3D survey.**

## 3.3 Grid Size and Fold

### 3.3.1 2D Surveys

When performing the inversions on the lower survey a pixel size of 1 m x 1 m was chosen. This size was chosen since it maintains a high fold in the straight ray tomography (Figure 3.15) while being small enough to pick up any significant voids in the pyramid. This pixel size results in a 38 by 37 grid model. This means there are a total of 1406 pixels and 2808 rays thus giving a 2808 x 1406 sized distance matrix  $\mathbf{A}$ .

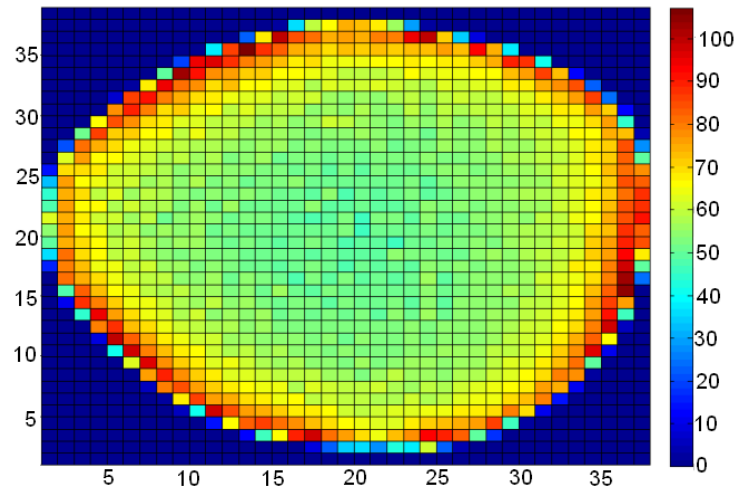


**Figure 3.15: Total fold (rays crossing per pixel) for straight ray tracing of the lower 2D survey. The x and y axes are the horizontal dimension of the survey and are given in meters.**

Once again for the upper survey a pixel size of 1 m x 1 m was used for the inversions. Since the upper 2D survey consists of a smaller area with more rays than the lower 2D survey a greater level of fold is seen (Figure 3.16). However, due to the gap in the circle of sources there is a region of smaller fold that could produce velocity errors. The 1 m grid size results in 24 x 23 grid layout with an  $\mathbf{A}$  matrix of size 3660 x 552.

The location of a looters' trench in the middle of the survey was the cause of some difficulties. Since straight ray tomography will pass multiple rays through the trench, there will be errors in the velocity model. To counteract this effect when performing straight ray tomography all rays passing through the location of the trench were omitted in the inversion. This resulted in a total of 3054 rays remaining. By dropping the amount of rays the fold is greatly reduced in the area of the trench (Figure 3.17). However, since the trench would cause velocity errors the amount the model is corrected offsets the lower fold. The velocity models were found using both the trench corrected and uncorrected model.

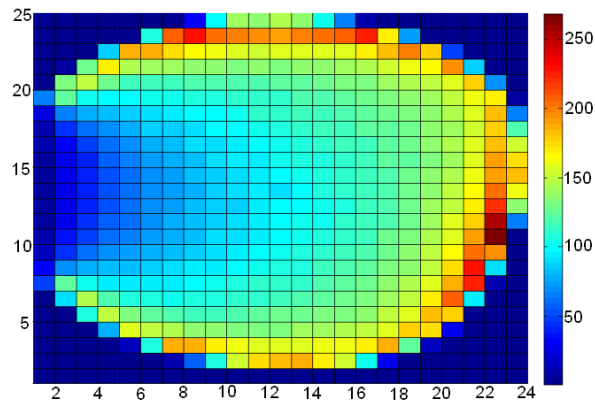


**Figure 3.16: Total coverage of rays per pixel for straight ray tracing of the upper 2D survey. The x and y axis are the horizontal dimension of the survey and are given in meters.**

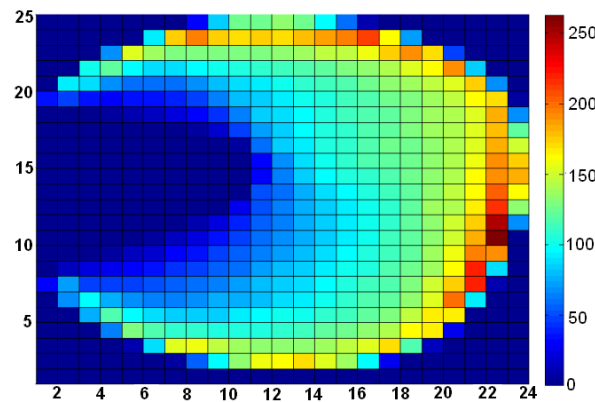


**Figure 3.17: Total coverage of rays per pixel for straight ray tracing of the upper 2D survey with all rays passing through the looters trench being ignored.**

### 3.3.2 3D Surveys

For all three different 3D surveys, a similar 2 m x 2 m x 2 m pixel size was chosen. This grid is larger than that of the 2D surveys as a result of the increase in area covered. To reduce the amount of pixels with very low fold a larger pixel size was chosen. In addition to the increase in fold per pixel there is also a dramatic decrease in computational time from a 1 m cube pixel to a 2 m cube pixel. Both the upper and lower 3D surveys show a fairly similar level of fold whereas the combined survey has a much higher fold as seen in Figure 3.18.

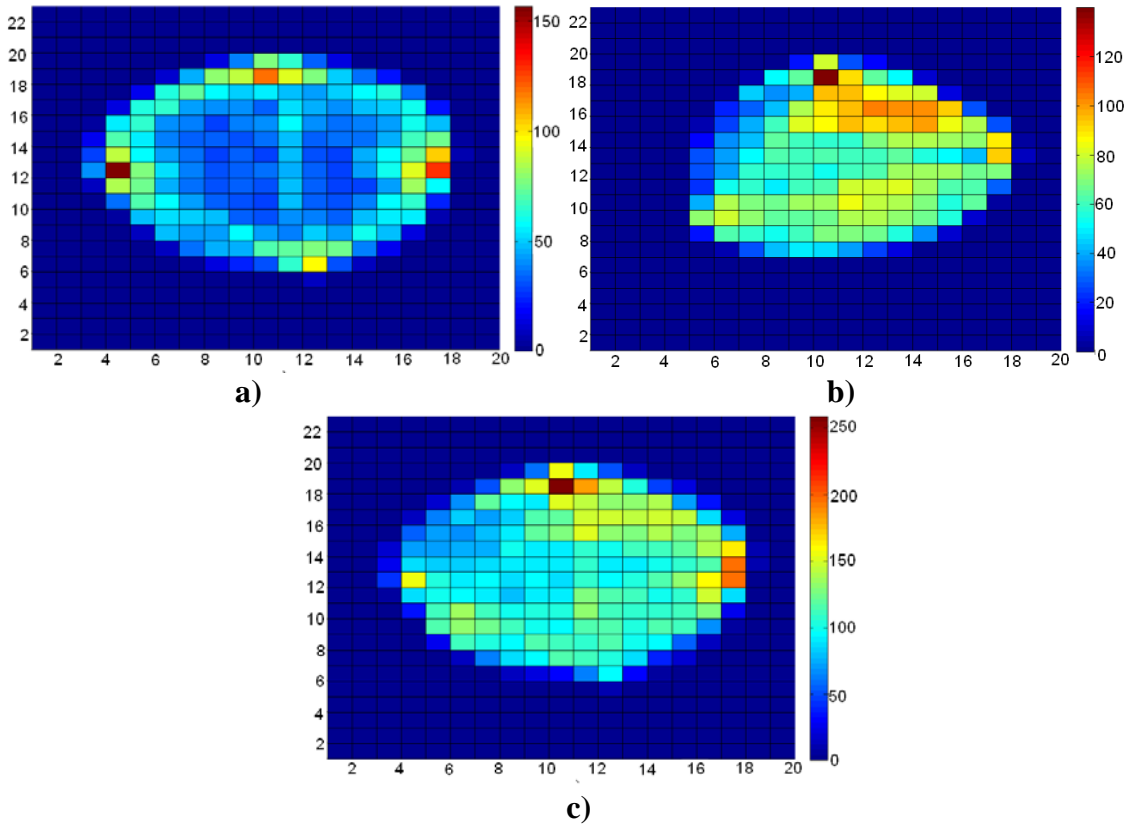


**Figure 3.18:** The total fold (m) of a 2m vertical level from straight ray tracing for the a) lower 3D survey, b) the upper 3D survey and c) the combined 3D survey.

### 3.4 Straight Ray Traveltime Tomography Results

Multiple different techniques were used to solve the different straight ray surveys. Straight ray tomography techniques were solved using Chuandong Xu's Matlab code `dm_calc` for 2D ray tracing and my own `dm_calc_3D` Matlab code for 3D ray tracing. The straight ray surveys were all solved using four different inversion techniques.

The first technique used was direct division, which is given by

$$P = \frac{T}{A^T}, \quad (3.1)$$

where  $\mathbf{P}$  is the matrix of the slowness',  $\mathbf{T}$  is the traveltime matrix, and  $\mathbf{A}$  is the distance matrix (See Appendix B for full description of all methods). The second method used is damped least squares. This method is solved using

$$P = (A^T A + \lambda I)^{-1} A^T T, \quad (3.2)$$

where  $\lambda$  is the damping factor and  $I$  is the identity matrix. Both the direct division and damped least squares were solved in Matlab using the self programmed DLS\_invers code.

The third method used in straight ray tomography was singular value decomposition (SVD). This method involves decomposing the distance matrix into three matrices resulting in the final equation of

$$P = V_p L_p^{-1} U_p^T T, \quad (3.2)$$

where,  $U$  is an  $m \times m$  orthonormal matrix of eigenvectors that span the data space,  $V$  is an  $n \times n$  orthonormal matrix that spans the model space and the singular values of matrix  $A$  are the diagonal components of the  $L$  matrix arranged in descending order.

Finally the last technique used was the conjugate gradient (CG) method. Unlike the previous methods, which were direct methods, the conjugate gradient method is an iterative method. CG uses an initial estimate and constantly minimizes a residual factor given by

$$R_i = B - DX_i, \quad (3.3)$$

where,  $R_i$  is the residual vector,  $X_i$  is the initial estimate,  $B=A^T T$  and  $D=A^T A$ . The SVD and CG method were solved using the tt\_inverse Matlab code developed by Chuandong Xu.

### **3.4.1 Lower 2D Survey**

The lower 2D survey was solved using all four different straight ray methods. A damping factor of  $1 \times 10^{-6}$  was used when solving the DLS and SVD methods. All four

methods provided similar results with the majority of velocities in the range of 200-800 m/s. These velocities are in a similar range as the previous surveys at Maax Na and Chan Chich (Xu and Stewart, 2000; *ibid*, 2001; *ibid*, 2002). Using all four methods, several negative velocities were derived. As these velocities are unphysical, they were set equal to zero for display. As well as the negative values, there also appeared to be several velocities that were unrealistically high. Based on the ultrasonic velocities found on rock samples from the Maax Na pyramid and the average velocities found in the tomographic inversions a high end limit of 3000 m/s was chosen. All velocities greater than this value were set equal to 3000 m/s for display purposes.

The results from the damped least squares method are seen in Figure 3.19. The velocity structure appears fairly homogenous with the exception of the very middle. In this middle section there are several very low velocity regions as well as some high velocity regions. It is a possibility that this may signify a void in the center of the pyramid. Another possible reason for this unstable region is the pyramid might have been built overtop of another collapsed structure resulting in a highly variable velocity in the center.

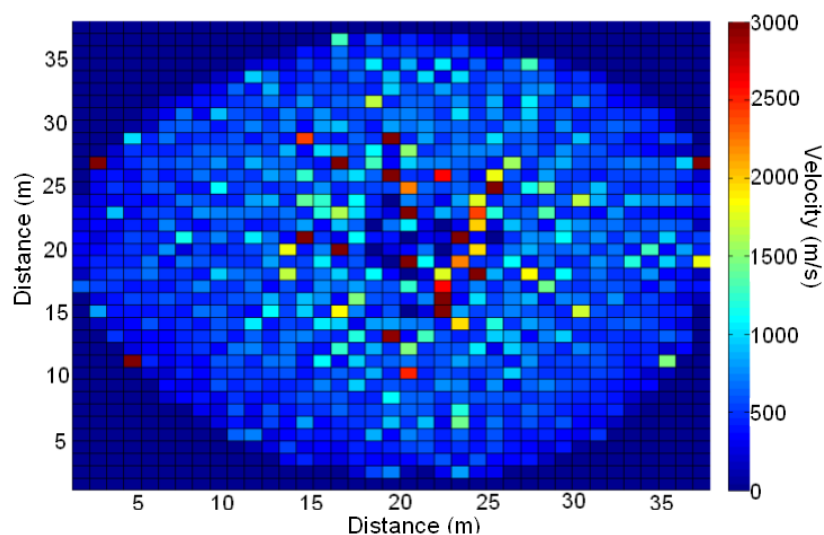


**Figure 3.19: The final velocity (m/s) map of the Maax Na pyramid found using damped least squares. All negative values have been set equal to zero and all velocities greater than 3000m/s are set equal to 3000m/s.**

This velocity structure does show many of the features that we expected to see. A low-velocity layer along the exterior of the pyramid is clearly seen when looking at the slowness graph (Figure 3.20). This was to be expected from the layer of loose soil that coats the exterior of the structure.

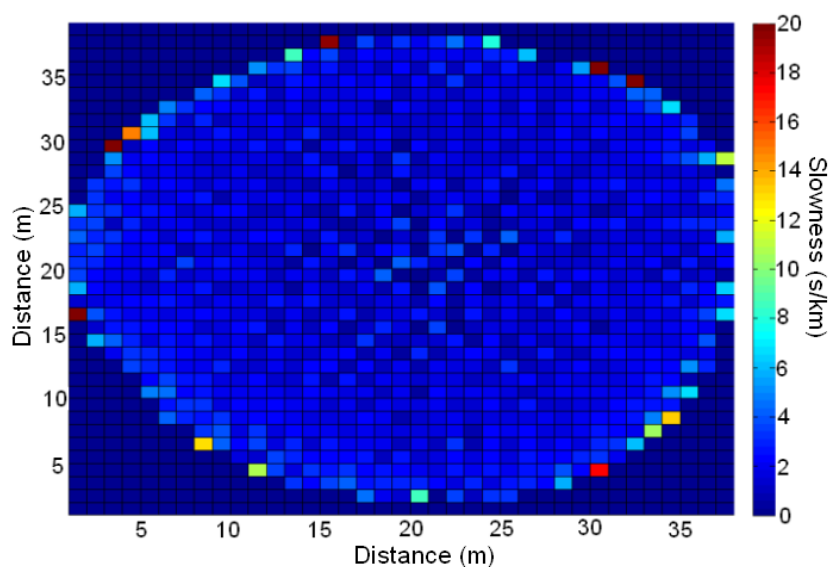


**Figure 3.20: The slowness values of the lower 2D survey found using damped least squares. Slowness values greater than 20 s/km were set equal to 20 s/km for display purposes.**

To help determine the accuracy of the inversion, the velocity model was used to find the estimated first break traveltimes. These traveltimes were compared to those that were measured from the actual data. Figure 3.21 shows the comparison between some measured and calculated traveltimes. It can be seen that the areas with the largest difference are those with the smallest traveltimes. The differences between the observed and calculated traveltimes were graphed in Figure 3.22. Most of the calculated times appear to be within 5 ms of the measured times. However, some differences are as high as 13 ms. The standard deviation and average of the absolute values of the differences were calculated. The damped least squares velocity model resulted in an average difference of 1.594 ms and a standard deviation of the differences of 2.296 ms. When the unphysical values are removed the average and standard deviation rise to 1.833 ms and 2.417 ms respectively. This average is below the expected error of the velocity model resulting in a sense of confidence in the model.

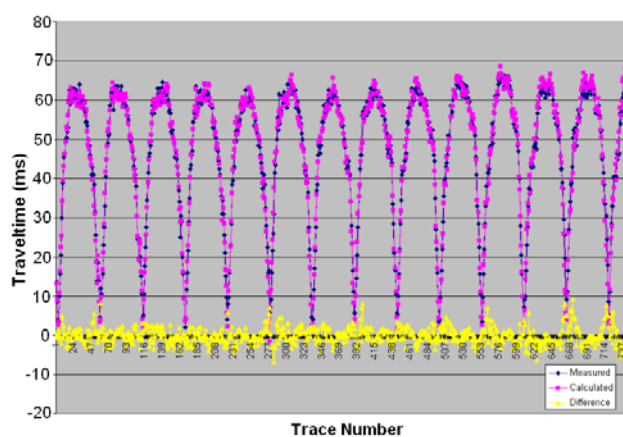


**Figure 3.21: The observed first-break times and calculated times from the lower 2D survey using the damped least squares inversion estimated slowness model.**

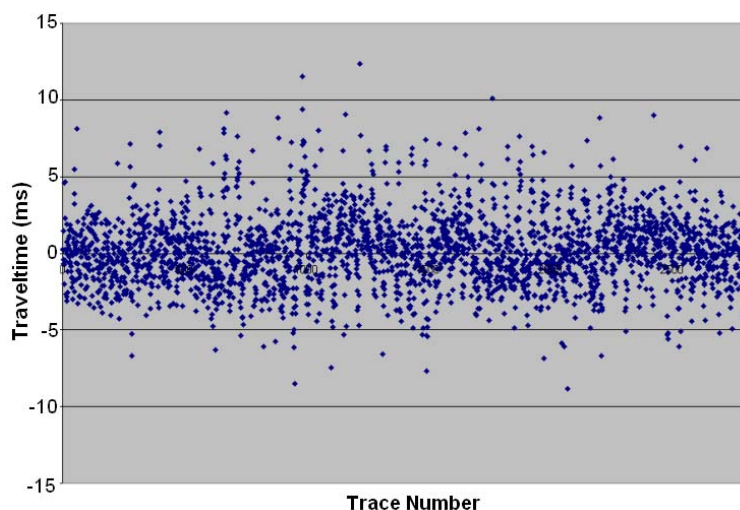


**Figure 3.22: Differences between observed and calculated traveltimes found for the lower 2D survey using damped least squares slowness model.**

### ***3.4.2 Upper 2D Survey***

All four methods were once again used to solve the traveltime inversion. The first inversion was undertaken with the ray paths crossing the trench left in. Once again all four models showed similar results and therefore only the damped least squared results will be shown in this section. The calculated slowness model results in an area of large slowness in the region of the trench (Figure 3.23). Also when looking at the trench area of the slowness model an area of very low slowness can be seen surrounding the higher areas. In many cases this area produced negative values, which were set equal to zero. Due to the fact that it is impossible for the rays to physically pass through the trench region an unreliable region of velocities was found. However, when looking at the velocity model of the non-trench area there appears to be velocities in the 200-500 m/s range, which is consistent with those found in the lower 2D survey. All unphysical velocity values were once again set equal to either zero or 3000 m/s depending on their value. To get a better indication of the velocity field outside of the trench all the rays passing through the trench were excluded.

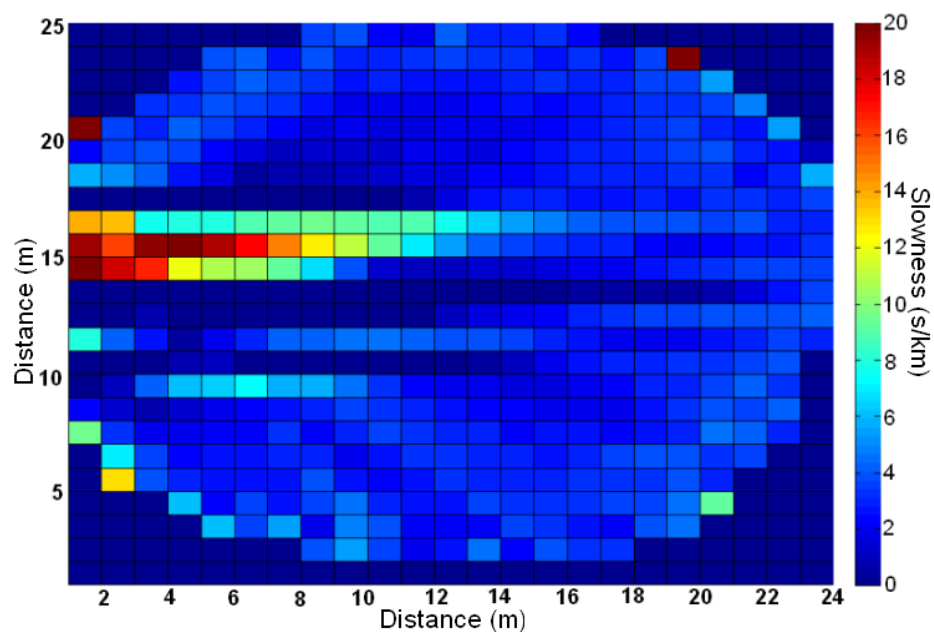


**Figure 3.23:** The slowness model of the upper 2D survey found using damped least squares. All slowness values greater than 20 s/km have been set equal to 20 s/km. All negative values are set equal to 0.

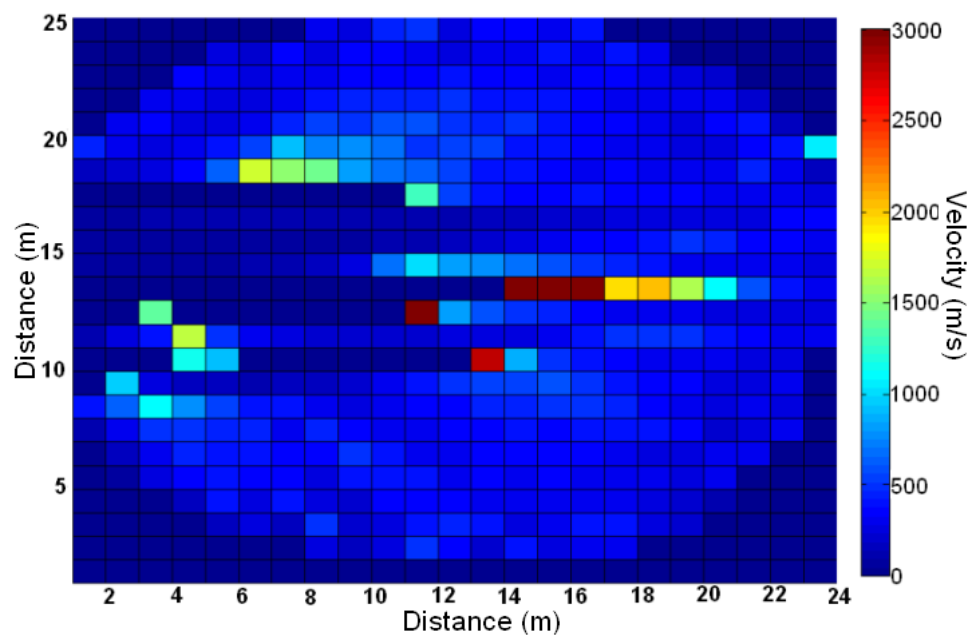


**Figure 3.24:** The velocity model of the upper 2D survey found using damped least squares. All velocity values greater than 3000m/s have been set equal to 3000m/s. All negative values are set equal to 0.

Even when all the rays passing through the trench have been removed there remains some effect of the trench left in the velocity model found. Looking at the

slowness model in Figure 3.25 low slowness residue appears to extend “fingers” out into the remaining velocity model. Also the areas that surround the trench seem to be producing high values. These value could potentially be correct as the regions surrounding the trench have been exposed to erosion and weathering possibly causing the sides to become more unconsolidated allowing for high slowness values. They could also partially be a result of the low fold in the area. Despite the effects from the trench the rest of the interior appears to be mostly homogenous with velocities in the range on 200-500 m/s. While there does not appear to be any additional voids in this section of the pyramid, the trench gives a valuable insight into what effects a void would have on the velocity model found. Using the trench as an example, a look for high slowness regions surrounded by low or negative values and “fingers” extending from the area of interest may help to find areas with voids.

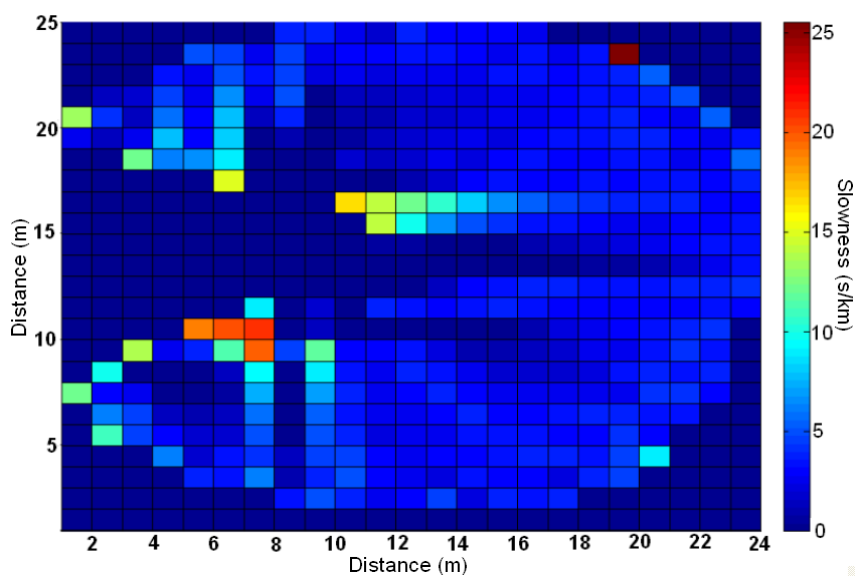


**Figure 3.25: The slowness model of the upper 2D survey found using damped least squares where all rays passing through the trench have been removed. All slowness values greater than 20 s/km have been set equal to 20 s/km. All negative values are set equal to 0.**

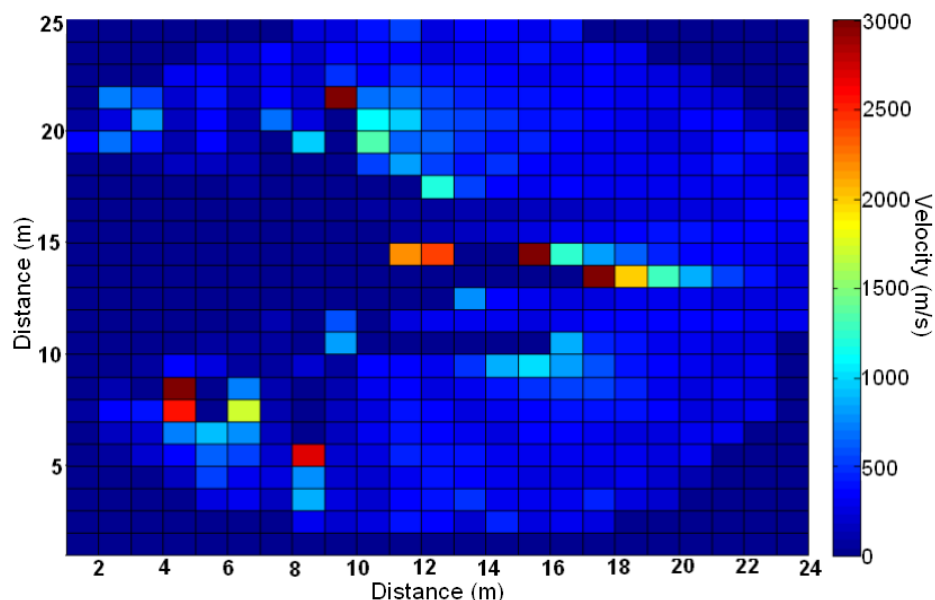


**Figure 3.26: The velocity model of the upper 2D survey found using damped least squares when all rays passing through the trench have been removed. All velocity values greater than 3000m/s have been set equal to 3000m/s. All negative values are set equal to 0.**

Traveltimes were calculated using both the slowness models with the trench removed and left in. The differences between these traveltimes and the observed traveltimes from the actual data were calculated. These differences can be seen in Figure 3.27. Once again the standard deviation and the average of the absolute value of the differences were taken. The standard deviation of the differences for the model with the trench left in is 2.108 ms with an average of 1.625 ms. Once the trench is removed the standard deviation and average become 2.114 ms and 1.603 ms respectively. Removing the trench did cause the average value of the differences to improve but not by a significant amount. A significant improvement can be seen when the unphysical values were constrained in the velocity model. The differences with all rays had an average and standard deviation of 4.201 ms and 7.407 ms while removing the rays passing through the

trench dropped the average and standard deviation to 2.708 ms and 4.866 ms respectively.

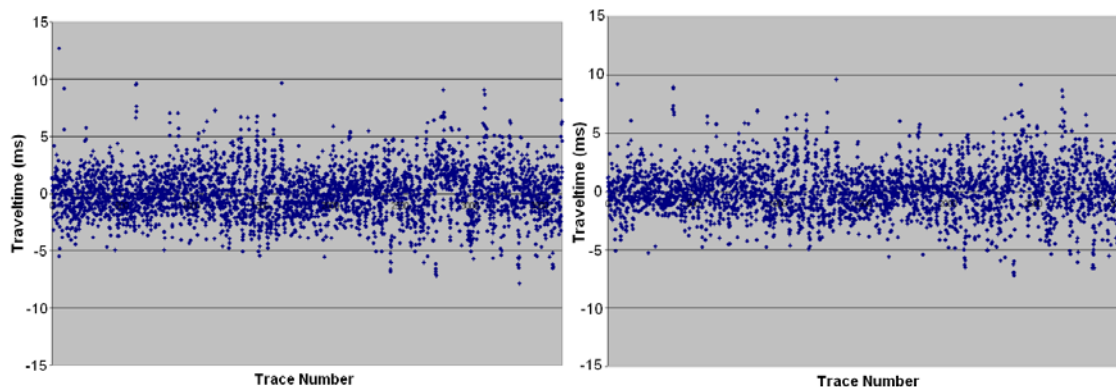


**Figure 3.27: Differences between observed and calculated traveltimes found for the upper 2D survey with all rays included (left) and upper 2D survey with trench removed (right) using damped least squares slowness model.**

### *3.4.3 Lower 3D Survey*

Due to the placement of additional sources on top of those from the lower 2D survey, the inversion was able to solve for a total of ten 2 m high slices as seen in Figure 3.28 (for all slices displayed individually see Appendix C). A high variability in the velocities is seen in the lowest two slices. These are the areas of lowest fold and can therefore not be expected to be as reliable as some of the other sections. Level 3 seems to maintain a homogenous structure with all the velocities being in the 200-800 m/s range that was to be expected. This is the level that contains the receivers and the majority of the sources. This results in a fold that is 3 to 5 times higher than that of other levels and a much more reliable velocity structure. The remaining levels do produce a majority of velocities in the 200-800m/s range, which is consistent with what we know from the 2D surveys. While most of the levels have high velocities that have been scaled down to 3000 m/s these appear mostly at the edges of ray coverage in areas of low fold. Examining the velocity levels, there does not appear to be any evidence of voids in the

velocity structures. Since level 6 is the level where the upper 2D survey was shot we would expect to see some version of the trench appearing. There is not a clear reference area seen for the trench; however, there is a high velocity region in the region of the trench. This may be a result of the location of the source points. Only the western most line of sources up the side of the pyramid would have any ray paths crossing the trench area. This western line runs up the side of the pyramid parallel to the trench. As a result of this layout the straight ray paths pass through only a small portion of the trench resulting in only a small number of pixels being greatly affected by the presence of the trench. To get a better picture of the trench, the upper 3D survey should be solved. One note of interest found from the lower 3D survey is that when the pixel size is increased the anomaly in the center of the lower 2D survey level (Level 2) disappears. This gives support to theory that the pyramid was built upon the loose rubble of some sort of previous construction. While it is still possible that there is a void in the pyramid if the void was of a significant size a low velocity anomaly should remain in the 3D survey.

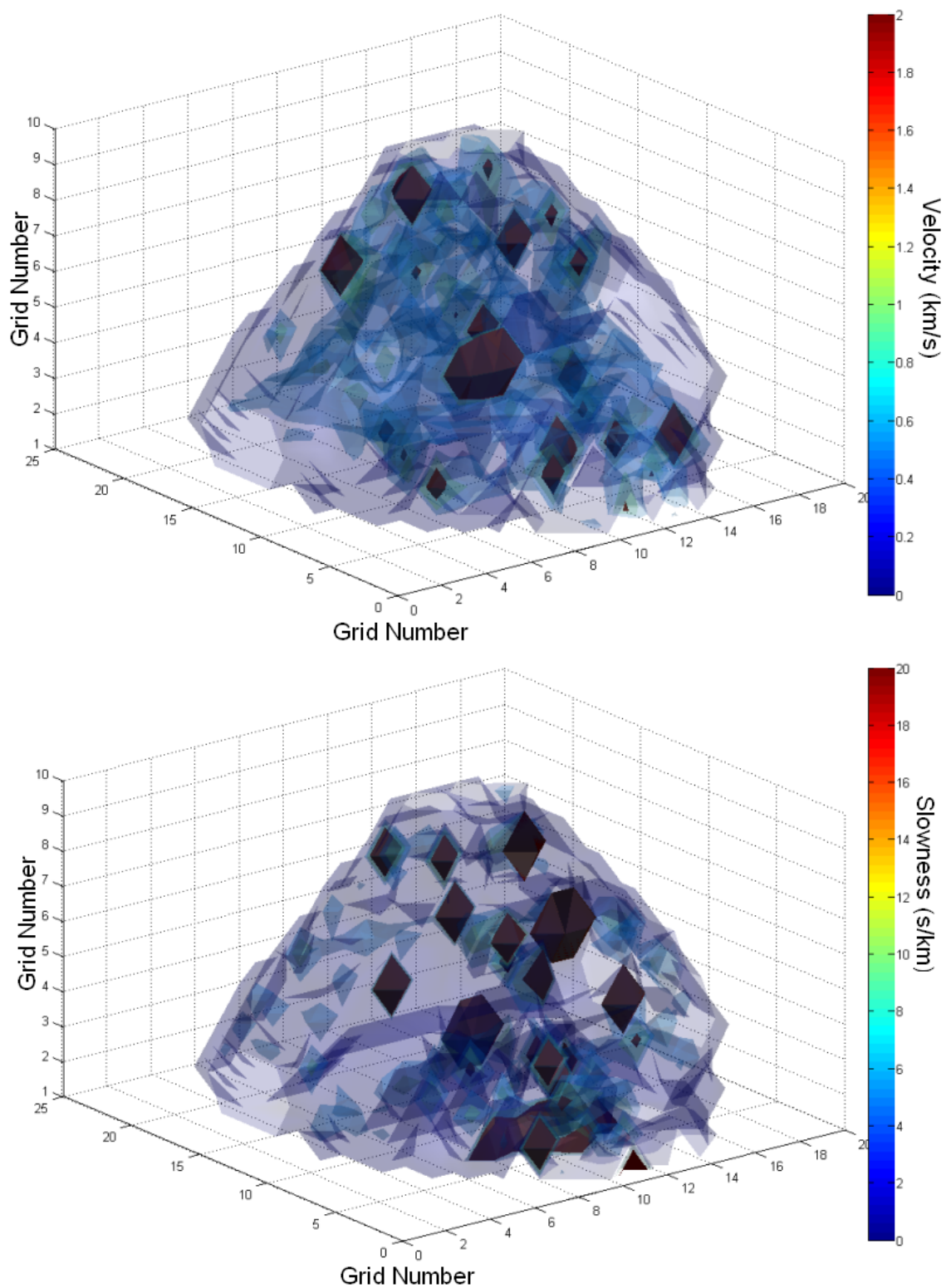


**Figure 3.28:** The derived velocity in km/s (top) and slowness in s/km (bottom) models for the lower 3D survey.

Once again the traveltimes of the first break measured times were compared to those found using the calculated velocity model. Using the differences between the two times an average of 2.038 ms and a standard deviation of 2.772 ms were found. These values are once again inside the expected error of the surveys. However, when comparing the differences seen in Figure 3.29 to those seen in the 2D surveys a larger number of differences greater than 10 ms can be seen. This could be a result of the larger grid size as well as the areas of low fold giving a more unreliable velocity model.

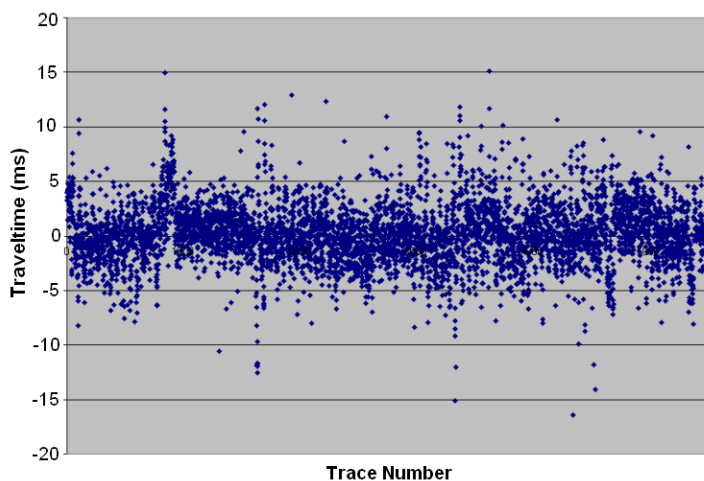


**Figure 3.29: Differences between observed and calculated traveltimes found for the lower 3D survey using damped least squares slowness model.**

#### ***3.4.4 Upper 3D Survey***

The upper 3D survey did not encompass as large an area of the pyramid as the lower 3D survey. Instead of the ten 2 m high vertical levels seen in the lower 2D survey the upper survey encompassed only seven levels as seen in Figure 3.30. Unlike the lower 3D survey, the trench can be distinguished in the upper 3D survey. A very high slowness region can be seen at level 6 which is the characteristic display of the trench as seen in the upper 2D survey. Level 6 is the level that contains the sources and receivers from the

2D upper survey therefore we would expect a similar structure. However, a portion of the trench can be seen in level 5 as both of these levels show high velocity regions beside a lower velocity region. Like the other surveys there are several negative and unphysical large velocities found in the models. These values are generally found in the areas of low fold and for display purposes have been set equal to zero or 3000m/s for negative and high velocities respectively. Despite these unphysical values the majority of velocities do tend to fall in the range given by the other surveys of 200-800 m/s. No clear velocity voids (except the trench) are found in the inside of the pyramid. However, with the lack of coverage and large pixel size it is possible that some voids may have been inadequately sampled (like the trench in the lower 3D survey) and therefore are unable to be distinguished. To better cover the whole pyramid the upper and lower 3D surveys can be combined.

The approximate accuracy of the survey was again examined using the differences between measured and calculated traveltimes. It is seen in Figure 3.31 that approximately the first 2000 traveltimes have a much smaller average difference than the remaining times. These traveltimes correlate to the sources that go up the sides of the pyramids. These sources should have very little interaction with the trench and therefore their raypaths go through more a more stable velocity model and result in lower differences in the traveltimes. The remaining traveltimes are associated with those from the upper 2D survey and a few of the sources from the sloped line closest to the trench. These sources all send rays directly through the location of the less accurate trench velocity and therefore result with a greater difference in traveltimes. A higher traveltime difference than that found in the upper 2D survey can also be explained by the increased

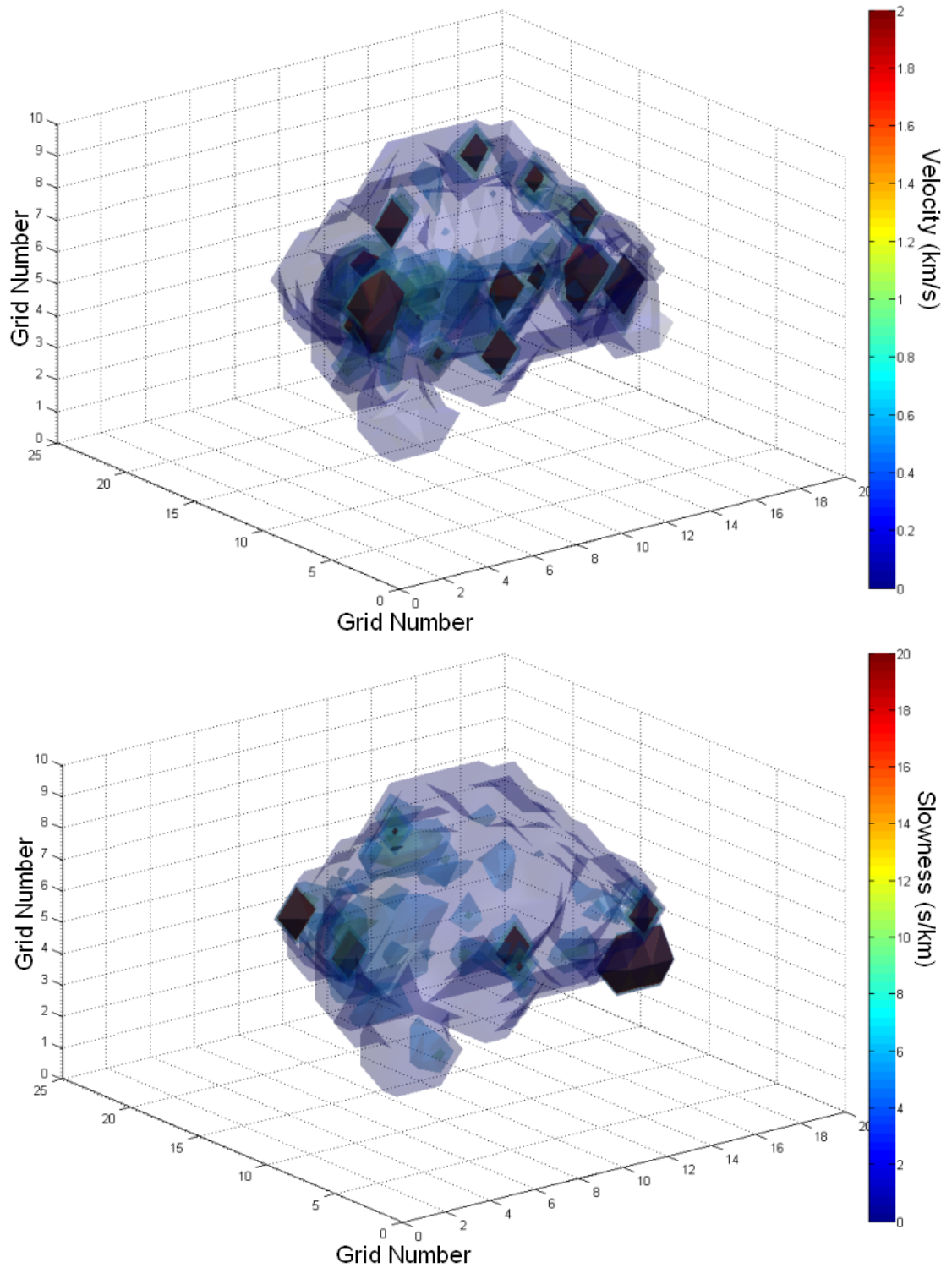


**Figure 3.30: The derived velocity in km/s (top) and slowness in s/km (bottom) models for the upper 3D survey.**

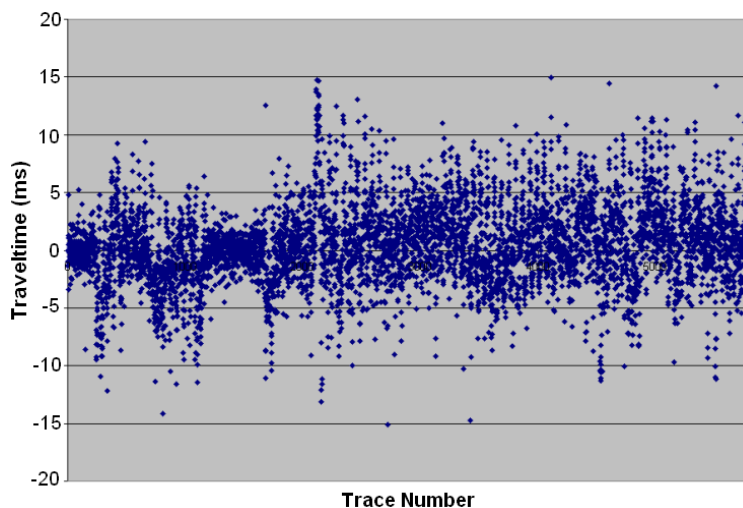


**Figure 3.31: The difference between the observed and calculated traveltimes found for the upper 3D survey using DLS.**

size of the pixels resulting in a velocity model that is less variable. The average and standard deviation for the upper 3D survey is given as 2.651 ms and 3.528 ms respectively. Despite the increase in the difference the average is still inside the estimated traveltime pick error of 5.16 ms.

### ***3.4.5 Combined 3D survey***

Unlike all the other surveys that were solved using four different methods (DD, DLS, SVD, and CG), the combined 3D survey was solved using only the conjugate gradient method. Conjugate gradient was chosen due to the reduced processing power and time needed for conjugate gradient over the other three methods. A total of 250 iterations were used in the inversion. Since all four methods previously gave similar results, we assume that they would for this larger problem.

When examining level one and two in Figure 3.32, it is seen that there remain several high velocity values and the velocity structure contains large velocity shifts. This is expected as the upper 3D section has little effect on these levels therefore a result

similar to that of the lower 3D survey is expected. The same effect can be seen when looking at the uppermost levels. In the remaining levels where the upper and lower surveys have both made significant contributions a fairly uniform structure can be seen in the center region of the pyramid with velocities in the expected range. There still remain several high velocity values along the edges of the calculated structure. These can be attributed to the low fold in these areas. One interesting feature of the combined 3D survey is that the trench does not clearly appear. There are several possible reasons as to why the trench does not clearly appear in the model. Since we are using straight rays that do not correspond to the actual ray path it is possible that the trench is being masked by the velocity errors. Another factor that would affect the visibility of the trench is the pixel size. Since the pixel size that is being used is quite large it is possible that the pixel encompasses an area that has both high velocity regions as well as the low velocity of the trench. When the values are averaged out it would cause a masking effect over the trench area.

Once again a new set of traveltimes were derived based on the modeled velocity structure. These times were compared to those found from first break picking. The differences between the two traveltimes can be seen in Figure 3.33. Similar to the other surveys the majority of differences appear to have a difference under 5 ms. The average of the absolute value of the differences and the standard deviation were taken to get a measurement of the accuracy of the survey. The average and standard deviation were found to be 3.051 ms and 3.981 ms respectively.

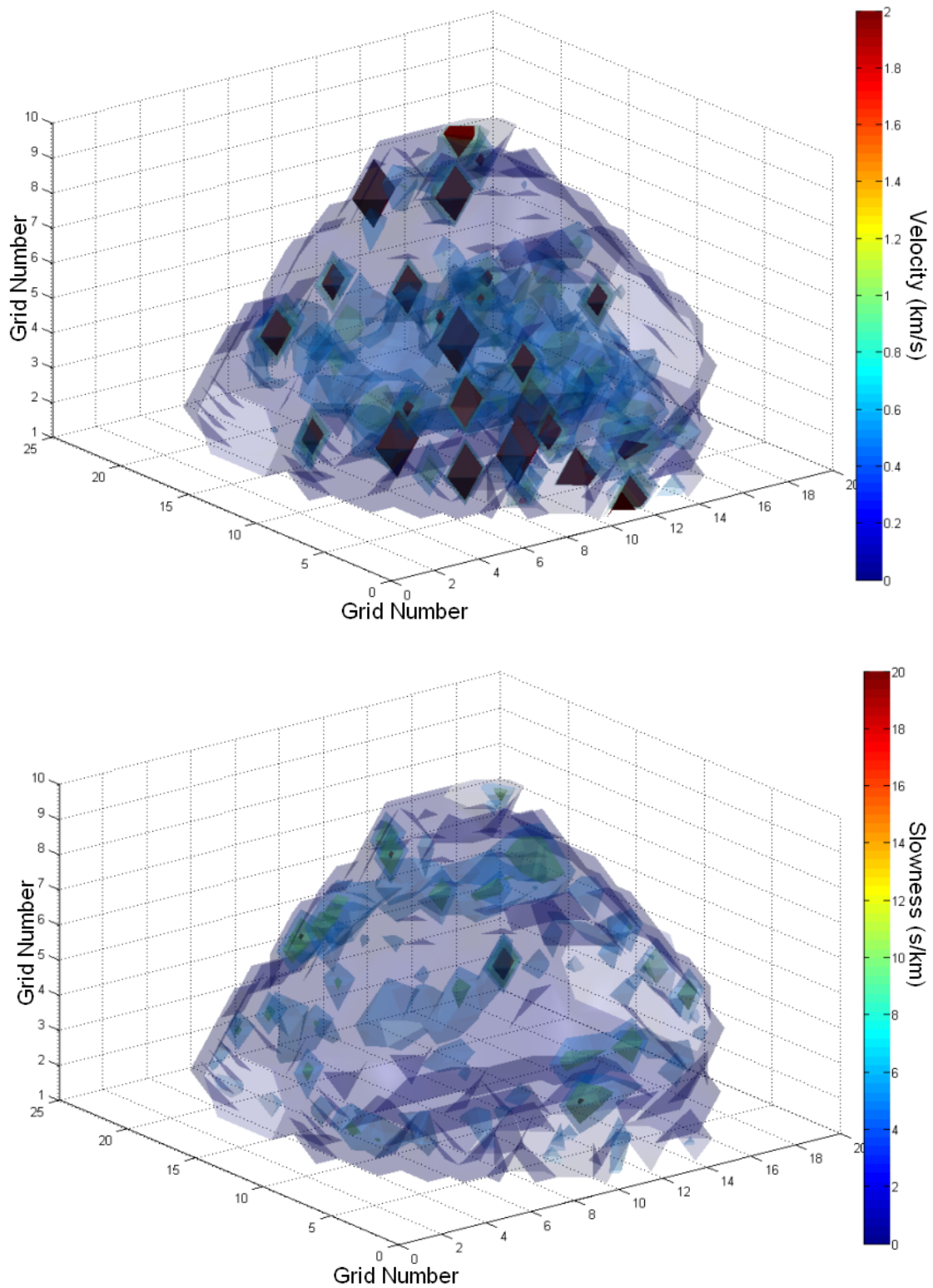


**Figure 3.32: The derived velocity in km/s (top) and slowness in s/km (bottom) models for the combined 3D survey.**

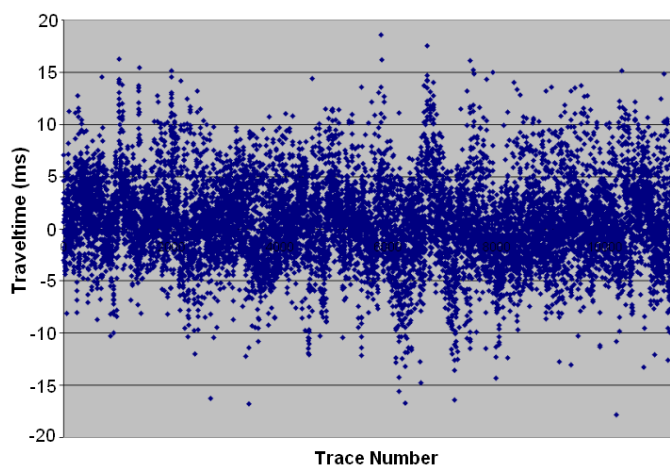


**Figure 3.33: The difference between the observed and calculated traveltimes found for the combined 3D survey using CG with 250 iterations.**

### **3.5 Straight Ray Amplitude Tomography Results**

There is additional information in the recorded seismic data. The amplitude of the first arrival contains further details of the pyramids interior. To get a better picture of the interior structure of the pyramid we use amplitude inversion (see Appendix B.5) in addition to the traveltime inversion. Using amplitude inversion, an attenuation model is created that can be compared to the derived velocity model. While we would expect the results to be similar it is possible that one method will better be able to image certain features.

To find the attenuation model the values for the initial amplitude must be found. Since an exact description of the shot is not available the initial amplitude of the shot was taken to be equivalent to the largest amplitude picked from each shot gather. This amplitude picked is associated with the amplitude picked from the nearest receiver location. This is the method that was used for all the shots associated with the 2D surveys since the largest distance away from a receiver was only 1 m in these surveys. The 3D surveys were unable to use this method. Instead the largest amplitude recorded for the

entire sloped line of shots was used for the 3D surveys. These amplitudes corresponded to closest shot to the ring of receivers for each line of shots. This method is not perfect and does introduce an element of error into the calculations. Since most of the shots tend to have a similar profile the error should be minimized and an adequate model of the interior structure should be found.

### ***3.5.1 Lower 2D Survey***

Similar to the traveltimes inversion surveys a grid size of 1 m by 1 m was used to find the attenuation model. The attenuation model was solved using all four methods with the damped least squares method being displayed here. As with the velocity models there were several negative values in the calculated models. For display purposes, these have all be set equal to zero. In addition, to better determine the interior structure, all attenuations greater than 2.5 Np/m were set equal to 2.5 Np/m for display purposes. Figure 3.34 shows the attenuation model of the lower 2D survey. This model shows much of the expected characteristics with a large attenuation along the soil-covered edges of the pyramid with a smaller fairly homogenous attenuation in the centre. One interesting feature found in the model is an area of high attenuation surrounded by low attenuation in the center of the pyramid. This is in the same position as the high slowness region in the traveltimes inversion results (Figure 3.20). This helps confirm the possibility that there might be a void in the center of the pyramid or that the pyramid was built upon a previous crumbled structure.

A determination of a measure of the accuracy of the attenuation model was found by comparing the measured calculated values of  $\ln(A_0/A)$ . The majority of the differences are within a value of 1 Np; however, there are differences as high as 3.8 Np.

An average of the absolute value of the differences was found to be 0.628 Np with a standard deviation of 0.477 Np. The differences found using the attenuation model (Figure 3.35) shows a similar trend to those found in Figure 3.22 using the velocity model giving confidence in the precision of the model.

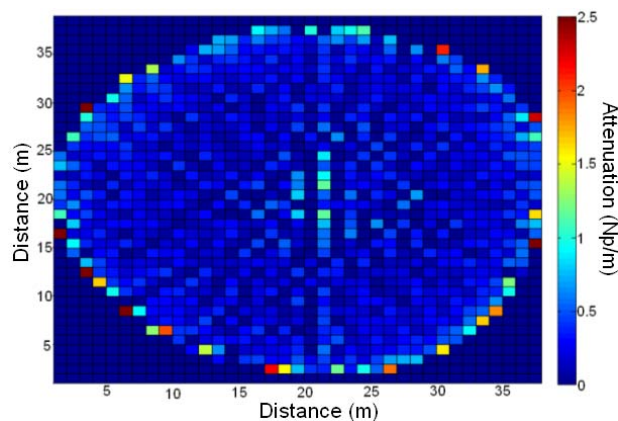


**Figure 3.34: The attenuation model of the lower 2D survey found using the DLS method.**

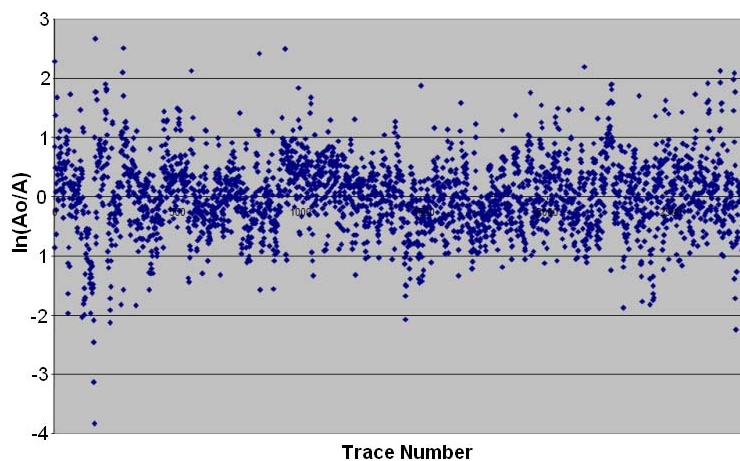


**Figure 3.35: The differences between the measure and calculated values of  $\ln(A_o/A)$  for the lower 2D survey using DLS.**

### 3.5.2 Upper 2D Survey

The upper 2D survey was again solved first using all available rays and then with all rays passing through the trench removed. The attenuation map found using all available rays is seen in Figure 3.36. All attenuation values have been bound to the range

of 0 to 5 Np/m with all values less than zero being set equal to zero and all values greater than 5 Np/m set equal to 5 Np/m for display purposes. Similar to the velocity model found through traveltimes inversion the attenuation model displays the trench as a combination of low attenuation values surrounded by high attenuation values. High attenuation artefacts from the trench can be seen stretching out from the trench location. To get a better idea of the attenuation away from the trench the rays passing through the location of the trench were disregarded.

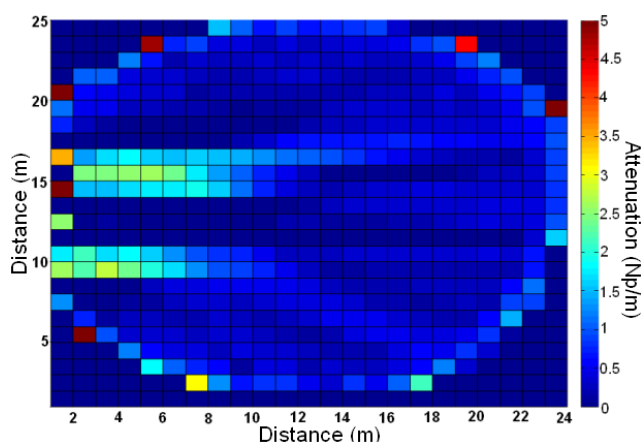


**Figure 3.36: The attenuation model of the upper 2D model found using all rays with the DLS method.**

The attenuation model of the upper 2D survey with the trench excluded shows a large number of high attenuation values located near the location of the deleted trench. These values could indicate the areas that have been disturbed surrounding the trench. Since the sides of the trench have been exposed to weathering and the build up of soil a high attenuation area is expected. There are a few low attenuation artefact fingers stretching out from the location of the trench; however, the majority of the interior appears to be homogenous. These artefacts may be the result of out of plane rays. The rays that near the trench location may, in reality, be dipping under the pyramid rather than bending around the trench. As this survey is assuming a 2D plane those rays would

not be taken into account and therefore cause errors. This survey does not take into account rays that may have been reflected or scattered. If these rays make up the first arrivals they would result in attenuation errors. Despite these potential errors, there is a good indication of the higher attenuation soil layer surrounding the pyramid.

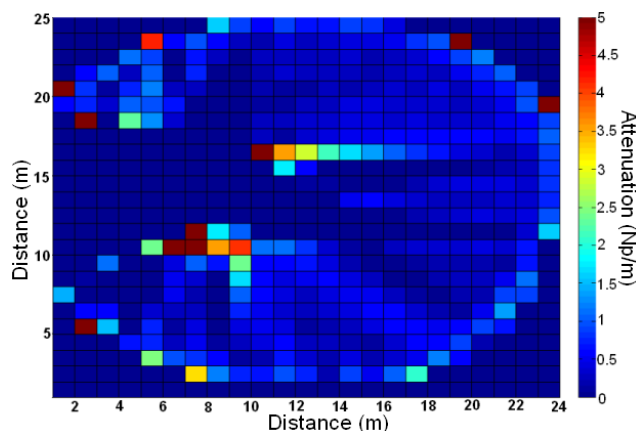


**Figure 3.37: The attenuation model of the upper 2D model with all rays passing through the trench disregarded.**

The difference between the observed and calculated amplitude ratios for the upper 2D survey with the trench included and trench removed are shown in Figure 2.38. The majority of the differences are within one with a maximum range of near three for both trench and no trench. The average of the absolute value of the differences and the standard deviations were found to be 0.474 Np and 0.617 Np for the trench included model and 0.480 Np and 0.627 Np for the trench removed model. Despite the rays through the trench being removed, the average difference for the trench removed model is greater than the trench included model. This is a result of the amplitude ratio values  $[\ln(A_o/A)]$  for the rays passing through the trench being close to the actual values observed. However, since the model included negative values and unrealistically high values it can be determined that the no trench model may be more accurate. When the

unphysical values are constrained the model with the trench removed shows a dramatic improvement in both average and standard deviation.

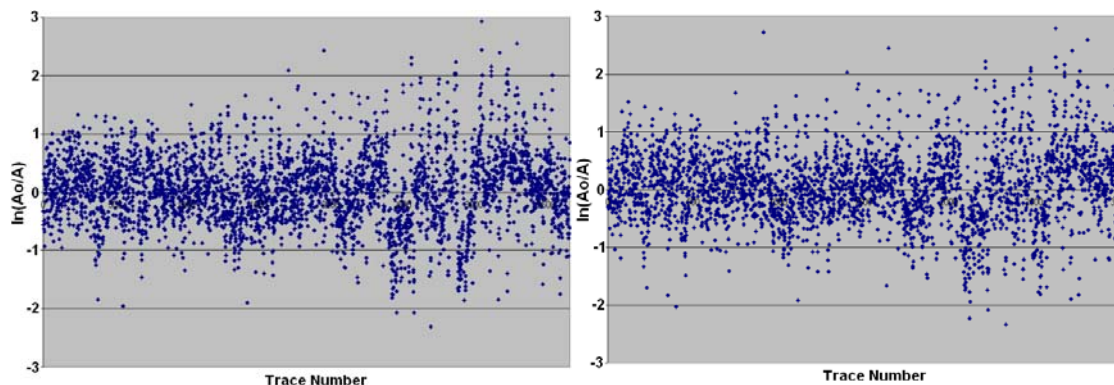


**Figure 3.38: The difference between the observed and calculated values of  $\ln(A_o/A)$  for the upper 2D survey with trench included (left) and removed (right).**

### 3.5.3 Lower 3D Survey

The lower 3D survey once again had the pixel size raised to be a 2 m x 2 m x 2 m pixel. The attenuation model for the lower 3D survey was found for ten different 2 m high levels. The derived model for these levels is shown in Figure 3.39 (for each slice separately see Appendix C). The attenuation model shows many of the features that have been seen in the previous surveys attenuation and velocity models. A large attenuation region along the perimeter of the pyramid is seen in levels three, four and five. In level six there is a high attenuation in the region of the trench. Unlike the velocity model found through travelttime inversion the trench provides a visible effect. It is also seen that the anomaly in the center of the lower 2D survey has once again disappeared in the model when the pixel size is increased to 2 m x 2 m.

The differences in the amplitude ratios were once again compared to give a measure of the accuracy of the attenuation model. The differences were then plotted and can be seen in Figure 3.40. The majority of differences once again appear to be within a

ratio of 1 Np. There do appear to be a few source points between trace 2000 and 3000 that give much larger differences. This may be a result of a bad initial amplitude pick for these sources. Since the initial amplitudes for the sloped line shots were estimated based on the source in the line closest to the receivers there may be some sources where the ratio is significantly different. Despite these difficulties the average of the absolute value of the differences and standard deviation remain similar to those found in the 2D surveys. The lower 3D model gives an average of 0.482 Np and a standard deviation of 0.668 Np.

#### ***3.5.4 Upper 3D Survey***

Solving the amplitude inversion of the upper 3D survey using a 2 m x 2 m x 2 m pixel size results in an attenuation model with seven different vertical levels. Once again the attenuation model shows a similarity with the velocity models found from the traveltimes inversion. Like the velocity model it is possible to distinguish the location of the trench in levels three, four and five. The high attenuation soil layer can be partially seen in levels four and five. Also the majority of the attenuations fall into the range consistent with all the other surveys. Levels three and four appear to have a large number of high attenuation values. These two levels have very little fold associated with them so that the attenuation associated with these levels is not as reliable as those in other levels.

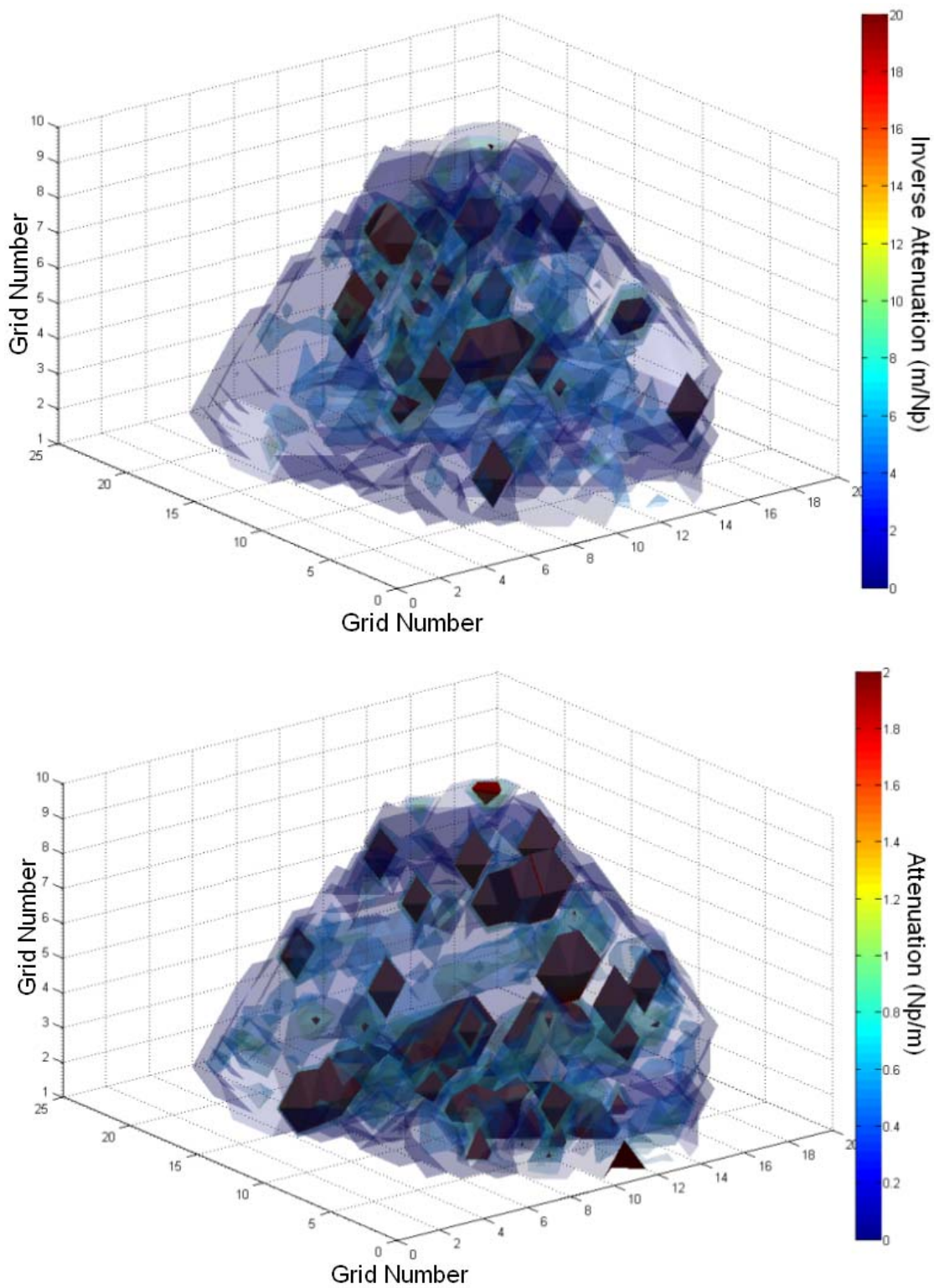


**Figure 3.39:** The derived inverse attenuation (top) and attenuation (bottom) models for the lower 3D survey.

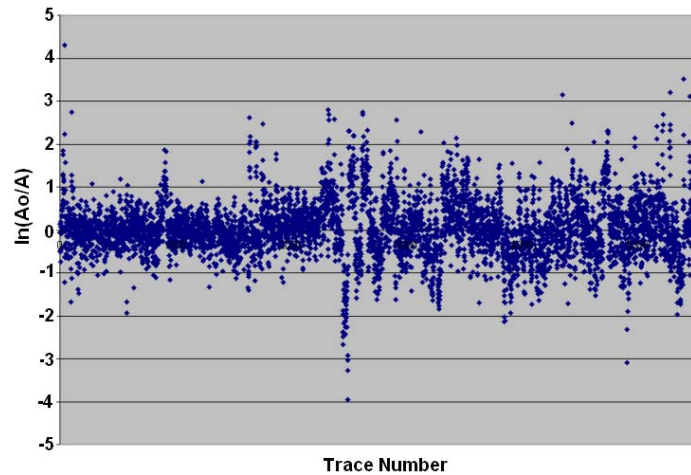


**Figure 3.40: The differences between the observed and calculated amplitude ratios of the lower 3D survey.**

The differences in the observed and calculated amplitude ratios were plotted in Figure 3.42. Like the lower 3D model, several shots appear to give larger differences. These might once again be associated with erroneous initial amplitudes affecting the amplitude ratios. Another interesting feature we see are that the slope shots (left side of Figure 3.42) produced more accurate amplitude ratios than those associated with the 2D survey. This may be a result of the trench. The ray paths from the 2D survey are more likely to be affected by the trench than those of the sloped shots. The average and standard deviation of the differences are similar to previous surveys with values of  $0.511 N_p$  and  $0.527 N_p$  respectively.

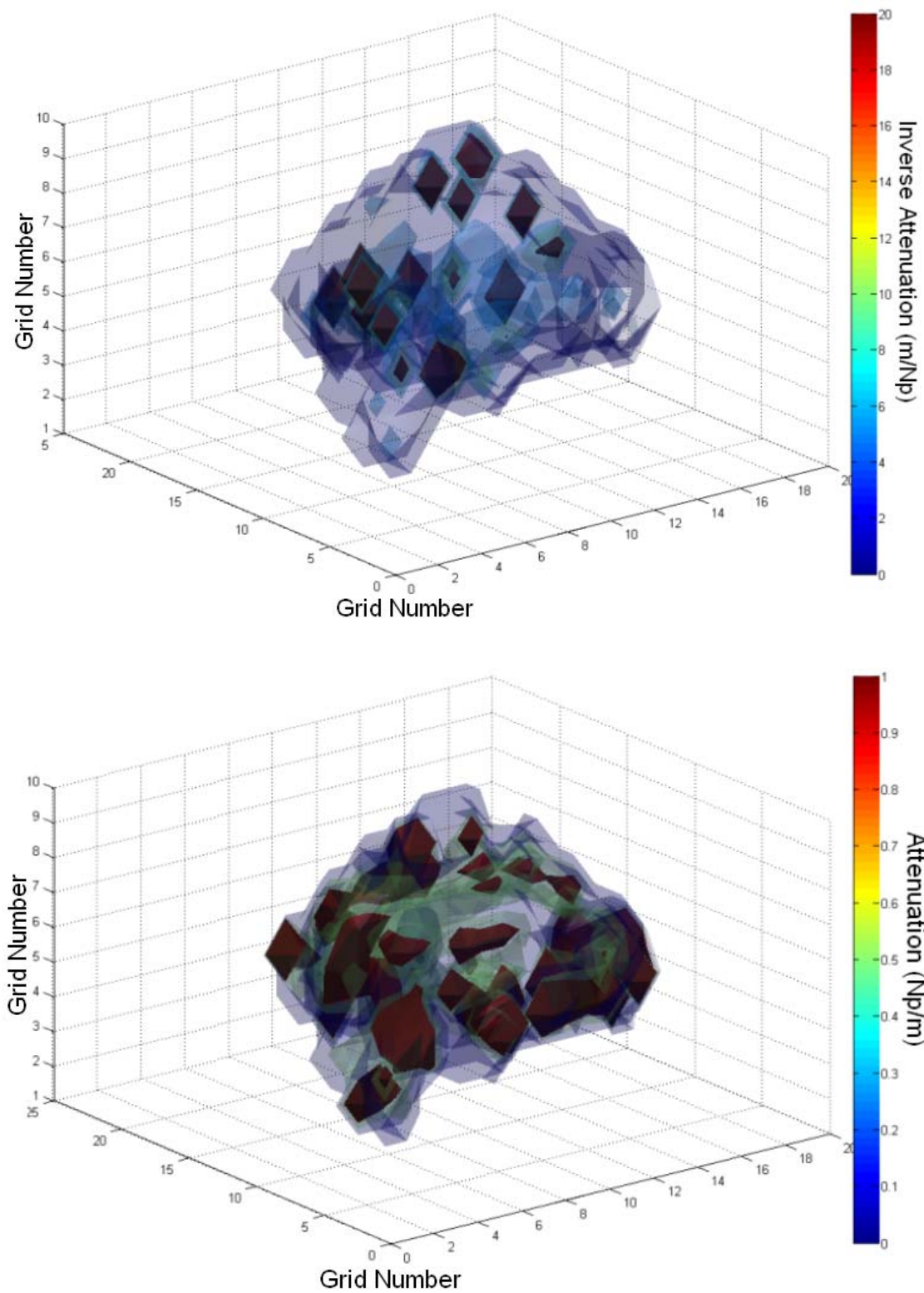


**Figure 3.41: The derived inverse attenuation (top) and attenuation (bottom) models for the upper 3D survey.**

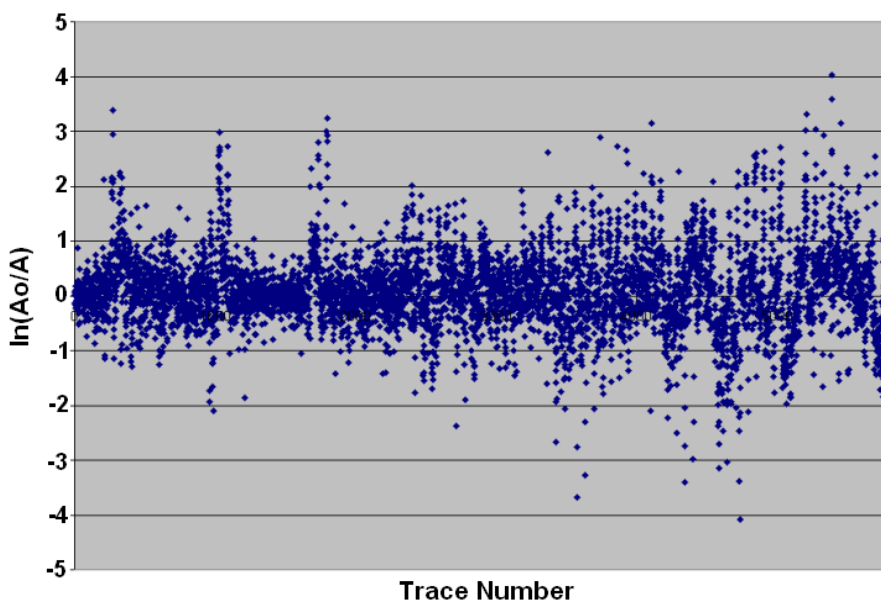


**Figure 3.42: The differences between observed and calculated amplitude ratios found for the upper 3D survey.**

### ***3.5.5 Combined 3D Survey***

The attenuation model found for the combined 3D survey shows a more stable model than those of the upper and lower models separately. While negative attenuation values are still in the model there are fewer unrealistic high attenuation values. Similar to the velocity model the attenuation model does not show a clear indication of the location of the trench. There is a small area of higher attenuation in the location of the trench but it is not as clearly defined as the upper 3D survey. To get a better image of the trench a smaller pixel size and greater coverage of the pyramid would be recommended. This is possibly troubling because if the attenuation model does not show the trench it is possible that another void may be masked in the model. Using the combined 3D model there does not appear to be any regions of archaeological interest in the interior of the pyramid.

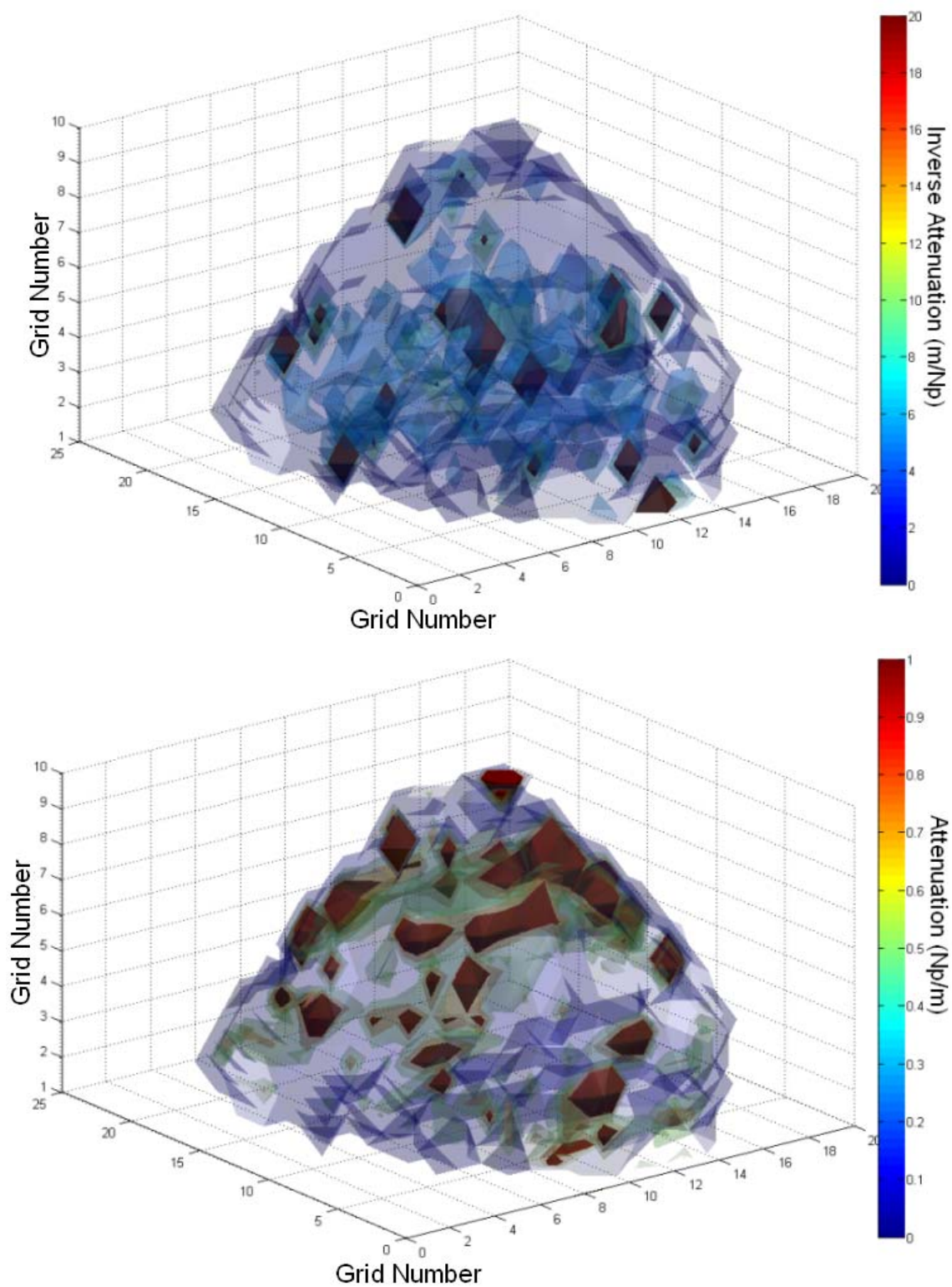


**Figure 3.43: The derived inverse attenuation (top) and attenuation (bottom) models for the combined 3D survey.**

The differences between the observed and calculated amplitude ratios were examined and plotted in Figure 3.44. As with the other amplitude surveys the majority of differences are within a range of 1 with the average difference being 0.606 Np. The standard deviation of the differences was calculated to be a value of 0.798 Np. These values a little bit higher than either the lower or upper 3D surveys. This is to be expected as with increased number of ray paths and the large pixel size there is a greater chance of rays experiencing a larger difference in attenuation ratio.

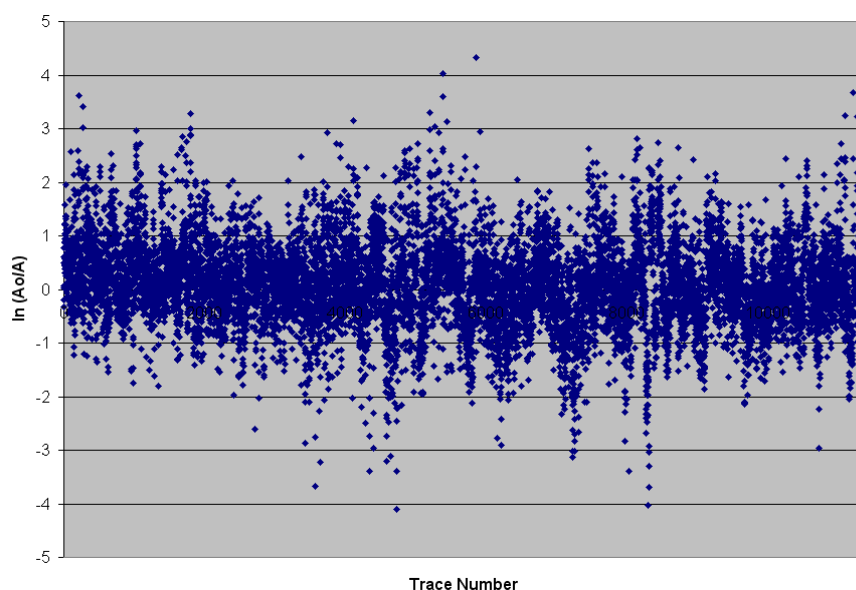


**Figure 3.44: The differences between observed and calculated amplitude ratios found for the upper 3D survey.**

### 3.6 Curved Ray Traveltime Tomography

To improve on the results of the straight ray inversions a curved ray tracer was implemented. The curved ray tracer improves on the straight ray results by allowing for a more realistic ray path through the medium. The curved ray tracer chosen for these surveys was a program named 2Dray\_tomo created by Zhou et al. (1992a). This curved ray tracer was chosen as there were no constraints on the source and receiver layout. It

was also shown by Zhou et al. (1992b) that the 2Dray\_tomo program is capable of identifying low and high velocity anomalies. Both the upper and lower 2D survey were solved using the curved ray tracer. While Zhou (1992a) also created a 3D curved ray tracer using the same method, the 3D surveys were not solved due to a lack of processing power and time.

To perform the ray tracing certain constraints had to be implemented into the program. The first value that was implemented was  $1 \times 10^{-6}$  for the damping factor. Since the ray tracer is based on tracing rays from nodes on the pixels 25 nodes, which is the maximum amount of nodes allowed, was chosen for the inversion. Zhou et al. (1992a) showed that constraining velocities into expected ranges increase the accuracy of the velocity model. To determine the best velocity range, multiple ranges were tried. To determine which velocity range gives the best model the root mean square of the change in traveltimes was examined.

The root mean squared (RMS) of the change in traveltimes is expressed as

$$RMS(\partial t) = \sqrt{\frac{\sum_j^M (t_{obs_j} - t_{syn_j})^2}{M}}, \quad (3.1)$$

where  $M$  is the number of rays,  $i$  is the model position,  $t_{obs}$  is the observed traveltimes and  $t_{syn}$  is the calculated traveltimes for the current model. This allows an indication of the accuracy of the models as it computes RMS of the residuals between the observed traveltimes and the calculated traveltimes.

### 3.6.1 Lower 2D Survey

Based on the velocity results found from the straight ray tomography a starting constant velocity model of 500 m/s was chosen to solve the inversion. Before running the curved ray trace program multiple velocity ranges were chosen. Since we are looking for empty voids where the waves will not cross a 1 m/s was used for all ranges as a minimum. Four upper velocity constraints were attempted including velocities of 2, 3, 4 and 5 km/s. The RMS values of the traveltimes residuals are shown in Figure 3.45.

Examining the  $RMS(\delta t)$  values in Figure 3.45, the smallest values are found when using a velocity range with a maximum of either 5 km/s or 2 km/s. The lowest value in the graph is located at iteration 90 of the max 2 km/s range. This low value is very close to that seen in iteration 43 of the 5 km/s range with a difference of only 0.0063 m/s. To determine which final model to use a closer look at other features must be considered.

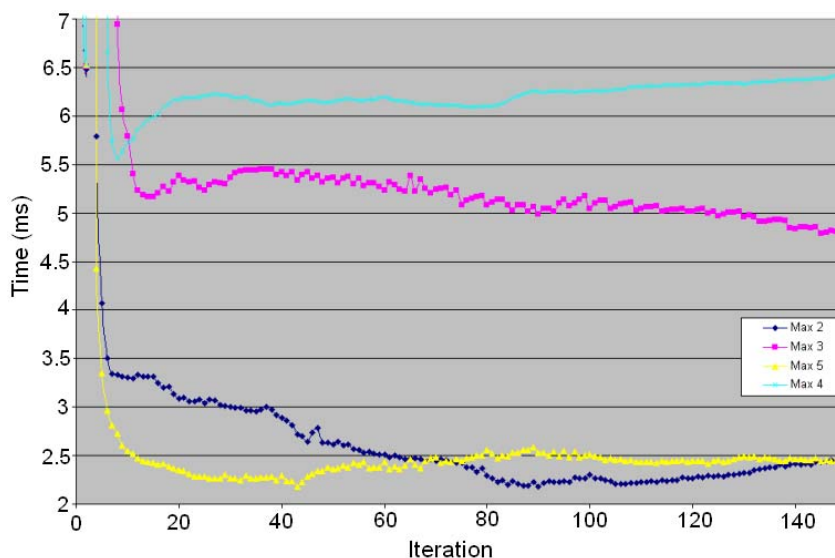


**Figure 3.45: The  $RMS(\delta t)$  values versus iterations for different velocity ranges on the lower 2D survey.**

Since the  $RMS(\delta t)$  provided insignificant evidence to which velocity range is the most accurate an examination of the standard deviation and average of the absolute value

of the differences from the observed and measured traveltimes was undertaken for both the 2 km/s and 5 km/s range (Figure 3.46). Once again both ranges produced very similar minimal values with the minimum being located at iteration 43 for the 5 km/s range and 90 for the 2 km/s range. It is the 5 km/s model that produces the smallest average value. However, the 2 km/s model has a lower standard deviation. Since the maximum 2 km/s model produced better looking results in two of the three statistics and agrees more closely to velocities found using rock samples from the pyramid it is determined that this model is likely more accurate. Due to the similar values both the 2 km/s and 5 km/s velocity models will be examined. The derived velocity model for the 2 km/s range can be seen in Figure 3.47. Since the rays are free to curve and bend several pixels contained no ray paths and therefore cannot be determined. These pixels are indicated with black. While it is not possible to get a completely accurate velocity of those pixels with no ray coverage it can be assumed that they are in the lower range as high velocity regions tend to attract rays whereas low velocity regions are typically skipped. The final ray paths found using the 2Dray\_tomo program are seen in Figure 3.48.

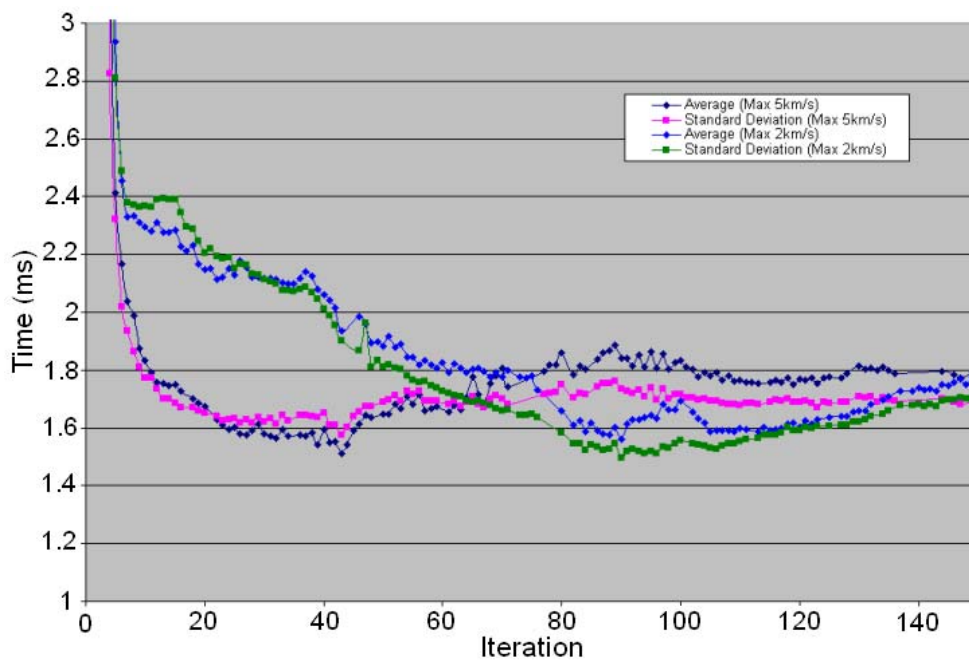


**Figure 3.46:** The standard deviation and average of the differences between observed first break traveltimes and calculated traveltimes.

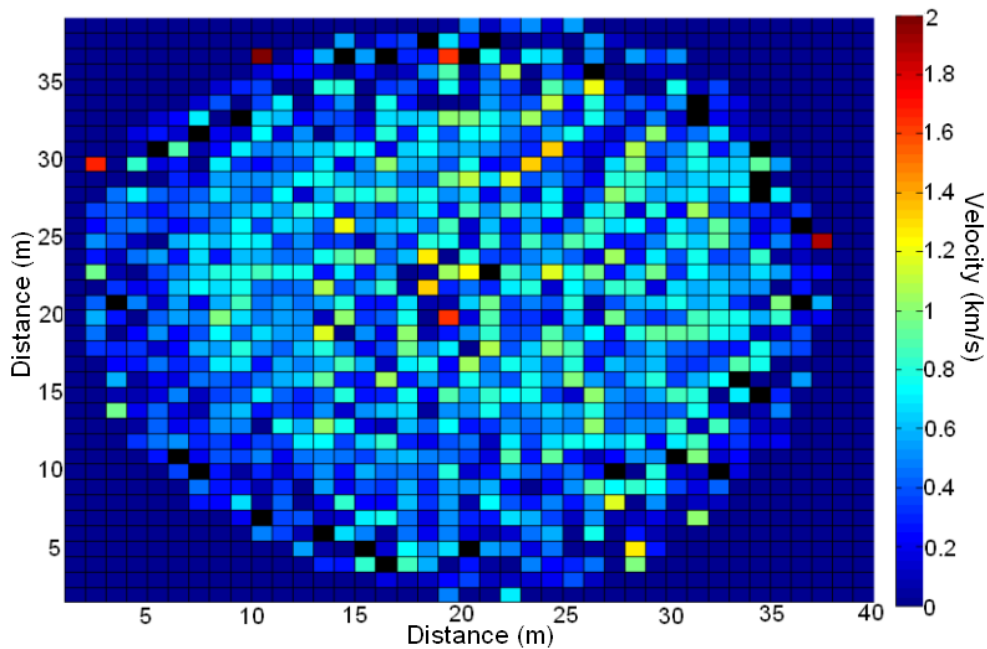


**Figure 3.47:** The derived velocity model (km/s) of the lower 2D survey found using a velocity range of 0.001 to 2.0 km/s. Skipped pixels designated in black.

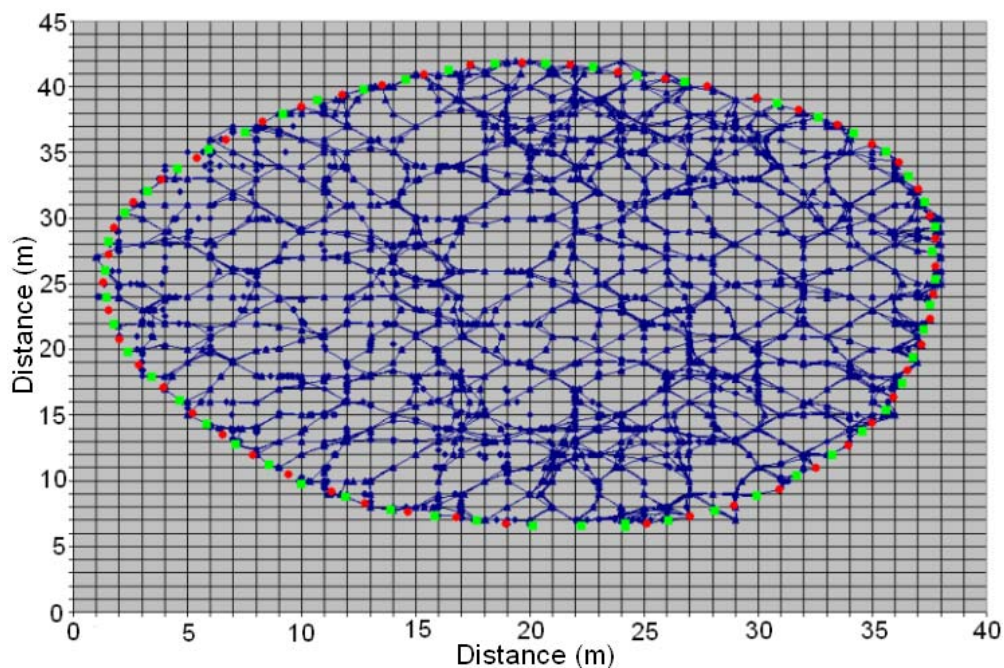


**Figure 3.48: The final raypaths from the first 35 sources in the lower 2D survey with velocity range of 0.001 to 2km/s. Sources and receivers displayed in red and green respectively.**

The velocity model found looks similar to that of the straight ray inversion. The low velocity soil layer is still visible along the exterior of the model. There also remains an indication of an anomaly in the center of the model. There are regions of higher velocity near other regions of very low velocity. This may again be showing that this pyramid was built on top of a previous structure or an area of loose rubble. The majority of velocity values appear to be within 200 to 1000 m/s with the lower velocities on the edge and a slowly increasing velocity towards the center. This is a slightly higher trend than that of the straight ray inversion.

Since the 2 km/s and 5 km/s model appeared to be similar in terms of accuracy, it was decided that the 5 km/s model should also be derived (Figure 3.49). The velocities appear to fall in the same range as those found in the 2 km/s range. There is also an indication of some velocity feature in the center. To better compare the 2 km/s and 5

km/s models, the 5 km/s model was filtered so that all velocities greater than 2 km/s were set equal to 2 km/s. The two models were plotted side by side to make an accurate comparison as seen in Figure 3.50. Both models appear to be very similar with only minor differences. This is encouraging that despite the different velocity constraints the model is approaching a similar structure.

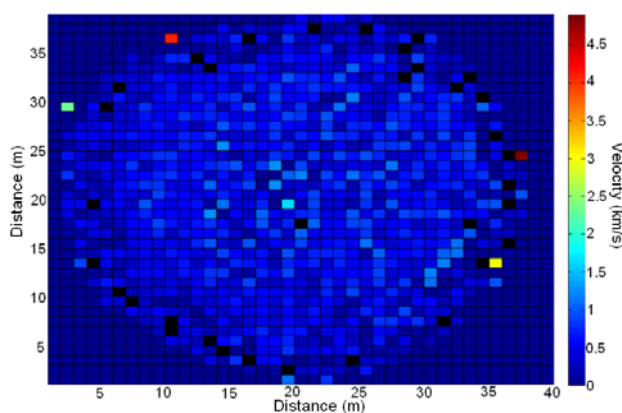


**Figure 3.49.** The derived velocity model (km/s) of the lower 2D survey found using a velocity range of 0.001 to 5.0 km/s.

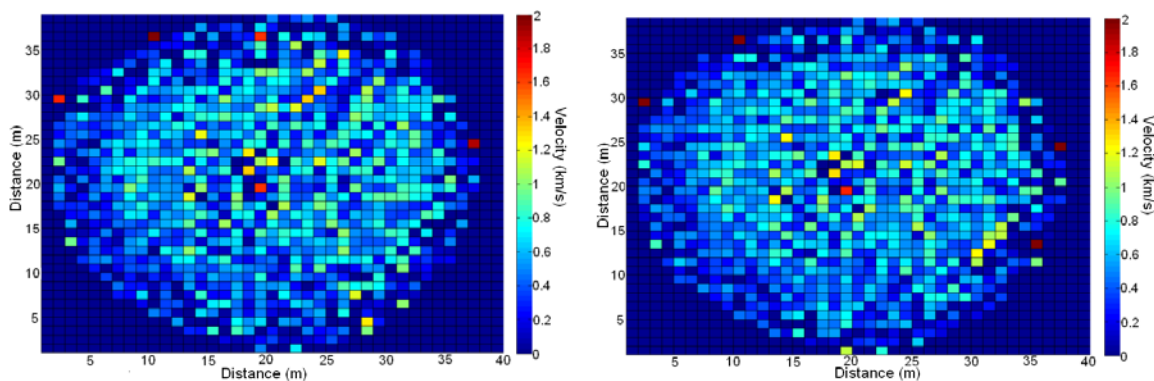


**Figure 3.50:** The 2 km/s max velocity model (left) and the 5 km/s max velocity model with all velocities greater than 2 km/s set equal to 2 km/s (right) found using curved ray tracing.

To further determine the accuracy of the model the differences between the observed and calculated traveltimes were analyzed. The differences are displayed in Figure 3.51. The average of the absolute value and standard deviation of the differences

was found. The average value was determined to be 1.556 ms whereas the standard deviation is 1.975 ms. These values are once again under the estimated error of traveltime picking. The average and standard deviation are also less than those found using straight ray tomography, which is to be expected, as the ray paths should be closer to reality.

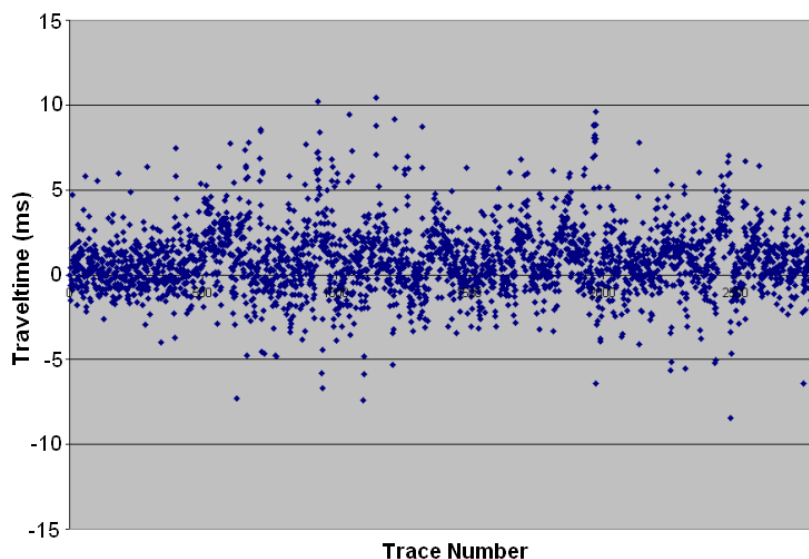


**Figure 3.51: Differences between observed and calculated traveltimes found for the lower 2D survey with a velocity model with a range of 0.001km/s to 2km/s.**

### **3.6.2 Upper 2D Survey**

Similar to the lower 2D survey, the upper 2D was solved using multiple velocity constraints to find the most accurate model and a constant starting velocity model of 500 m/s. Similar to the straight ray inversion, the curved ray results showed large velocity instabilities in the region of the trench (See Appendix C) and therefore the rays that were expected to pass through the location of the trench were ignored resulting in a total of 3054 rays. The  $RMS(\delta t)$  values were once again examined to determine which velocity range produced the most accurate model. To attempt to improve the results, the starting constant velocity model was modified to include the trench (Figure 3.52). By including

the trench with a velocity of 0 m/s it requires the ray paths to bypass the trench location, hopefully making the results more accurate.

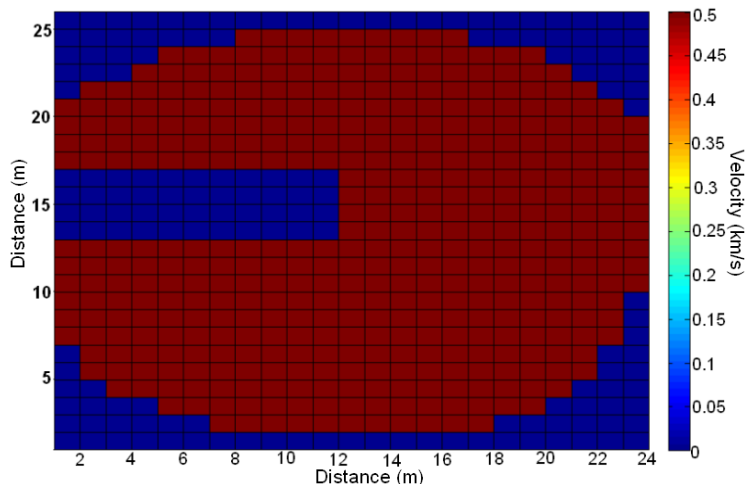


**Figure 3.52: The starting velocity model (km/s) with the trench included.**

Several velocity ranges were solved for a total of 150 iterations. The  $\text{RMS}(\delta t)$  values of all the iterations were found and the lowest value was chosen as the most accurate iteration. Using the iteration with the lowest  $\text{RMS}(\delta t)$  value for each velocity constraint the average and standard deviation of the differences between the measured and calculated traveltimes were derived to determine which velocity range produced the most accurate result. After examining the velocity constraints (Figure 3.53), the range of 0.15 to 0.5 km/s appears to give the most accurate result.

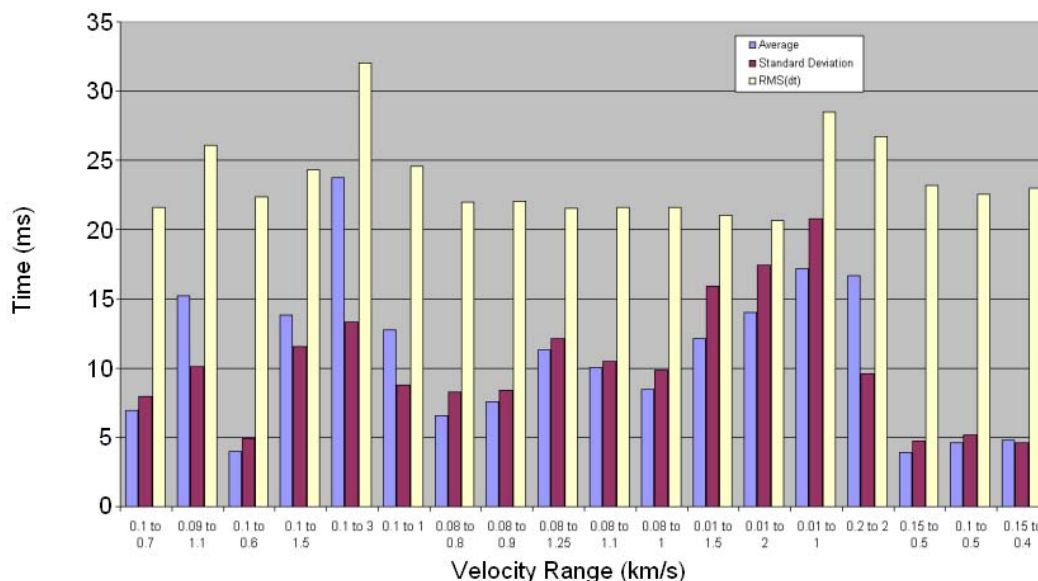


**Figure 3.53: The RMS( $\delta t$ ), average and standard deviation of the differences between the observed and calculated traveltimes for multiple velocity constraints.**

As the velocity range of 0.15 to 0.5 km/s is so tight the resultant velocity model (Figure 3.54) displays a fairly homogenous interior. There are no clear velocity anomalies, which may point to regions of archaeological significance. The velocity model may appear more homogenous than in reality as there is the possibility of out of plane rays. This survey assumes that all the rays remain in the 2D plane. However, if the rays went slightly above or below the plane in order to avoid a low velocity region the final velocity model would appear homogenous while in reality small anomalies may have been present.

The differences between the observed and calculated traveltimes were once again graphed to help determine the accuracy of the model (Figure 3.55). The majority of differences fall within 5 ms with few values being larger than 15 ms. The average and standard deviation of the differences were solved and are equal to 3.90 ms and 4.72 ms respectively. These values are greater than those found in the straight ray tracing. However, the straight ray inversion contained multiple unphysical values and if these

values are constrained to 0 m/s for negative values and 3000 m/s for high velocity values the average and standard deviation increase to 2.71 ms and 4.87 ms respectively. While the average remains lower for the straight ray the standard deviation rises above that of the curved ray with several differences above 20 ms with some reaching heights of near 60 ms. Since the curved ray tracer allows for more realistic ray paths it is possible that the curved model may be more accurate. It is encouraging that the velocity constraints of 0.15 to 0.5 km/s fall into the range of velocities found using the straight ray inversion.

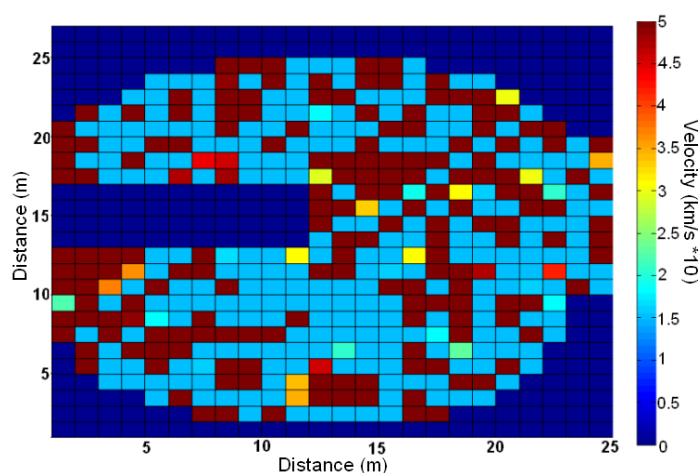


**Figure 3.54: The final velocity model of the upper 2D survey the trench starting velocity model and velocity constraints of 0.15 to 0.5 km/s.**

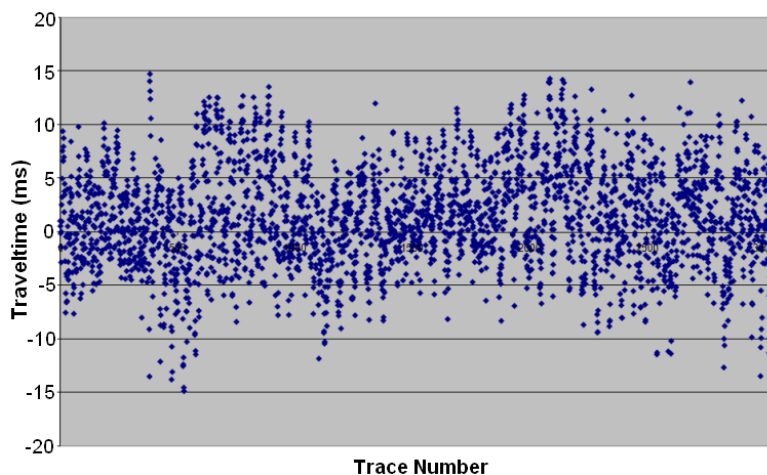


**Figure 3.55: Differences between observed and calculated traveltimes found for the upper 2D survey with a velocity model with a range of 0.15 km/s to 0.5 km/s.**

### **3.7 Curved Ray Amplitude Tomography**

The 2Dray\_tomo program was also used to solve for an attenuation model. Since the 2Dray\_tomo program is designed to find only the velocity model it is only possible to convert it to solve for the inverse of the attenuation. Instead of using traveltimes in the program the amplitude ratio values given by the equation  $\ln(A_o/A_i)$  were used instead. Instead of solving for the root mean squared of the traveltimes the root mean squared of the amplitude ratios was solved instead.

#### ***3.7.1 Lower 2D Survey***

The inverse attenuation model for the lower 2D survey was derived using six constraint ranges. The upper values used were 10, 20 and 100 (m/Np) with the lower range values being equal to 0.2 and 0.4 (m/Np). These values were chosen based on the attenuation values found in the straight ray inversion. The RMS values were again examined to find which value produces the most accurate result. The  $\text{RMS}(\ln(A_o/A_i))$  values reveal that the 0.2 to 10 (m/Np) range produce the smallest values with the minimum value being located at iteration 97 (Figure 3.56). The values after approximately the 90<sup>th</sup> iteration show a fairly consistent value with no large deviations in value.

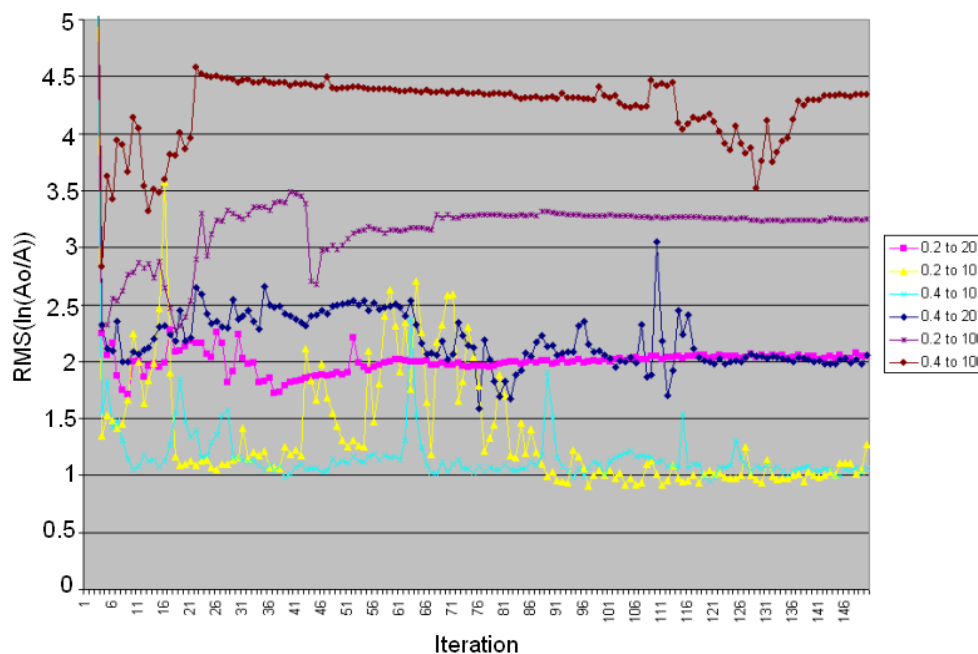


**Figure 3.56: The RMS of the amplitude ratio values versus iterations for different inverse attenuation ranges on the lower 2D survey.**

Iteration 97 of the 0.2 to 10 m/Np range was chosen as the most accurate model. The attenuation and inverse attenuation models were derived and are displayed in Figure 3.57. The attenuation map shows a great deal of attenuation contrast in the interior of the pyramid with the attenuation being either high or really low.

The differences between the observed and calculated amplitude ratios were solved and found to have the majority of values within a range of one (Figure 3.58). The average and standard deviations of the differences were found to be 0.700 Np and 0.891 Np respectively. The average value is close to that found in the straight ray amplitude inversion. However, the standard deviation is significantly higher. It is possible that the curved ray model is more accurate due to a lack of unphysical values in the model. However, this model is not what was expected based on the results of the curved ray velocity model and the straight ray amplitude inversion results. There is a small indication of the high attenuation soil zone around the exterior of the pyramid in some

portions of the model. From the previous surveys a near homogenous interior was to be expected whereas, this model is producing large contrasts. The center of the pyramid does appear to display a low attenuation preference but the unstable region visible in the other inversions is not clearly seen in this model. The 2Dray\_tomo program may not be an appropriate program to use when attempting amplitude inversions.

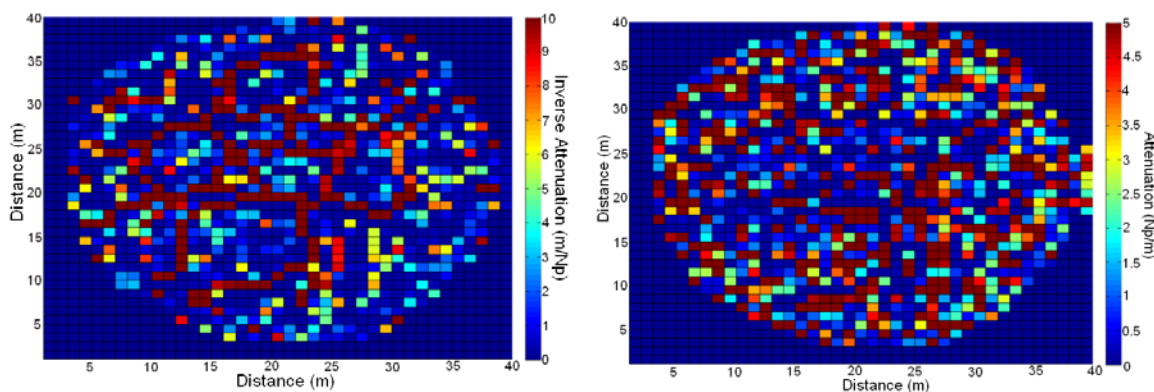


**Figure 3.57:** The inverse attenuation (left) and attenuation (right) model of the 97<sup>th</sup> iteration with the range of 0.2 to 10 m/Np of the lower 2D survey.

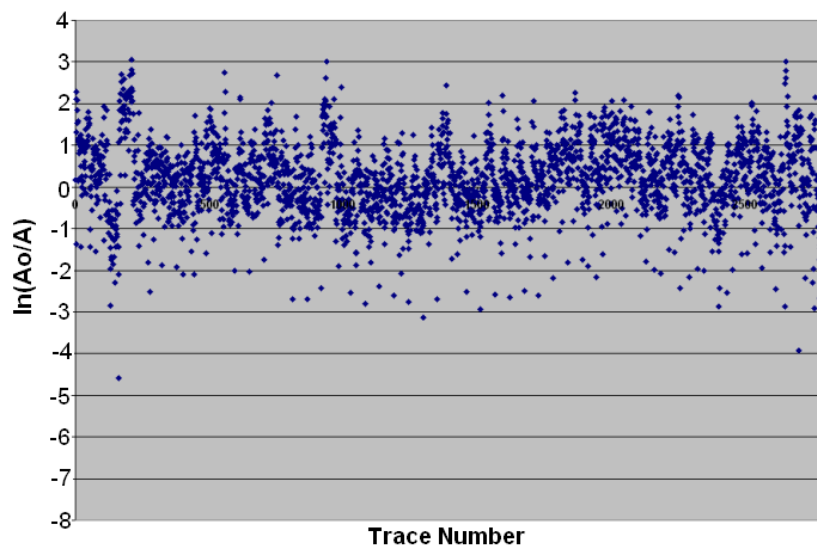


**Figure 3.58:** The differences between the observed and calculated amplitude ratios of the lower 2D survey found using an inverse attenuation range of 0.2 to 10 m/Np.

### ***3.7.2 Upper 2D Survey***

Due to the location of the trench the attenuation models produced using all rays and a constant attenuation model produced unreliable results (see Appendix C). To attempt to avoid these issues the rays with the highest chance of passing through the trench location were ignored as well as an initial starting model that excludes the region of the trench was used. To ensure the largest chance of accuracy twelve different inverse attenuation constraints were solved to a total of 150 iterations. The iteration with the lowest value for the RMS of the inverse attenuation was chosen as the most accurate model for each constraint. The measured and calculated traveltimes of all these models were compared and the average and standard deviation of the differences were derived (Figure 3.59).

The constraint with the lowest values was found with the range of 0.2 to 20 m/Np and therefore this range was chosen as the most accurate model. The inverse attenuation and attenuation models are seen in Figure 3.60. As with the lower survey, the upper survey displays large attenuation contrasts in the center of the pyramid. There is an indication of the high attenuation soil layer but it is not as clearly seen as with the straight ray inversion. Due to the instability of the model it is impossible to determine whether any regions that may be of archaeological significance are located in this section.

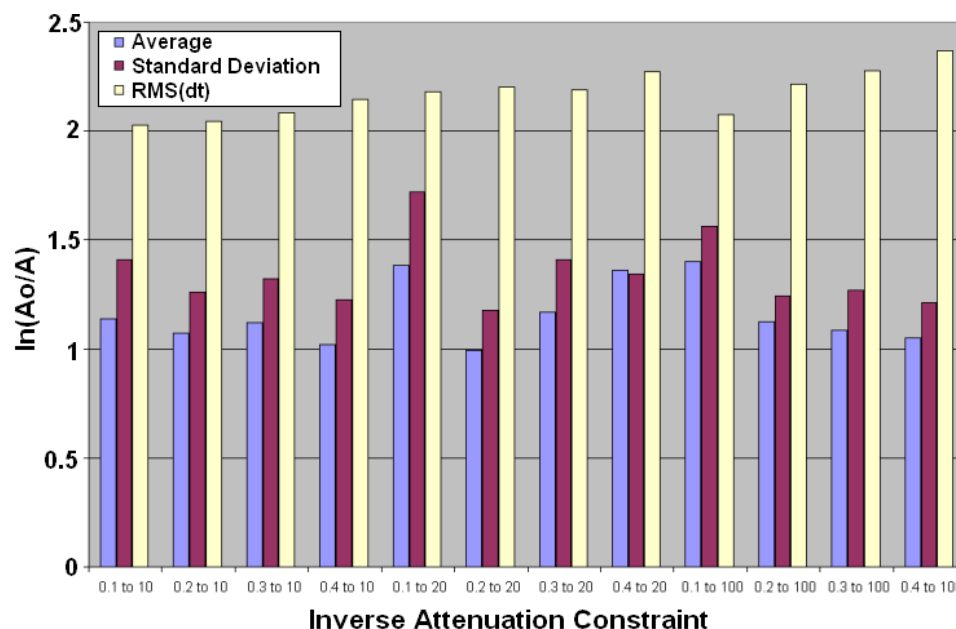


**Figure 3.59: The RMS( $\ln(A_o/A)$ ), average and standard deviation of the differences between the observed and calculated amplitude ratios for multiple inverse attenuation constraints.**

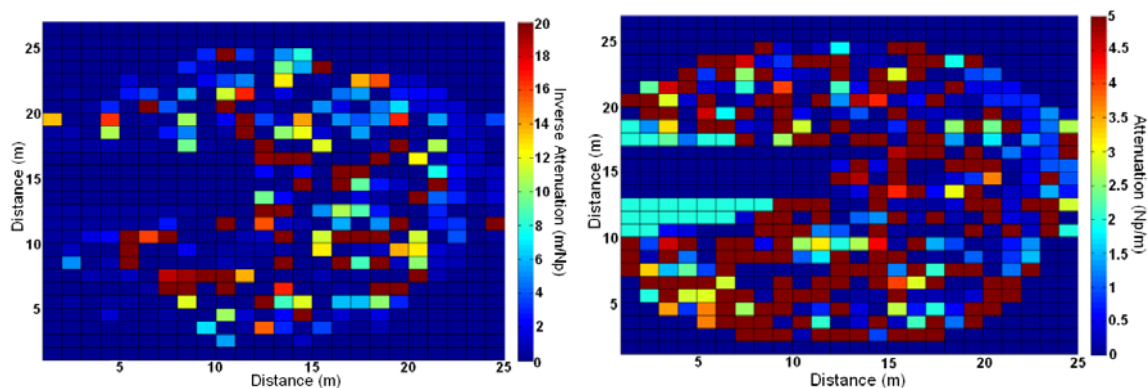


**Figure 3.60: The inverse attenuation (left) and attenuation (right) model of upper 2D survey with the range of 0.2 to 20 m/Np.**

The differences between the observed and calculated amplitude ratios were again examined to help determine the accuracy of the attenuation model. The majority of the differences again fall under a ratio of 1 Np. Solving for the average and standard deviation of the differences values of 0.99 Np and 1.18 Np were found respectively. These values are approximately two times higher than those found using the straight ray inversion. It is difficult to determine which result is more accurate. The straight ray

inversion has unphysical values and contains attenuation artefacts from the trench location whereas the curved ray model shows large attenuation contrasts and has higher average differences.

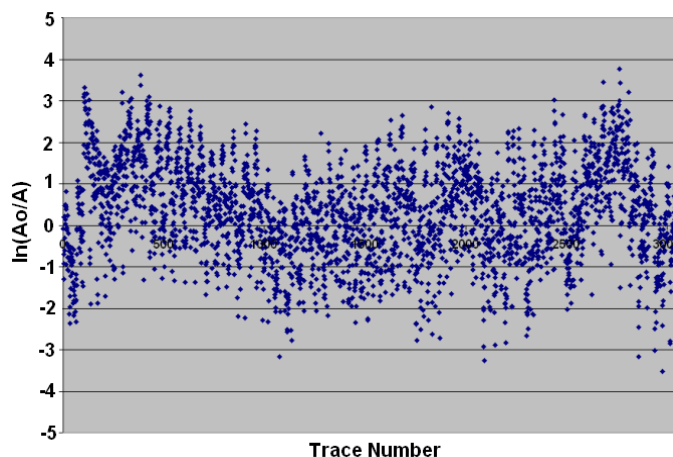


**Figure 3.61: The differences between the observed and calculated amplitude ratios of the upper 2D survey found using an inverse attenuation range of 0.2 to 20 m/Np.**

### 3.8 Summary

The straight ray and curved ray travelt ime inversion for the lower 2D survey produced similar velocity structures. This structure contains a low velocity exterior with a slowly increasing velocity interior with a zone of unstable velocities in the center. The majority of velocities fell into the expected velocity range of 200 - 800 m/s found in the previous work described in Xu and Stewart (2000; *ibid*, 2001). The low velocity (unconsolidated) region in the interior of the lower 2D survey may be a result of the pyramid being built on the top of a previous structure or an area of loose rock rubble. The straight ray amplitude inversion results produced a very similar interior structure to those of the travelt ime inversions including the anomaly in the center. This is encouraging that the results found are producing consistent images of the interior of the pyramid.

The upper 2D survey produced multiple difficulties due to the location of a looter's trench in the pyramid. This trench was characterized in the straight ray traveltimes inversion models by a region of low velocity surrounded by regions of very high velocity. The same high and low velocity regions in the area of the trench were found using the curved ray inversion. The trench proved to affect the velocity structure away from itself as low velocity artefacts were seen stretching out from the location of the trench. In regions that appear to be producing accurate results the velocities do remain in the same range as the lower 2D survey of 200-800 m/s. The trench could be the cause of such intense problems due to the assumption of the survey being 2D. While including the trench in the model should help improve the results if the survey was truly 2D it is possible that the wave propagated under the trench as opposed to around the trench causing errors in the raypaths.

When solving the 3D surveys the straight ray methods both produced results that showed velocities in the appropriate ranges. It was also discovered that straight ray tomography produces the possibility of masking velocity anomalies. The looter's trench was clearly visible in the upper 3D survey but when combined with the lower 3D survey the trench is much harder to locate. This result means that it is possible that a smaller velocity anomaly such as a small room could be masked resulting in it being missed in the interpretation. It is possible to help avoid this problem by increasing the amount of sources and receivers to cover the entire area of the structure being examined. The amplitude inversions of the 3D surveys again showed similar results to that of the traveltimes inversions. The high attenuation soil layer was clearly visible in many of the layers and realistic values were displayed in most regions with sufficient fold.

Finally, solving the amplitude inversion using curved ray tracing produced possible difficulties. Based on both the straight ray amplitude inversions and the curved ray traveltimes a nearly homogenous interior was expected for the lower survey with only a small area of unstable values. The attenuation map found produced large contrasts in attenuation for the majority of the interior. There does appear to be a slight area of high attenuation in the region of the soil layer; however, it is not clearly visible. This same effect was noticed in the upper survey where large attenuation contrasts were displayed in regions where the expected model, from the straight ray inversions, was mostly homogenous. The problems may be associated with the 2Dray\_tomo program that was not initially developed to perform attenuation inversions and therefore may not be the most appropriate program to use. Also since the program can only derive inverse attenuation values and can only solve to two decimal places the accuracy of the attenuation model may be limited.

## Chapter Four: GPR Tomography

Ground penetrating radar (GPR) has often been used in archaeology to help locate objects and structures buried in the earth (Conyers, 1995; da Silva Cezar et al., 2001; Aitken, 2008). GPR is sensitive to the electromagnetic properties of the subsurface and therefore can detect some subsurface anomalies, which may be of interest to archaeologists. However, since GPR usually has a limited penetration distance, seismic techniques have been used instead when performing tomography over larger paths. While seismic tomography has been proven effective (see Cardarelli and de Nardis, 2001; Allen and Stewart, 2007; Polymenakos and Papamarinopoulos, 2007) the equipment can be heavy and expensive. In addition, the receivers (geophones) require planting. This makes it difficult to work in often remote areas where archaeological excavations are taking place. GPR is a possible solution to this problem as the equipment is lighter, more mobile, less expensive and doesn't require planting.

In 2008, a team from the University of Calgary (consisting of Dr. R. Stewart and M. Allen) returned to Maax Na to undertake a GPR test. This test survey was performed around the perimeter of the pyramid approximately half way up. The survey involved a thirty-meter line or half circumference with receiver points every 20 centimetres. The equipment used was the pulseEKKO PRO system with 100 MHz antennas and 1000V transmitter (Figure 4.1). Eight passes were made over the 30 m half circumference with the transmitter at a different position each time. This resulted in a total of eight shot points with 151 receiver positions as seen in Figure 4.2. The locations of the receivers have an elevation range of approximately 1 m making this a slightly 3D survey. However, since

the vertical difference is so small the survey will also be solved in 2D ignoring any vertical effects.

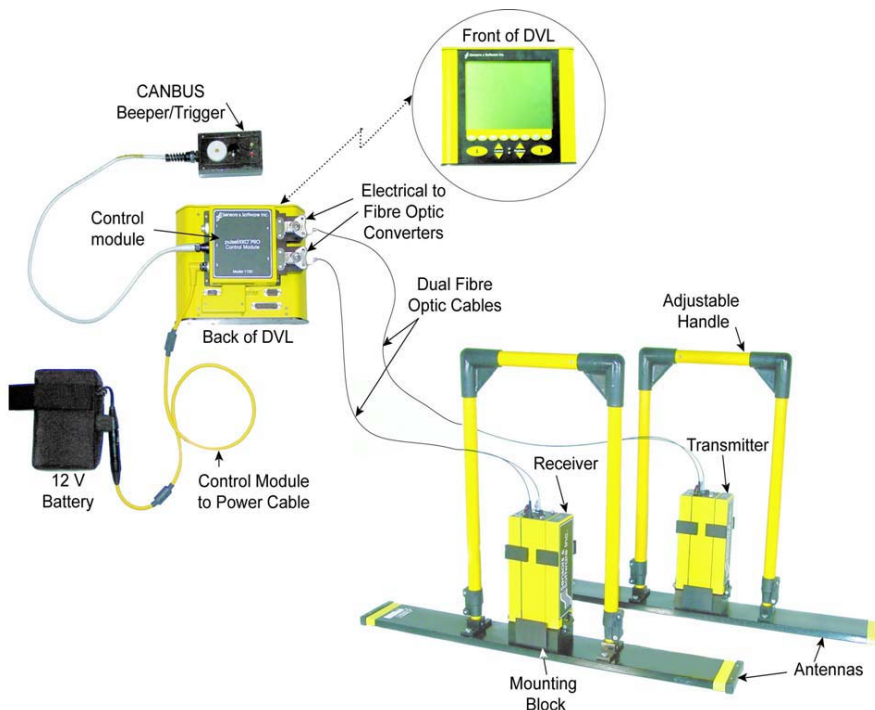


**Figure 4.1: Sensors and Software's pulseEKKO PRO system. (Sensors and Software, 2006)**

#### 4.1 Data Analysis

Unlike the seismic surveys, the direct transmission is not the first arrival time seen on a GPR shot gather. Instead, an airwave will typically arrive first. For our work, this airwave will be ignored and the transmission through the pyramid will be found. A raw shot gather from this survey can be seen in Figure 4.3, with both the air and direct wave indicated. Another problem with the GPR survey is that the signal may not transmit through the entire pyramid. GPR has a more limited range than that of seismic, therefore some initial processing should be completed to reveal as much of the direct wave as possible. Due to the lack of signal, many of the receiver points cannot be used since the signal is too weak to distinguish on the shot gather.

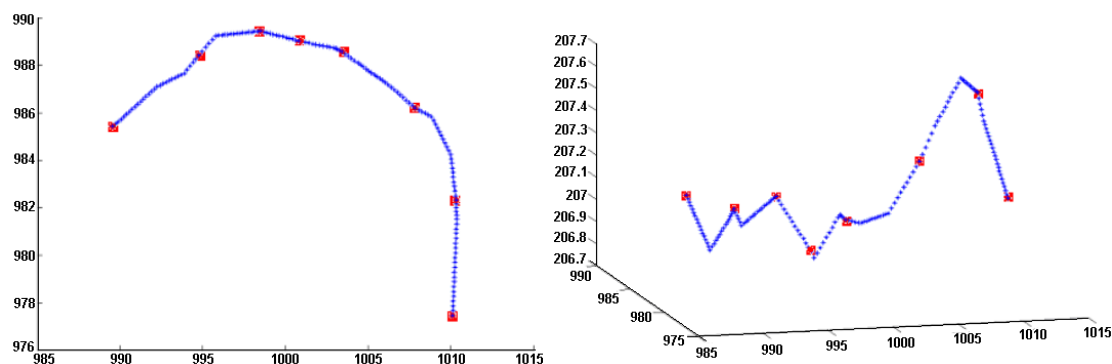


**Figure 4.2: Layout of the GPR survey in 2D (left) and 3D (right) perspective. Receiver locations are shown in blue and transmitter locations in red.**

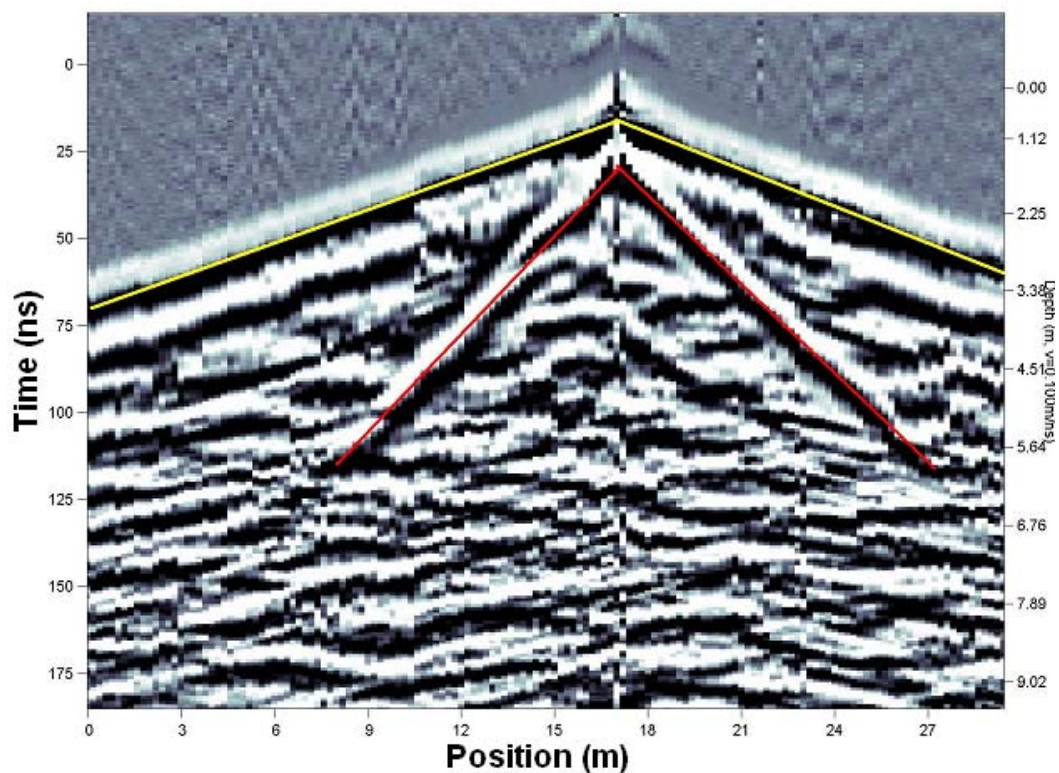


**Figure 4.3: A raw shot gather from the GPR survey with the airwave marked in yellow and the direct wave marked in red**

The 100 MHz antennae on the pulseEKKO PRO system produced on average a relatively broadband signal up to 140 MHz. The peak frequency appears to be approximately 50 MHz for all the shots. Figure 4.4 shows the frequency/amplitude graph

as well as the time/amplitude graph for the shot from position two. The remaining shots display similar results.

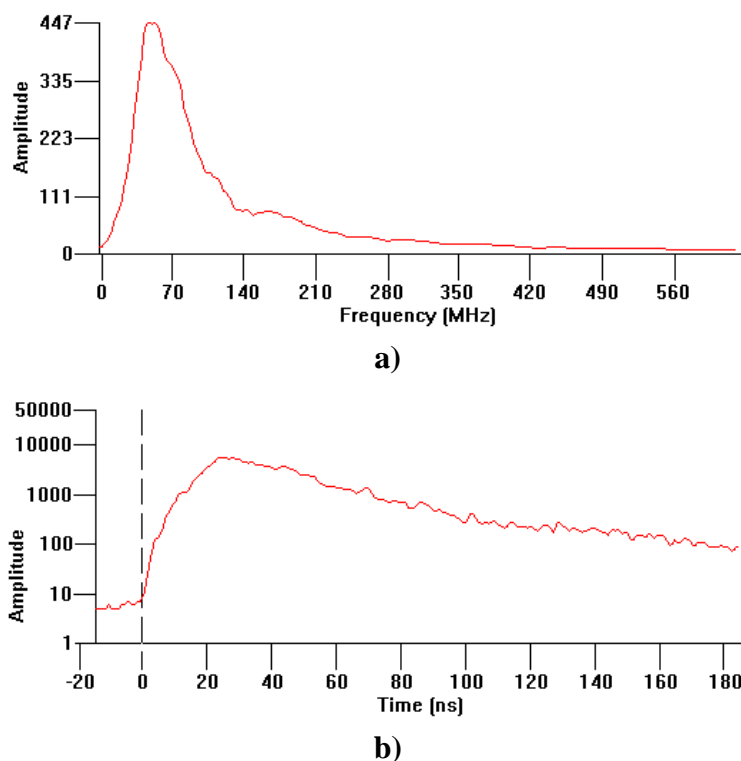


**Figure 4.4:** The a) amplitude frequency graph and b) amplitude time graph for shot 2.

To emphasize the direct transmitted wave, an FK filter was applied to the shot gathers. The filter was designed to eliminate as much of the shot gather as possible while maintaining the direct transmission wave (Figure 4.5). By applying the FK filter, a clear view of the transmission wave without the airwave and much of the noise is seen, as displayed in Figure 4.6. It can also be seen that the wave is visible for a longer period of time than on the raw shot gather. Therefore we have data from further penetration.

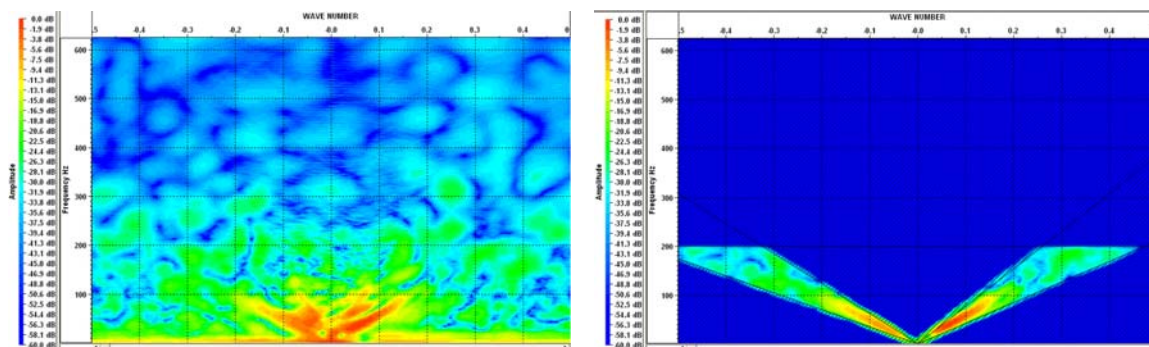


**Figure 4.5: The initial FK spectrum (left) and final FK spectrum (right) after applying the FK filter.**

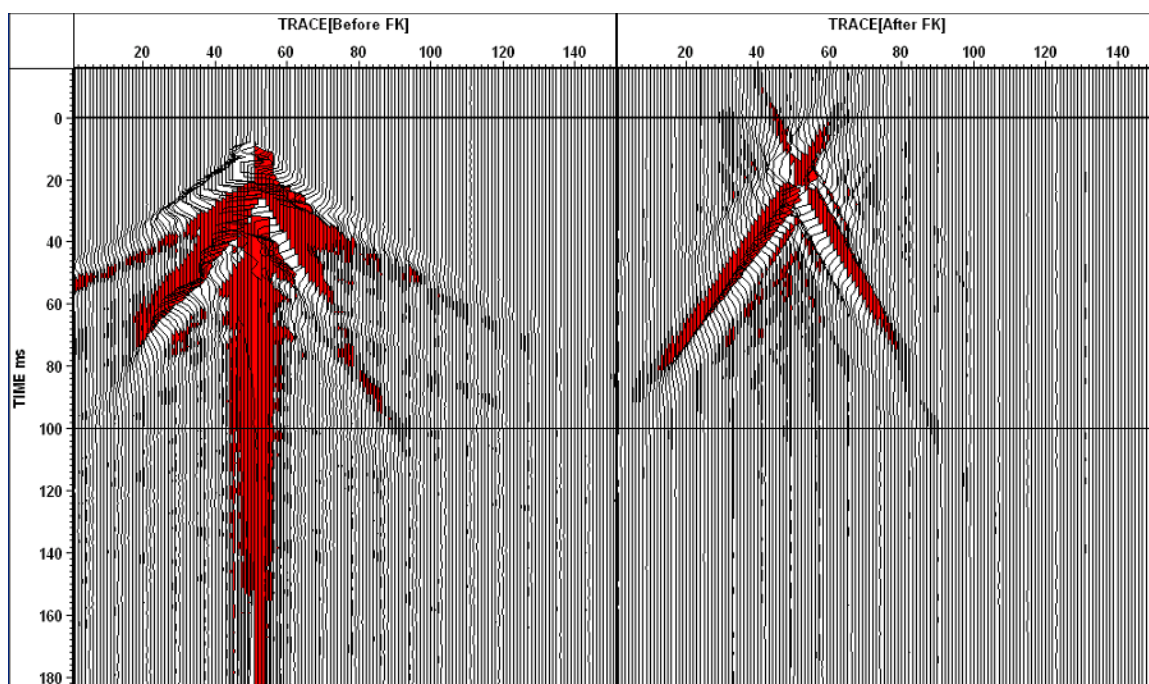


**Figure 4.6: The raw shot gather (left) and the shot gather after applying the FK filter.**

Despite concerns about the depth of penetration looking at the filtered shots the transmission wave appears to clearly penetrate to a depth of 15 to 20 m. When picking the traveltimes multiple picks located on receivers near the source point had to be ignored due to interference of the transmission wave by the airwave. After applying the FK filter several artefacts are visible. These artefacts only interfere with the transmitted wave in

the regions where the airwave and transmitted wave meet. These regions have already been excluded from the traveltime picks and therefore the artefacts do not affect the final model. Once all reliable picks had been made a total of 735 traveltimes remained.

In solving for the velocity structure a grid size of 0.5 m by 0.5 m was used for both the straight and curved ray techniques. This grid size was chosen due to the close spacing of the receiver locations. Since a large percentage of area that this GPR survey is covering is the loose soil layer the velocity can quickly change and a smaller grid size will better image this. The resulting small grid size does result in a lower fold; however, the majority of pixels retain an acceptable level of fold.

Unlike the seismic surveys, the GPR survey is not amenable to amplitude inversion at this stage. The raw shot gathers are too noisy to accurately pick amplitudes for the transmitted wave. Even after the FK filter was applied the amplitudes appear to have been modified with some appearing to be saturated. This results in amplitudes that have been modified and therefore are no longer accurate for amplitude inversion.

#### **4.2 2D Straight Ray Tomography**

To solve the straight ray inversion direct division, damped least squares, singular value decomposition and the conjugate gradient method were all used. All methods displayed similar results with the conjugate gradient method used with a total 30 iterations being displayed in this section. The derived velocity structure resulted in several negative values. Since these negative values are not physical they were set equal to zero. Along with the negative values there were a few velocity values that appeared too high to be physical. These high velocity values were set equal to 0.2 m/ns.

The velocity value of 0.2 m/ns was considered the maximum based on previous years' GPR surveys performed on the plaza area of Maax Na by Aitken and Stewart (2004). In these surveys, velocities were found to range between 0.072 to 0.106 m/ns in wet conditions and 0.122 to 0.140 m/ns in dry conditions. Since the plaza was made of similar carbonate as the pyramid, these velocities were used as a guideline in determining the maximum velocity. A maximum velocity of 0.2 m/ns was set as the fill in the pyramid may be less dense than that of the plaza and therefore may have slightly faster velocity. The final velocity structure can be seen in Figure 4.7.

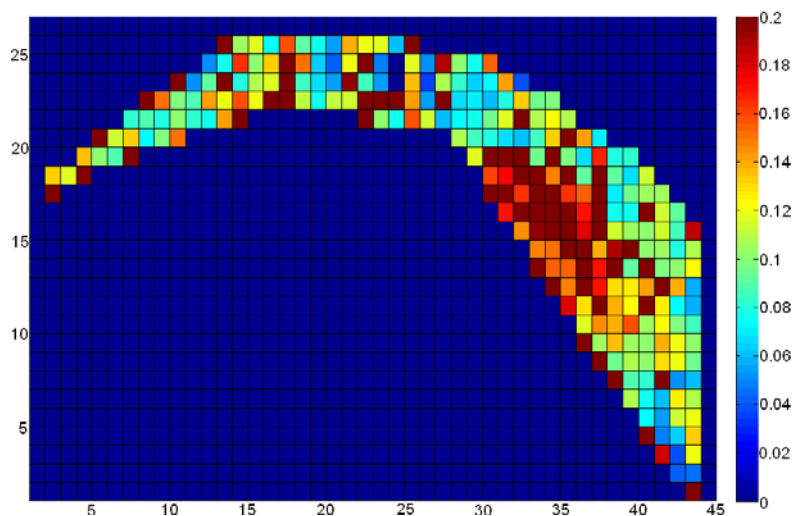


**Figure 4.7: The final 2D velocity (m/ns) structure derived from straight ray travelt ime inversion. All negative values set to 0 m/ns. All velocities greater than 0.2 m/ns are set equal to 0.2 m/ns.**

After looking at the fold and straight ray paths (Figure 4.8), the highest accuracy pixels should be located along the fringes of the pyramid. This is what is seen in the velocity model. The majority of high values were all found further into the interior of the pyramid, which has much less ray coverage than other areas. To better image these areas, further ray coverage is needed.

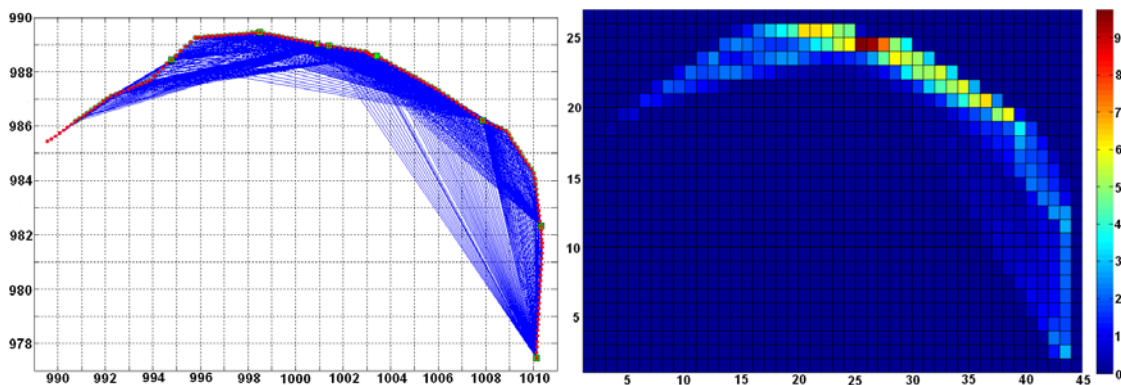


**Figure 4.8: The straight ray paths (left) and fold (right) for the GPR survey using straight ray tomography.**

A new set of traveltimes was derived based on the modeled velocity structure found by the straight ray tracing. The negative and high velocity values were included in the model. The derived traveltimes were compared to the original traveltimes picks. The results can be seen in Figure 4.9. The average of the absolute value of the differences were found to be 1.710 ns with a standard deviation of 2.412 ns.

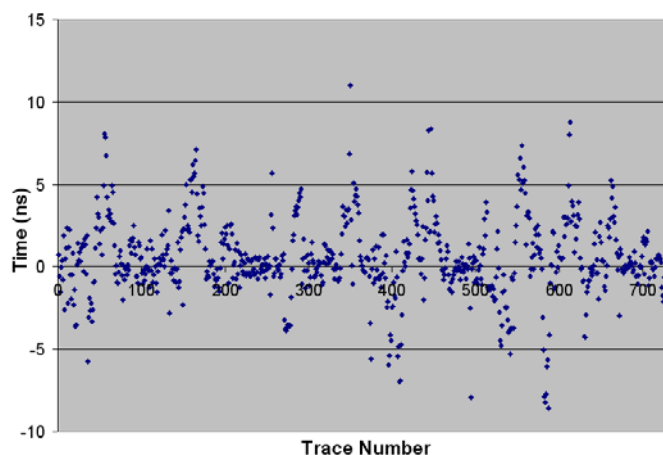


**Figure 4.9: The difference between the measured and calculated traveltimes of the 2D GPR survey.**

Figure 4.9 shows that there are several regions with high differences. To determine the reasons for these values the measured and calculated values are both graphed with the differences in Figure 4.10. The largest differences in general appear in

the rays that have the shortest distance to travel. These are the rays that are expected to have the largest difference as they pass through a limited number of pixels resulting in the rays having limited effect on the total velocity model. Since these rays have such a small distance to travel even a small velocity error can produce a large error in traveltimes.

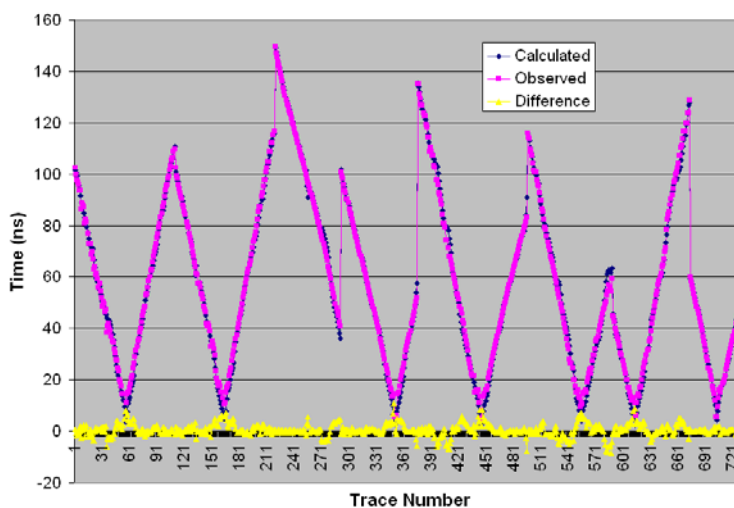


**Figure 4.10: The measured and calculated traveltimes from the GPR velocity model.**

### 4.3 3D Straight Ray Tomography

Since the sources and receivers were placed over a vertical contour of 1 m it is possible to solve for the velocity structure using 3D ray tracing techniques. Due to limited processing power the 3D survey will only be solved using straight ray techniques. To directly compare the 3D results to those of the 2D survey a grid size of 0.5 m by 0.5 m by 1 m was chosen. This allows all the sources and receivers to be contained in a single vertical level. The only difference between the 2D and 3D survey will be the distance the rays travel and therefore the fold. The two folds are compared in Figure 4.11. The differences in fold between the 2D and 3D survey appear to be minimal and therefore should only have a minimal affect on the velocity model.

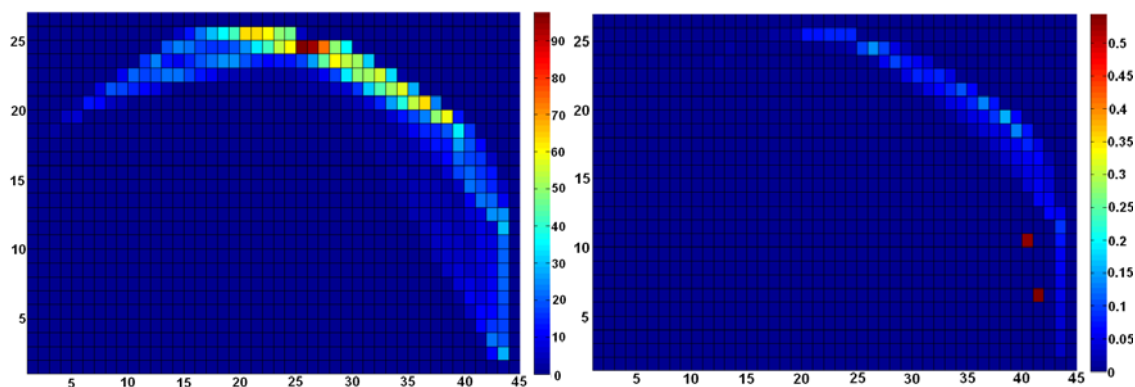


**Figure 4.11: The straight ray fold for the 3D GPR survey (left) and the difference between the 3D and 2D GPR survey folds (m) (right).**

Similar to the 2D survey, the 3D survey was solved using all four methods (DD, DLS, SVD and CG) with the conjugate gradient method using 30 iterations being displayed here. The velocity structure found is very similar to that of the 2D survey with the outer fringes of the model having the most realistic values and many of the unphysical values being located closer to the interior of the pyramid (Figure 4.12).

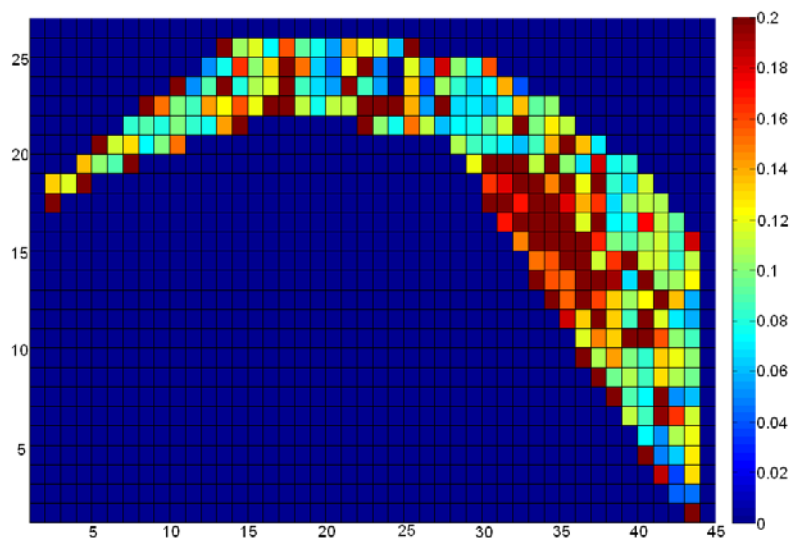


**Figure 4.12: The final 3D velocity (m/ns) structure derived from straight ray travelt ime inversion. All negative values set to 0 m/ns. All velocities greater than 0.2 m/ns are set equal to 0.2 m/ns.**

To determine whether the 3D survey provided any beneficial results a look at the differences between observed and calculated traveltimes is undertaken. The differences of the 3D survey (Figure 4.13) appear very similar to those of the 2D survey. Finding the average difference and the standard deviation of the differences values of 2.932 ns and 3.234 ns respectively. These values are both under those of the 2D survey giving evidence that the 3D survey does provide more accurate results. However, the differences are only 0.01 ns for the average and 0.008 ns for the standard deviation. These differences are not of large enough significance to justify performing the 3D survey. If the sources and receivers were placed over larger vertical contours the 3D survey would continue to improve on that of the 2D survey. However, if the vertical contour is at a minimum 2D ray tracing provides adequate results.

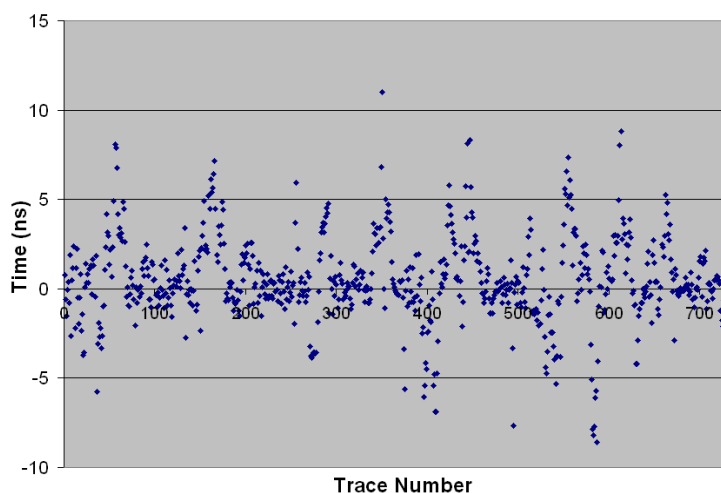


**Figure 4.13: The difference between the measured and calculated traveltimes of the 3D GPR survey.**

#### 4.4 2D Curved Ray Tomography

To solve for the velocity structure using curved ray traveltime inversion the 2Dray\_tomo program created by Zhou et al. (1992a). This program uses the minimum traveltime method of Moser (1991) and Zhuo et al. (1992a). This method uses a number

of nodes on the grids that are connected to create the shortest path between source and receiver as well as a fast and efficient damping L2-norm inversion algorithm (Zhou, 1992b). For this survey the maximum amount of 25 nodes per grid were used along with a damping factor of  $1 \times 10^{-6}$ .

Based on the velocities found from the straight ray tomography, a constant starting velocity model of 0.1 m/ns was chosen for the curved ray tomography. As with the seismic surveys multiple velocity constraints were tested to find the most accurate model. Seven different velocity ranges were solved for a total of 100 iterations. The  $\text{RMS}(\delta t)$  values were solved for each iteration in each velocity range. These values were graphed and compared in Figure 4.14. Unlike in the seismic surveys, the  $\text{RMS}(\delta t)$  values do not appear to give a clear picture of which velocity range is giving the best results. None of the velocity ranges appear to be clearly converging, as there is a high variability of values from one iteration to the next. The larger ranges produce more variability in both the  $\text{RMS}(\delta t)$ ; however, this is to be expected as these ranges allow the velocity to change to a larger variety of values than the other ranges.

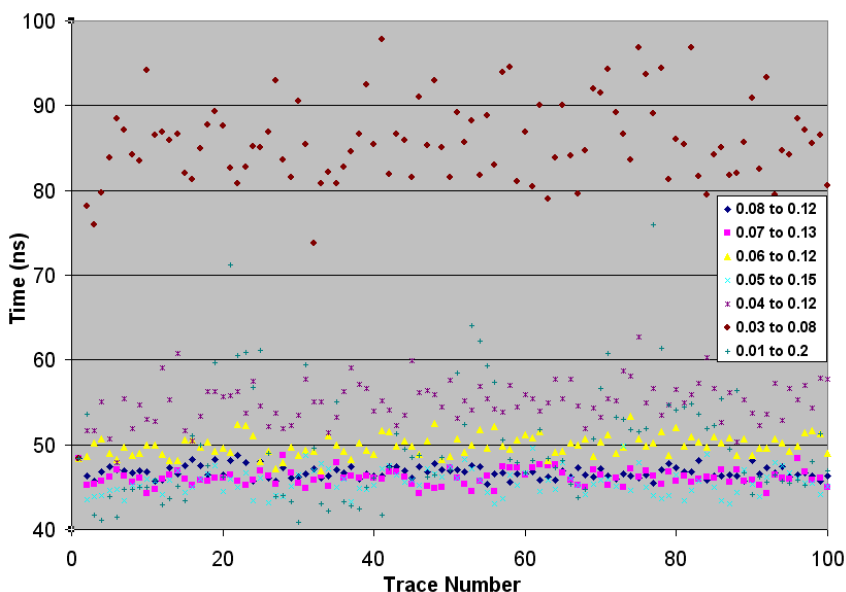


**Figure 4.14: The  $\text{RMS}(\delta t)$  values for the GPR survey with several different velocity ranges.**

Since the RMS values are not clearly indicating one model as being more accurate than any other another feature must be considered. To help the determination the standard deviation and average of the absolute value of the differences between the observed and calculated traveltimes for the 100<sup>th</sup> iteration were compared. Figure 4.15 shows that the smallest values for the averages and standard deviations are given by the 0.08 to 0.12 m/ns and 0.07 to 0.13 m/ns velocity ranges. This is not the final answer since it is only for one iteration. However, it minimizes the ranges that need to be further examined. The averages for all iterations for both the 0.08 to 0.12 m/ns and 0.07 to 0.13 m/ns velocity were solved (Figure 4.16) to determine which model is the most accurate. To insure that the 100<sup>th</sup> iteration was indicative of the average for all the iterations the 0.06 to 0.12 m/ns range was also included in the graph.

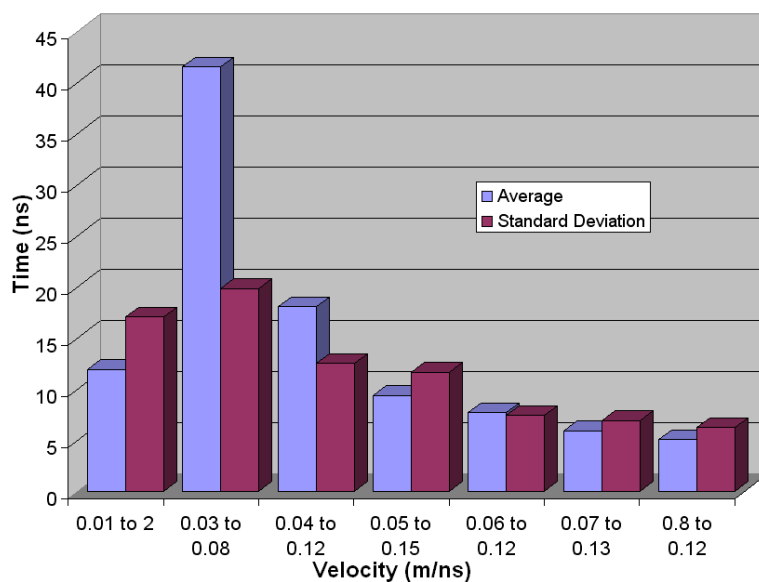


**Figure 4.15: Comparison between the average and standard deviation of the differences between the observed and calculated traveltimes for the 100<sup>th</sup> iteration for multiple velocity ranges.**

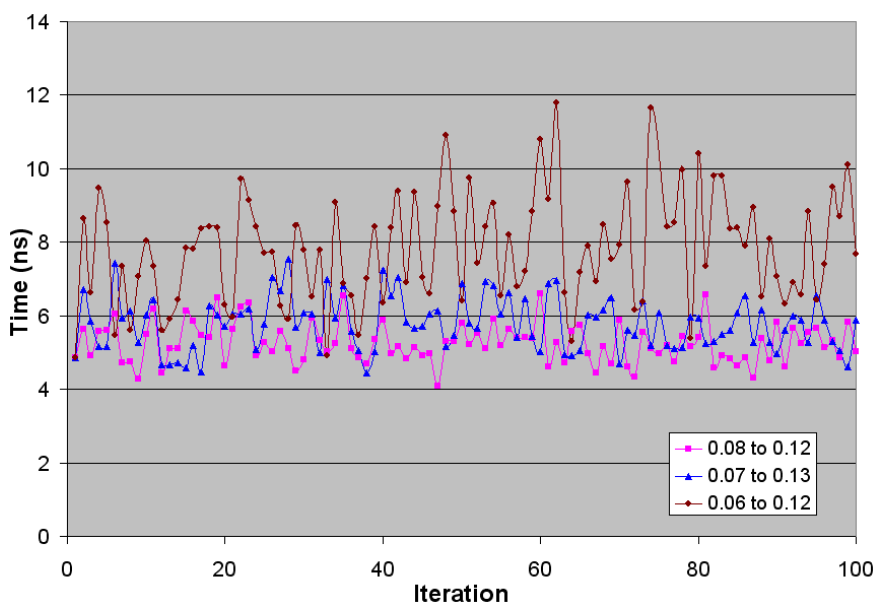


**Figure 4.16: Average of the differences between measured and calculated traveltimes for each iteration of curved ray traveltimes inversion.**

The velocity range of 0.08 to 0.12 m/ns produces the lowest average values.

Therefore it was determined that this range is the most accurate. Upon comparison iteration 47 proved to give the lowest average and therefore was used to create the velocity model in Figure 4.17.

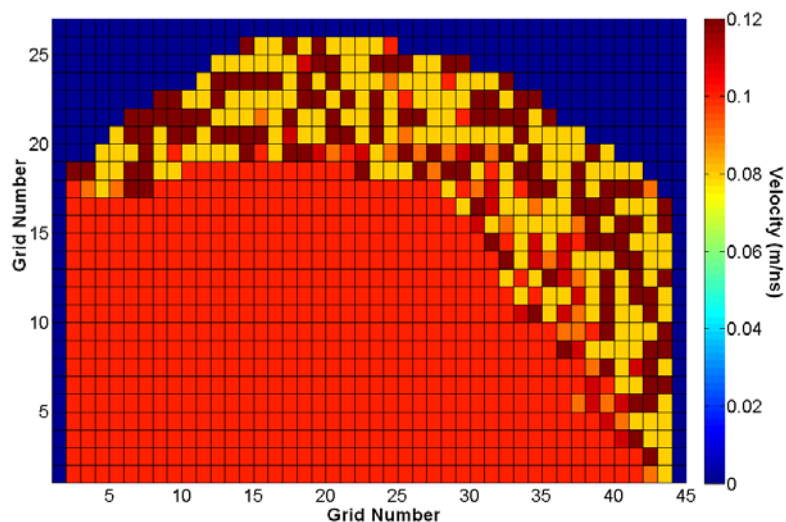


**Figure 4.17: The final velocity model (m/ns) derived from the curved ray traveltime inversion. Parts of the initial model of 0.1 m/ns remain in areas of no ray coverage.**

The velocity model displays a highly variable velocity region. This is to be expected as the majority of coverage takes place in the loosely consolidated soil layer where the velocity can change rapidly. A look at the ray paths of the 47<sup>th</sup> iteration (Figure 4.18) shows that once again the majority of the fold lies along the exterior of the pyramid. However, since the velocities have been constrained the more interior values appear more realistic than their straight ray counterparts.

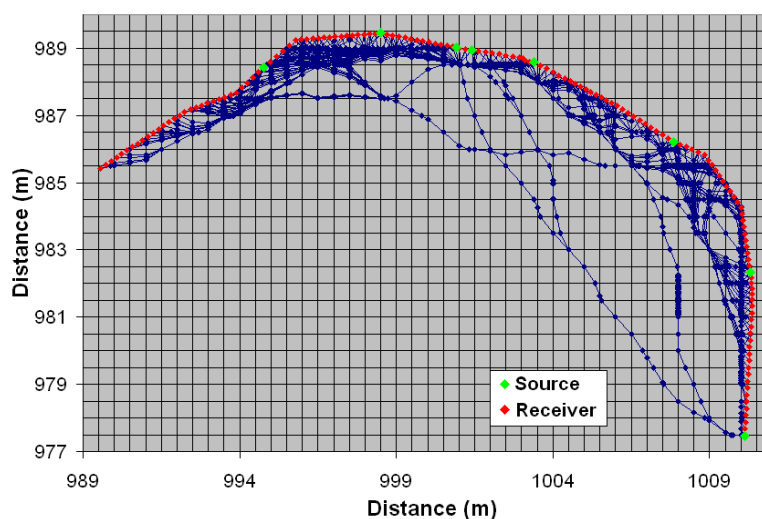


**Figure 4.18: The raypaths from the 47<sup>th</sup> iteration of the GPR survey found using curved ray tracing and a velocity range of 0.08 to 0.12 m/ns.**

The differences between the observed and calculated traveltimes (Figure 4.19) show similar high difference features to those of the straight ray traveltimes. These can once again be explained by graphing both the observed and calculated traveltimes (Figure 4.20). Like the straight ray model the larger differences appear in the rays that travel the smallest distance and therefore contribute little to the final velocity model. The other large differences appear at the longest distance rays. These are the rays that may not have been visible before the FK filter and therefore the signal is not as strong in these areas. This results in the traveltimes time picks being harder to distinguish and therefore may cause a larger error. The final reason for the differences is that there are a limited number of rays with large distances meaning that the fold remains lower and the rays only contribute to a small area of the velocity model. This could result in the model not being as accurate as it could be if additional ray coverage was available.

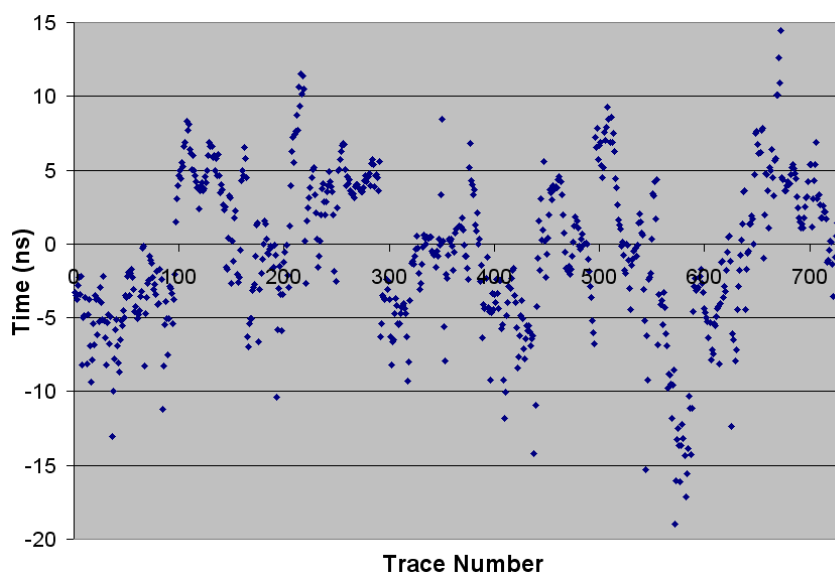


**Figure 4.19: Differences between measured and calculated traveltimes for the 47<sup>th</sup> iteration velocity model.**

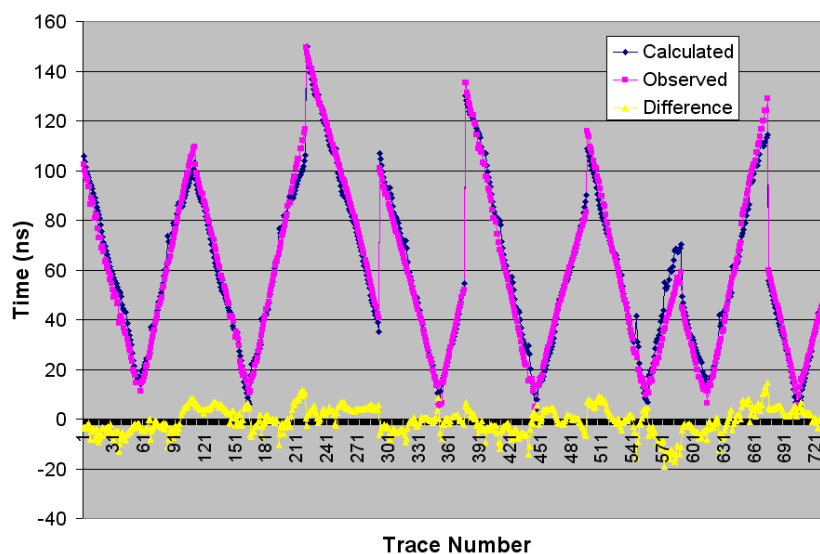


**Figure 4.20: The observed and calculated traveltimes of the 47<sup>th</sup> iteration of the GPR survey with a velocity constraint of 0.08 to 0.12m/ns.**

The average difference and standard deviation of the differences was found to be 4.068 ns and 5.058 ns respectively. While the average difference and standard deviation of the curved ray inversion is higher than that of the straight ray there are no unphysical values in the curved ray trace resulting in what is a more reliable velocity structure. If the unphysical values in the straight ray model were modified to be equal to 0 m/ns and 0.2 m/ns depending on their value the derived average and standard deviation would dramatically increase to a level of 50.9 ns and 166.1 ns respectively. To get a better velocity model a larger amount of source or receivers should be included allowing for a high fold and larger possible velocity range.

#### 4.5 Summary

In analyzing the capability of GPR in being used in large structure tomography, it was seen that our 100 MHz, 1000 V system can transmit approximately 10 m on either side of the source point. Using a lower frequency antenna, such as the 50 MHz or 25 MHz antennae, should expand the penetration depth.

The straight ray traveltimes inversion produced a velocity model with the majority of velocities in an acceptable range determined by previous GPR surveys in the plaza area. However, there were several negative as well as excessively large velocity values given. These unphysical values tended to appear in areas of low fold. Therefore, with increased source points, the values should further converge to the actual velocity model.

The curved ray model was able to produce a precise velocity model after finding appropriate velocity constraints of 0.08 m/ns to 0.12 m/ns. Using these constraints the average difference between the measured and calculated traveltimes was reduced to 4.068 ns. This was a little higher than that of the straight ray inversion; however, since the curved ray had no unphysical values the curved ray velocity model is more likely to be accurate. To increase the accuracy, a greater number of source and receiver points must be included which should allow the velocity constraints to be widened.

## Chapter Five: Conclusions and Future Work

### 5.1 Conclusions

The objective of this thesis was to determine whether hammer seismic and GPR tomography techniques were viable for assisting archaeologists in exploring the interior of large archaeological structures. Specifically, these techniques were applied on the main pyramid at Maax Na in the hopes of locating a void or identifying the remains of previous structures upon which the pyramid had been built. Several 2D and 3D surveys were acquired on the pyramid and using traveltimes and amplitude picks velocity and attenuation maps were derived using straight and curved ray tracing techniques.

#### *5.1.1 Seismic and GPR Viability*

- Hammer seismic shots produced similar frequency spectra indicating source repeatability.
- Hammer sources propagated through the entire structure allowing for low noise shot gathers and clear first breaks.
- GPR using 100 MHz antennae showed a wave penetration of approximately 10 meters on either side of the source location, which is inadequate for full tomography.
- After applying an FK filter to the raw shot gathers the transmitted wave became visible and traveltimes could be more accurately taken.

#### *5.1.2 Straight Ray Tomography*

- The straight ray techniques produced seismic and GPR velocity maps with velocity values in the expected range found using ultrasonic measurements on rock samples and previous GPR surveys in the plaza area.

- The derived attenuation and velocity maps produced similar structures giving confidence in the results of the inversion.
- Straight ray tomography produced several unphysical values (negative and unrealistically high) in all the models. These values typically appeared in areas of low fold. This can be corrected by including a greater amount of source and receiver points.

### ***5.1.3 Curved Ray Tomography***

- The curved ray technique produced similar 2D models as the straight ray seismic models. This is a good indication that both the straight and curved ray techniques are producing accurate results.
- The curved ray results included velocity constraints eliminating the appearance of unphysical values in the derived models.
- The 2Dray\_tomo program appeared to have difficulty when deriving attenuation models.

### ***5.1.4 Regions of Archaeological Significance***

- The looter's trench in the upper 2D survey provided an example of the effect of a large void on traveltimes and amplitude tomography. Both the straight and curved ray techniques produced a region of low velocities surrounded by regions of large velocities. These same features of low value regions surrounded by large value regions were also seen in the derived attenuation models.
- The lower 2D seismic survey produced a velocity and attenuation anomaly in the center of the pyramid. This feature was present in the velocity and attenuation models derived using straight ray inversion as well as the curved ray velocity

model. This feature could be associated with a small void in the center of the pyramid or the rubble of a pre-existing structure on which the pyramid was built.

- The region of instability is no longer visible in the 3D surveys where the pixel size is increased to 2 m. This favours the explanation that the instability is caused by a region of rubble. If the instability were a large void there would be a high probability of some indication of it appearing in the velocity model.
- The remaining regions of the upper and lower 2D survey as well as the 3D surveys show near homogenous velocity and attenuation models. This is a good indication that there are no regions of archaeological significance in these areas.
- The GPR survey did not display any clear regions of interest. The GPR survey was limited in its coverage with the majority of the coverage being along the exteriors of the pyramid and therefore was not expected to find any regions of interest.

Ultimately, both the GPR and seismic methods provided interpretable models of the interior of the pyramid. Both methods have been shown to be effective and viable options for imaging the interior of structures. To produce the highest quality models, a large number of sources and receivers should be included in the surveys. This will allow for a smaller grid size that may allow smaller features to be imaged.

While a region of interest was discovered in the lower 2D seismic survey it should be noted that these features might be caused by a number of different factors. However, it still allows the archaeologist to potentially direct their excavations and while it does not guarantee significant finds it may increase the probability.

## 5.2 Future Work

While images of the interior of the pyramid were found it is possible that a more accurate image could be derived with a more comprehensive survey. If additional source and receiver points were added a higher fold and therefore more accurate model would be achieved. It was shown that GPR with 100 MHz antennae is not capable of penetrating adequate distances through the pyramid. In order to take full advantage of this technique a survey should be performed, with lower frequency antenna, covering the full circumference of the pyramid and therefore truly testing the capability of the technique.

There are also additional methods that could be used to further image the pyramid using the existing survey data. The 3D surveys should be solved using the curved ray techniques to better image the pyramid as an entirety. In this thesis, only the transmitted P-wave was used in the inversion process. It is also possible to perform the inversions using reflected, refracted and scattered waves. Figure 5.1 and Figure 5.2 show the stacks of the lower 2D seismic survey and the GPR survey respectively. In these figures, there are strong reflections that may be of interest. By using these waves in the inversion it may be possible to better image regions of interest since these regions would produce strong reflections. An examination of the distance versus travelttime and amplitude graphs (Figure 5.3 and Figure 5.4) may also direct us to regions that may be of interest.

The 2Dray\_tomo program performed the travelttime inversions with results that appear to be accurate. However, the program had difficulties imaging the upper survey with the trench as well as the amplitude inversions. To improve the results a more complex ray propagation should be implemented. Also it may be possible to overcome

these difficulties using full waveform inversion. This could by pass the use of rays and may improve the derived models.

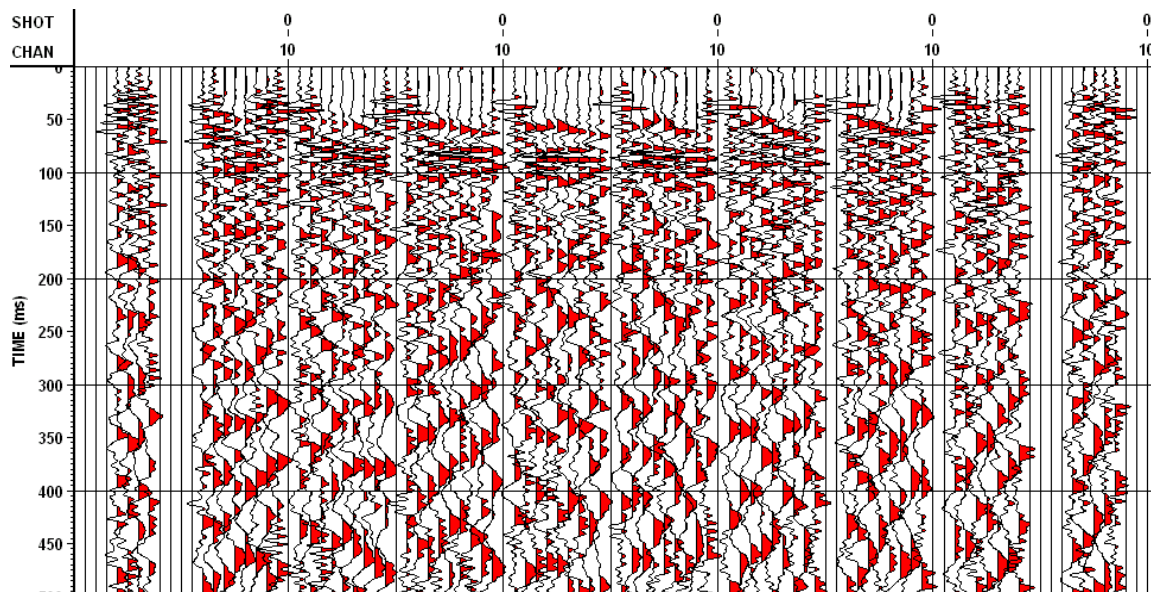


**Figure 5.1: The stack of the lower 2D seismic survey (courtesy of Paul Hebert).**

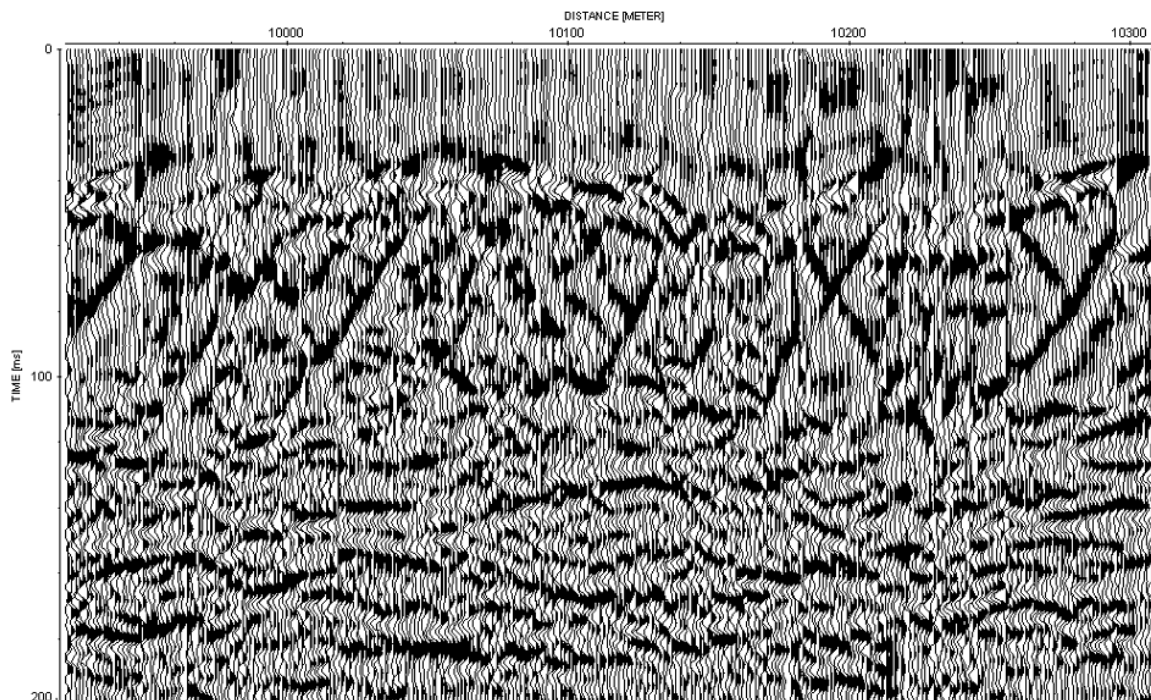


**Figure 5.2: The stack of the GPR surveys after an FK filter removed the airwave. Survey was scaled to use ms instead of the original ns. (courtesy of Paul Hebert).**

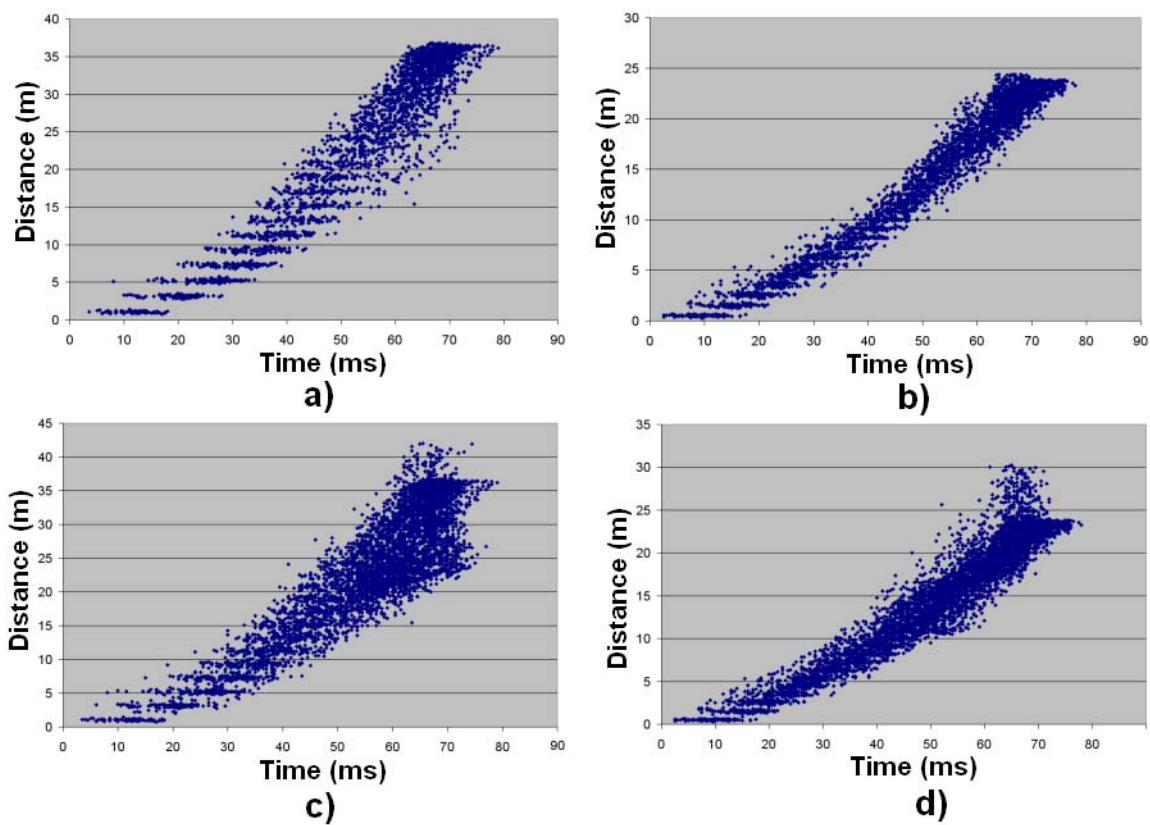


**Figure 5.3: The straight ray distance from source to receiver vs. the traveltime for the a) lower 2D, b) upper 2D, c) lower 3D and d) upper 3D surveys.**

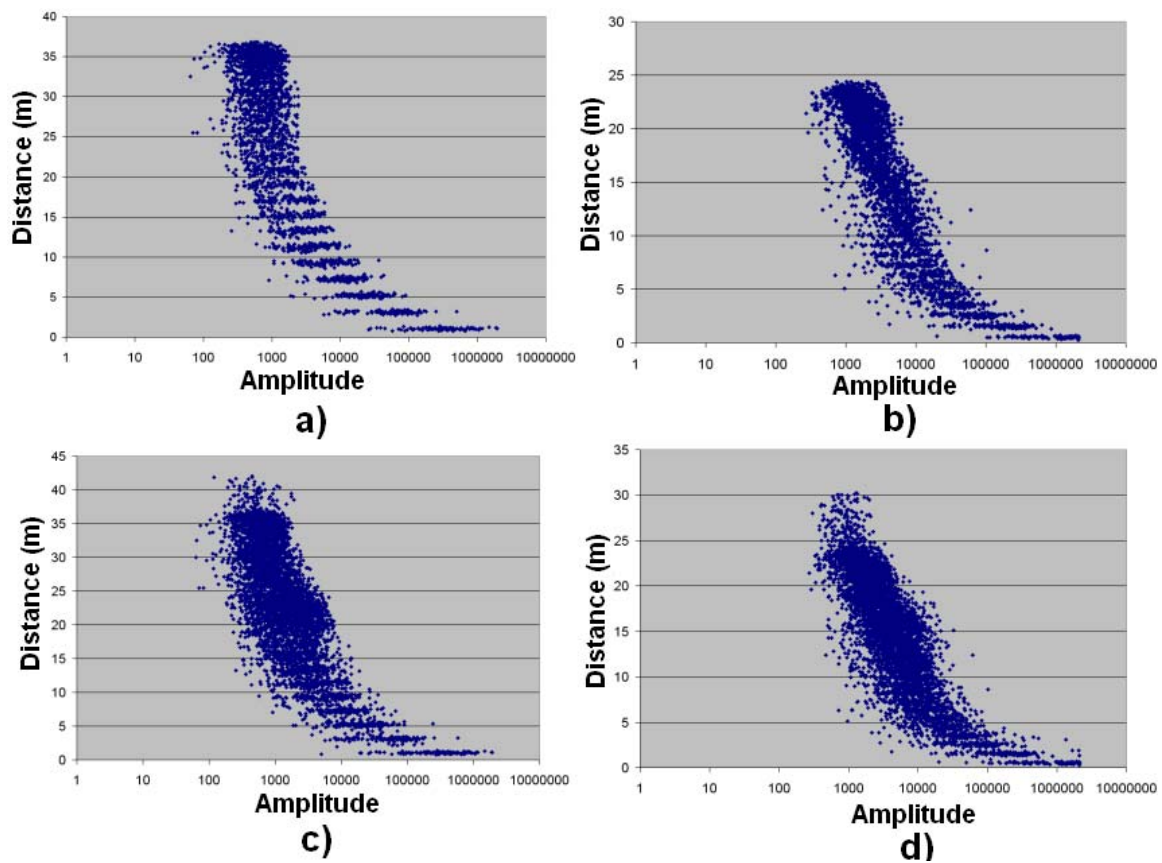


**Figure 5.4:** The straight ray distance from source to receiver vs. the amplitude for the a) lower 2D, b) upper 2D, c) lower 3D and d) upper 3D surveys.

## References

- Aitken, J., 2008, Exploring Maya ruins in Belize using GPR: M.Sc. Thesis, University of Calgary.
- Aitken, J. and Stewart, R.R., 2002, A geological/geoscience overview of the hydrocarbon exploration potential of Belize, Central America: CREWES Research Report, **14**.
- Aitken, J. and Stewart, R.R., 2003, Ground-Penetrating Radar (GPR) imaging of near-surface structure in a carbonate environment: CREWES Research Report, **15**.
- Aitken, J., and Stewart, R.R., 2004, Investigations using ground penetrating radar (GPR) at a Maya plaza complex in Belize, Central America: 10<sup>th</sup> International Conference on Ground Penetrating Radar, 447-450.
- Aki, K. and Richards, P., 1980, Quantitative Seismology – Theory and Methods: W.H. Freeman Co., Vol.2.
- Allum, C., 2004, Welcome to the Monkey House: Bowdoin Magazine, **76**, 18-25.
- Asquith, G., and Kryowski, D., 2004, Basic Well Log Analysis: 2<sup>nd</sup> Ed, AAPG Methods in Exploration Series, **16**.
- Assefa, S., McCann, C., and Sothcott, J., 2003, Velocities of compressional and shear waves in limestones: Geophysical Prospecting, **51**, 1-13.
- Baechle, G.T., Colpaert, A., Eberli, G. P., and Weger, R. J., 2008, Effects of microporosity on sonic velocity in carbonate rocks: The Leading Edge, **27**, 1012-1018.
- Baechle, G.T., Weger, R. J., Eberli, G. P., Massaferrro, J. L., and Sun, Y.-F., 2005, Changes of shear moduli in carbonate rocks: Implications for Gassmann applicability: The Leading Edge, **24**, 507-510.
- Bateson, J. H., and Hall, I. H. S., 1977, The geology of the Maya Mountains, Belize: Overseas Memoir 3, Her Majesty's Stationery Office.
- Batzle, M., 2006, Properties and behavior of pore fluids for geophysical applications: Canadian Soc. Explor. Geophys., Short Course, Calgary, Alberta (mbatzle@mines.edu)
- Batzle, M.L., Han, D.-H., and Hofmann, R., 2006, Fluid mobility and frequency-dependent seismic velocity – direct measurements: Geophysics, **71**, N1-N9.

- Barton, N., 2007, Rock quality, seismic velocity, attenuation and anisotropy: Taylor and Francis Group.
- Belize Environmental Consultancies Ltd., 2006, EIA: Seismic Activities in the Orange Walk District, Belize: RMS Seismic Surveys.
- Bellman, R., 1958, On a routing problem: *Quart. Appl. Math.*, **16**, 88-90.
- Blaylock, J. J., 1999, Interpretation of a baseline 4-D multicomponent seismic survey at Vacuum Field, Lea County, New Mexico: MSc. Thesis, Colorado School of Mines.
- Brennan, M. L., 2008, Personal Communication, Graduate School of Oceanography; University of Rhode Island, Narragansett, R.I.
- Canadian Museum of Civilization, 2004, <http://www.civilization.ca/civil/maya/mmc07eng.html>. Accessed December 13, 2006.
- Cardarelli, E., and de Nardis, R., 2001, Seismic refraction, isotropic anisotropic seismic tomography on an ancient monument (Antonino and Faustina temple AD 141): *Geophysical Prospecting*, **49**, 228-240.
- Cardarelli, E., Cercato, M., and Di Filippo, G., 2007, Assessing foundation stability and soil-structure interaction through integrated geophysical techniques: a case history in Rome (Italy): *Near Surface Geophysics*, **5**, 141-147.
- Cardarelli, E., Fischanger, F., and Piro, S., 2008, Integrated geophysical survey to detect buried structures for archaeological prospecting. A case-history at Sabine Necropolis (Rome, Italy): *Near Surface Geophysics*, **6**, 15-20.
- Carrara, E., Carozzo, M. T., Fedi, M., Florio, G., Negri, S., Paoletti V., Paolillo, G., Quarta, T., Rapolla, A., and Roberti, N., 2001, Resistivity and radar surveys at the archaeological site of Ercolano: *Journal for Environmental and Engineering Geophysics*, **6**, 123-132.
- Castagna, J.P., Batzle, M. L., and Kan, T.K., 1993, Rock physics – The link between rock properties and AVO response, in *Offset-dependent reflectivity- Theory and Practice of AVO analysis*, J.P. Castagna and M. Backus, eds. *Investigations in Geophysics*, No. 8, Society of Exploration Geophysicists, 3-36.
- Claerbout, J. F., 1986, Conjugate Gradient Tutorial: Stanford Exploration Project Report, **48**, 351-358.
- Coe, M. D., 2001, *The Maya*: 6<sup>th</sup> Ed. Thames & Hudson.

- Colpaert, A., 2007, Geophysical characterization of Carboniferous-Permian carbonate platforms in the Barents Sea based on 3D-seismic data analysis and rock physics modeling: PH.D. thesis, University of Tromsø.
- Colpaert, A., Baechle, G.T., Brevik, I., Weger, R. S., Eberli, G.P., and Mienert, J., 2006, Elastic properties and fluid substitution in carbonate rocks from experimental velocity data and pore shape analysis: The Sound of Geology Workshop, CIPR, Norway.
- Conyers, L. B., 1995, The use of ground-penetrating radar to map the buried structures and landscape of the Ceren site, El Salvador: *Geoarchaeology*, **10**, 275-299.
- Da Silva Cezar, G., Ferruccio da Rocha, P.L., Buarque, A., and da Costa, A., 2001, Two Brazilian archaeological sites investigated by GPR: Serrano and Morro Grande: *Journal of Applied Geophysics*, **47**, 227-240.
- De, D. S., D. F. Winterstein, and M. A. Meadows, 1994, Comparison of P- and S-wave velocities and Q's from VSP and sonic log data: *Geophysics*, **59**, 1512–1529.
- Domenico, S. N., 1984, Rock lithology and porosity determination from shear and compressional wave velocity: *Geophysics*, **49**, 1188-1195.
- Fasquelle, R. A., and Fash Jr., W. L., 1991, Maya Artistry Unearthed: *National Geographic*, **180**, 94-105.
- Gardmer, G. H. F., Gardner, L. W., and Gregory, A. R., 1974, Formation velocity and density – The diagnostic basics for stratigraphic traps: *Geophysics*, **39**, 770-780.
- Geis, W.T., Stewart, R.R., Jones, M.J., and Katopodis, P.E., 1990, Processing, correlating and interpreting converted shear waves from borehole data in southern Alberta: *Geophysics*, **55**, 660-669.
- Geology and Petroleum Office, Ministry of Science Technology and Transportation, Belmopan, Belize, 1995, Petroleum Potential of Belize, Central America.
- Goodman, D., Salvatore, P., Nishimura, Y., Patterson, H., and Gaffney, V., 2004, Discovery of a 1<sup>st</sup> century AD Roman amphitheatre and other structures at the Forum Novum by GPR: *Journal for Environmental and Engineering Geophysics*, **9**, 35-41.
- Hagin, P.N. and Zoback, M.D., 2004, Viscous deformation of unconsolidated reservoir sands – part 1: Time-dependent deformation, frequency dispersion, and attenuation: *Geophysics*, **69**, 731-741.

- Hemsing, D. B., 2007, Laboratory determination of seismic anisotropy in sedimentary rock from the Western Canadian Sedimentary Basin: M.Sc. Thesis, University of Alberta.
- Hooker, R., 1996, Civilizations in America; The Mayas:  
<http://www.wsu.edu/~dee/CIVAMRCA/MAYAS.HTM>, accessed May 1, 2007.
- Jones, S. B., Thompson, D. D., and Timur, A., 1976, A unified investigation of elastic wave propagation in crustal rocks: Presented at Rock Mechanics Conference.
- Johnson, D. B., 1977, Efficient algorithms for shortest paths in sparse networks: Journal of the ACM, **24**, 1-13.
- Johnston, D. H., 1978, The attenuation of seismic waves in dry and saturated rocks: Ph.D. Thesis, Massachusetts Institute of Technology.
- Karastathis, V. K., Papamarinopoulos, S., and Jones, R.E., 2001, 2-D velocity structure of the buried ancient canal of Xerxes: an application of seismic methods in archaeology: Journal of Applied Geophysics, **47**, 29-43.
- King, M.S., 1964, Wave velocities and dynamic elastic moduli of sedimentary rocks: Ph.D. thesis, University of California, Berkeley.
- Klema, V. C. and Laub, A. J., 1980, The singular value decomposition: its computation and some applications: IEEE Transactions on Automatic Control, **AC-25**, 164-176.
- Kuster, G. T., and Toksöz, N. M., 1974, Velocity and attenuation of seismic waves in two-phase media: Part 1. Theoretical formulations: Geophysics, **39**, 607-618.
- Library of Congress, 2005, Belize: A Country Study,  
<http://lcweb2.loc.gov/frd/cs/bztoc.html>, accessed April 18, 2007.
- Lines, L.R. and Newrick, R.T., 2004, Fundamentals of Geophysical Interpretation: SEG Geophysical Monograph Series, **13**.
- Lines, L.R., and Treitel, S., 1984, Tutorial a review of least-squares inversion and its application to geophysical problems: Geophysical Prospecting, **32**, 159-186.
- Madsen, K., Nielsen, H.B., and Tingleff, O., 2004, Methods for non-linear least squares problems: Informatics and Mathematical Modelling, Technical University of Denmark.
- Mahmoudian, F., 2006, Linear AVO inversion of multi-component surface seismic and VSP Data: M.Sc. Thesis, University of Calgary.

- Mavko, G., Mukerji, T., and Dvorkin, J., 1998, *The Rock Physics Handbook: Tools for seismic analysis in porous media*: Cambridge University Press.
- Merlanti, F., and Musante, B., 1994, Seismic tomography: application for archaeological purposes: *Geoarchaeology*, **9**, 317-329.
- Michelena, R. J., 1993, Singular value decomposition for cross-well tomography: *Geophysics*, **58**, 1655-1661.
- Moser, T.J., 1991, Shortest path calculation of seismic rays: *Geophysics*, **56**, 59-67.
- Norikatsu, M., and Yasuaki, K., 2003, Effective porosity and compression strength of Ryukyu limestone in Pleistocene Epoch in the Quaternary period: *Science Bulletin of the Faculty of Agriculture, University of the Ryukyus*, **50**, 131-138.
- Olver, P.J., and Shakiban, C., 2006, *Applied Linear Algebra*: Pearson Prentice Hall
- Olympus NDT, 2007, Phased Array Tutorial, <http://www.olympusndt.com/en/ndt-tutorials/phased-array/>, accessed July 2, 2008
- Polymenakos, L., and Papamarinopoulos, St. P., 2007, Using seismic traveltime tomography in geo archaeological exploration: an application at the site of Chatby cemeteries in Alexandria, Egypt: *Near Surface Geophysics*, **5**, 209-219.
- Program for Belize (PFB), 2003, About Program for Belize: <http://www.pfbelize.org/about.html>, accessed May 1, 2007.
- Pujol, J., 2007, The solution of nonlinear inverse problems and the Levenberg-Marquardt method: *Geophysics*, **72**, W1-W16.
- Sams, M.S., Neep, J.P., Worthington, N.H., and King, M.S., 1997, The measurement of velocity dispersion and frequency-dependent intrinsic attenuation in sedimentary rocks: *Geophysics*, **62**, 1456-1464.
- Schicht, Th., Lindner, U., Heckner, J., Strobel, G. and Rappsilber, I., 2007, Seismic tomography on the castle hill in Quedlinburg: *Near Surface Geophysics*, **5**, 339-343.
- Schmitt, D. R., 1999, Seismic attributes for monitoring of a shallow heated heavy oil reservoir: A case study: *Geophysics*, **64**, 368-377.
- Schuster, G. T., 1996, Resolution limits for crosswell migration and traveltime tomography: *Geophysics Journal International*, **127**, 427-440.

- Sensors & Software, 2006, pulseEKKO PRO: User's Guide: Sensors & Software.
- Stewart, R. R., 1984, Vertical-seismic-profile (VSP) interval velocities from travelttime inversion: *Geophysical Prospecting*, **32**, 608–628.
- Stewart, R.R., Huddleston, P.D., and Kan, T.K., 1984, Seismic versus sonic velocities: A vertical seismic profiling study: *Geophysics*, **49**, 1153-1168.
- Stewart, R.R., 1991, *Exploration Seismic Tomography: Fundamentals*: SEG Course Notes Series, **3**.
- Stielin, H., 1962, *Living Architecture: Mayan*: Grosset and Dunlap.
- The Programme for Belize Archaeological Project (PfBAP), Belize, Central America, 2005. Programme for Belize Archaeological Project and nearby sites: at Austin: <http://uts.cc.utexas.edu/~marl/location.html>; accessed February 15, 2007. Ap
- Perry-Castañeda Library Map Collection, 2007, Political Map of Belize: University of Texas at Austin, [http://www.lib.utexas.edu/maps/americas/belize\\_pol\\_03.jpg](http://www.lib.utexas.edu/maps/americas/belize_pol_03.jpg); accessed March 20, 2007.
- Wang, Z.J., Hirsche, W. K., and Sedgwick, G., 1991, Seismic velocities in carbonate rocks: *J. Can. Petro. Tech.*, **30**, 112-122.
- Watanabe, T. and Sassa, K., 1996, Seismic attenuation tomography and its application to rock mass evaluation: *Int. J. Rock Mech. Min. Sci. and Geomech. Abstr.*, 33 (5), 467-477 in Barton (2007).
- Woolf, G., 2005, *Ancient Civilizations: The illustrated guide to belief, mythology and art*: Duncan Baird Publishers.
- Wright, A. C. S., D. H. Romney, R. H. Arbuckle, and V. E. Vial, 1959, *Land Use in British Honduras*. Colonial Research Publications No. 24. Her Majesty's Stationary Office.
- Xu, C. and Stewart R.R., 2000, Seismic tomography of a Maya pyramid: Chan Chich, Belize: CREWES Research Report, **12**, 563-575.
- Xu, C. and Stewart R.R., 2001, Seismic tomography of a Maya pyramid ruin, Chan Chich, Belize: CREWES Research Report, **13**, 843-850.
- Xu, C. and Stewart, R. R., 2002, *Seismic Tomography of Maya Pyramid Ruins: Belize, Central America: 2002 CSEG Conference, Expanded Abstracts*.

Yilmaz, O., 2001, Seismic data analysis: processing, inversion and interpretation of seismic data: Vol 2. Society of Exploration Geophysicists, 1528-1530.

Zhou, B., Greenhalgh, S.A. and Sinadinovski, C., 1992a, Iterative algorithm for the damping minimum norm, least squares and constrained problem in seismic tomography: *Exploration Geophysics*, **23**, 497-505.

Zhou, B., Sinadinovski, C. and Greenhalgh, S.A., 1992b, Non-linear inversion travel-time tomography: imaging high-contrast inhomogeneities: *Exploration Geophysics*, **23**, 459-464.

**APPENDIX A: ROCK PROPERTY VALUES****A.1. Photographs of Rock Samples**

**Figure A.1: The three cores taken from the Maax Na pyramid before any modifications (left) and after being cut (right).**

## A.2. Tables of Measurements for Dry and Saturated Maax Na Samples

<b>Sample 1</b>	Side1	Side 2	Side 3
Middle	43.66	42.57	67.59
Left	42.82	40.88	
Right	44.23	43.18	
<b>Sample 2</b>			
Middle	40.31	47.54	51.62
<b>Sample 3</b>			
Middle	20.73	52.47	58.56

**Table A.1: The distances (mm) measured for all sides and samples.**

<b>Sample 1</b>	<i>Location</i>	<i>Time 1</i>	<i>Time 2</i>	<i>Time 3</i>	<i>Time 4</i>	<i>Time 5</i>	<i>Average</i>
<i>Side 1</i>	Middle	11.44	10.96	11.16	11.08	11.04	11.14
	Left	10.68	10.84	10.64	10.84	10.80	10.76
	Right	10.52	10.68	10.56	10.76	11.04	10.71
<i>Side 2</i>	Middle	10.88	10.88	10.80	10.92	10.92	10.88
	Left	10.60	10.28	10.56	10.44	10.64	10.50
	Right	10.88	10.60	10.44	10.80	10.76	10.70
<i>Side 3</i>	Middle	18.30	18.20	18.10	18.40	18.10	18.22
<b>Sample 2</b>							
<i>Side 1</i>	Middle	13.12	13.24	13.12	13.00	13.16	13.13
<i>Side 2</i>	Middle	14.10	13.88	14.40	15.20	15.32	14.58
<i>Side 3</i>	Middle	16.44	16.52	16.08	16.50	16.40	16.39
<b>Sample 3</b>							
<i>Side 1</i>	Middle	15.00	14.96	14.88	14.68	15.04	14.91
<i>Side 2</i>	Middle	29.30	30.50	30.40	30.00	30.20	30.08
<i>Side 3</i>	Middle	33.00	33.20	33.00	33.30	33.30	33.16

**Table A.2: Traveltimes ( $\mu$ s) of ultrasonic pulse through the dry rock samples using 1 MHz P-wave transducers.**

<b>Sample 1</b>	<i>Location</i>	<i>Time 1</i>	<i>Time 2</i>	<i>Time 3</i>	<i>Time 4</i>	<i>Time 5</i>	<i>Average</i>
<i>Side 1</i>	Middle	19.40	19.60	19.30	19.80	19.80	19.58
	Left	18.60	18.60	18.30	18.70	18.40	18.52
	Right	18.40	18.80	18.30	18.20	18.40	18.42
<i>Side 2</i>	Middle	19.40	18.90	19.00	18.80	18.90	19.00
	Left	18.00	17.80	18.00	17.60	17.80	17.84
	Right	17.80	17.90	18.40	18.00	18.00	18.02
<i>Side 3</i>	Middle	30.90	31.10	31.20	30.80	30.80	30.96
<b>Sample 2</b>							
<i>Side 1</i>	Middle	24.50	24.00	24.00	24.50	24.50	24.30
<i>Side 2</i>	Middle	26.00	26.70	25.80	26.30	26.30	26.22
<i>Side 3</i>	Middle	27.80	28.70	28.30	29.30	30.00	28.82
<b>Sample 3</b>							
<i>Side 1</i>	Middle	31.80	31.60	31.40	31.90	32.00	31.74
<i>Side 2</i>	Middle	56.00	55.60	55.00	56.20	55.20	55.60
<i>Side 3</i>	Middle	61.00	61.60	61.20	61.00	61.40	61.24

**Table A.3: Traveltimes ( $\mu\text{s}$ ) of ultrasonic pulse through the dry rock samples using 1 MHz S-wave transducers.**

<b>Sample 1</b>	<i>Time 1</i>	<i>Time 2</i>	<i>Time 3</i>	<i>Time 4</i>	<i>Time 5</i>	<i>Average</i>
<i>Side 1</i>	12.6	12.00	12.40	12.20	12.40	12.32
<i>Side 2</i>	11.8	11.60	11.80	11.80	12.40	11.88
<i>Side 3</i>	22.4	22.40	21.60	22.80	22.60	22.36
<b>Sample 2</b>						
<i>Side 1</i>	16.6	16.90	17.10	16.90	16.70	16.84
<i>Side 2</i>	18.2	18.90	19.10	19.20	18.90	18.86
<i>Side 3</i>	19.6	19.20	20.20	19.70	19.60	19.66
<b>Sample 3</b>						
<i>Side 1</i>	18.4	18.60	18.40	18.50	18.50	18.48
<i>Side 2</i>	32.8	33.40	33.40	34.20	33.60	33.48
<i>Side 3</i>	35.2	36.00	36.40	36.00	36.80	36.08

**Table A.4: Traveltimes ( $\mu\text{s}$ ) of ultrasonic pulse through the rock samples using 100 kHz P-wave transducers.**

<b>Sample 1</b>	Side1	Side 2	Side 3
Middle	377	329	687
<b>Sample 2</b>			
Middle	677	740	524
<b>Sample 3</b>			
Middle	268	177	143

**Table A.5: The differences (m/s) between the velocities found with the 1 MHz transducers and the 100 kHz transducers.**

<b>Sample 1</b>	Side1	Side 2	Side 3
Middle	1.76	1.75	1.70
Left	1.72	1.70	
Right	1.72	1.68	
<b>Sample 2</b>			
Middle	1.85	1.80	1.76
<b>Sample 3</b>			
Middle	2.13	1.85	1.85

**Table A.6: The Vp/Vs measurements for all samples using the measurements from the 1 MHz transducers.**

		Side 1	Side 2	Side 3
<b>Vp 1 MHz</b>	<b>Sample 1</b>	2.45	2.45	2.42
	<b>Sample 2</b>	2.31	2.34	2.32
	<b>Sample 3</b>	1.89	2.00	2.01
<b>Vp 100 kHz</b>	<b>Sample 1</b>	2.39	2.17	1.79
	<b>Sample 2</b>	2.40	2.20	1.95
	<b>Sample 3</b>	2.30	2.22	1.97
<b>VS 1 MHz</b>	<b>Sample 1</b>	1.80	1.67	1.32
	<b>Sample 2</b>	1.80	1.71	1.45
	<b>Sample 3</b>	1.79	1.70	1.45

**Table A.7: The Gardner derived densities ( $\text{g/cm}^3$ ) of the dry rock samples using Vp and Vs from the 1 MHz and 100 kHz transducers. A coefficient of 1.47 was used for the Vs calculation.**

Sample 1	Location	Time 1	Time 2	Time 3	Time 4	Time 5	Average
Side 1	Middle	12.76	12.88	13.08	13.04	13.06	12.96
	Left	12.64	12.68	12.72	12.76	12.74	12.71
	Right	12.24	12.14	12.22	12.16	11.92	12.14
Side 2	Middle	12.2	12.28	12.5	12.46	12.48	12.38
	Left	12.18	12.04	12.1	12.08	12.14	12.11
	Right	11.7	11.92	11.74	11.8	11.86	11.80
Side 3	Middle	20.64	20.52	20.48	20.52	20.6	20.55
<b>Sample 2</b>							
Side 1	Middle	13.66	13.54	13.66	13.52	13.58	13.59
Side 2	Middle	15.64	15.56	15.46	15.44	15.52	15.52
Side 3	Middle	16.64	16.62	16.52	16.68	16.64	16.62
<b>Sample 3</b>							
Side 1	Middle						N/A
Side 2	Middle						N/A
Side 3	Middle	33.36	33.35	33.37	33.3	33.42	33.36

**Table A.8: Traveltimes ( $\mu\text{s}$ ) of ultrasonic pulse through the water saturated rock samples using 1 MHz P-wave transducers.**

Sample 1	Location	Time 1	Time 2	Time 3	Time 4	Time 5	Average
Side 1	Middle	23.80	24.00	22.00	23.40	23.20	23.28
	Left	25.80	26.00	26.00	26.80	26.20	26.16
	Right	23.40	23.20	23.80	23.20	23.80	23.48
Side 2	Middle	24.00	24.20	24.40	24.20	23.80	24.12
	Left	26.20	25.00	25.20	24.60	24.00	25.00
	Right	23.40	23.60	23.80	23.80	23.00	23.52
Side 3	Middle	40.20	40.80	40.60	40.40	41.20	40.64

**Table A.9: Traveltimes ( $\mu\text{s}$ ) of ultrasonic pulse through the water saturated rock samples using 1 MHz S-wave transducers.**

Sample 1	P-wave			S-wave		
	Side1	Side 2	Side 3	Side1	Side 2	Side 3
Middle	3368	3438	3289	1875	1765	1663
Left	3370	3376		1637	1635	
Right	3645	3658		1884	1836	
<b>Sample 2</b>						
Middle	2966	3063	3106			
<b>Sample 3</b>						
Side 3			1755			

**Table A.10: The P and S-wave velocities (m/s) of the water saturated rock samples found using the 1 MHz transducers.**

Sample 1	Side1	Side 2	Side 3
Middle	1.80	1.95	1.98
Left	2.06	2.06	
Right	1.93	1.99	

**Table A.11:** The Vp/Vs measurements for water saturated sample one using the 1 MHz transducers.

		Side 1	Side 2	Side 3
<b>Vp 1Mhz</b>	Core 1	2.36	2.37	2.35
	Core 2	2.29	2.31	2.31
	Core 3			2.01
<b>Vs 1Mhz</b>	Core 1	2.26	2.22	2.19

**Table A.12:** The Gardner derived densities ( $\text{g/cm}^3$ ) of the water saturated rock samples using Vp and Vs from the 1 MHz transducers. A coefficient of 1.93 was used for the Vs calculation.

		<b>Core 1</b>		
		Side 1	Side 2	Side 3
<b>Dry Limestone</b>	Vp	0.23	0.23	0.25
	Vs	0.20	0.20	0.21
<b>Dry Dolomite</b>	Vp	0.29	0.29	0.31
	Vs	0.29	0.28	0.30
<b>Density</b>		0.22	0.22	0.22
<b>Wet Limestone</b>	Vp	0.22	0.21	0.23
	Vs	0.20	0.22	0.24
		<b>Core 2</b>		
		Side 1	Side 2	Side 3
<b>Dry Limestone</b>	Vp	0.32	0.30	0.31
	Vs	0.31	0.28	0.29
<b>Dry Dolomite</b>	Vp	0.38	0.36	0.37
	Vs	0.40	0.37	0.37
<b>Density</b>		0.40	0.40	0.40
<b>Wet Limestone</b>	Vp	0.26	0.25	0.25
	Vs			
		<b>Core 3</b>		
		Side 1	Side 2	Side 3
<b>Dry Limestone</b>	Vp	0.63	0.63	0.63
	Vs	0.52	0.46	0.46
<b>Dry Dolomite</b>	Vp	0.55	0.51	0.51
	Vs	0.59	0.53	0.53
<b>Density</b>		0.54	0.54	0.54
<b>Wet Limestone</b>	Vp			0.40
	Vs			

**Table A.13:** The estimated porosity using the dry limestone and dolomite relations of Batzle (2006), the wet limestone relations of Assefa (2003) and the density relations.

## APPENDIX B: INVERSION TECHNIQUES

### B.1. Traveltime Picking

The first step in performing traveltimes tomography is making the traveltimes picks from the raw shot gathers. The first positive zero crossing was chosen as the location of the traveltimes pick (Figure B.1). Initially an automated program (VISTA) was used to make the picks. These automatic picks were then hand corrected to ensure the quality of each individual pick. Most of the first breaks appeared clearly and in areas of little noise. This increases the accuracy of the picks. If the first break pick was difficult to distinguish an AGC was applied to the shot gather to help distinguish the first breaks.

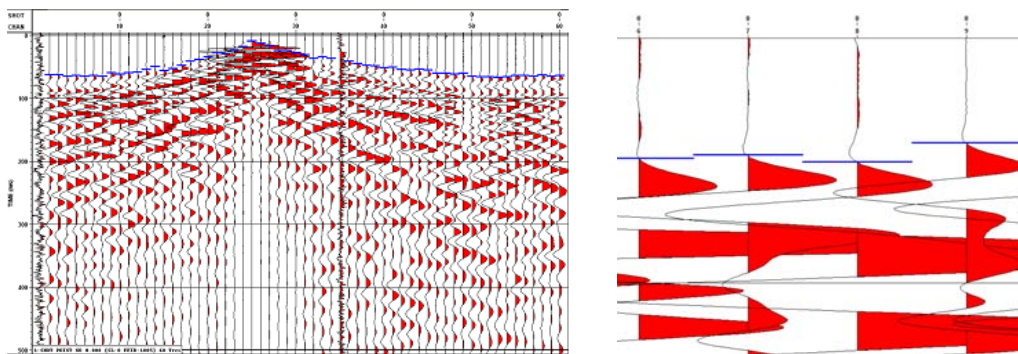


**Figure B.1:** A shot gather with 500ms AGC (left) and a zoomed in portion of the shot gather with traveltimes picks in blue

### B.2. Amplitude Picking

To pick the amplitudes from the shot gathers a similar technique to traveltimes picking was used. Instead of the first positive zero crossing the peak positive amplitude of the first break was chosen (Figure B.2). The picks were again initially found using an automated program and then corrected by hand. Most of the picks appeared quite clearly and were easily distinguished. In the case of two combined peaks a determination was made based on the shape of the peak.

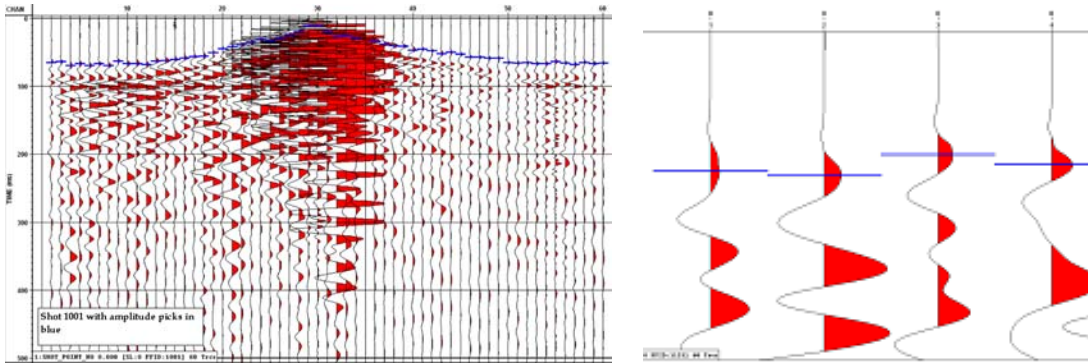


**Figure B.2: A shot gather (left) and a zoomed in portion of the shot gather with amplitude picks in blue**

### **B.3. Straight Ray Techniques**

#### ***B.3.1. Direct Division (DD)***

To find the velocity structure inside the temple an inversion technique must be used. In this case a series expansion method was chosen. This method involves dividing the area of interest, in this case the pyramid, into pixels. From here we can use ray tracing through the pixels to find a sum of the pixel values (Stewart, 1991). The pixels can be defined to have a length  $l$  and a height  $h$ . The distance that the ray travels through a pixel can be given by  $d$  where  $D$  gives the total length of the ray (Figure B.3). Finally the slowness was set equal to  $p$ .

Since the travel times of the rays are known we want a formula that incorporates both the travel time, which we know, and the velocity or slowness, which we want to find out. The travel time of a ray traveling through a single pixel is given by

$$t = dp . \tag{B.1}$$

Using the equation for the travel time through a single pixel we can find the equation for travel time through all the pixels. This can be expressed for the first given ray as,

$$t^i = d_1^i p_1 + d_2^i p_2 + d_3^i p_3 + \dots + d_M^i p_M, \quad (\text{B.2})$$

$$= \sum_{j=i}^M d_j^i p_j,$$

where  $M$  is the number of pixels in the object,  $j$  is the pixel number, and  $i$  is the ray number (Stewart, 1991).

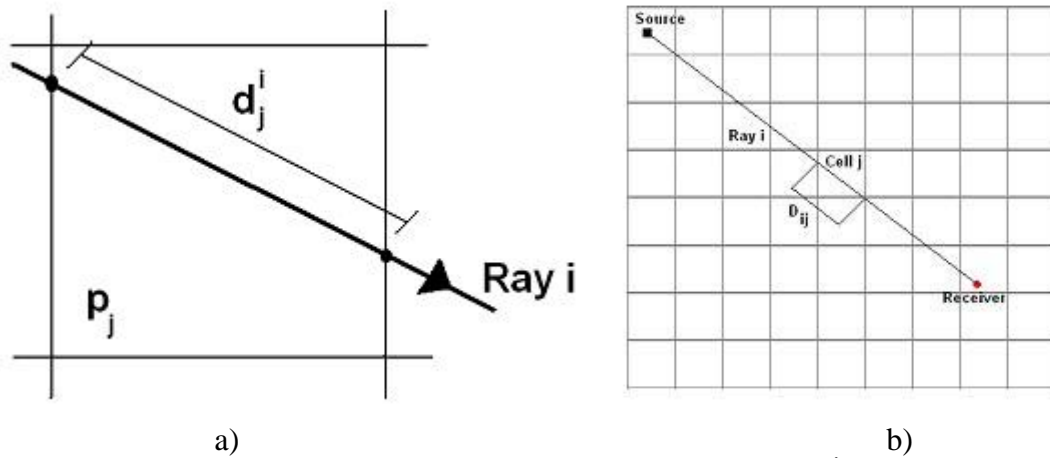


**Figure B.3:** A ray propagating through a) a single pixel where  $d_j^i$  is the distance that ray  $i$  travels in pixel  $j$  and  $p_j$  is the slowness of pixel  $j$  and the traveltime is given by  $t=dp$ , (Stewart, 1991) and b) a series of pixels where the travel time is given by

$$t_i = \sum_{j=i}^M d_j^i p_j \quad (\text{reproduced from Lines and Newrick, 2004}).$$

Finally, the equation for any given ray is expressed as,

$$t_i = \sum_{j=i}^M d_j^i p_j. \quad (\text{B.3})$$

Each shot receiver pair makes up one equation giving a system of linear equations. Expressing this equation in matrix form,

$$T = AP \quad (\text{B.4})$$

where  $\mathbf{T}$  is the traveltime vector,  $\mathbf{A}$  is the raypath geometry matrix and  $\mathbf{P}$  is the slowness vector.

Using this equation, it is possible to find the traveltimes of the rays given the slowness values and the ray path. However, since we have the traveltimes and are looking for the slowness values we must solve the inverse problem. The exact solution for this inverse problem is given by

$$P = A^{-1}T. \quad (\text{B.5})$$

To solve for the slowness using matrix values Equation B.5 was modified to the direct division equation given by

$$P = \frac{T}{A^T}. \quad (\text{B.6})$$

This solution is often seen as being inadequate in the presence of noise, redundant or insufficient observations (Stewart, 1991). The direct division method is often accused of producing undesirable results in these situations.

### ***B.3.2. Damped Least Squares (DLS)***

In the presence of noise the least squares is seen as an improvement on direct division. The least squares method described by Lines and Treitel (1984) and Yilmaz (2001) can be derived starting with the exact solution to the inversion problem given in Equation B.5. Rearranging this equation using the model slowness values, the modeled traveltimes can be given by

$$T' = AP, \quad (\text{B.7})$$

where  $T'$  is the modeled traveltimes.

Given the expression for both the observed ( $T$ ) and modeled ( $T'$ ) traveltimes an expression for the error between the two can be given by

$$e = T - T', \quad (\text{B.8})$$

substituting Equation B.7 into Equation B.8 the error is given as

$$e = T - AP. \quad (\text{B.9})$$

To find the best slowness model the cumulative squared error needs to be minimized with respect to the slowness vector. Starting with the squared cumulative error given by

$$S = e^T e, \quad (\text{B.10})$$

the error value shown in Equation B.9 is substituted in to get

$$S = (T - AP)^T (T - AP). \quad (\text{B.11})$$

Expanding the right side of Equation B.11 results in

$$S = (T^T T - P^T A^T T - T^T AP + P^T A^T AP). \quad (\text{B.12})$$

The minimum of  $\mathbf{S}$  with respect to  $\mathbf{P}$  is given when

$$\frac{\partial S}{\partial P} = 0. \quad (\text{B.13})$$

Substitution Equation B.12 into Equation B.13 gives

$$\frac{\partial}{\partial P} (T^T T - P^T A^T T - T^T AP + P^T A^T AP) = 0. \quad (\text{B.14})$$

Solving the differentiation with respect to  $\mathbf{P}$ , we obtain the normal equations

$$A^T AP = A^T T. \quad (\text{B.15})$$

Rearranging for the slowness we get

$$P = (A^T A)^{-1} A^T T. \quad (\text{B.16})$$

This is the least-squares solution. This equation may be too time consuming; often the normal equations are solved instead. The normal equations can be found by simply

multiplying both sides of the original equation given in Equation B.4. If the distance matrix  $\mathbf{A}$  is square and invertible then

$$\left(\mathbf{A}^T \mathbf{A}\right)^{-1} = \mathbf{A}^{-1} \left(\mathbf{A}^T\right)^{-1}. \quad (\text{B.17})$$

Plugging this value back into Equation B.16 the equation reduces to that of Equation B.5 with the error terms cancelling out giving zero error. However, since most cases do not give a square invertible matrix the full least squares solution is used. These solutions may not be adequate in many situations.

Commonly in geophysical inversion problems the  $\mathbf{A}$  matrix is not square and of full rank. This results in many of these problems being over-determined, where the number of data points exceeds the number of model parameters (Lines and Treitel, 1984). To avoid many of the problems with singularities and arrive at a numerically stable technique the damped least-squares or Marquardt-Levenberg method is used.

The damped least squares equation, described by Lines and Treitel (1984), is found by applying the constraint that the sum of the squares of the parameter change vector, in our case  $\mathbf{P}$ , be bounded by a finite quantity  $P_0^2$ . The effect of using this constraint is a smoothing of the parameter change vector.

We want to start with the squared cumulative error as in Equation B.10; however, since the error is now minimized by the constraint that  $P^T P = P_0^2$  we want to minimize a cost function of

$$S(P, \lambda) = e^T e + \lambda (P^T P - P_0^2), \quad (\text{B.18})$$

where  $\lambda$  is a Lagrange multiplier.

Substitution in the values of  $\mathbf{e}^T$  and  $\mathbf{e}$  given in Equations B.8 and B.9 and differentiating with respect to  $\mathbf{P}$ , a modified version of the normal equations is found in equation B.15 resulting in an equation of

$$\left(A^T A + \lambda I\right)P = A^T T. \quad (\text{B.19})$$

Solving for  $\mathbf{P}$  the final damped least squares equation is found to be

$$P = \left(A^T A + \lambda I\right)^{-1} A^T T, \quad (\text{B.20})$$

where  $\lambda$  is the damping factor and  $\mathbf{I}$  in the identity matrix.

To take full advantage of the damped least squares method the damping factor must be carefully considered. The damping factor must be large enough that the solutions are well behaved near singularities but small enough to maintain fast convergence rates.

It can be proven that the inverses of the parameters inside the parenthesis in Equation B.20 exist by looking at the definition of positive definite and semidefinite matrices. A square matrix  $\mathbf{C}$  is positive semidefinite if

$$y^T C y \geq 0; y \neq 0. \quad (\text{B.21})$$

To make the matrix  $\mathbf{C}$  positive definite the  $\geq$  in Equation B.21 is replaced by  $>$ . If  $\mathbf{C}$  is positive definite and  $\lambda > 0$  then its inverse exists.

Pujol (2007) describes three results from these definitions that show that the inverse of the parameters in the parenthesis in Equation B.20 exists. The first result is shown by looking at an arbitrary matrix  $\mathbf{A}$ . Given the matrix  $\mathbf{A}$ ,  $\mathbf{A}^T \mathbf{A}$  must either be positive semidefinite or definite since

$$y^T \left(A^T A\right) y = (Ay)^T Ay = |Ay|^2 \geq 0, y \neq 0. \quad (\text{B.22})$$

From this equation there are two possibilities. If the inverse of  $\mathbf{A}^T\mathbf{A}$  exists its eigenvalues will be greater than zero resulting in  $\mathbf{A}^T\mathbf{A}$  being positive definite. If the inverse does not exist some of the eigenvalues will be zero making  $\mathbf{A}^T\mathbf{A}$  a positive semidefinite matrix.

The second result described by Pujol shows that any diagonal matrix  $\mathbf{D}$  with elements greater than zero must be positive definite. This is shown by

$$y^T D y = \sum_i d_i y_i^2 > 0; \quad y \neq 0, \quad d_i > 0. \quad (\text{B.23})$$

The final result states that given a positive semidefinite matrix  $\mathbf{C}$  and a positive definite matrix  $\mathbf{P}$  then  $\mathbf{C}=\lambda\mathbf{P}$  is positive definite if  $\lambda>0$  shown by

$$y^T (\mathbf{C} + \lambda\mathbf{P})y = y^T \mathbf{C}y + \lambda y^T \mathbf{P}y > 0; \quad y \neq 0, \quad \lambda > 0. \quad (\text{B.24})$$

These three results are important because if  $\mathbf{C}=\mathbf{A}^T\mathbf{A}$  in Equation B.24 it can be seen that the parameters in the parenthesis in Equation B.19 exist as long as  $\lambda>0$ . Finally in this case where the diagonal matrix  $\mathbf{P}$  is the identity matrix  $\mathbf{I}$  the eigenvalues of  $\mathbf{C}+\lambda\mathbf{I}$  are  $\lambda_i+\lambda$  which will always be positive when  $\lambda>0$ . Using these results it was shown that the damped least squares equation is a valid equation and can be solved.

### ***B.3.3. Singular Value Decomposition (SVD)***

The singular value decomposition method was developed as a way to solve a rectangular system as opposed to the square system derived in the least squares method (Lines and Treitel, 1984). The benefit of singular value decomposition is that it provides a precise way of analyzing a matrix, which results in a stable and approximate inverse. For any general matrix of order  $m \times n$  that maps the model space to the data space there is matrix decomposition (Mahmoudian, 2006). The SVD method involves factoring the  $\mathbf{A}$  matrix into the product of three matrices given by the equation.

$$A = ULV^T, \quad (\text{B.25})$$

where  $\mathbf{U}$  is an  $m \times m$  orthonormal matrix of eigenvectors that span the data space,  $\mathbf{V}$  is an  $n \times n$  orthonormal matrix that spans the model space. The columns of  $\mathbf{U}$  are equivalent to the eigenvectors of  $\mathbf{A}\mathbf{A}^T$  and the columns of  $\mathbf{V}$  are the eigenvectors of  $\mathbf{A}^T\mathbf{A}$  (Michelena, 1993). The singular values of a matrix  $\mathbf{A}$  are the positive square roots of the eigenvalues of the matrix  $\mathbf{A}^T\mathbf{A}$ . The singular values of matrix  $\mathbf{A}$  are the diagonal components of the  $\mathbf{L}$  matrix arranged in descending order.

Instead of solving for the full decomposition Menke (1989) showed that it was possible to use a reduced SVD where

$$A = ULV^T = U_p L_p V_p^T. \quad (\text{B.26})$$

The matrices  $\mathbf{U}_p$  and  $\mathbf{V}_p$  consist of the first  $p$  columns of  $\mathbf{U}$  and  $\mathbf{V}$  related to the non-zero singular values in the  $\mathbf{L}$  matrix (Mahmoudian, 2006). The  $\mathbf{L}$  matrix is a  $p \times p$  matrix with all the nonzero singular values from the matrix  $\mathbf{A}$ .

Having decomposed the matrix  $\mathbf{A}$  the next step is to substitute Equation B.26 back into our initial Equation B.4 resulting in the expression

$$U_p L_p V_p^T P = T. \quad (\text{B.27})$$

Multiplying both sides by  $\mathbf{U}_p^T$  to obtain

$$L_p V_p^T P = U_p^T T. \quad (\text{B.28})$$

Rearranging Equation B.28 for the matrix  $\mathbf{P}$  the singular value decomposition formula for the slowness is given as

$$P = V_p L_p^{-1} U_p^T T. \quad (\text{B.29})$$

Using Equation B.28 and following the method of Lines and Treitel (1984) the equation is recast into terms of its individual non-null singular values ( $l_i$ ) and its eigenvectors  $u_i$  and  $v_i$ . The resulting form of the vector inner product relations is given by

$$l_i v_i^T P = u_i^T T \text{ for } i=1,2,\dots, n. \quad (\text{B.30})$$

The inner product of  $v_i^T P$  is the magnitude of the projection of the parameter change vector  $\mathbf{P}$  onto the  $i^{\text{th}}$  eigenvector  $v_i$  where the inner product of  $u_i^T T$  is the magnitude of the discrepancy vector  $\mathbf{T}$  onto the  $i^{\text{th}}$  eigenvector of  $u_i$  (Lines and Treitel, 1984). These two inner products are connected by the  $i^{\text{th}}$  singular value  $l_i$ . Therefore, from this equation we see that if  $u_i^T T$  is small, the eigenvector of  $u_i$  will contribute little to the final solution. Another problem can be seen by rearranging Equation B.30 so that

$$P = \frac{1}{l_i} v_i u_i^T T. \quad (\text{B.31})$$

From this equation it can be seen that if  $l_i$  were small the corresponding term of

$\frac{1}{l_i} v_i u_i^T T$  would be very large resulting in the  $v_i u_i^T T$  term contributing a large amount to

the solution  $\mathbf{P}$ . To counteract these issues the damping factor was once again used.

To determine how the damping factor can be included into the SVD equations we think back to the expression for damped least squares (Equation B.20), which was proven to be a valid equation containing the damping factor. We now want to modify this equation to fit the SVD method. The first step as described by Lines and Treitel (1984) is to rewrite the  $\mathbf{A}^T \mathbf{A}$  term into terms of  $\mathbf{U}$ ,  $\mathbf{L}$  and  $\mathbf{V}$  using Equation B.25:

$$\mathbf{A}^T \mathbf{A} = \mathbf{V} \mathbf{L}^2 \mathbf{V}^T. \quad (\text{B.32})$$

Substitution this result  $(A^T A + \lambda I)$  becomes

$$\begin{aligned} (A^T A + \lambda I) &= VL^2V^T + \lambda I \\ &= V(L^2 + \lambda I)V^T. \end{aligned} \quad (\text{B.33})$$

Taking the inverse

$$\begin{aligned} (A^T A + \lambda I)^{-1} &= V(L^2 + \lambda I)^{-1}V^T \\ &= V \operatorname{diag}\left(\frac{1}{l_j^2 + \lambda}\right)V^T. \end{aligned} \quad (\text{B.34})$$

Plugging Equations B.34 and B.25 back in to Equation B.20 the equation becomes

$$\begin{aligned} P &= V \operatorname{diag}\left(\frac{1}{l_j^2 + \lambda}\right)V^T VLU^T T \\ &= V \operatorname{diag}\left(\frac{l_j}{l_j^2 + \lambda}\right)U^T T. \end{aligned} \quad (\text{B.35})$$

Comparing Equation B.35 with the undamped SVD equation given in Equation B.31 it

can be seen that to apply the damping factor to SVD the diagonal elements in  $\mathbf{L}$  must

replace  $\frac{1}{l_j}$  with  $\frac{l_j}{l_j^2 + \lambda}$ . As a result of the addition of the damping factor even when  $l_j$

approaches zero, division by zero will not occur.

The SVD method has an advantage over that of direct division and DLS. Through SVD a model and data resolution matrix can be found which defines how well the estimated solution matches the true solution. The model resolution matrix is found using the generalized inverse matrix of  $\mathbf{A}$  (Mahmoudian, 2006). Recalling the SVD of matrix  $\mathbf{A}$  shown in equation B.25 the generalized inverse matrix is equal to

$$A_g^{-1} = V_p L_p^{-1} U_p^T. \quad (\text{B.36})$$

Combining Equation B.4 and B.5 the solution becomes

$$P = A_g^{-1}T \cong (A_g^{-1}A)P. \quad (\text{B.37})$$

The model resolution matrix is equal to  $\mathbf{A}_g^{-1}\mathbf{A}$ . Looking more closely at this equation and substituting in the SVD of  $\mathbf{A}$  and  $\mathbf{A}^{-1}$  the equation is

$$A_g^{-1}A = V_p L_p^{-1} U_p^T U_p L_p V_p^T. \quad (\text{B.38})$$

The matrices of  $\mathbf{U}_p$  and  $\mathbf{V}_p$  are orthogonal and therefore  $\mathbf{U}^T\mathbf{U}=\mathbf{V}^T\mathbf{V}=\mathbf{I}$ . However, when  $\mathbf{U}_p$  and  $\mathbf{V}_p$  are no longer complete  $\mathbf{U}_p\mathbf{U}_p^T$  and  $\mathbf{V}_p\mathbf{V}_p^T$  do not equal  $\mathbf{I}$ . Therefore, when analysing Equation B.38 it can be reduced down to the final model resolution equation of

$$R_m = A_g^{-1}A = V_p V_p^T. \quad (\text{B.39})$$

If the resolution were perfect the resolution matrix would be the identity matrix.

The diagonal elements of the resolution matrix provide good measures of the model resolution. The model resolution matrix separates the parameters into two groups, the group that contributes to the data (non-zero eigenvalues) and the groups that do not contribute (zero eigenvalues). This corresponds to the grids that have raypaths crossing them and those without respectively (Xu and Stewart, 2000).

The data space resolution matrix can be found in a similar way (Xu and Stewart, 2000). Once again starting with Equation B.4 then substituting in to Equation B.5 for the matrix  $\mathbf{P}$  resulting in the equation

$$T = (AA_g^{-1})T. \quad (\text{B.40})$$

The data resolution matrix is given by  $\mathbf{A}\mathbf{A}_g^{-1}$ . Substituting in for  $\mathbf{A}$  and  $\mathbf{A}_g^{-1}$  and reducing in the same manner as the model resolution matrix, the final data resolution matrix is given by

$$R_d = A_g^{-1} A = U_p U_p^T. \quad (\text{B.41})$$

The data resolution matrix determines the difference between the observed and predicted data.

#### ***B.3.4. Conjugate Gradient (CG)***

The conjugate gradient method is different from the other methods we have looked at so far. The previous methods (DD, DLS and SVD) are all direct methods of finding the solution whereas the conjugate gradient method is an iterative method. The difference with an iterative method is that instead of finding the answer in a single calculation, iterative methods come to multiple answers that lead closer and closer to the actual solution.

The conjugate gradient method starts with the least squares solution starting with the normal equations described as

$$A^T A P = A^T T. \quad (\text{B.42})$$

Following the method described in Yilmaz (2001)  $\mathbf{D}$  is defined by

$$D = A^T A, \quad (\text{B.43})$$

and  $\mathbf{B}$  is defined as

$$B = A^T T, \quad (\text{B.44})$$

resulting in

$$D P = B. \quad (\text{B.45})$$

To recursively find an estimated value for  $\mathbf{P}$  we start with an initial estimate  $\mathbf{X}_0$ . This initial estimate can be defined as a null vector and is terminated when the residual vector  $\mathbf{R}_i$  defined by

$$R_i = B - DX_i \quad (\text{B.46})$$

becomes a null vector. Where  $\mathbf{X}_i$  is the parameter vector estimate after the  $i^{\text{th}}$  iteration and if the matrix  $\mathbf{D}$  has dimensions  $n \times n$  the conjugate gradient method will yield the solution after  $m < n$  iterations.

The initial values used in the conjugate gradient method are given by

$$c_{-1} = 1, \quad (\text{B.47})$$

$$G_{-1} = 0, \quad (\text{B.48})$$

and

$$R_0 = B - DX_0. \quad (\text{B.49})$$

To start the recursion, first compute the initial residual error  $c_0$  using

$$c_i = R_i^T R_i, i = 0, 1, 2, \dots, m, \quad (\text{B.50})$$

where  $c_i$  is the residual energy after the  $i^{\text{th}}$  iteration. Input the derived value of  $c_0$  and the value of  $c_{-1}$  given in Equation B.47 to the formula

$$b_{i-1} = \frac{c_i}{c_{i-1}}, \quad (\text{B.51})$$

using the derived value of  $b_{-1}$  and the values of  $\mathbf{G}_{-1}$  (Equation B.48) and  $\mathbf{R}_0$  (Equation B.49) in the equation

$$G_i = R_i + b_{i-1}G_{i-1} \quad (\text{B.52})$$

a value of  $\mathbf{G}_0$  can be obtained.

Applying the equations:

$$Q_i = DG_i, m \leq n, \quad (\text{B.53})$$

$$d_i = G_i^T Q_i, \quad (\text{B.54})$$

$$a_i = \frac{c_i}{d_i}, \quad (\text{B.55})$$

and

$$X_{i+1} = X_i + a_i G_i \quad (\text{B.56})$$

a value for the parameter vector estimate  $\mathbf{X}_1$  can be derived. Finally the new residual vector  $\mathbf{R}_1$  is given by

$$R_{i+1} = R_i - a_i Q_i \quad (\text{B.57})$$

Plug the value of  $\mathbf{R}_1$  back into Equation B.50 and repeat the calculations of Equation B.49 through Equation B.57. This could be done for any specified number of iterations where  $m < n$ .

The proposed advantage of the CG method is in large surveys with a large amount of model parameters. The direct methods tend to be very time consuming whereas the conjugate gradient method remains relatively fast in comparison.

## **B.4. Curved Ray Technique**

### ***B.4.1. Shortest Path Calculation***

There are two traditional approaches for curved ray tracing: shooting and bending. The shooting method consists of shooting a fan of rays leaving a single source point and solving by differential equations found by ray theory. The other traditional method is bending. This method is based on Fermat's principle and tries to find the minimum time between two points. However, these two methods have serious drawbacks (Moser, 1991). The shooting method often suffers from convergence problems; it is also unable to find diffracted raypaths or those in shadow zones. The bending method is able to find a

minimum traveltime; however, it is not possible to determine whether the path is an absolute minimum traveltime or a local minimum traveltime.

To avoid these issues the method of shortest path calculation derived by Moser (1991) was used. The shortest path calculation method uses the shortest paths in networks as its starting point. This method is an efficient time saver as it allows for the calculation of the raypaths and traveltimes of the first arrivals for all points simultaneously. The shortest path calculation works by representing the model area by a network of nodes connected to further nodes in its vicinity (Figure B.4). The ray is able to pass from one node to another via these connections. The distance between the nodes is used as a weighted function for the traveltimes. To give reasonable approximations of the raypaths the nodes must be adequately distributed throughout the network. In this case the nodes are distributed along the cell boundaries. In order for the nodes to be connected there cannot be any cell boundary between them. The seismic velocity is sampled at each node and the resulting traveltime is the Euclidian distance multiplied by the average of the two node velocities.

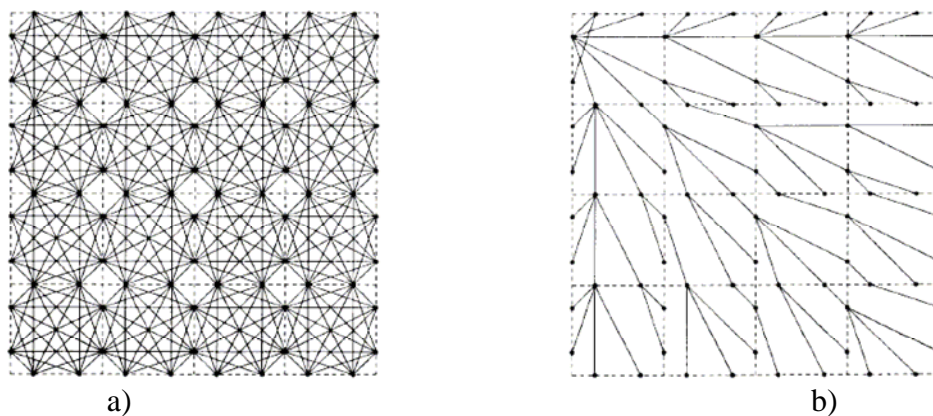


**Figure B.4: Cell organization of a network (a) Dashed lines: cell boundaries. Black circles: nodes. Solid lines: connections. (b) Shortest paths from one node to other nodes in a homogeneous model (Moser, 1991).**

The traveltime of the shortest path from source node  $s$  to node  $i$  is expressed as  $tt(i)$ . The shortest traveltimes from the source node  $s$  can be described by Bellman's (1958) equations given as

$$tt(i) = \min_{j \neq i} [tt(j) + d_{ij}] \quad i, j \in N \quad (\text{B.58})$$

with the initial condition

$$tt(s)=0, \quad (\text{B.59})$$

where  $d_{ij}$  is the matrix representing the weight functions and  $N$  is a set containing  $n$  nodes. The traveltime to node  $i$  is the minimum of the traveltimes from the starting node  $s$  to node  $j$  plus the weight of the connection between node  $i$  and  $j$  (Moser, 1991). When first solving Bellman's equation all initial traveltimes are infinite except for  $tt(s)=0$  allowing us to repeat the non-linear recursion given in Equation B.58 until no traveltime can be updated.

To find the shortest path the nodes must be arranged. The first step in the algorithm described by Moser (1991) is to divide the nodes into a set  $P$  of nodes with known traveltimes and a set  $Q$  of nodes with unknown traveltimes. At the start of the algorithm  $P$  will be empty and  $Q$  will consist of  $n$  nodes. However, the minimum traveltime for node  $s$  is known (Equation B.59) and therefore can be placed in  $P$ . Since the traveltime of  $s$  is known all neighbouring nodes can now be updated according to Equation B.58. The smallest traveltime from these surrounding nodes will not be updated anymore and can therefore be transferred to  $P$ . This step is repeated using all the nodes in  $Q$  connected to the latest value to be placed into  $P$ . Then repeated  $n$  times until the shortest paths from the source point  $s$  to all nodes are found.

When solving this algorithm it was found that searching for the minimum traveltime among the surrounding nodes was the most time consuming step. To help the computational speed a method described by Johnson (1977) was introduced. The first step in picking the minimum traveltime is to get rid of all the times left in Q. Since these values are infinite they can still be updated and must not be the minimum. The remaining values are sorted in a “heap” arranged such that

$$a(i) \leq a(2i), \quad (\text{B.60})$$

and

$$a(i) \leq a(2i + 1) \quad (\text{B.61})$$

for  $i=1, \dots, n/2$ .

The advantage of this method can be seen using the example traveltimes found in Moser 1991, of

$$77, 80, \infty, 75, 89, 97, 90, 93, \infty, 70, 101, 99, 87, \infty, 74, 91.$$

After the infinite values from Q are removed and the values are sorted by equation B.60 and B.61 the traveltimes are in the following order

$$70, 75, 74, 80, 87, 77, 93, 89, 101, 99, 97, 90, 91.$$

When placed in the tree structure of Figure B.5 the advantage of this method is seen.

Looking at each level of the tree the number of elements grows exponentially with the height of the heap. This means that there are only  $\log n$  levels for a total of  $n$  nodes. Also the minimum node can be found quickly as it is on the highest level (Moser, 1991). This results in the total number of operations for the calculation of the shortest path tree is given by

$$\log n + \log(n-1) + \dots + \log 1 + mxn = O(n \log n). \quad (\text{B.62})$$

This results in the computational time being almost linear to that of the number of nodes.

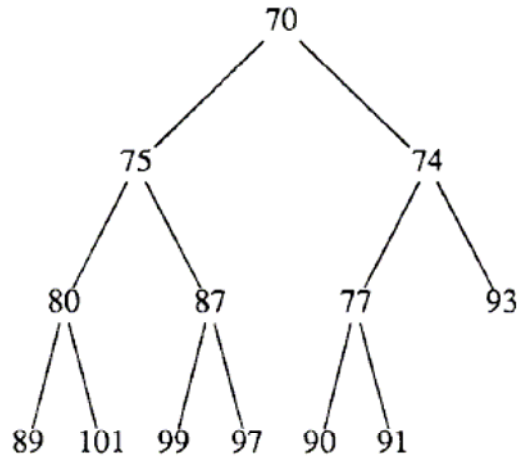


**Figure B.5: The tree structure of a heap (Moser, 1991)**

#### ***B.4.2. Finding the distance (Jacobian) matrix***

Now that the ray tracing technique has been established the next step in the inversion process is to determine the distance each ray passes through the cells.

Following the method of Zhou (1992b) an arbitrary velocity medium that is parameterized by a set of grid points along the cells is established. The velocity

distribution of each cell can be expressed as a first-order surface function expressed as

$$V_c(x, y) = a_0 + a_1x + a_2y + a_3xy \quad (\text{B.63})$$

$$a_{k-1} = \sum_{l=1}^4 (-1)^{k+1} \frac{\Delta_{lk} V_l}{\Delta}; \quad (k = 1, 2, 3, 4) \quad (\text{B.64})$$

where  $V_l$  is the velocity of the  $l^{\text{th}}$  node in a cell;  $\Delta$  and  $\Delta_{lk}$  are the 4<sup>th</sup> order determinant and accompanying determinate respectively. Both of these determinants are dependent on the coordinates of the rectangular cell (Zhou, 1992b). The coefficient  $a_k$  is found through

Equation B.64 as the velocity structure is determined. If the cell is of constant velocity then

$$V_c(x, y) = a_0. \quad (\text{B.65})$$

After differentiating and combining Equations B.63 and B.64 the expression becomes

$$\frac{\partial V_c(x, y)}{\partial V_l} = \sum \left[ \frac{\partial a_0}{\partial V_l} + \frac{\partial a_1}{\partial V_l} x + \frac{\partial a_2}{\partial V_l} y + \frac{\partial a_3}{\partial V_l} xy \right] \quad (\text{B.66})$$

$$\frac{\partial a_{k-1}}{\partial V_l} = (-1)^{k+1} \frac{\Delta_{lk}}{\Delta}; \quad (k, l = 1, 2, 3, 4). \quad (\text{B.67})$$

Plugging the preceding equations for the velocity-traveltime equation the elements of the Jacobian matrix can be found using

$$\frac{\partial(t_j)}{\partial V_l} = \sum \left[ \frac{\partial a_0^{(n_j)}}{\partial V_l} I_0 + \frac{\partial a_1^{(n_j)}}{\partial V_l} I_1 + \frac{\partial a_2^{(n_j)}}{\partial V_l} I_2 + \frac{\partial a_3^{(n_j)}}{\partial V_l} I_3 \right], \quad (\text{B.68})$$

$$\begin{aligned} I_0 &= -\int_{R_n} \frac{ds}{V_c^2(x, y)}; & I_1 &= -\int_{R_n} \frac{x ds}{V_c^2(x, y)}; \\ I_2 &= -\int_{R_n} \frac{y ds}{V_c^2(x, y)}; & I_3 &= -\int_{R_n} \frac{xy ds}{V_c^2(x, y)}; \end{aligned}$$

where  $n$  is the number of the  $n$ th cell,  $ds$  is the segment of the trajectory in a cell,  $n_j$  is the number of the cells passed by the  $j^{\text{th}}$  trajectory,  $R_n$  is a segment of the ray path through the  $n^{\text{th}}$  cell (Zhou, 1992b). The trajectory in a cell can be seen to satisfy the differential equation

$$\frac{d}{ds} \left[ \frac{1}{V_c} \frac{d\bar{x}}{ds} \right] = -\frac{1}{V_c^2} [a_1 + a_3 y, a_2 + a_3 x] \quad (\text{B.69})$$

### ***B.4.3. Iterative Inversion Algorithm***

Now that all the matrices have been established an iterative inversion algorithm has to be developed to update the velocity structure of the model. Many different methods were examined to use in this program. It was decided that a damped minimum norm least squares constrained solution (DMNLS-1) would provide the best result (Zhou, 1992b).

The DMNLS-1 begins with a modified version of the normal equations for the damped least squares problem seen in Equation B.19 where

$$[\lambda C_m + A^T C_d A] Z_p P = A^T C_d T \quad (\text{B.70})$$

where C is a positive matrix operator related to ‘soft’ bounds on the data, m and d refer to the model and data space respectively and  $Z_p P$  is a truncation operator.  $Z_p P$  is defined as

$$Z_m P = \begin{cases} P_i & a_i \leq P_i \leq b_i \\ a_i & P_i < a_i \\ b_i & P_i > b_i \end{cases} \quad (\text{B.71})$$

where a and b are ‘hard’ bounds estimated from conventional seismic velocity analysis (Zhou, 1992). The values of Z, C, a and b are all information that must be determined prior to the inverse taking place. This prior information helps reduce the non-uniqueness of the solution and helps the solution converge on the correct structure.

The DMNLS-1 algorithm incorporates the conjugate gradient method to solve for equation B.70. This algorithm follows the conjugate gradient above with the difference becoming that instead of  $B = A^T T$ , B is now

$$B = A^T C_d T, \quad (\text{B.72})$$

and D becomes

$$D = (\lambda C_m + A^T C_d A). \quad (\text{B.73})$$

For this inversion problem both  $C_m$  and  $C_d$  are diagonal or banded matrices. It can be seen that if  $C_m$ ,  $C_d$ , and  $Z_p = I$  then Equation B.70 reduces back to that of the damped least squares equation seen in Equation B.19.

This algorithm was seen to have four desirable features associated with it (Zhou, 1992a). The first advantage is that consideration was given to both primary estimation of the model and the error of the traveltimes picks. Another advantage is less sensitivity to data error than some of the other popular methods (See Zhou, 1992a). The third advantage was since there is prior information inputted into the algorithm the chance of arriving at the correct solution is greatly increased. Finally the last advantage is this method takes advantage of the sparsity of the matrix to reduce the overall computational time of the matrix.

### B.5. Amplitude Inversion

Amplitude inversion follows the same techniques as the traveltimes inversions. The expression for transmitted amplitudes can be given as

$$A^i = A_0^i e^{-\sum_j d_j^i \alpha_j}, \quad (\text{B.74})$$

where,  $A^i$  is the transmitted amplitude of the  $i^{\text{th}}$  ray,  $A_0^i$  is the initial amplitude of ray  $i$  and  $\alpha_j$  is the attenuation constant of the  $j^{\text{th}}$  pixel (Stewart, 1991). Rearranging equation B.74 to resemble the format of the traveltimes equation (Equation B.3) results in the formula

$$\ln \left[ \frac{A_0^i}{A^i} \right] = \sum_j d_j^i \alpha_j. \quad (\text{B.75})$$

Using this equation instead of Equation B.3 the same inversion techniques can be used.

## APPENDIX C: ADDITIONAL CURVED RAY MODELS

### C.1. Upper 2D Survey

#### C.1.1. Traveltime Tomography

The upper 2D survey was solved using a starting constant velocity model. All the rays were included in the inversion. The most accurate velocity model was found when the derived model was constrained between the velocities 0.001 to 2.0 km/s as seen in Figure C.1.

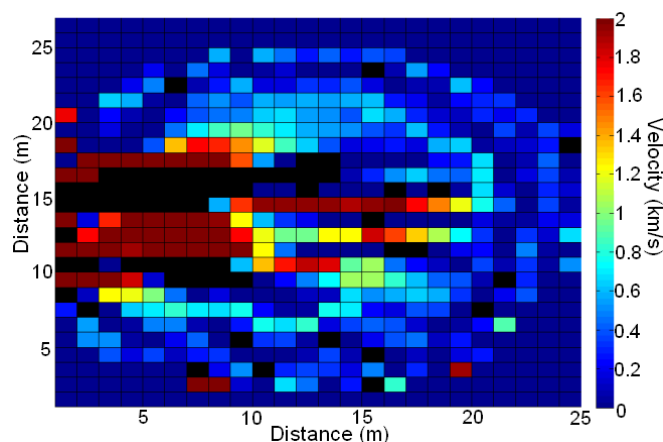


**Figure C.1:** The derived velocity model (km/s) of the upper 2D survey found using a velocity range of 0.001 to 2.0 km/s. Skipped pixels designated in black.

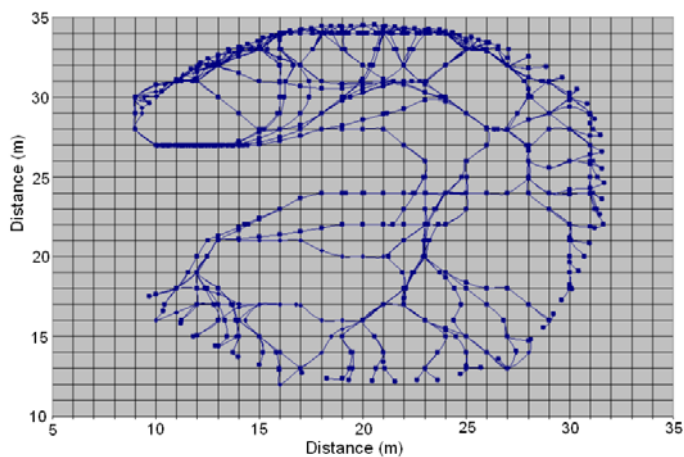


**Figure C.2:** The raypaths for the first 20 sources of the upper 2D survey solved with a curved ray tracer and a velocity range of 0.001 and 2 km/s.

To improve the previous models a starting model, seen in Figure 3.52, was implemented. As with the previous models all rays were included in the inversion. Multiple velocity constraints were attempted starting with the constraints of the previous models (0.001 to 2.0 km/s) and progressing to the most accurate model given with the constraints of 0.1 to 0.8 km/s.

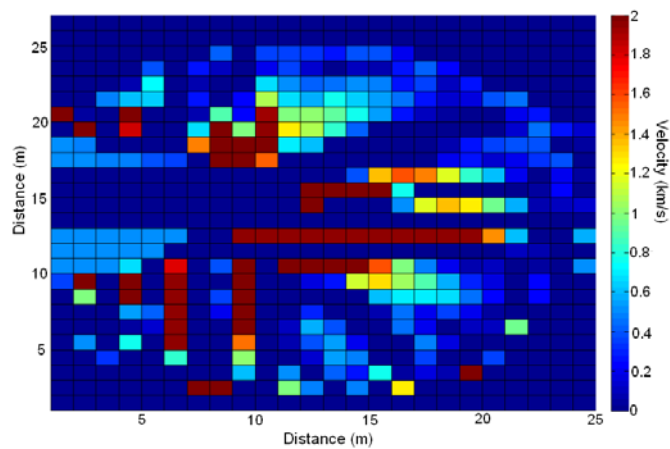


**Figure C.3:** The final velocity model (km/s) of the third iteration found using the trench starting velocity model and velocity constraints of 0.01 to 2 km/s.

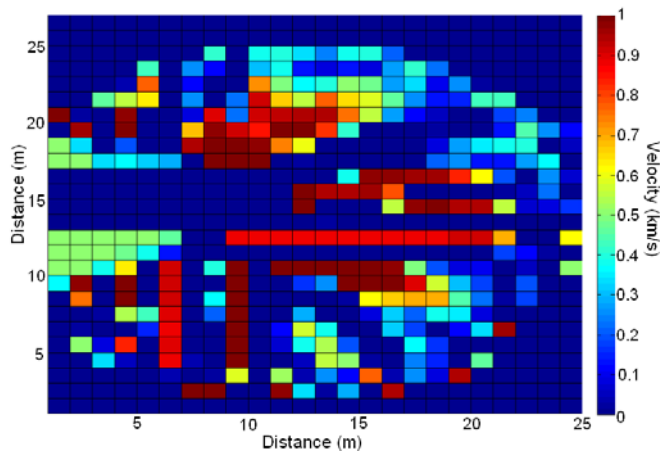


**Figure C.4:** The final velocity model (km/s) of the upper 2D survey using the third iteration found, the trench starting velocity model and velocity constraints of 0.01 to 1 km/s.

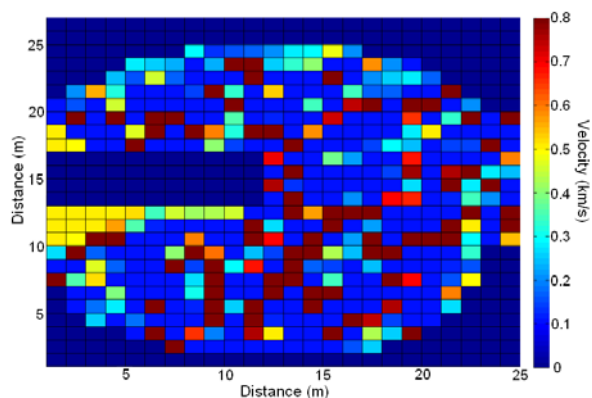


**Figure C.5: The final velocity model (km/s) of the upper 2D survey using the 10th iteration found, the trench starting velocity model and velocity constraints of 0.1 to 0.8 km/s.**

### *C.1.2. Amplitude Inversion*

When solving for the attenuation model all rays were included. The inversion was then solved using a starting constant attenuation model.

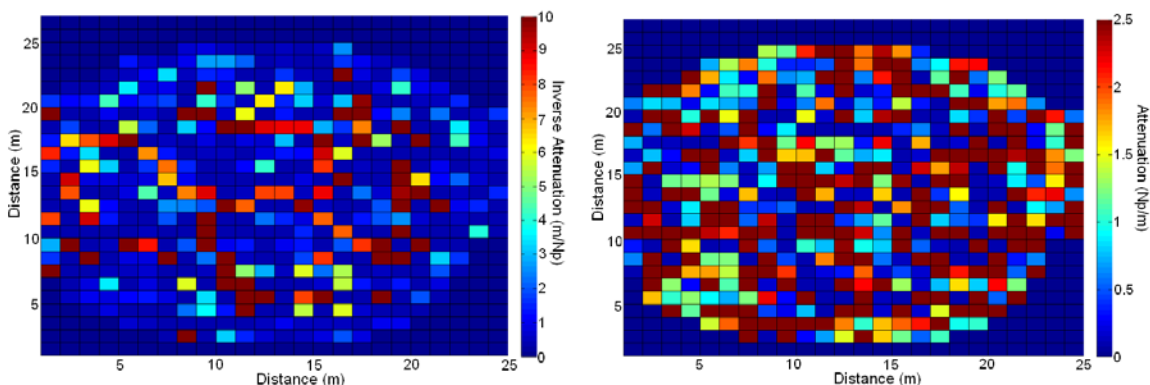


**Figure C.6: The inverse attenuation (left) and attenuation (right) model found using the 74<sup>th</sup> iteration of the 0.4 to 10 m/Np constrained curved ray tomography of the upper 2D survey.**

The same trench-shaped initial model was implemented in the amplitude inversion calculations. The most accurate result was again found using the inverse attenuation constraints of 0.4 to 10 m/Np. The final model is displayed in Figure C.7.

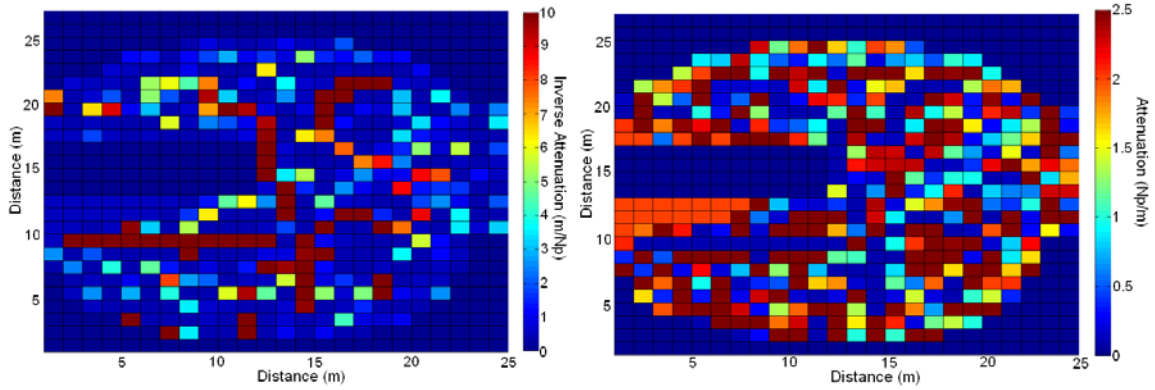


**Figure C.7: The inverse attenuation (left) and attenuation (right) model found using the 69<sup>th</sup> iteration of the 0.4 to 10 m/Np constrained curved ray tomography of the upper 2D survey with the trench starting model.**

### C.2. 3D Models Plotted by Vertical slice

All the 3D surveys discussed in Chapter Three have been graphed and displayed by individual slice to provide a different perspective on the models.

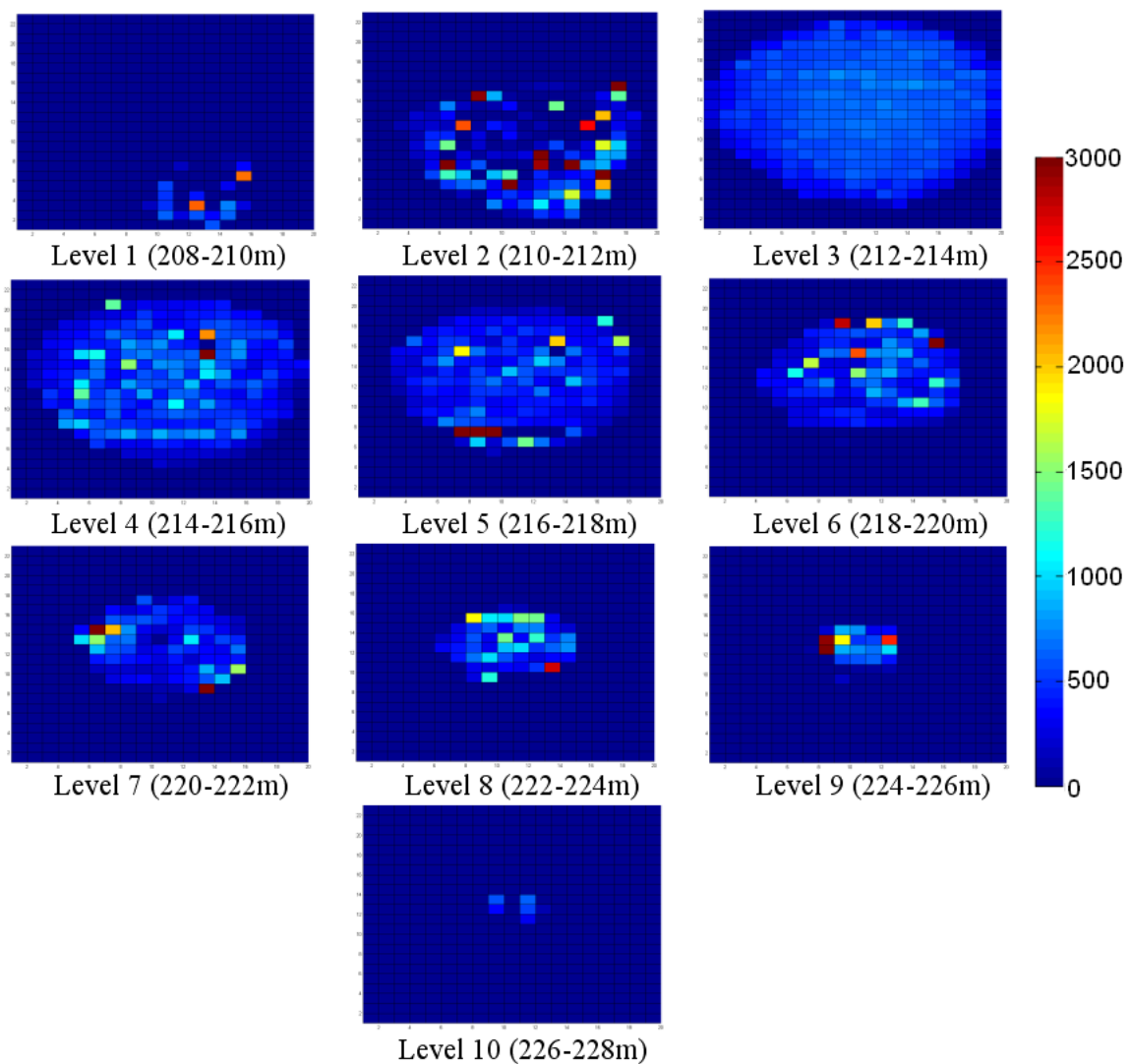


**Figure C.8: The velocity structure (m/s) found using damped least squares for the lower 3D survey. All negative values are set equal to 0 and all values greater than 3000 m/s set equal to 3000 m/s.**

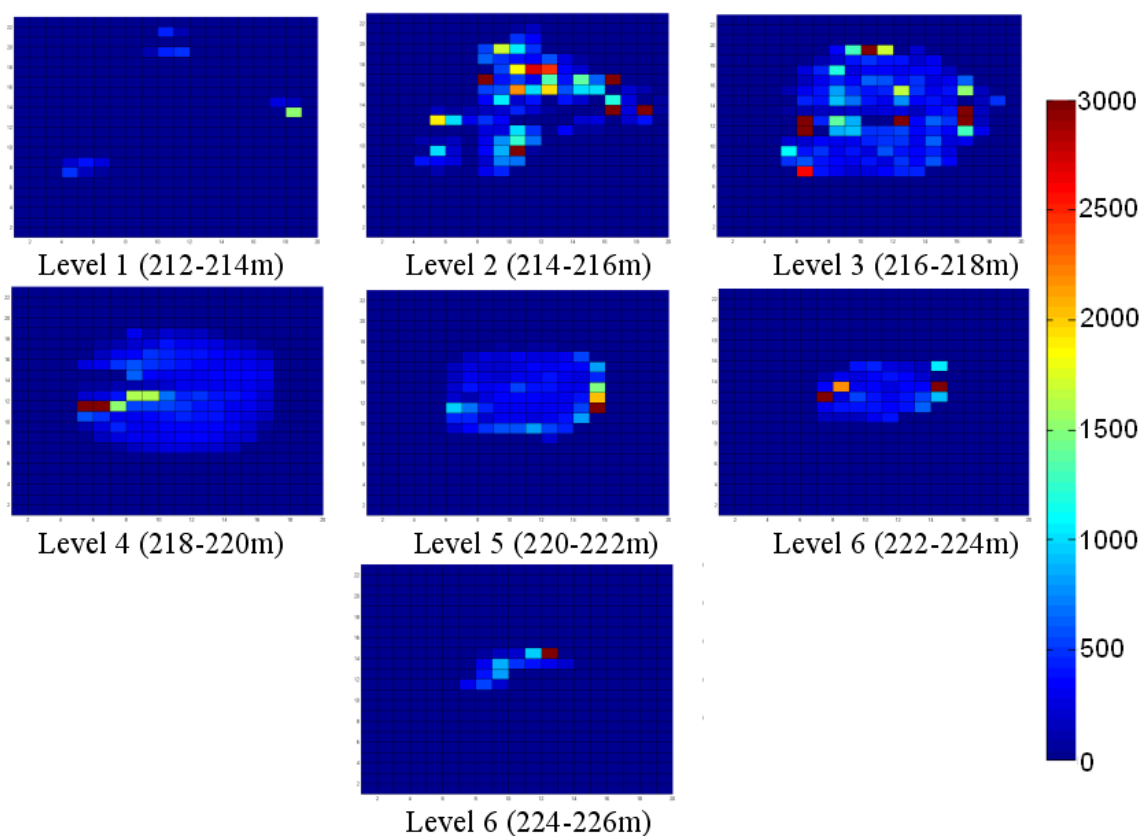


**Figure C.9: The velocity structure (m/s) found using damped least squares for the upper 3D survey. All negative values are set equal to 0 and all values greater than 3000 m/s set equal to 3000 m/s.**

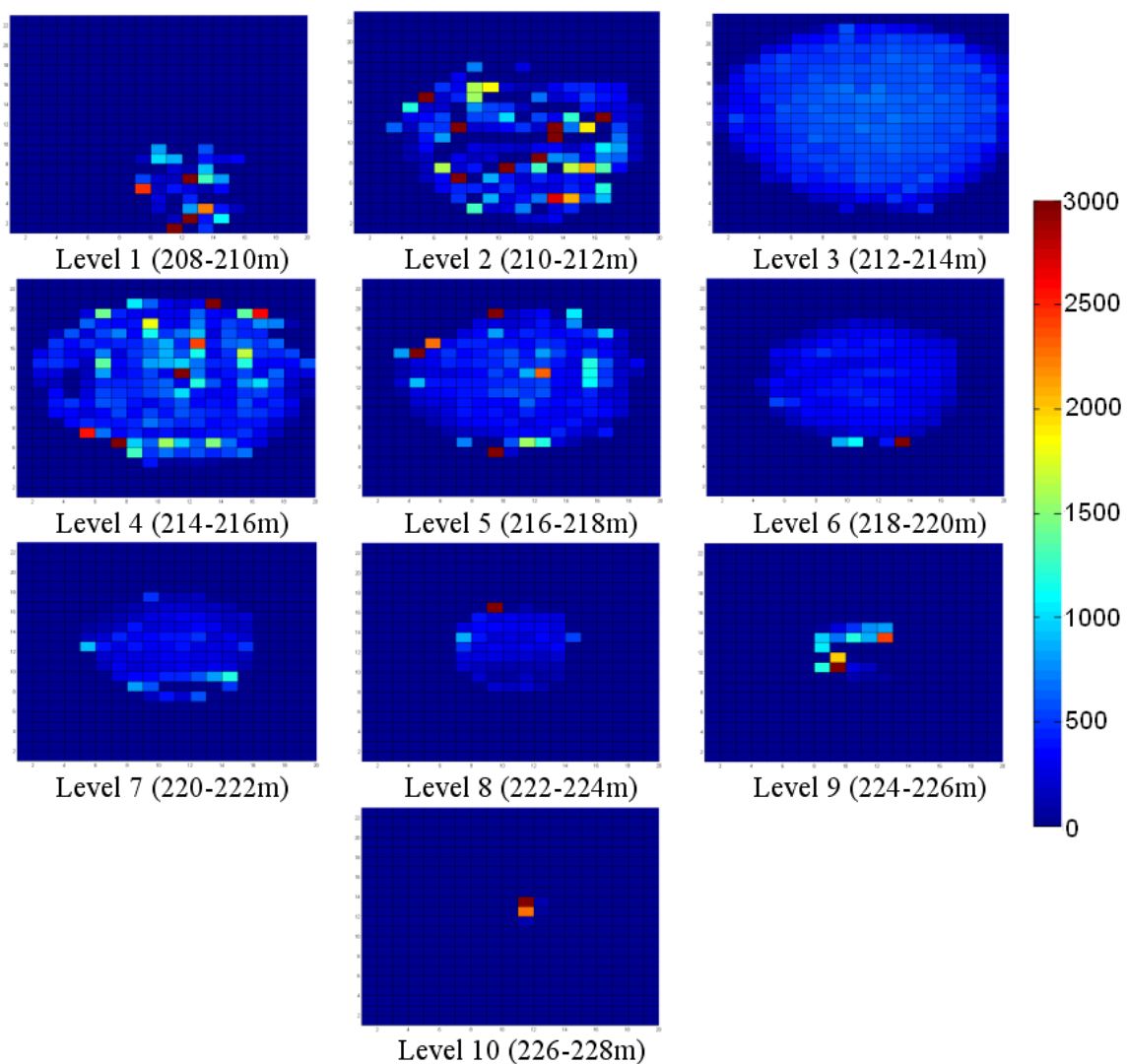


**Figure C.10: The velocity structure (m/s) of the combined 3D survey found using the conjugate gradient method with 250 iterations. All negative values are set equal to 0 and all values greater than 3000 m/s set equal to 3000 m/s.**

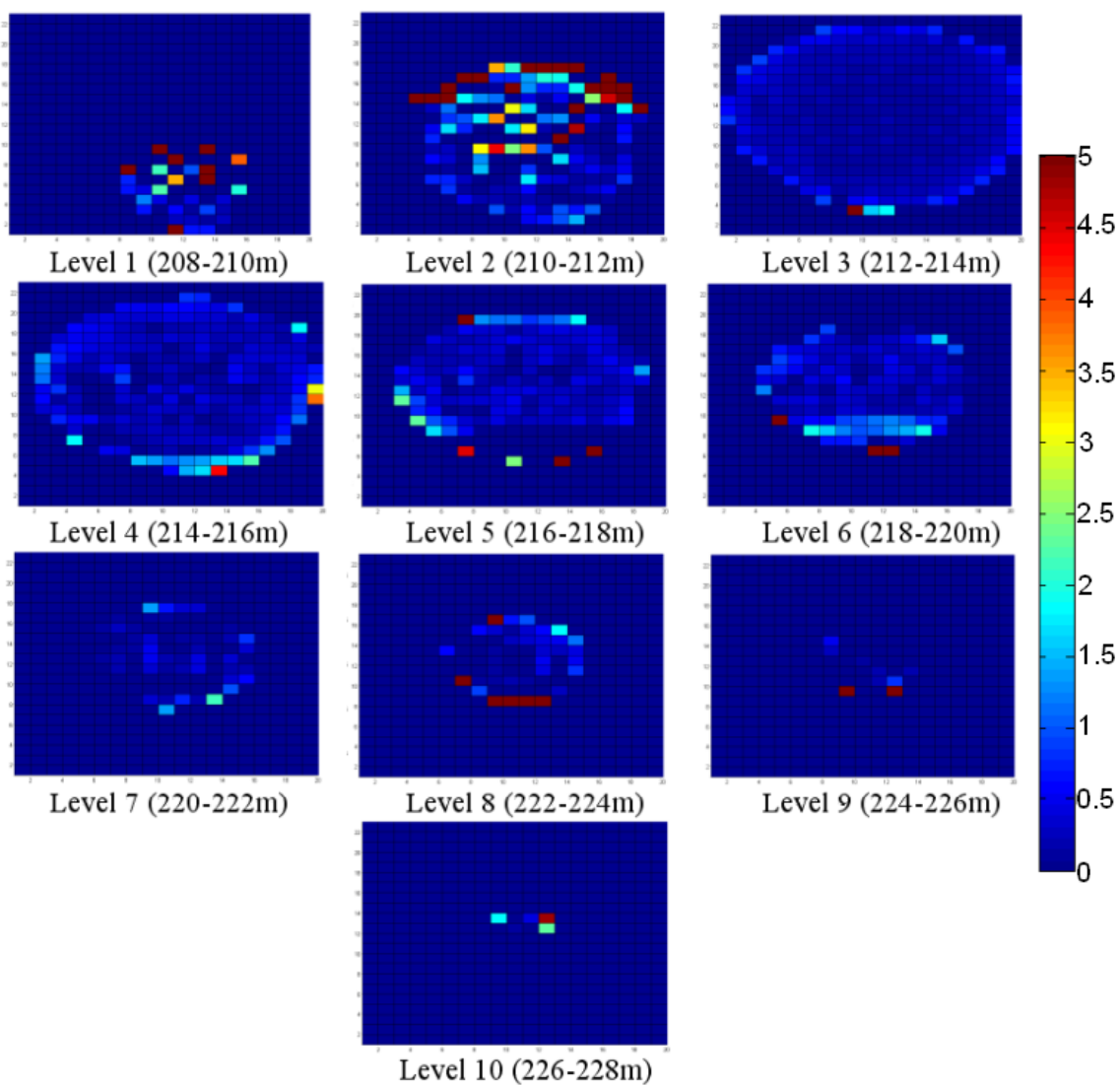


**Figure C.11: The attenuation model (Np/m) of the lower 3D survey found using DLS. All negative values have been set equal to zero and all values greater than 5 have been set equal to 5.**

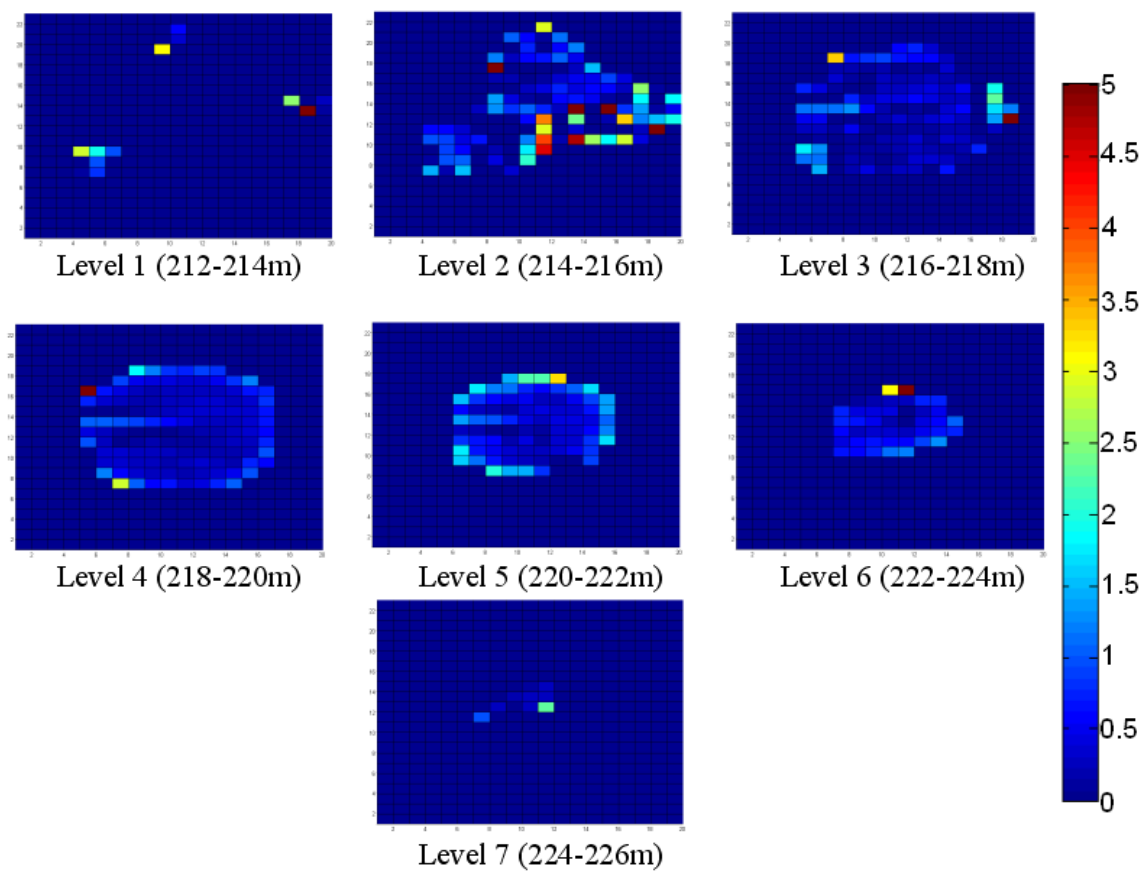


**Figure C.12: The attenuation model (Np/m) of the upper 3D survey found using DLS. All negative values have been set equal to zero and all values greater than 5 have been set equal to 5.**

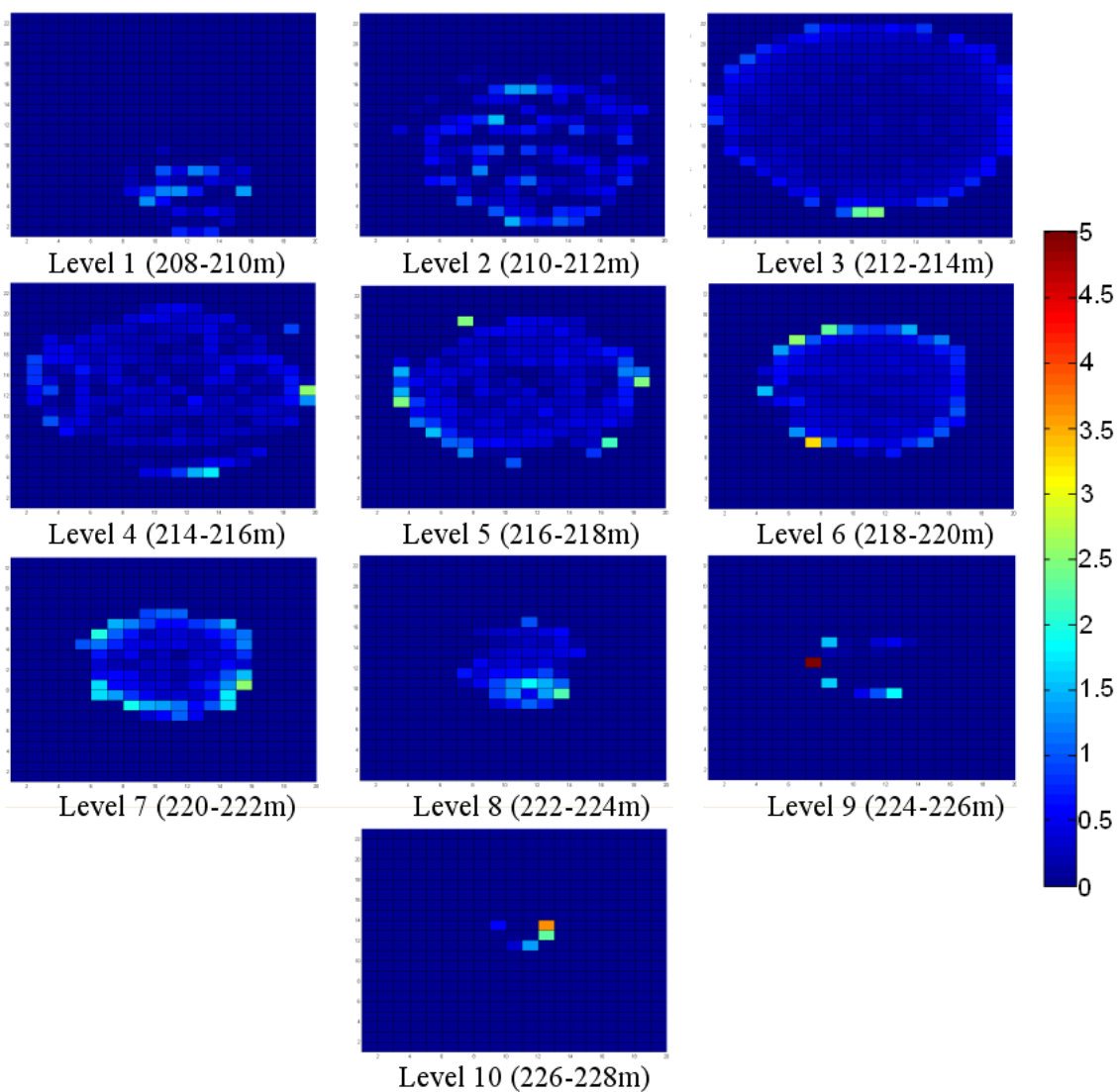


**Figure C.13: The attenuation structure (Np/m) for the combined 3D survey found using CG with 250 iterations. All negative values and values greater than 2.5 have been set to 0 and 2.5 respectively for display purposes.**

## **APPENDIX D: RESOLUTION AND ERROR ANALYSIS**

The efficiency of ray-based tomography is based on four different attributes. These attributes are the angular coverage, data quality, amplitude and dimensional size of the inhomogeneities, and a priori information about the medium and data (Zhou et al, 1992b). Both the 2D seismic surveys consist of nearly 360-degree angular coverage allowing for more efficient tomography. The 3D seismic and GPR surveys contain less coverage making an efficient answer more difficult. The seismic survey appears to produce a strong signal through the pyramid with little noise again lending itself to an accurate inversion. Since the transmitted wave in the GPR survey is not the first break the transmitted wave is subject to a greater amount of noise reducing the data quality. With the use of the FK filter the noise is reduced allowing for better data quality.

Since the amplitude and dimensional size of the inhomogeneities are not initially known this cannot be used as an indication of the efficiency. Since prior seismic tomography was performed on the Maax Na pyramid an expected seismic P-wave velocity range was known before the inversions were performed. While GPR had not been performed on the Maax Na pyramid surveys were performed in the plaza area. Since the plaza is made of similar limestone a GPR velocity range was known prior to tomography.

### **D.1. Error in Traveltime Picks**

There are many different causes of possible error when estimating the first break traveltimes. The first major cause of possible error is the instrument error. It has been suggested that instrument error can be of the order of 1.0 ms. These errors are a result of systematic delays that either cancel out in the interval velocity calculations or can provide

a small shift in the shallow velocities (Stewart, 1984). Another cause of possible error is the sampling rate of the data. In this case the sampling rate was 0.5 ms. This creates a maximum error of 0.25 ms for every pick.

A mathematical expression for the measure of error in the measurement of arrival time of the first motion is given by Stewart (1984) as

$$\Delta t = \frac{1}{f_m \log_2 \left( 1 + \frac{S^2}{N^2} \right)}, \quad (\text{D.1})$$

where,  $f_m$  is the frequency of the arrival and S/N is the signal-to-noise ratio. The peak frequency in the seismic surveys was 40 Hz. This frequency was used as the frequency of the arrival. An estimated signal-to-noise ratio for the seismic shots of 5.26 was found by dividing the RMS of the peak arrival amplitude by the RMS of the peak noise amplitude. Solving Equation D.1 using these numbers a traveltime error of 5.16 ms was found. Since the frequency and signal to noise ratio is different in the GPR surveys a different error is found. The GPR survey had a peak frequency of 50 MHz and estimated signal-to-noise ratio of 2.46. Using Equation 3.1 a traveltime pick error of 7.10 ns was found for the GPR survey.

## D.2. Resolution Matrices

All the different surveys were solved with straight ray inversion using the singular value decomposition method. SVD has a unique feature of being able to derive both a model resolution and data resolution matrix (see Appendix B). The model resolution was found to be

$$R_m = A_g^{-1} A = V_p V_p^T, \quad (\text{D.2})$$

while the data resolution matrix was given as

$$R_d = A_g^{-1} A = U_p U_p^T. \quad (\text{D.3})$$

where  $U_p$  is the matrix of eigenvectors with non-zero eigenvalues that span the data space, and  $V_p$  is the matrix of eigenvectors with non-zero eigenvalues that spans the model space.

### D.2.1. 2D Seismic Surveys

A look at the eigenvalue matrix ( $\Lambda$ ) reveals the total amount of non-zero eigenvalues (Figure D.1). The lower and upper 2D surveys produce 1355 and 544 non-zero eigenvalues respectively. Eliminating all eigenvalues less than  $10^{-10}$  further filtered the non-zero eigenvalues. These values, ranging from  $10^{-10}$  to  $10^{-96}$ , were removed as they are believed to be errors due to machine resolution. This reduces the non-zero eigenvalues to a total of 1082 and 463 respectively. The remaining eigenvalues allow the  $U_p$  and  $V_p$  matrices to be  $2808 \times 1082$  and  $1406 \times 1082$  for the lower survey and  $3660 \times 463$  and  $552 \times 463$  for the upper survey.

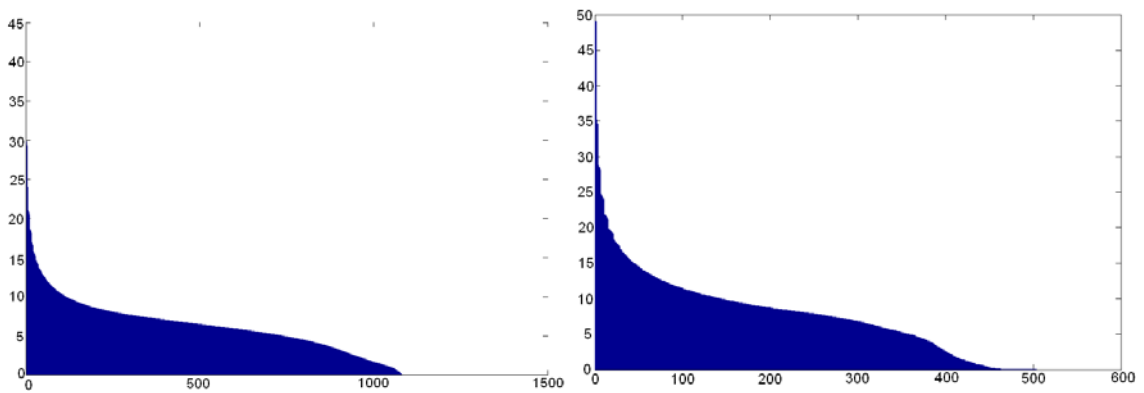


**Figure D.1: Display of the diagonal elements of the eigenvalue matrix  $L$  for the 2D lower survey (left) and 2D upper survey (right).**

The model resolution matrix separates the model parameters into two different categories, the non-zero eigenvalues that contribute to the data and the zero eigenvalues that have no contribution to the data (Xu and Stewart, 2000). All of the diagonal elements for both the upper and lower surveys show only values of 0 or 1 (Figure D.2). This is an indication that each parameter is being estimated independently from the others (Mahmoudian, 2006). The model parameters that show a diagonal value of 0 correspond to grids with no ray coverage. The remaining non-zero values correspond to those grids that can be solved. The lower survey displays a total of 1082 solvable grids with the upper survey resulting in 463 solvable grids. While the model resolution matrix indicates which grids can be solved and where they are located it does not reveal how trustworthy the solved values are.

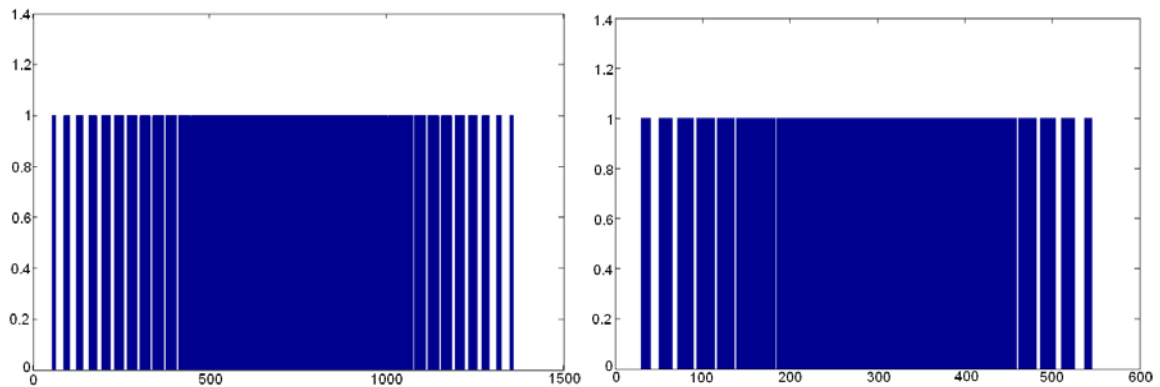


**Figure D.2: Display of the diagonal elements of the model space resolution matrix  $V_p V_p^T$  for the 2D lower survey (left) and 2D upper survey (right).**

The data resolution matrix enables a look at the discrepancy between the observed and predicted data. If there were no discrepancy between the observed and predicted data the data resolution matrix would be equivalent to the identity matrix. A look at the diagonal elements of the data space resolution matrix shows that the values have a large range (Figure D.3). The larger values correspond to a higher covariance level. In both the

lower and upper surveys the larger values correspond to the rays that have the longest distance to travel. The shortest distance rays have the smallest covariance level. The lower survey displays a higher average value than that of the upper survey. This is as expected as the upper survey was greatly affected by the location of a looters trench, which made the resultant velocity model less reliable.

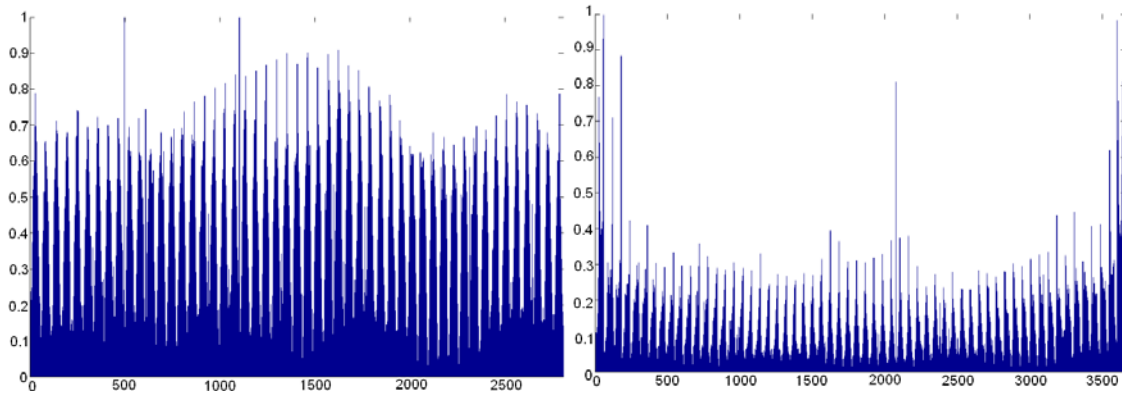


**Figure D.3: Display of the diagonal elements of the data space resolution matrix  $U_p U_p^T$  for the 2D lower survey (left) and 2D upper survey (right).**

### *D.2.2. 3D Seismic Surveys*

The graph of the diagonal elements of the  $\Lambda$  matrix (Figure D.4) displays the amount of non-zero eigenvalues in the lower and upper 3D surveys. After excluding the eigenvalues with values less than  $10^{-10}$  the lower survey has a total of 1318 remaining eigenvalues whereas the upper survey has 594 remaining eigenvalues. Therefore,  $V_p$  and  $U_p$  are the matrices formed from the first 1318 columns of the  $U$  and  $V$  matrix for the lower and the first 594 columns for the upper survey.

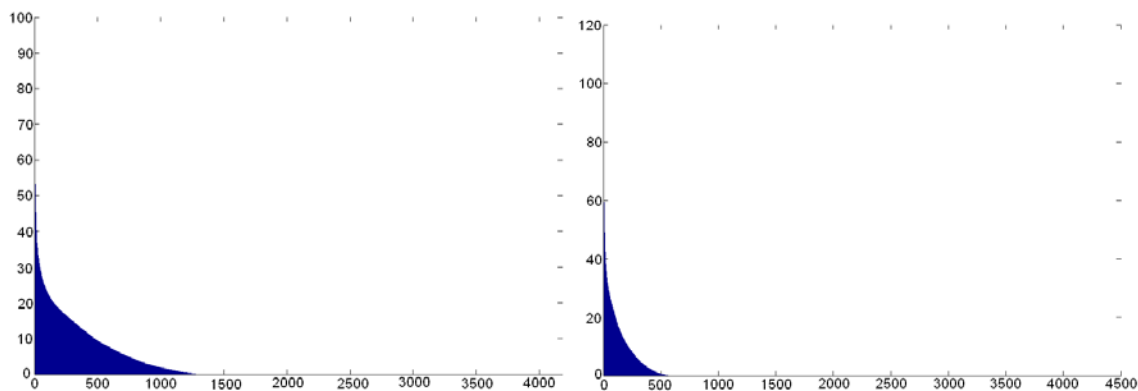


**Figure D.4: Display of the diagonal elements of the eigenvalue matrix  $L$  for the 3D lower survey (left) and 3D upper survey (right).**

The model space resolution matrix once again indicates which grid locations have ray coverage, and therefore contribute to the data (Figure D.5). A total of 1326 contributing grids were found for the lower survey and 594 for the upper. Unlike the 2D surveys, the 3D surveys show non-zero values that are not equal to one. The model parameters with value between 0 and 1 correspond to areas of low fold with fold values of 3 m or less. These are grids that contribute little to the final models. The upper 3D survey shows a lot fewer grids with ray coverage. This is as expected as the lower survey has source and receiver locations lower than those of the upper as well as the top receiver is on a higher vertical contour for the lower than the upper.

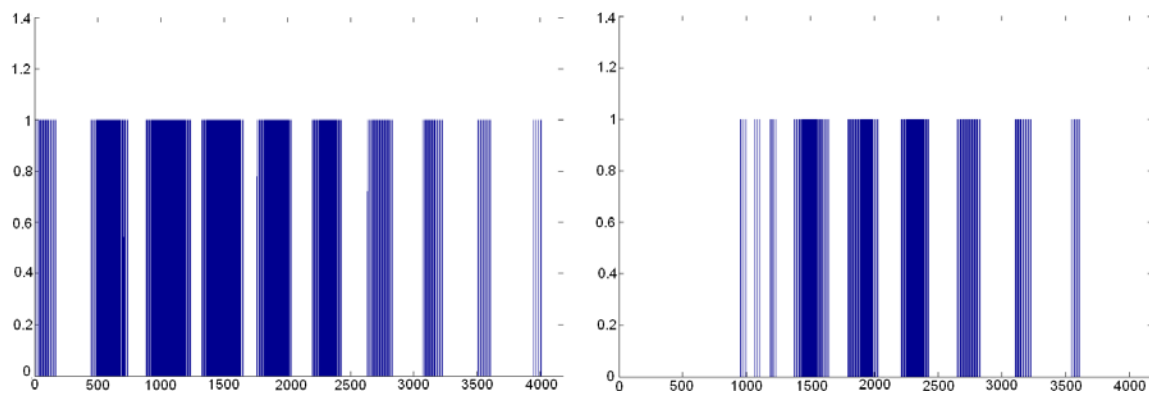


**Figure D.5: Display of the diagonal elements of the model space resolution matrix  $V_p V_p^T$  for the 3D lower survey (left) and 3D upper survey (right).**

The data space resolution matrix (Figure D.6) for the lower 3D survey shows a larger amount of high values in approximately the first 2200 and the last 200 parameters. The beginning region corresponds to those sources that were placed up the slopes of the pyramid. These sources produce rays that have to travel a further distance than those found in the 2D survey resulting in a higher coherence. There is also a section of high coherence in the final parameters that correspond to those sources that did not fit in the 2D survey and were placed down the slope. There were also receivers that were excluded from the 2D survey and were re-included in the 3D survey. These receivers were also placed on the slope down the side of the pyramid resulting in longer distances for the rays. This allows for a larger number of high values to be included in the middle section that corresponds to the 2D survey. The upper 3D survey displays the same high value feature at the start corresponding to the slope shots. The remaining parameters correspond well to those of the 2D survey with the difference being a result of the difference in pixel size.

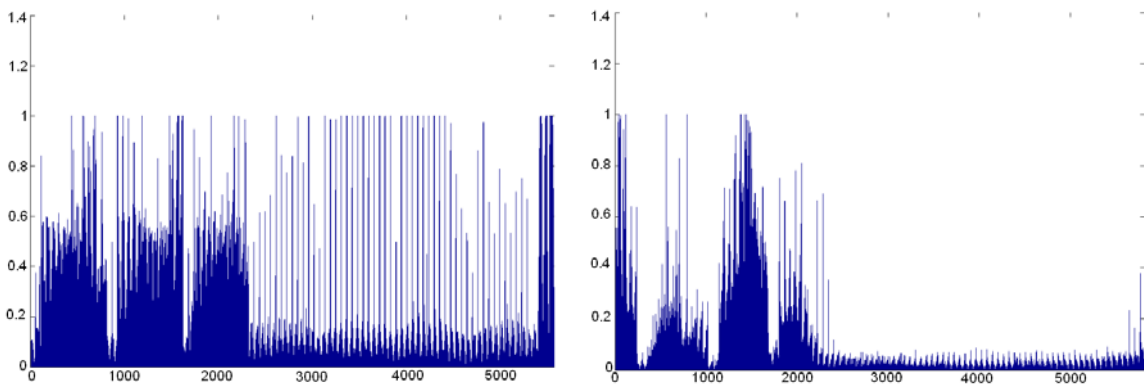


**Figure D.6: Display of the diagonal elements of the data space resolution matrix  $U_p U_p^T$  for the 3D lower survey (left) 3D upper survey (right).**

### ***D.2.3. GPR Survey***

A total of 241 non-zero eigenvalues were found for the 2D and 3D GPR surveys (Figure D.7) after all values smaller than  $10^{-10}$  were filtered. This results in the  $V_p$  and  $U_p$

being formed from the first 241 columns of  $\mathbf{V}$  and  $\mathbf{U}$  with  $\mathbf{V}_p$  and  $\mathbf{U}_p$  being a matrix of 1144 x 241 and 735 x 241 respectively. The first matrix found was the model resolution matrix displayed in Figure D.8. If the resolution were perfect the model resolution matrix would be the identity matrix. There are multiple values in the model resolution matrix that are not the expected values of 0 and 1. There are a total of 280 grids with ray coverage however, a total of only 241 non-zero eigenvalues were found. This is an indication that some estimates found were dependent on others. The 3D survey shows very similar results to those of the 2D with only a slight change in some of the values between 0 and 1.

The data space resolution matrices for the 3D and 2D GPR surveys (Figure D.9) show similar results. Since the GPR signal transmitted only through approximately 10 m of earth on either side of the transmission point there are only a few regions of high coherence. The majority of the points fall in the lower range that corresponds to the smaller distance traveled.

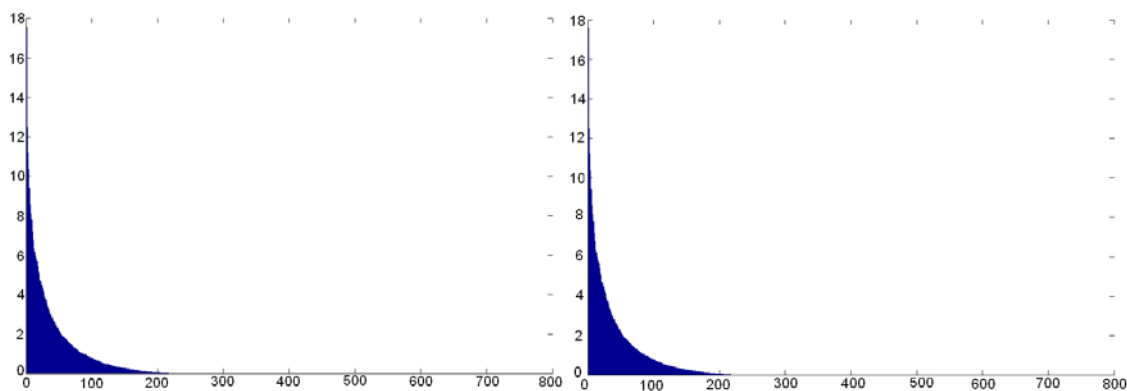


**Figure D.7: Display of the diagonal elements of the eigenvalue matrix  $\Lambda$  for the 2D (left) and 3D (right) GPR survey.**

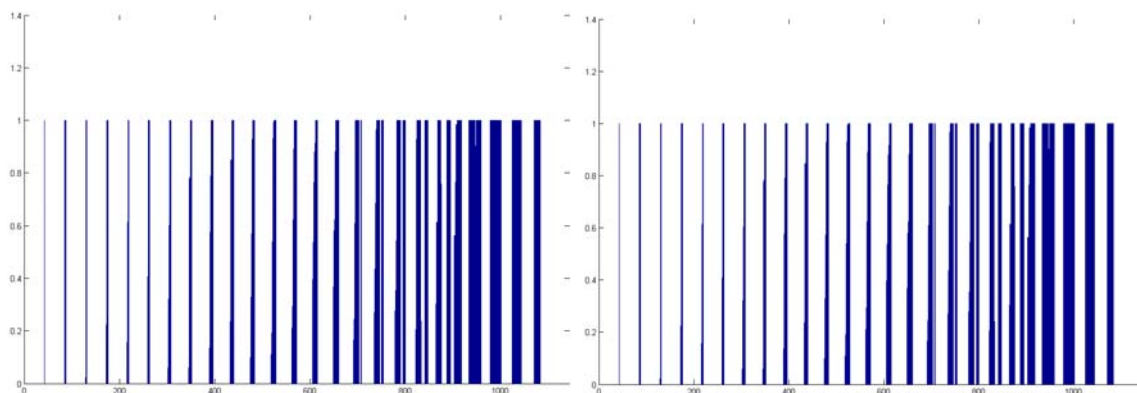


**Figure D.8: Display of the diagonal elements of the model space resolution matrix  $V_p V_p^T$  for the 2D (left) and 3D (right) GPR matrix.**

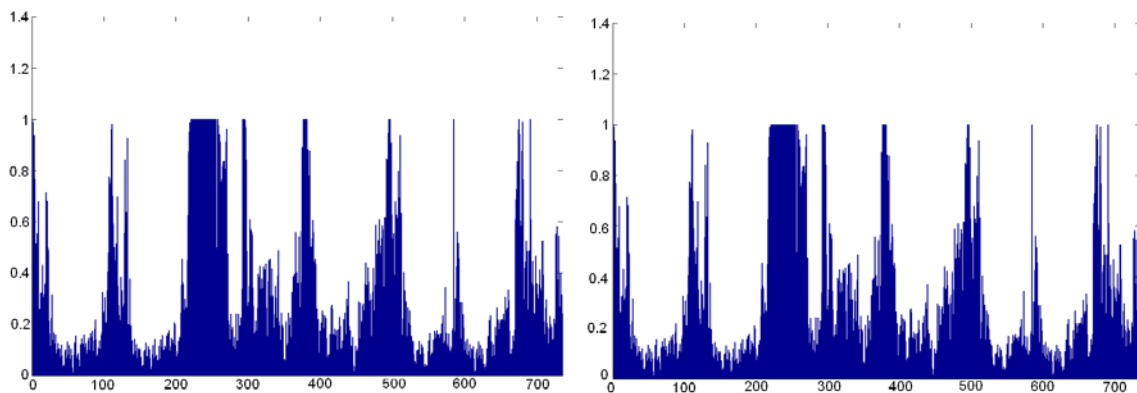


**Figure D.9: Display of the diagonal elements of the data space resolution matrix  $U_p U_p^T$  for the 2D (left) and 3D (right) GPR survey.**

## **APPENDIX E: COMPARISON OF STRAIGHT RAY INVERSION METHODS**

As mentioned in the previous chapters both the seismic and GPR surveys were solved using straight ray tracing using four different traveltimes inversion techniques. These techniques include direct division, damped least squares, singular value decomposition and conjugate gradient. To determine which method is the most beneficial for the surveys each method was directly compared.

To compare the different methods three different statistics were examined. The first statistic examined are the differences between the first break traveltimes observed from the shot gathers and the calculated traveltimes found using the derived velocity model and the distance matrix **A**. The standard deviation and average of the absolute value of the differences will both be compared. The second feature that will be compared is the computation time of each program. This is a vital statistic if the inversion method has a minimal advantage in other categories but takes a great deal longer it may be advantageous to use a faster method. The third and final statistic being compared is the amount of unphysical values produced by the inversion method. Unphysical values are derived velocity values that are negative or higher than the believed upper limit of velocities in the pyramid. These upper limits are determined from the properties of the rock samples taken from the pyramid and based on the results of the inversions.

### **E.1. Seismic Surveys**

#### ***E.1.1. Lower 2D Survey***

The first survey examined is the lower 2D seismic survey. A look at the velocity models found from all four methods show that the general structure appears to be very similar (Figure E.1). All four methods show the same range of velocities with a low

velocity region in the center. Upon closer examination the three direct methods (DD, DLS and SVD) show almost identical velocity models whereas the iterative conjugate gradient method with 30 iterations is similar but has visible differences. It is possible that after 30 iterations the conjugate gradient method has not finished converging and therefore the velocity model for the conjugate gradient method after 250 iterations will be included in the comparisons.

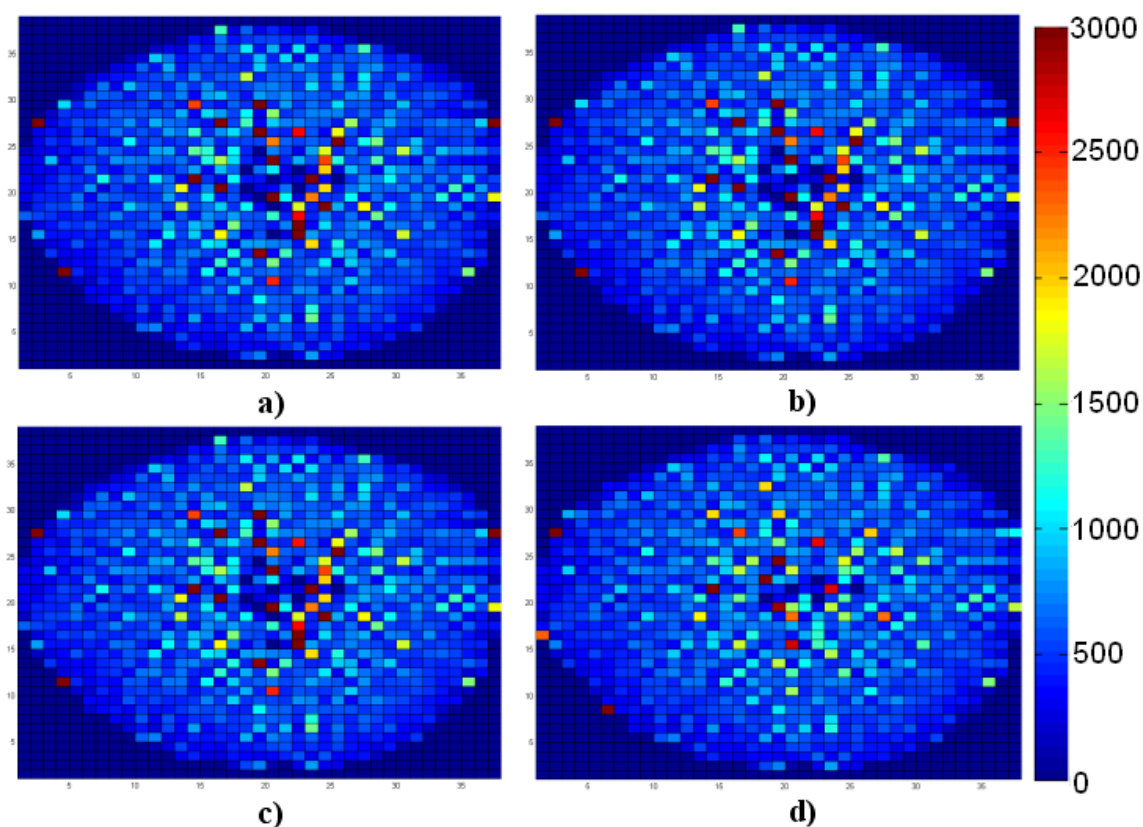


**Figure E.1: The derived velocity structures of the lower 2D survey found using a) DD, b) DLS, c) SVD and d) CG with 30 iterations. All values greater than 3000 m/s and less than 0 m/s are set equal to 3000 m/s and 0 m/s respectively.**

After solving 250 iterations of the conjugate gradient method the velocity model (Figure E.2) derived now more closely approaches that of the direct methods. Now that all four methods appear to give the same results a closer look at the differences between

the observed traveltimes and the calculated traveltimes found using the derived velocity models is used to determine the most appropriate inversion method.

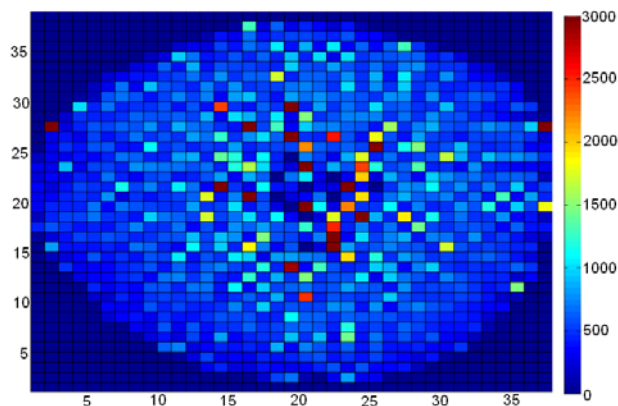


**Figure E.2: The derived velocity structure in m/s of the lower 2D survey found using CG with 250 iterations**

The graphs of the differences in traveltimes for all four methods once again appear near identical (Figure E.3). The only method with any distinguishable differences is the conjugate gradient method with 30 iterations. This is as expected since the velocity models appear identical for each of the other methods. To determine which method is the best the average difference and standard deviation of the differences were calculated and displayed in Table E.1. The average and standard deviation of all three direct methods are exactly the same. The CG methods show a slightly higher average difference and standard deviation at 30 iterations. This difference was reduced to 0.001 ms when the CG gradient was increased to include 250 iterations. There is no clear way to distinguish which of these three methods performed better based on these statistics as all methods produced such similar results.

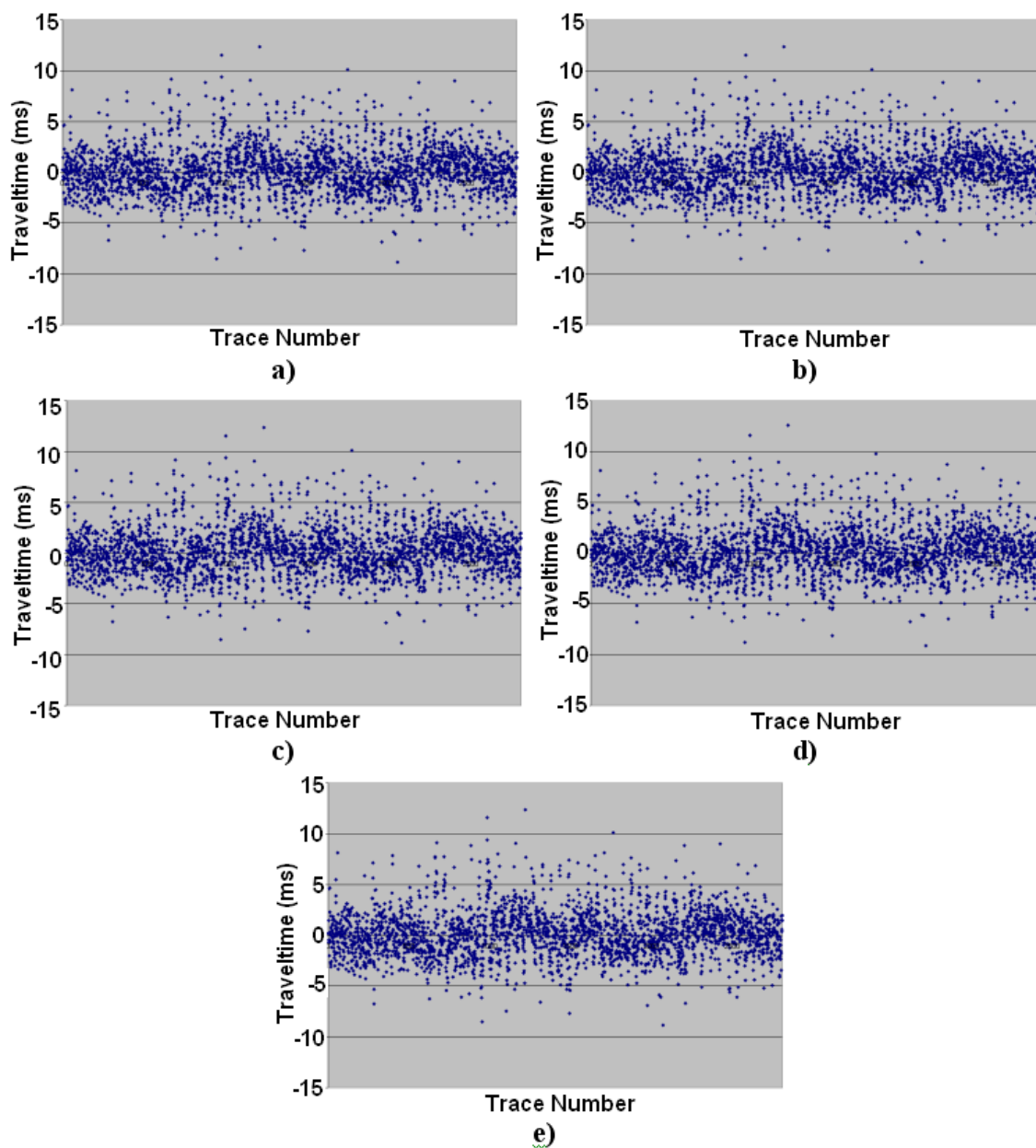


**Figure E.3: The differences between the observed and calculated traveltimes found using the velocity models derived from a) DD b) DLS c) SVS d) CG with 30 iterations and e) CG with 250 iterations.**

	<b>DD</b>	<b>DLS</b>	<b>SVD</b>	<b>CG 30 iter</b>	<b>CG 250 iter</b>
<b>Average (ms)</b>	1.594	1.594	1.594	1.628	1.595
<b>Standard Deviation (ms)</b>	2.296	2.296	2.296	2.338	2.297

**Table E.1: The standard deviation and average of the differences between the observed and calculated traveltimes for the lower 2D survey.**

The next statistic that was examined was the number of unphysical values. Both negative values and velocities greater than 3000 m/s were considered unphysical based on the rock properties and the velocity model results. Once again all the results appear very similar except for those given by the CG method with 30 iterations (Figure E.4). The 30-iteration CG method contains fewer unphysical values than all the other methods. The total number of low and high unphysical values for the lower 2D survey can be seen in Table E.2. The CG method using 30 iterations has a significantly lower number of unphysical values. This gives an indication that the CG method may be the best method to use. When using 250 iterations the CG method produces a very similar amount of unphysical values to the other methods; however, is still 1 value lower.

Looking at both the differences and the unphysical values there is still no clear method that has a significant advantage over the others. While the three direct approaches gave better results when looking at the traveltimes difference the CG method produced fewer unphysical values. A final statistic that may be able to determine the most appropriate method to use is the computation time. All four methods were solved in Matlab using the same Pentium 4 2.4 GHz computer with 512mb RAM. Each method was run a total of five times and averaged to reduce any error in times. The results for the lower 2D survey can be seen in Table E.3. The CG method with 30 iterations produces the fastest run times followed by the CG with 250 iterations and then the DLS method. A surprising feature is that even when using 250 iterations the CG method remains faster than the other three methods. The SVD method produces significantly slower times than the other methods with times 10 times slower than the 250-iteration CG and the DLS.

However, since the survey consists of a relatively small number of shots and receivers all the times remain relatively quick.

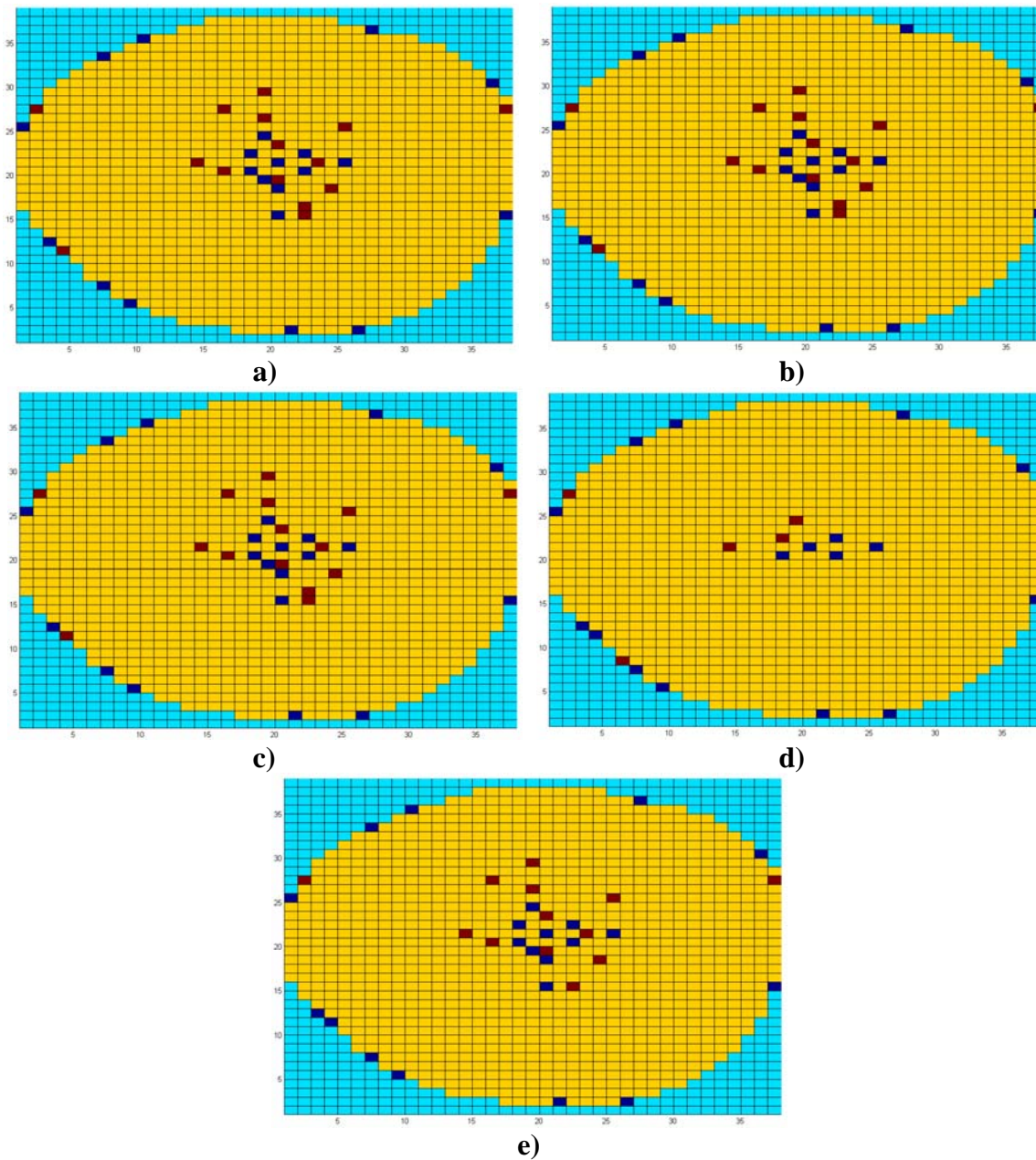


**Figure E.4: The unphysical velocity locations found using a) DD b) DLS c) SVD d) CG with 30 iterations and e) CG with 250 iterations. Negative velocities shown in blue with velocities greater than 3000 m/s shown in red.**

<b>Velocities</b>	<b>DD</b>	<b>DLS</b>	<b>SVD</b>	<b>CG (30 iter)</b>	<b>CG (250 iter)</b>
<b>Negatives</b>	21	21	21	17	22
<b>&gt;3000m/s</b>	15	15	15	5	13
<b>Total</b>	36	36	36	22	35

**Table E.2: The number of unphysical values in the velocity models of the lower 2D surveys.**

<b>Run #</b>	<b>DD</b>	<b>DLS</b>	<b>SVD</b>	<b>CG (30 iter)</b>	<b>CG (250 iter)</b>
<b>1</b>	14.93	11.39	105.12	3.80	11.13
<b>2</b>	14.96	11.12	126.27	3.76	10.85
<b>3</b>	14.96	10.81	121.85	3.73	10.95
<b>4</b>	15.36	13.97	119.22	3.71	11.53
<b>5</b>	15.03	9.50	114.91	3.78	10.88
<b>Average</b>	<b>15.05</b>	<b>11.36</b>	<b>117.47</b>	<b>3.75</b>	<b>11.07</b>

**Table E.3: The run times in seconds of the inversion techniques for the lower 2D survey.**

For the lower 2D survey there is no inversion method that produces a significant advantage over the other methods. The three direct methods produced the lowest traveltimes differences while the CG methods produced fewer unphysical values. Due to the size of this survey all the run times were relatively short with CG using 30 iterations having the quickest run time. To find if one method is advantageous over the other methods other surveys have to be considered.

### *E.1.2. Upper 2D Survey*

A similar comparison of the different straight ray methods was undertaken on the upper 2D survey. When examining the differences between the observed and calculated traveltimes all methods again produced a similar graph. Figure E.5 shows the graph of the differences for the singular value decomposition method. Using the differences in traveltimes the average and standard deviations were found (Table E.4). Once again the three direct methods have the same values with the conjugate gradient method with 250 iterations being very similar. The 30-iteration CG once again has the highest values. However, the difference from the other methods remains small.

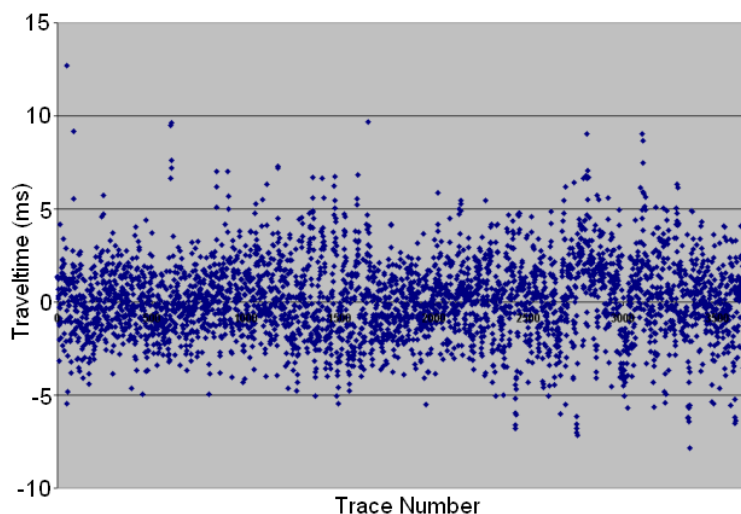


**Figure E.5: The differences between the observed and calculated traveltimes found using the velocity model derived from SVD.**

	<b>DD</b>	<b>DLS</b>	<b>SVD</b>	<b>CG (30 iter)</b>	<b>CG (250 iter)</b>
<b>Average (ms)</b>	1.625	1.625	1.625	1.650	1.625
<b>Standard Deviation (ms)</b>	2.108	2.108	2.108	2.139	2.109

**Table E.4: The standard deviation and average of the differences between the observed and calculated traveltimes for the lower 2D survey.**

The next comparison made on the upper 2D survey was the amount of unphysical values. Unphysical values were determined to be any velocity less than zero or greater than 3000 m/s. Figure E.6 shows the location of all the unphysical values for all five methods. Similar to the traveltime differences DD, DLS and SVD all show the same amount of unphysical values. As seen in Table E.5, both the 30- and 250-iteration CG method show a fewer amount of non-physical values. The 30-iteration CG shows a significantly fewer amount of both the unphysical high and low velocity values.

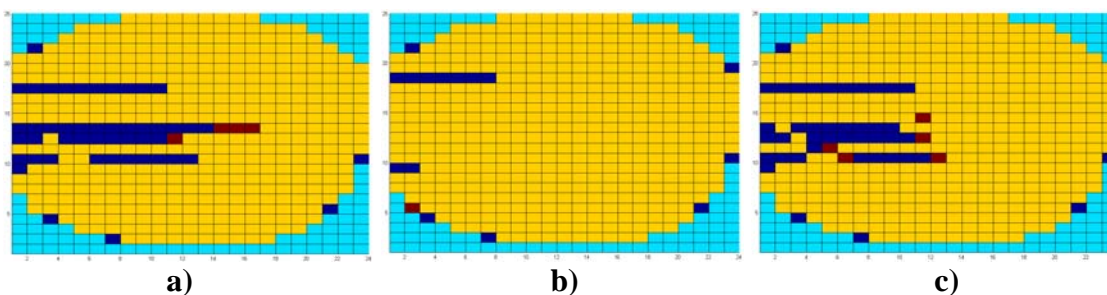


**Figure E.6: The unphysical velocity locations found using a) DD, DLS, SVD b) CG with 30 iterations and c) CG with 250 iterations for the upper 2D survey. Negative velocities shown in blue with velocities greater than 3000 m/s shown in red.**

Velocities	DD	DLS	SVD	CG (30 iter)	CG (250 iter)
Negatives	48	48	48	15	42
> 3000m/s	4	4	4	1	5
<b>Total</b>	52	52	52	16	47

**Table E.5: The number of unphysical values in the velocity models of the lower 2D surveys.**

The next statistic examined for all the different straight ray traveltimes methods was the computation time. Table E.6 shows that CG with 30 iterations once again has the fastest computation time. The second fastest method is the DLS with the 250 iteration CG following shortly after. Again, SVD is significantly slower than the other methods.

Run #	DD	DLS	SVD	CG (30 iter)	CG (250 iter)
<b>1</b>	4.19	1.65	12.32	0.785	2.09
<b>2</b>	4.21	1.64	12.37	0.808	2.21
<b>3</b>	4.24	1.60	12.23	0.806	2.18
<b>4</b>	4.18	1.59	12.26	0.810	2.17
<b>5</b>	4.18	1.63	12.42	0.760	2.22
<b>Average</b>	<b>4.20</b>	<b>1.62</b>	<b>12.32</b>	<b>0.794</b>	<b>2.17</b>

**Table E.6: The run times in seconds of the inversion techniques for the upper 2D survey.**

With the upper 2D survey there is once again no method that has a significant advantage over the other methods. The three direct methods remain the most accurate when considering traveltimes differences whereas CG has fewer unphysical values. The

CG and DLS methods appear to have the fastest computation time but all methods are solved within a reasonable amount of time.

### *E.1.3. Lower 3D survey*

The lower 3D survey gives the first chance to compare the different methods on a larger survey. The lower 3D survey has a much larger area of coverage as well as a larger amount of rays. A look at the differences between the measured and calculated traveltimes starts to show a separation in the average and standard deviation (Table E.7). The three direct methods remain very close with DD having a slightly lower average difference than the other two. The CG method with 250 iterations shows the lowest standard deviation value for the differences with an average that is only slightly above those of the direct methods.

	<b>DD</b>	<b>DLS</b>	<b>SVD</b>	<b>CG (30 iter)</b>	<b>CG (250 iter)</b>
<b>Average (ms)</b>	2.033	2.038	2.035	2.121	2.042
<b>Standard Deviation (ms)</b>	2.762	2.772	2.763	2.836	2.760

**Table E.7: The standard deviation and average of the differences between the observed and calculated traveltimes for the lower 3D survey.**

The number of unphysical values shows the same trend as the 2D surveys (Table E.8). The lowest number of unphysical values is seen in the CG methods. One difference from the 2D surveys is that the DLS method is producing more unphysical values than DD or SVD. The computation times of the lower 3D survey follow the same trend as the 2D surveys. Table E.9 displays all the computational times with CG having the quickest times with both the 30 and 250 iterations. With the increase in survey size the difference in computational time is now starting to become significant with a large difference in time separating the fastest (CG) and the slowest (SVD). This makes the CG method more

attractive as it has similar results in the traveltimes differences whereas it has superior results in both unphysical values and computation time.

	<b>DD</b>	<b>DLS</b>	<b>SVD</b>	<b>CG (30 iter)</b>	<b>CG (250 iter)</b>
<b>Negative</b>	157	161	155	32	123
<b>&gt; 3000m/s</b>	13	14	15	62	26
<b>Total</b>	170	175	170	94	149

**Table E.8: The number of unphysical values in the velocity models of the lower 2D surveys.**

<b>Run #</b>	<b>DD</b>	<b>DLS</b>	<b>SVD</b>	<b>CG (30 iter)</b>	<b>CG (250 iter)</b>
<b>1</b>	186.19	209.26	7778.29	52.89	108.04
<b>2</b>	192.04	205.69	7582.52	55.93	104.73
<b>3</b>	189.40	276.62	7874.46	54.90	108.45
<b>4</b>	190.67	257.15	7719.01	51.05	105.31
<b>5</b>	187.10	220.34	7938.72	52.20	108.79
<b>Average</b>	<b>189.08</b>	<b>233.81</b>	<b>7778.60</b>	<b>53.39</b>	<b>107.06</b>

**Table E.9: The run times in seconds of the inversion techniques for the lower 3D survey.**

#### *E.1.4. Upper 3D Survey*

The upper 3D survey displays some interesting results when looking at the standard deviation and average of the differences between the observed and calculated traveltimes (Table E.10). The DD method was found to produce the most accurate results. For the first time the 250-iteration CG method is producing more accurate results than the DLS and SVD methods, which are close behind, while the 30-iteration CG once again produced the least accurate model. When looking at both the upper and lower 3D surveys the 250 iteration CG method has improved from the 2D surveys with the standard deviation being near the lowest value in both surveys and the average being the second lowest in the upper 3D survey. This may be an indication that as the survey size increases the CG gradient method should become the method of choice.

The amount of unphysical values (Table E.11) again shows a similar trend to those in the other surveys. The lowest amounts of unphysical values appear in the CG methods with 30 iterations producing the fewest number. The three direct methods once again produce very similar distributions of negative and high velocity values. With the CG method producing the fewest amounts of unphysical values it appears that it is establishing itself as the preferred method for this survey.

	<b>DD</b>	<b>DLS</b>	<b>SVD</b>	<b>CG (30 iter)</b>	<b>CG (250 iter)</b>
<b>Average (ms)</b>	2.640	2.651	2.651	2.711	2.646
<b>Standard Deviation (ms)</b>	3.522	3.528	3.528	3.586	3.527

**Table E.10: The standard deviation and average of the differences between the observed and calculated traveltimes for the upper 3D survey.**

	<b>DD</b>	<b>DLS</b>	<b>SVD</b>	<b>CG (30 iter)</b>	<b>CG (250 iter)</b>
<b>Negatives</b>	74	74	74	28	69
<b>&gt; 3000m/s</b>	17	17	16	34	16
<b>Total</b>	91	91	90	62	85

**Table E.11: The number of unphysical values in the velocity models of the upper 3D survey.**

The computation time (Table E.12) once again shows a significant advantage for the conjugate gradient method. The next fastest method was DD with an increased time of 50 seconds. The SVD once again is significantly slower than the other methods and may not be advantageous to use with the extra time. The CG again shows a clear advantage as the 250-iteration CG method has the second lowest average traveltime difference and the CG methods display the least amount of unphysical values and smallest computation times.

## **E.2. GPR Survey**

By examining the results of the four different methods on the GPR surveys, an indication of which method works the best on a very small survey can be determined. The

GPR surveys contain only approximately a quarter of the rays of the 2D seismic surveys and therefore can be representative of the smaller sized surveys. Since the 2D and 3D GPR surveys were very similar the results of both will be examined at the same time.

Run #	DD	DLS	SVD	CG (30 iter)	CG (250 iter)
<b>1</b>	161.92	288.79	6040.15	47.79	99.48
<b>2</b>	151.40	247.38	6151.17	44.84	100.83
<b>3</b>	154.66	257.93	6100.20	46.72	99.98
<b>4</b>	141.75	238.75	6149.75	44.62	98.92
<b>5</b>	153.22	260.59	6098.89	44.59	109.21
<b>Average</b>	<b>152.59</b>	<b>258.69</b>	<b>6108.03</b>	<b>45.71</b>	<b>101.68</b>

**Table E.12: The run times in seconds of the inversion techniques for the lower 3D survey.**

Unlike the seismic surveys, the GPR survey produces significantly different velocity models depending on the method used (Figure E.7). The CG method appears to provide the most accurate velocity model based on greater appearance of velocity structure in the areas of low coverage. The three direct approaches produce few distinguishable velocities in these regions. To help determine whether this visual assessment is correct differences between the observed and calculated traveltimes were solved.

The standard deviation and average of the differences between the observed and calculated traveltimes were solved and displayed in Table E.13. The results show some interesting features. The DD method produces the best average value for the 3D and second best for the 2D survey. The lowest standard deviations are found using the DD and SVD method. All methods with the exception of the 30 iteration CG method showed improvement from the 2D to 3D. It is difficult to choose the most accurate method based solely on this data as the different methods produced similar but varied statistics with no single method dominating all categories.

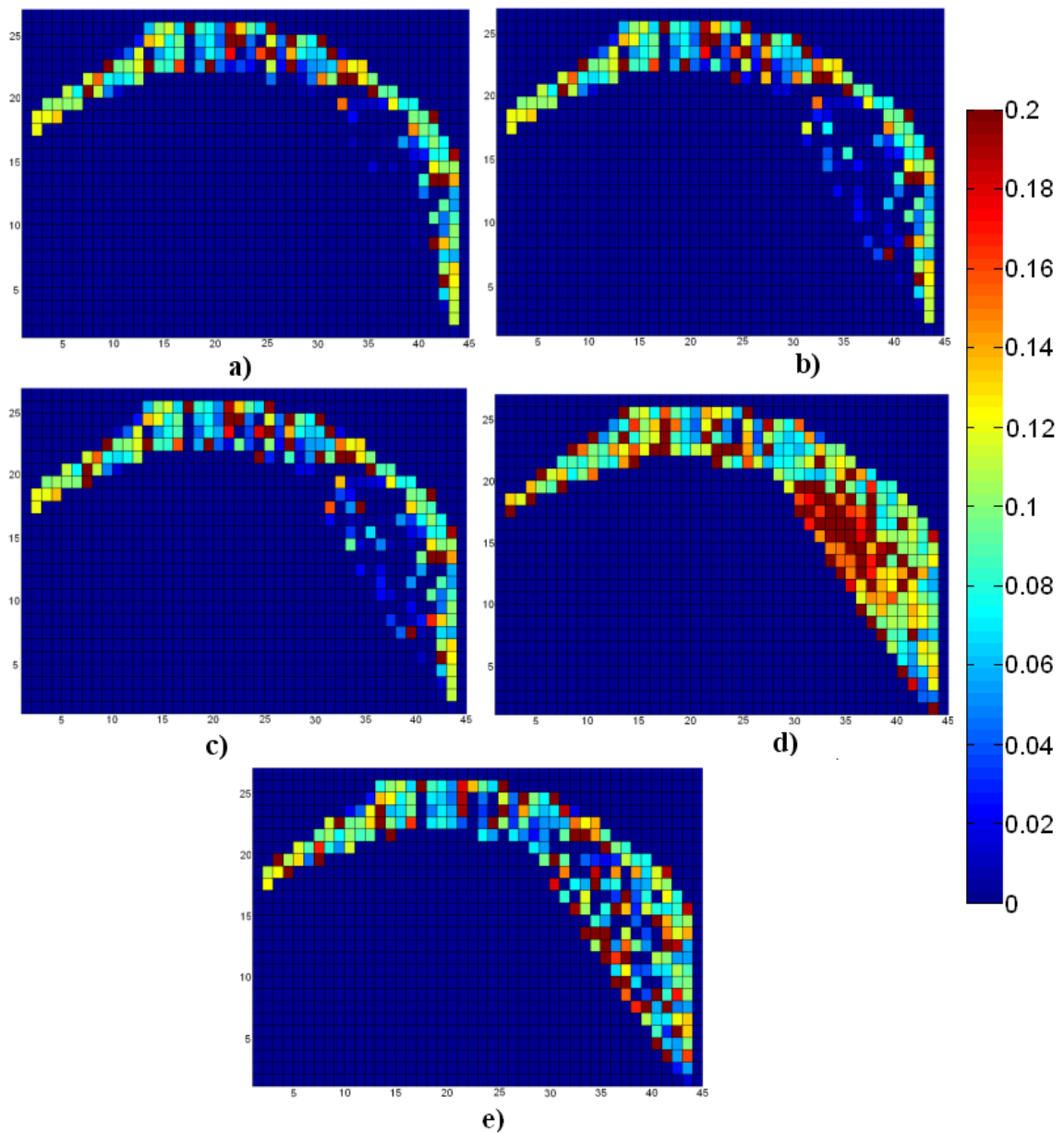


**Figure E.7: The derived velocity structures of the 2D GPR survey found using a) DD, b) DLS, c) SVD d) CG with 30 iterations and e) CG with 250 iterations. All values greater than 0.2m/ns and less than 0 m/ns are set equal to 0.2 m/ns and 0 m/ns respectively.**

	<b>DD</b>	<b>DLS</b>	<b>SVD</b>	<b>CG (30 iter)</b>	<b>CG (250 iter)</b>
<b>2D Average (ns)</b>	1.568	1.650	1.567	1.710	1.602
<b>2D Standard Deviation (ns)</b>	2.314	2.362	2.314	2.412	2.329
<b>3D Average (ns)</b>	1.562	1.609	1.563	1.714	1.594
<b>3D Standard Deviation (ns)</b>	2.308	2.322	2.309	2.411	2.322

**Table E.13: The standard deviation and average of the differences between the observed and calculated traveltimes for the GPR 2D and 3D survey.**

The unphysical values also show a few interesting features (Table E.14). The three direct approaches showed improvement with the move from 2D to 3D. This is to be expected as the ray path becomes closer to its actual length. The CG gradient does not show this expected improvement. The values remain close between the 2D and 3D surveys; however, there is a slight increase in the 3D survey for the CG method. For the first time the DD method is producing fewer unphysical values than the 250 iteration CG method. The 30-iteration CG method remains the best method producing the fewest number of unphysical values. One interesting feature that has been observed throughout the different surveys is the distribution of the unphysical values between high and low values. The CG method has consistently produced fewer negative velocities and a greater number of high values. The larger number of high velocity values is the preferred distribution as there is no possibility a negative velocity could be physical while it is possible that there would be a region of unexpectedly high velocity in the pyramid allowing for the possibility that a small percentage of the high values may in fact be physical.

The 3D and 2D GPR surveys showed very comparable traveltimes therefore only the traveltimes of the 2D survey are displayed in Table E.15. The CG method with 30 iterations again provides the fastest times. The second fastest method was found to be

DD. The SVD method is significantly slower than those of the other methods. The DD method appears to have established itself as the most accurate method on the GPR surveys. The DD and CG methods both provide evidence that they may be the most appropriate method to use on the GPR surveys. The 30-iteration CG method provided the fewest unphysical values, the quickest computation times and the second lowest standard deviation behind the 250 iteration CG method. The CG method also showed improvement when the survey became 3D, which could be an indication that CG is more versatile. The DD provided better results in the average traveltime differences and followed closely behind the 30-iteration CG method in both unphysical values and computation time.

	<b>DD</b>	<b>DLS</b>	<b>SVD</b>	<b>CG (30 iter)</b>	<b>CG (250 iter)</b>
<b>2D Negatives</b>	62	78	76	7	46
<b>2D &gt;0.2m/ns</b>	20	22	22	61	35
<b>2D Total</b>	<b>82</b>	<b>100</b>	<b>98</b>	<b>68</b>	<b>81</b>
<b>3D Negatives</b>	62	78	74	7	43
<b>3D &gt; 0.2 m/ns</b>	20	20	22	62	42
<b>3D Total</b>	<b>82</b>	<b>98</b>	<b>96</b>	<b>69</b>	<b>85</b>

**Table E.14: The number of unphysical values in the velocity models of the 2D and 3D GPR surveys.**

<b>Run #</b>	<b>DD</b>	<b>DLS</b>	<b>SVD</b>	<b>CG (30 iter)</b>	<b>CG (250 iter)</b>
<b>1</b>	1.81	2.73	36.32	1.11	4.50
<b>2</b>	1.81	2.64	36.32	1.12	4.47
<b>3</b>	1.80	2.63	36.34	1.13	4.47
<b>4</b>	1.84	2.68	36.38	1.11	4.45
<b>5</b>	1.81	2.61	36.95	1.11	4.45
<b>Average</b>	<b>1.81</b>	<b>2.66</b>	<b>36.46</b>	<b>1.12</b>	<b>4.47</b>

**Table E.15: The run times in seconds of the inversion techniques for the 2D GPR survey.**

### **E.3. Summary**

Three different statistics were examined when comparing the different straight ray traveltime inversion techniques. The first statistic was the differences between the

observed and calculated traveltimes found using the derived velocity models. The standard deviation and average of these traveltime differences were solved and compared. The three direct methods (DD, DLS, SVD) provided similar results that tended to be more accurate than those of the 30- and 250-iteration CG for the 2D seismic surveys. When increasing the survey size to those of the 3D seismic surveys the 250-iteration CG found a smaller standard deviation for both the upper and lower and also found the smallest average for the upper survey. These trends changed once again when decreasing the survey size as in the GPR surveys. In the case of both the 2D and 3D GPR surveys the DD and SVD found the lowest averages and smallest standard deviations. The GPR survey did not provide any clearly advantageous method based on traveltime differences.

When considering the number of unphysical values the CG method consistently produced the fewest amount in all the different surveys with the one exception being DD having fewer than the 250 iteration CG method in the GPR surveys. This provides credibility to the fact that the CG method may be the best method to use to provide the most accurate result despite the higher averages in traveltime differences. This may be the case as the calculated traveltimes were found using the velocity models with the unphysical values included. The exception may once again be in very small surveys like the GPR survey where the DD method provided fewer unphysical values than the 250 iteration CG method as well as a lower average traveltime difference.

The computation time was the final feature considered in deciding which method was the most advantageous to use. The 30-iteration CG method consistently provided the fastest results. In the smaller GPR and 2D seismic surveys the computation times remained small for all methods with the exception of the SVD method. When the survey

size increased the CG method provided significantly faster result using both 30 and 250 iterations.

Despite the small increase in the average difference between the observed and calculated traveltimes the CG remains the most beneficial method. It was also seen that if the average differences are a concern the amount of iterations could be increased resulting in a better average while maintaining its advantage in unphysical values and computation time in larger surveys. In smaller surveys the computation time was less of an issue resulting in DD also being considered. DD provided low averages while maintaining a relatively low computation time and number of unphysical values. If the survey being undertaken has a very large fold where unphysical values are not an issue and is small enough that computation times remain short the DD may provide better results.